STUDY OF PEPTIDE-MINERAL INTERACTIONS

LIANG MEI KEAT

A thesis submitted in partial fulfilment of the
requirements of Nottingham Trent University
for the degree of Doctor of Philosophy

January 2010

Abstract

The studies of peptide-mineral interactions presented within this thesis aimed to identify and understand the effect(s) induced by peptides/selected motifs on amorphous silica and crystalline zinc oxide (ZnO) formation. The effect of imidazole functionality on silica formation was studied using polyvinylimidazole (PVI) and polyhistidine (P-His). The effect of zinc oxide-binding peptides (ZnO-BPs) on the morphology and formation of ZnO were studied using G-12 (GLHVMHKVAPPR) and EM-12 (EAHVMHKVAPRP), and their derivatives, GT-16 (GLHVMHKVAPPRGGGC) and EC-12 (EAHVCHKVAPRP) respectively. The influence of these additives on reaction kinetics, their effect on the precipitates, and their level of incorporation into the precipitates were investigated. This series of studies revealed three common characteristics of peptide-mineral (ZnO-BPs-ZnO and imidazole-silica) interactions.

Firstly, a specific functionality of the biomolecule was responsible for the effect induced while a supporting functionality enhanced the effect. The imidazole group of PVI and P-His catalysed the condensation of monosilicic acid but the peptide backbone and more flexible imidazole enhanced the catalytic capability of P-His with respect to PVI having a similar concentration of imidazole groups. The presence of G-12 and GT-16 reduced the aspect ratio of ZnO crystals formed via an adsorption-growth inhibition mechanism. However the addition of a GGGC-tag on GT-16 weakens the adsorption of GT-16 on the (10-10) face of ZnO crystals. This gave rise to selective adsorption of GT-16 on the (0002) face, with a greater reduction of the crystal aspect ratio. For the EM/EC-12 peptides, metal ion complexation that leads to a delay/suppression of ZnO formation was higher for EC-12 compared to EM-12 and was caused by the more efficient complexation of Zn^{2+} with the peptide containing cysteine.

Secondly, additives can interact with different species in the reaction. Imidazole interacts with neutral monosilicic acid via hydrogen bonds but protonated species of imidazole interact with anionic polysilicic acid via electrostatic interactions. Although EM-12 only interacts with Zn^{2+} in solution, EC-12 was able to interact reversibly with the solid phases formed in the course of reaction.

Thirdly, the type of interaction and interacting species determine the level of additive incorporation and its effect on the concentration of reactants remaining in solution when equilibrium is reached. Peptide-surface interactions generally result in incorporation of the peptide into the solid phase (G-12, GT-16, and EC-12) as opposed to the situation where complexation of reactant species in solution shown by EM-12 did not result in peptide incorporation.

The use of peptides/motifs (biomolecules) isolated from combinatorial libraries for silica and ZnO synthesis has been shown to be a promising approach for morphology and reaction control. It is particularly exciting when their use can be extended to the generation of ZnO which has non-biological origin. By understanding the phenomenal complexity of the behaviour of biomolecules in (bio)mineralising systems, the ground rules in their interactions (with species in (bio)mineralising systems) can be generated and exploited for the synthesis of novel nanomaterials with properties tailored for specific applications.

Dedication

To Swee Yong, Isabelle and our families, without whom the completion of this work would not be possible.

Acknowledgements

First and foremost my thanks go to Professor Carole Perry for offering me the opportunity to carry out this research, her guidance throughout my study, and patience in the compilation of it. Thanks also go to those in the inorganic research department some of whom I have spent the last few years working with, especially, Akhilesh Rai, Tim Green, Muhammad Sohail Zafar, Lindsey Philbin, Graham Hickman, Marion Limo, and Valeria Puddu. Extra special thanks go to Siddharth Patwardhan who helped me to “jump-start” the project and for providing motivation from time to time, Olivier Deschaume for the wonderful molecular modelling results that complement the experimental findings in this study, and David Belton for his assistance in HPLC work. I also want to convey my gratitude to people who have come and gone but have added a lot of flavours and meanings in these three years at Nottingham Trent University including, Agathe Fournier, Heather Currie, Graham Tilburey, Tamar Saison, Asmita Prabhune, Maria del mar Munoz Serrano, Miquel Fabra Gemeno, and Michael Garton. Thanks also to those who helped in collecting data associated with this thesis including, (but in no particular order), Mary Smith from the analytical laboratory, and Mark Sladen and Karen Fowler from the general laboratory; and generally everybody in the chemistry department who have made the time spent at Nottingham Trent University not only rewarding but also very entertaining. Finally funding for this research was gratefully received from AFOSR, US Air Force Office of Scientific Research, FA9550-06-1-0154.

Contents

Chapter 1: Introduction

Chapter 2: Experimental Methods

Chapter 3: Imidazole Catalysed Silica Synthesis: Progress towards Understanding the Role of Histidine in (Bio)silicification

Chapter 4: Studies of ZnO Morphology Modification by Zinc Oxide-Binding Peptides via Selective Adsorption

Chapter 5: Studies of the Delayed Formation of ZnO via the Complexation of Zn^{2+} with ZnO-Binding Peptides

Chapter 6: General Discussion, Conclusions and Future Work

Chapter 1
Introduction

1.1 Bio-Inspired Inorganic Materials Synthesis: An Overview

The superiority of the properties obtained via biomolecule-mediated synthesis is demonstrated by the unique properties, ornate structures and well-controlled growth of biominerals in living organisms.[1] The use of biomolecules for inorganic materials synthesis has been shown to be a promising approach.[2] It is particularly exciting when their use can be proliferated to the generation of metal oxides and metallic elements of non-biological origin. Furthermore, many inorganic materials produced by the bio-inspired approach have been shown to be "workable" when subjected to application testing.[3-7] The biomolecules involved have been identified by very different approaches. The biologist's approach uses conventional methods to extract biomineralising proteins from the hard tissues of biominerals followed by bioextract isolation, purification and cloning.[8-15] As an example, if we consider the mineral silica, the use of the biologist's approach has led to the discovery of silaffins and long-chain polyamines (LCPAs) from diatoms,[9, 10] and silicatein and LCPAs from sponges.[11, 12, 15] These biosilica-associated biomolecules have been studied extensively and have been found to affect the formation of silica,[10, 16-20] silicone,[17] titania,[21] zirconia,[21] and gold on titania[22] *in vitro*. However, the bioextracts obtained from the biologist's approach often contain many proteins which are species-specific, differently active in biomineralisation, and each distributed spatially and temporally in complex ways within the organism itself.[23]

As an alternative to the use of extracted biomolecules (natural or synthesized), model molecules[24] whose properties are already well-known and may exhibit some structural or functional similarity with the extracted biomolecules have been employed. These model molecules are simpler and thus the identification of active moiety(ies) which affect the formation of a mineral *in vitro* is possible. Inspired by biosilica-associated

biomolecules, the following model molecules have been extensively used to study silica[18, 25-33] and mineralized titanium[34] formation: R5 the 19-mer precursor of silaffins-$1A_1$ (Sil-$1A_1$);[18, 25, 30, 34] putrescine;[26] poly(allylamine) (PAA);[34] poly-$_L$-lysine (PLL);[27, 28, 31, 35] poly(allylamine hydrochloride) (PAH);[27] spermine, spermidine and their analogues;[29] propylamines;[32] and amino acids.[31, 33] Generally the presence of these additives has either played the role of a catalyst[18, 26, 29-32] or morphology/size modifier.[27, 28, 32, 34] The effects of these additives are discussed in detail in **Section 1.3**.

The combinatorial biology technique is a well-established technique for biological ligand identification and the mapping of antibodies epitopes, etc.[23, 36] This technique has also been used for the identification of materials-binding peptides because this approach does not require a prior knowledge of the desired amino acid sequence. Moreover peptides that bind to minerals of non-biological origin can be identified.[37-41] In the present context of biomolecule-mediated material synthesis, the combinatorial technique involves the selection of peptides capable of interacting with the surfaces of inorganic materials from a random library (over a billion unique sequences) and then taking this information and attempting to use it to generate materials *de novo in vitro*. The identification of peptides that bind metals and alloys, oxides, sulfides, simple salts such as calcium carbonate, semiconducting materials, and other materials such as zeolites, carbon nanotubes, fullerenes and polymers has proven successful using this approach.[23, 36, 42-44]

The studies of peptide-mineral interactions reported in this thesis aimed to explore the effects of biomolecules/material-binding peptides, mainly identified from phage display libraries, on the synthesis of silica (SiO_2) and zinc oxide (ZnO). Thus, in the section following, **Section 1.2**, a review of the studies involving silica-binding peptides (SiO_2-BPs) and zinc oxide-binding peptides (ZnO-BPs) is presented while the effects of biomolecules on silica formation *in vitro* are discussed in **Section 1.3**. In **Section 1.4**, the properties and applications of ZnO are described. The growth habits of ZnO crystals and the comparison of different synthesis routes are also included in this section. The effects of various biomolecules (amino acids, dipeptides, proteins, ZnO-BPs etc.) on ZnO formation are reviewed in **Section 1.5**. These effects have been grouped and are presented in **Section 1.5** as (i) modification of ZnO morphology, (ii) formation of ZnO nanocomposites, (iii) suppression of ZnO formation, and (iv)

catalysis of ZnO formation. As and when applicable, similar effects induced by non-biomolecular additives will be included for comparison. In the last section of this chapter, **Section 1.6**, the aims of this project are explained and the scope of the project is outlined.

1.2 Combinatorial Libraries and the Identification of Inorganic Material-Binding Peptides

1.2.1 Combinatorial display technique

The combinatorial display technique has been used to screen for biological activities such as catalytic properties, altered affinity, and specificity to target materials. The specificity of a protein for a surface may originate from a chemical recognition mechanism (hydrogen bonding, polarity, and charge effects), structural recognition mechanism (size and morphology), or both.[23] Phage display (PD) and cell surface display (CSD) are commonly used but most research has been performed using a filamentous phage such as M13. A typical affinity selection experiment is a five-step process: (i) generation of random libraries, (ii) binding, (iii) elution, (iv) amplification, and (v) clone sequencing.[23, 36] 7-mer or 12-mer random libraries of peptides are generated by inserting randomized oligonucleotides within certain genes encoded on phage genomes (viral genome) or on bacterial plasmids (DNA plasmid). Thus, each phage or cell produces and displays a different, but random peptide. The target surface to which a peptide ligand is sought is exposed to a PD/CSD combinatorial peptide library for several hours followed by the elimination of non-binders by washing. The bound phages or cells are next eluted from the surface and the amplification process follows. The eluted phages are amplified by reinfecting the host while in CSD, cells are allowed to grow. This completes a round of biopanning and 3-5 cycles of biopanning are repeated to enrich for tight binders. Finally, the individual clones are sequenced to obtain the amino acid sequence of the peptides binding to the target substrate materials.[23, 36]

Despite being very useful, there are limitations to this screening approach. Firstly, the elution of bound phages from the inorganic surfaces may lead to the loss of good binders.[23] Secondly, screening buffers may modify the surface of target materials thus the binding of a new surface is studied rather than the intended ones.[23] Thirdly, growth competition or poor expression of a peptide due to rare codons, misfolding, degradation or inefficient export may also bias the screen.[23] Fourthly, the affinity of a peptide identified depends on whether fusions are to coat proteins pIII or pVIII.[36] Coat proteins pIII and pVIII have different number of copies of the fusion product, thus the type of coat protein impacts the binding affinity and their ability of to adopt a 'free' structure in solution.[44] Last but not least, there is no quantitative information on how much peptide is displayed on the surface and the exact location of binding in relation to the surface is not available.[44]

1.2.2 The identification and studies of silica-binding peptides (SiO_2-BPs) and zinc oxide-binding peptides (ZnO-BPs)

The exhaustive list of polypeptide sequences exhibiting affinity for various inorganic materials in literature[23, 36] is an indication of the extensive use of the combinatorial display method in the study of inorganic materials synthesis. In this section, only the identification and studies involving SiO_2-BP and ZnO-BPs are discussed. As shown in **Table 1.1**, eight 12-mer SiO_2-BPs have been identified by Naik *et al*.,[45] using biogenic silica as the binding target (except for Si4-7) and coat protein pIII. The biogenic silica formed by the catalysis of R5 (SSKKSGSYSGSKGSKRRIL) was a network of spheres with diameter of 400-600nm. Based on the study of the silica precipitation activity and the peptide sequence relationship, the authors believed that the position of the residues would affect the silica precipitation activity of the peptide although the position rules are yet to be discovered. The main finding that emerged from this study was the identification of three sequence characteristics of an ideal silica precipitating peptide: the presence of hydroxyl- and imidazole-containing amino acids, and high cationic charge under silica precipitation conditions.

Table 1.1 Summary of SiO_2-BPs identified using combinatorial phage display.[45, 46]

Target Materials	Label	Sequences	pI	No. of His	No. of Ser	Binding Affinity	Silica (nmol) [a] [Rank]
Biogenic silica 400-600nm	Si4-1	MSPHPHPRHHHT	9.59	5	2	[b] 1	680 [1]
	Si4-10	RGRRRRLSCRLL	12.30	0	1	[b] 2	73 [7]
	Si3-8	KPSHHHHHTGAN	8.78	5	2	[b] 4	420 [3]
	Si3-3	APPGHHHWHIHH	7.24	6	0	[b] 6	60 [8]
	Si3-4	MSASSYASFSWS	5.27	0	6	[b] 5	187 [6]
	Si-4-3	MSPHHMHHSHGH	7.01	6	2	[b] 3	240 [5]
	Si4-8	APHHHHPHHLSR	9.83	6	1	[b] 7	334 [4]
	Si4-7 [c]	LPHHHHLHTKLP	8.78	5	1	NA	500 [2]
Silica 82nm [d]	Pep1	KSLSRHDHIHHH	8.78	5	2	-	-
Silica 82nm [d]	Pep7	LDHSLHS	5.97	2	2	-	-
Silica 15nm [d]	Pep2	YITPYAHLRGGN	8.60	1	0	-	-
Silica 450nm [d]	Pep4	MHRSDLMSAAVR	9.37	1	2	-	-
Thermally grown SiO_2 [e]	Et1	HPPMNASHPHMH	7.10	4	1	[f] 0.365	[g] Not precipitating silica
	Et2	HTKHSHTSPPPL	8.77	3	2	[f] 0.279	
	Et3	HVSHFHASRHER	9.62	4	2	[f] 0.234	
	Et4	HLASGHSIHYRT	8.77	3	2	[f] 0.073	
	Et5	HQAHNHTHPSSL	7.10	4	2	[f] 0.068	
	Et6	HGSKANHPHIRA	11.00	3	1	[f] 0.053	
	Et7	HTPSNHRHTHNW	9.78	4	1	[f] 0.050	
	Et8	HAPHTHMRSWSA	9.77	3	2	[f] 0.034	
	Et9	HVSHHATGHTHT	7.16	5	1	[f] 0.023	
	Et10	HKLPSASRHHFH	11.00	4	2	[f] 0.022	
	Et11	HTTPSHLHPHSR	9.78	4	2	[f] 0.021	
	Et12	DPSTHQHPPHKH	7.10	4	1	[f] 0.014	
	Et13	SPQHTHHARIKN	11.00	3	1	[f] 0.0066	
	Et14	HINHHHDTPSYR	7.10	4	1	[f] 0.0057	
	Et15	HPGVHSHPSPTP	7.02	3	2	[f] 0.0052	
	[h] sEt1	TVVQTYSMVTRA	8.41	0	1	[f] 0.106	
	[h] sEt2	FSYRQSPPPPLY	8.59	0	2	[f] 0.025	
	[h] sEt3	IMQNSISSPEML	4.00	0	3	[f] 0.010	

Remarks:

[a]nmol of silica precipitated by SiO_2-BPs; [b]Phage binding assay ranking (Rank 1 = more units bound); [c]Different silica target materials; [d]Unpublished data from Professor Carole Perry's group; [e]Thermally grown SiO_2 films are typical SiO_2 layers used in metal oxide semiconducting field effect transistor (MOSFET); [f]Analytical biopanning yield. During successful biopanning experiments, phage yields increase from one round to another round of selection enrichment. Enrichment was observed in this experiment and the relative yield of binding phage increased 55 fold (from 0.00834% to 0.466%) from the first to the third round of affinity selection; [g]Authors did not specify the sequence tested; [h]sEt1, sEt2, and sEt3 were isolated from phage library with non-histidine containing sequences.

Abbreviations:

His – histidine, Ser – serine, pI – isoelectric point, NA – not available.

Based on a series of studies performed by Roach *et al.*,[47] the curvature of the binding surface affects the binding affinity, secondary structure, and the packing of bovine serum albumin (BSA) and fibrinogen on the surface of silica particles. The effect of

surface curvature on the secondary structure of adsorbed molecule has also been observed from the adsorption of leucine-rich Ac10L peptide on gold surfaces.[48] From another set of SiO_2-BPs (unpublished data from Professor Carole Perry's group) isolated from silica particles of different diameters (curvature), besides Pep1 showing a certain level of sequence similarity (underlined) with Si4-1, and both Pep1 and Pep7 contain high fractions of histidine and serine residues, these SiO_2-BPs appear different from those obtained by Naik *et al*., even when silica particles were of comparable sizes. This may suggest that the surface of biogenic silica is different from its non-biogenic counterpart.

The third set of SiO_2-BPs was obtained by Eteshola *et al*.[46] by using a thermally grown SiO_2 film as the binding target. The phage display library used was similar to that used by Naik *et al*..[45] Regardless of the binding affinity of these SiO_2-BPs, the sequences are enriched with histidine but not with other basic amino acids such as lysine and arginine. According to the authors, these SiO_2-BPs did not precipitate silica. Under the biopanning conditions (pH 7.4), histidine was 3.8% protonated compared to essentially 100% for arginine and lysine (based on their pK_a values). The detailed analysis of data by the authors came to following conclusions. Firstly, electrostatic interaction may not be the dominating interacting force for the interaction of histidine with SiO_2 films. The histidine imidazole, which could act as either a proton donor/acceptor at physiological pH, may interact with hydrophobic moieties or form hydrogen bonds with both positively and negatively charged moieties. Secondly, histidine is not essential for SiO_2 film binding due to, (i) the non-histidine containing sequences were able to bind on the SiO_2 film (sEt1, sEt2 and sEt3), and (ii) Et9 with the highest number of histidine have a very low biopanning yield. Thirdly, the presence of histidine residue at the N-terminus, not observed in SiO_2-BPs isolated by other research groups, may contribute to the binding of peptide to thermally grown SiO_2 but not to precipitated silica. This "selectivity" may have arisen from the difference in surface conditions between two silica surfaces, being highly hydroxylated for precipitated silica but not for thermally grown SiO_2.

ZnO-BPs isolated by four independent research groups are listed in **Table 1.2**. Two highly similar sequences, ZnO-1 (GLHVMHKVAPPR) and Z1 (EAHVMHKVAPRP), have been identified by Tomczak *et al*.[39] and Umetsu *et al*.[41] respectively. The 67%

sequence similarity between ZnO-1 and Z1 was remarkable. The binding affinity of ZnO-1 was outstandingly high compared to other sequences isolated by Umetsu *et al*. but no binding data was available for Z1. As shown in **Table 1.2**, the sizes of ZnO targets used for peptide binding were different between these two sets of ZnO-BPs however both libraries used were of M13 pIII coat protein.

The affinity of ZnO-1 to ZnO and its ability to catalyse ZnO formation were studied and presented in the same report.[41] The affinity and selectivity of ZnO-1 to ZnO particles (over ZnS and Eu_2O_3) was tested and confirmed by exposing immobilized ZnO-1 to a fluorescent ZnO particle suspension. The ZnO-1 was immobilized on a gold-plated polypropylene surface using a cysteine binder at the C-terminus and a GGGS linker was added before the C-terminus for flexibility. Interestingly, in a ZnO precipitation test, only TZnO-1 (ZnO-1 with GGGSC-tag added on its C-terminus) has been shown to catalyse ZnO formation from a stable $Zn(OH)_2$ sol but not in the presence of ZnO-1. As for Z1 isolated by Tomczak *et al*.,[39] the study of TZ1 (Z1 with GGGC-tag added on its C-terminus) on ZnO formation revealed that TZ1 alters ZnO morphology by reducing the aspect ratio of the ZnO crystals grown. The study of TZ1 by Tomczak *et al*. is discussed in **Section 1.5.1** in greater detail.

Kjærgaard *et al*.[38] attempted *E. coli* for CSD to isolate ZnO-BPs. 25 individual ZnO-binding clones were sequenced and 11 sequences have been identified (**Table 1.2**). The binder with highest binding frequency, pJKS9, exhibits significant homology to a putative zinc-containing helicase of *S. pombe* where the level of sequence similarity was 50% when the arginine-serine pair from the cell (RS in the middle of the sequence) was not taken into consideration. *E. coli* with a pJKS9 insert and the *S. pombe* segment insert showed ZnO selectivity (over CdO) and both have similar binding strength to ZnO particles. The analysis of all 11 isolated sequences came to the identification of enriched residues (histidine, arginine, aspartic acid and methionine) and binding motifs such as RX_2RS (solid-underlined), PXRS (dotted-underlined), THNKX (double-underlined), and RHXKD (italicized).

Table 1.2 Summary of ZnO-BPs[37-39, 41] and Zn^{2+}-BPs[49] identified using combinatorial display methods.

Target Materials	Label	Sequences	[a] pI	Binding Affinity	[b] GRAVY	Display
ZnO	ZnO-1	EA**HVMHKVAP**RP	8.86	[c]1222	-0.633	[d] PD[41]
Particles	ZnO-2	QNTATAVSRLSP	9.75	[c] 15.6	-0.375	PhD-12
(1μm)	ZnO-3	ATHTNQTHALYR	8.80	[c] 16.2	-1.158	
	ZnO-4	VSNHKALDYPTR	8.57	[c] 91.1	-1.100	
	ZnO-5	DSGRYSMTNHYS	6.74	[c] 33.3	-1.575	
	TZnO-1[e]	EAHVMHKVAPRPGGGSC	8.33	NA	-0.394	
ZnO [f]	Z1	GL**HVMHKVAP**PR	11.00	NA	-0.208	[h] PD[39]
Nanopowder	TZ1 [g]	GLHVMHKVAPPRGGGC	9.51	NA	-0.075	PhD-12
ZnO [f]	pJKS9	NTRMTARQH$_{RS}$ANHKSTQRA$_{RS}$	12.48	[i] 8/25	-1.935	[j] CSD[38]
	pJKS10	VFLPSILGW$_{RS}$RLDDQGVAA$_{RS}$	5.93	[i] 2/25	0.315	*E. coli*
	pJKS12	TRNKHTTAR$_{RS}$VAPGIGEPS$_{RS}$	11.71	[i] 3/25	-1.150	
	pJKS14	IMHVRLRAR$_{RS}$A*RHMKD*ADP$_{RS}$	11.83	[i] 1/25	-1.025	
	pJKS17	PIIIRSRIN$_{RS}$HGRTKATPA$_{RS}$	12.48	[i] 1/25	-0.680	
	pJKS18	RGLRNILML$_{RS}$YDSRSMRPH$_{RS}$	11.83	[i] 2/25	-0.935	
	pJKS11	TRRGTHNKD$_{RS}$	10.83	[i] 4/25	-2.767	
	pJKS16	TVPK*RHPKD*$_{RS}$	9.99	[i] 1/25	-2.078	
	pJKS45	IAKKTHNKQ$_{RS}$	10.30	[i] 1/25	-1.811	
	pJKS15	YDSRSMRPH$_{RS}$	8.33	[i] 1/25	-2.033	
	pJKS46	TASRHTEPH$_{RS}$	6.61	[i] 1/25	-1.822	
ZnO film	Class I					[l] CSD[37]
Cathodically	CN179	RIGHG**RQIRK**PL	12.30	[k]100±17	-1.142	
Deposited	CN155	VRTRDDA**RTHRK**	11.54	[k] 69±5	-2.292	
	CN120	PASRVEKNGV**RR**	11.71	[k] 13±6	-1.417	
	Class II					
	CN146	MRHSSSGEPRLL	9.37	[k] 84±12	-0.883	
	CN111	PAGLQVGFAVEV	4.00	[k] 78±13	1.117	
	CN185	RTDDGVAGRTWL	5.96	[k] 61±7	-0.775	
Zn^{2+}	B1	SHTHALPLDF	5.92	NA	-0.080	[m] PD[49]
Immobilized	B2	GRVHHHSLDV	7.02	NA	-0.660	
on Sepharose	B3	GQSSGGDTDD	3.67	NA	-1.750	
beads	B4	GQWTPRGDDF	4.21	NA	-1.620	
	B5	GRCCPSSCDE	4.75	NA	-1.983	
	B6	GPAKHRHRHRVGQMHDS	11.71	NA	-0.760	

Remarks:
[a]pI values (isoelectric point) were obtained using pI/Mw calculator at Expasy (http://www.expasy.ch or http://us.expasy.org); [b]GRAVY, grand average of hydropathicity indicates the solubility of protein. It is obtained by dividing the sum of hydropathy values of all amino acid residues in the peptide with the number of residues in the sequence. Positive and negative values indicates hydroplibicity and hydrophilicity respectively (http://www.expasy.ch/cgi-bin/protparam); [c]Binding affinity = $[O/I]_{pep}/[O/I]_{Control}$ where [O/I] is the ratio of the number of bound peptides to the number of peptide initially in the binding assay; [d] PhD-12 Phage Display Peptide Library Kit (New England Biolabs, Beverly, MA); [e]TZnO-1 is a GGGSC-tagged ZnO-1 used for the study of ZnO precipitation; [f]Purchased from Sigma Aldrich; [g]TZ1 is a GGGC-tagged Z1 used for the study of the effect of this peptide on ZnO morphology; [h]PhD-12 Phage Peptide Display Kit (New England Biolabs, Ipswich, MA); [i]Binding frequency of the sequence among the isolated bound sequences; [J]The random library was constructed by inserting various numbers of synthetically synthesized 33-bp oligonucleotides into the *Bgl*II linker site. The presence of *Bgl*II overhangs in the linker resulted in an arginine-serine (RS) flanking sequence for each insertion; [k]Number of adhering cells obtained as per the authors standard procedures were normalised to the highest binder, CN179; [l]FliTrx library (Invitrogen, Carlsbad, CA). The ZnO-BPs obtained are disulfide-constrained 12-mer; [m]Phage libraries were constructed by the authors.
Abbreviations:
PD – Phage display, CSD – Cell surface display, NA – not available.

Thai *et al*. used the FliTrx cell surface display method to identify disulfide constrained 12-mer ZnO-BPs.[37] Six sequences identified were shown to be enriched in tryptophan (W), glycine (G), and arginine (R) but depleted in tyrosine (Y), proline (P) and serine (S). These sequences can be subdivided into two classes. Class I sequences are hydrophilic and positively charged with motif such as RX_2RK bold), RR (bold and underlined) where the RK motif is unique for ZnO compared to CuO-BPs shown in the same report. No particular motif was observed for Class II ZnO-BPs and these sequences are completely different from the Cu_2O-BPs obtained.

One earlier study by Barbas *et al*.[49] identified peptide sequences that conferred the ability to coordinate Zn^{2+} in a phage displayed semi-synthetic combinatorial antibody library. Histidine did not present in half of the identified sequences but at least one of the following residues; cysteine (C), glutamate acid (E), and aspartic acid (D) which are known to bind Zn^{2+} in zinc enzymes of living organisms,[50] were present in those sequences for which histidine was absent. To determine if there is correlation between the presence of strong Zn^{2+} binding residues[50, 51] in strong ZnO-BPs and the observed binding strength, the number of histidine (H), cysteine (C), methionine (M), glutamate acid (E) and aspartic acid (D) residues, was plotted against different ZnO-BPs and Zn^{2+}-BPs, **Figure 1.1**. This analysis showed that the 28/29 sequences contain at least one of the Zn^{2+}-binding amino acid residues but the strongest ZnO-BP for each set (marked with an asterisk) does not necessarily contain the highest number of histidine/cysteine/glutamate acid/aspartic acid residues. This suggests that the secondary structure of these peptides may have a significant influence on binding affinity of peptide on ZnO.

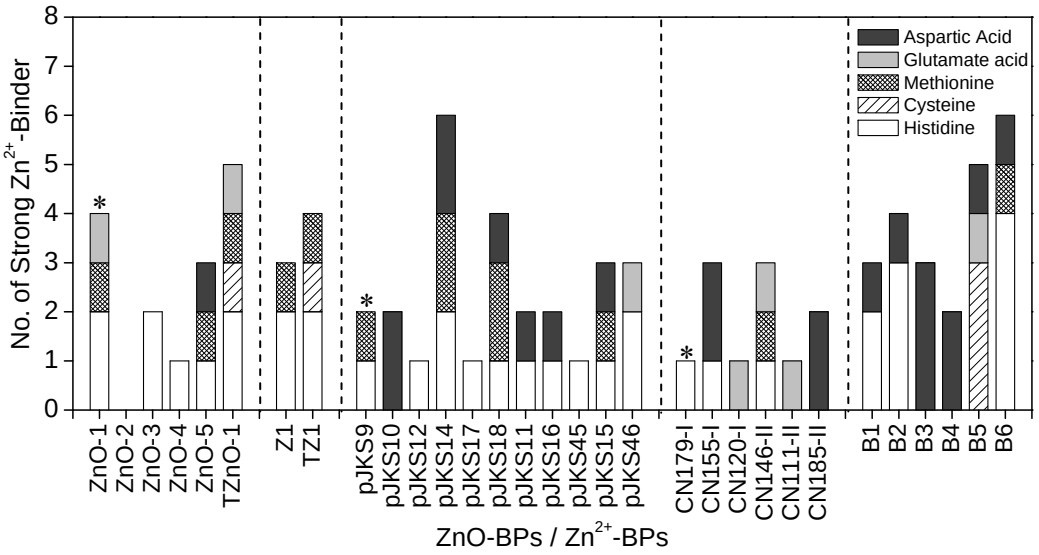

Figure 1.1 The number of strong Zn^{2+}-binding residue, histidine (H), cysteine (C), methionine (M), glutamate acid (E) and aspartic acid (D), in peptides identified using combinatorial display method. Strongest ZnO-BP from each set is marked with an asterisk.

1.3 Biomolecules that Affect Silica Formation

For more than one hundred years biosilicas were marvelled at for their exquisite hierarchical structures, functional diversity, and well-controlled *in vivo* formation in living organisms. The siliceous components of diatoms, sponges, radiolarian and plants demonstrate the intricate and hierarchical structures of biosilica.[1, 19, 52-55] The effects of biomolecules on silica formation have been extensively studied by different research groups around the world. In this section, the effects of silaffins, silicatein, LCPAs, and their model molecules on silica formation *in vitro* are discussed.

1.3.1 Silaffins, long-chain polyamines (LCPAs), and their model molecules

Silaffins isolated from diatoms has been characterized and the effects of its components on silica formation *in vitro* have been extensively studied.[9, 10, 18, 19, 56, 57] Biomolecules intimately associated with the biosilica were obtained by dissolution with hydrofluoric acid (HF) or aqueous ammonium fluoride solution (NH_4F). The latter

method produced silaffins with higher molecular masses compared to HF extraction, indicating the existence of HF-labile modifications. Therefore the results obtained by NH_4F extraction, which is likely to preserve the *in vivo* structure of silaffins, were termed native silaffins to distinguish it from those obtained by HF extraction. The subunits of natural silaffins are abbreviated as natSil-1A (6.5kDa), natSil-1B (10kDa), and natSil-2 (40kDa).[56] Natural silaffins contain substantial amount of phosphorus which is absent in silaffins extracted using HF.[56, 58]

The dissolution of the biosilica of *C. fusiformis* by HF extracted three polypeptides, namely Sil-1A (4kDa), Sil-1B (8kDa) and Sil-2 (17kDa), **Figure 1.2a**. The prosequence and signal peptide (**Figure 1.2a-b**) are the components of Sil-2. The prosequence contains many acidic residues, glutamate acid (E) and aspartic acid (D), which corresponds to 11.4% and 14.8% of the total residues in the prosequence respectively. Protein sequence analysis revealed that Sil-1A represents a mixture of two very similar peptides, Sil-$1A_1$ and Sil-$1A_2$, which also showed high degree of sequence homology to Sil-1B (**Figure 1.2b**). The comparison of chemical structures of Sil-$1A_1$ and Sil-$1A_2$ presented in **Figure 1.2c** and **Figure 1.2d** respectively showed that (i) all lysine residues in Sil-$1A_1$ and Sil-$1A_2$ are modified;[9] (ii) Sil-$1A_1$ contains three different modified lysine residues representing ε-N,N-dimethyllysine (position 4), ε-N,N,N-trimethyl-δ-hydroxylysine (position 13) and LCPA-modified lysines (positions 3 and 15);[9] (iii) Sil-$1A_2$ only contains two different modified lysine residues representing ε-N,N-dimethyllysines (position 4 and 15) and LCPA-modified lysines (positions 3 and 14);[10] (iv) only KK lysine pairs are present in Sil-$1A_2$ but two isolated K were present in Sil-$1A_1$ besides one KK pair;[10] (v) LCPA consists of linear chains of N-C-linked propylamine where the polyamine chain is attached to putrescine or a putrescine derivative;[19] and (vi) the chain length of the propylamine and the methylation pattern of LCPAs are diatom species dependent.[10]

The silica precipitation activities of Sil-1A, natSil-1A, natSil-2, LCPAs *in vitro* have been studied extensively.[9, 10, 18, 19, 56, 58] It was found that Sil-1A and LCPAs are capable of precipitating silica at pH 5.5 only in the presence of phosphate buffer, while the presence of phosphate is not essential for natSil-1A which already contains functional groups such as phosphate, sulphate and carbohydrate. Kröger *et al*. suggested that the

ability of these biomolecules to self-assemble is essential for their silica precipitating activity.[56] Post-translationally modified natSil-1 is zwitterionic (cationic LCPAs and anionic phosphate) thus natSil-1 could self assemble via electrostatic interactions into a template for silicic acid polycondensation. The inability of natSil-2 (with both positive and negative moieties) to precipitate silica even in the presence of phosphate was explained by its heavy glycosylation.[19, 58] Heavily glycosylated natSil-2 is a highly polyanionic protein making it incapable of precipitating silica from silicic acid solution *in vitro*. In the presence of other silaffins components such as natSil-1 or LCPAs, natSil-2 acts as a regulator via electrostatic interactions to produce silica structures with a wide diversity of morphologies.[58]

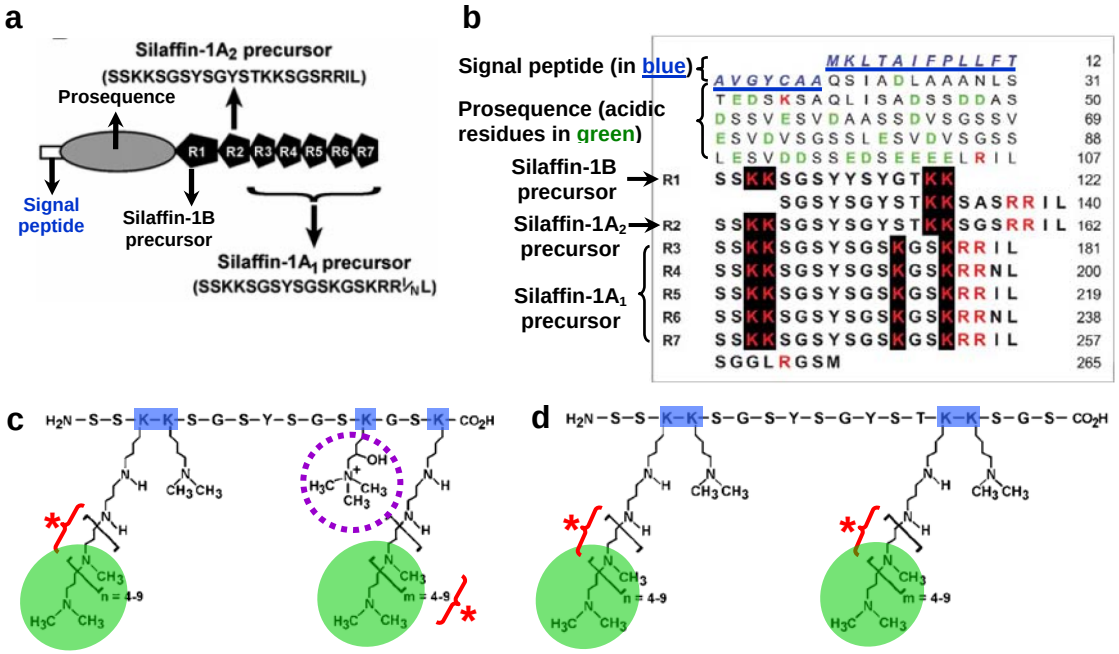

Figure 1.2 (a) Schematic structure of the silaffins precursor polypeptide sil1p where the *black pentagons* denote the repeating unit elements from which the silaffins are generated while the amino acid sequences of repeating units R2–R7 are *bracketed*.[9] (b) Amino acid sequence of sil1p showing the signal peptide (underlined blue italics), acidic amino acid residues (bold green), and basic amino acid residues (bold red).[18, 54] The silaffin-generating C-terminal domain is shown in bold letters with boxed lysine residues. R1 to R7 indicate the repeating sequence elements within the C-terminal domain. The column of numbers on the right indicates the amino acid positions.[19] (c) and (d) show the chemical structures of silaffin-1A$_1$ and silaffin-1A$_2$ respectively[9] where the polypeptide backbones are depicted by the one-letter amino acid code. The chemical structures of the side chains of only the modified lysine residues are shown. The modified lysines are in blue boxes while the putrescine homologue and N-methyl propylamine are shaded in green and marked with a red asterisk respectively. The *N*,*N*,*N*-trimethyl-δ-hydroxy group attached to one of the lysine in (c) is circled with purple dotted line.

A wide range of model molecules have been derived from the silaffins and LCPAs isolated from diatoms. The summary of the studies involving these model molecules are shown in **Table 1.3**. A variety of precursors can be used to produce monosilicic acid in water namely TEOS (tetraethoxysilane), TMOS (tetramethoxysilane), K_2SiCat_3 (dipotassium silicon triscatecholate complex) and Na_2SO_3 (sodium silicate). Monosilicic acid is stable at level below ca. 100ppm (~1mM) but condenses when supersaturation is reached at around 100-200ppm.[59] The formation of silica is seen to involve three distinct stages: (i) polymerization to form stable nuclei, (ii) growth of the nuclei to form spherical particles, and (iii) particle aggregation to form branched chains or other structures.[60] Most of the model molecules have been shown to either catalyse the condensation of monosilicic acid, promote aggregation of silica particles, or act as a template for silica formation.[52]

The catalytic ability of R5, a 19-mer peptide from Sil-$1A_1$, was studied by using hydrolysed TMOS.[18, 25, 30] Kröger *et al*. have shown that higher pH (pH 7) was required for R5 to precipitate comparable amounts of silica to that which Sil-1A could generate at pH 5.[18] This implied that lysine modification of Sil-1A is required for its silica precipitating activity at pH 5, the physiological pH of diatoms. Knecht and Wright[25] identified the RRIL motif of R5 as being essential for silica precipitation *in vitro*. R5 and R5 truncates that contain the RRIL motif were shown to self assemble into active silica precipitating assemblies (700-950nm) which were not observed for R5 truncates in the absence of RRIL. In most instances, networks of near-spherical particles were obtained in the presence of R5 however Naik *et al*.[30] have shown that the use of flow dynamics could modify silica morphology to arch shape and fibrillar structures.

Besides R5, the effects of amino acids, oligo-peptides, and polypeptides have also been studied. Among them, the effect of lysine and polylysine at near-neutral pH has been extensively studied.[31, 33, 35, 61-64] Both lysine and PLL (poly-$_L$-Lysine) could catalyse silica formation/growth[31, 33, 61, 62, 64] however the latter can also act as a template.[28, 61, 63] The morphology of silica produced can be tuned from spherical to hexagonal plates by increasing the degree of polymerisation (DP) of PLL to higher than 100 as shown by Tomczak *et al*..[28] This transformation arises from the α-helical secondary structure of PLL at DP>100,[28] as opposed to random coil for PLL with DP<100, and this effect was

not affected by the handedness of the polylysine used.[61] The presence of phosphate and silicate is required for this secondary structure transformation to take place.[28]

Lysine in the form of oligomers or polypeptides have been shown to catalyse silica precipitation more effectively than its monomeric counterpart.[33, 62, 64] This trend was also shown by arginine and proline.[33, 64] The synergistic effect of polypeptides over their amino acids becomes rational when the catalysis of silica formation/growth is considered as a process of bringing reacting species, whether neutral monosilicic acid or anionic polysilicic acid species, into proximity. According to Coradin *et al*.,[33] additives interact with monosilicic acid and polysilicic acid via hydrogen bond and electrostatic interactions respectively.

Model molecules of LCPAs have been studied such as putrescine homologues,[26] natural polyamines,[29] propylamines,[32] simple amines[65, 66] etc. The LCPA isolated from *S. turris* was capable of precipitating silica only in the presence of multivalent anions.[19, 67] This can be explained by the formation of microscopic phase separation/emulsion microdroplets as the template via electrostatic interaction between polyamine and multivalent anions such as phosphate ions.[19, 68] The role of multivalent anions was supported by the formation of larger silica particles when the concentration of phosphate was increased and/or when phosphate ions with higher negative charge was used.[19] The formation of microdroplets/microemulsion being essential for the demonstration of polyamine's catalytic role was also observed in the presence of putrescine homologues,[26, 32, 68] PAA (polyallylamine),[68] and propylamines.[32] Therefore the size of the amine spacer which affects the hydrophobicity of the additive, would in turn influence its capability to catalyse silica formation/growth.[32] The use of naturally occurring polyamines such as spermine and spermidine was found to increase silica growth rate and reduced the porosity of silica formed.[29]

Table 1.3 The effects of model molecules inspired by silaffins and LCPAs on silica formation and silica morphology – Part I

Origin	Additives	Reaction Conditions			Effects		Remarks
		Precursor	pH / T (°C)	Buffer	Silica precipitation	Morphology	
Silaffins	R5[18]	Hydrolysed TMOS	pH 3 – 7 (5 mins)	Sodium phosphate citrate	The precipitated amount at pH 7 was comparable to that produced by Sil-1A at pH 5. [a]	NA	Lysine modification of Sil-1A by phosphate is required for silica precipitating activity at physiological pH.
	R5[30] (effects of flow dynamics on morphology)	Hydrolysed TMOS	pH 8 (2-5 mins)	Sodium phosphate citrate	R5 catalysed silica formation. [b]	Network of roughly spherical particles (400-600nm), arch shape and fibrillar structures.	Application of a linear shear force and the presence of an interfacial reaction surface both affect the deposition of silica and morphology of silica formed.
	R5 and R5 truncates[25]	Hydrolysed TMOS	~ pH 5 (5 mins)	Sodium phosphate citrate	R5 catalysed silica formation. R5 truncates showed lower activity while R5 truncates without RRIL motif is inactive.	Network of roughly spherical particles. (245-450nm)	RRIL motif is critical in the formation of active silica precipitating assemblies. Silica precipitating R5 and R5 truncates self-aggregate in reaction solution.
	Poly-$_L$-Lysine[28] (effects of M_w)	Hydrolysed TMOS	pH 7.5	Sodium phosphate	PLL catalysed silica formation and also act as a template.	PLL_{222} (α-helix) – hexagonal plates. PLL_{20} (random coil) – spherical silica.	PLL-mediated silica precipitation by bringing the silicate species in close proximity via electrostatic interactions and hydrogen bond. The presence of phosphate and silicate is required for the secondary structure transformation to take place.
	Poly-$_L$-Lysine[61]	Hydrolysed TMOS	pH 7.0 ambient (5 mins) pH 6.0 for PLL + PAH	Potassium phosphate	PLL catalysed silica formation.	Spherical particles (200-400nm) obtained. In the presence of both PAH and PLL, hexagonal plates produced.	PLL facilitates silicification at neutral pH. The control over silica morphologies was observed by the presence of an additional polyamine in the system.
	Poly-$_L$-Lysine Poly-$_D$-Lysine[63] (DP=112~233)	Hydrolysed TMOS or sodium silicate	pH 7.0 ambient	Potassium phosphate	PLL catalysed silica formation and also act as a template.	Hexagonal silica plates (amorphous).	The formation of PLL^{28} helices is a prerequisite to the hexagonal silica synthesis and the handedness of polylysine does not affect the formation of hexagonal silica.
	Poly-$_L$-Lysine[35] (effect of confine space)	Sodium silicate	pH 5 (10 mins)	None	PLL catalysed silica formation.	Membrane pores with impregnated PLL were used as mould to produce silica tubes.	Localization of PLL at pore internal surface modified the silica morphology.
	Oligo-lysine[62] (n=1-4)	Sodium silicate	pH 7.2 ambient	Tris-HCl	Catalytic activity of oligo-lysine increased as the DP was increased.	Larger oligo-lysine produced larger silica particles	Larger oligo-lysine brought more silicic acid together at proximity to promote aggregation.

[a] R5 has no silica precipitation activity at pH < 7 but Sil-1A's activity is maximal around pH 5. [b] In the absence of R5, hydrolysed TMOS forms gel within 24 hours.

Table 1.3 The effects of model molecules inspired by silaffins and LCPAs on silica formation and silica morphology – Part II

Origin	Additives	Reaction Conditions			Effects		Remarks
		Precursor	pH / T (°C)	Buffer	Silica precipitation	Morphology	
Silaffins	Lysine and PLL[33]	Sodium silicate	pH 4.9 - pH 7.2 - pH 9.2 -	Acetate Tris-HCl Tris-HMAM[c]	Catalysed silica formation at pH > 7. PLL was a better catalyst than lysine.	NA	Additives interact with neutral silicic acid species via hydrogen bond and with polysilicic acid species via electrostatic interactions. PLL catalysed condensation of silicic acid more effectively than lysine did.
	Lysine and PLL Arginine and PLA[64]	Sodium silicate	pH 7.2	Tris-HCl	The gelation activity of lysine and arginine increased as a function of their DP.	Colloidal silica aggregates	Additives act as gelation agent of silica oligomers via electrostatic interactions. The polypeptides of lysine and arginine catalysed condensation of silicic acid more effectively than their monomers.
	Amino acids (AAs)[d] and Lysine-oligomers[31]	Hydrolysis of K_2SiCat_3	pH 7.0 ambient	None	Lysine and its oligomeric species increased the aggregation rate of silica particles	N-containing AAs generate larger particles and AA with OH- and hydrophobic groups smaller silica particles than the control.	Additives affect the kinetics of small oligomer formation, the growth of aggregate structures and the morphology and surface properties of the silica produced. The effects of amino acid are related to their pI and hydrophobicity.
	Polyhistidine[69]	TMOS	pH 7.0 ambient	Potassium phosphate, phosphate-citrate	Catalysed silica formation	Silica particles (50nm, 150-200nm)	Proposed to be a templating effect.
LCPAs	PAA Polyallyamine[68] (n~160)	TMOS Phosphate	pH 5.8 20°C	None	Catalysis of silica formation. The amount of silica precipitated increase with phosphate concentration.	Spherical silica particles.[e]	Microscopic phase separation caused by electrostatic interaction between PAA and multivalent anions (phosphate ions) is necessary for silica precipitation.[f]
	Propylamines [g]	Hydrolysis of K_2SiCat_3	pH 6.8 ambient	None	All propylamines (C3N3, C3N5, C3N7) and the longer-chain ethyleneamines (C2N5 and C2N6) significantly enhanced condensation rates.	Nonporous silica was produced. A mixture of hollow and solid silica particles were formed.[h]	Two factors critical to the influence of propylamine on silica formation: (i) the ability of the amines to produce microemulsions (hydrophobicity) and (ii) the presence of charged and uncharged amine groups within a molecule. [i]

[c] Tris–(hydroxymethyl) aminomethane. [d] Gly, Arg, Asn, Gln, Gly, Ser, Thr, Tyr, Pro, Ala, and Lys. [e] Silica diameter increased with [phosphate] in the presence of PAA. [f] A threshold level of phosphate ion is required to induce microscopic phase separation. [g] The effect of three structural features were studied: the degree of polymerization, the level of amine methylation, and the size of the amine chain spacers. [h] The fraction of hollow particles increased as the DP of propylamine was increased. [i] The second factor helps to catalyze silicic acid condensation by a proton donor/acceptor mechanism.

Table 1.3 The effects of model molecules inspired by silaffins and LCPAs on silica formation and silica morphology – Part III

Origin	Additives	Reaction Conditions			Effects		Remarks
		Precursor	pH / T (°C)	Buffer	Silica precipitation	Morphology	
LCPAs	Putrescine homologues [j][26]	Hydrolysis of K_2SiCat_3	pH 6.8 ambient	None	Longer hydrophobic portion catalysed silica formation and increased growth rate at greater extend	Silica particles produced have lower porosity.	Catalysis has occurred as a result of reduced solvation layer of monosilicic acid via the formation of micelles by putrescine homologues.
	Spermine, Spermidine and analogues [k][29]	Hydrolysis of K_2SiCat_3 or TMOS	pH 7.0 ambient	None	Increased growth rate as a function of N-to-N distance.	TMOS precursor produced more discrete silica particles than K_2SiCat_3 precursor. PEHA (high N-to-N distance) produced non-porous silica.	The increase of growth rate may be driven by reduction of silica particles repulsion via surface charge compensation by the additives.
	LCPA [l][19, 67]	TMOS	pH 5.5 ambient	Sodium phosphate / Sodium acetate	Silica formed within minutes in phosphate buffer but not in sodium acetate buffer.	Silica particle size increased with (i) concentration of phosphate, and (ii) the use of phosphate ions with higher negative charge.	The catalytic function of LCPA required the presence of multivalent anions. Formation of emulsion microdroplets by polyamine is essential for the demonstration of its catalytic role.
	Amines [m][65, 66]	TMES [n]	~ pH 5	-	Acidic amines (imidazole and pyridine) and longer polyamines increased the hydrolysis rate and condensation rate.	NA	Postulated a nucleophile-catalyzed hydrolysis mechanism where the conjugate base of the amine attacks Si to form a pentacoordinated intermediate with TMES. Condensation is interpreted as an acid-catalyzed S_N2 mechanism.

[j] Alkyldiamines tested have constant concentration and only the hydrophobic portion of the additive varied as the chain length of the diamine increased. [k] Monoethylenediamine (MEDA), diethylenetriamine (DETA), triethylenetetramine (TETA), tetraethylenepentamine (TEPA), pentaethylenehexamine (PEHA). [l] Natural polyamine isolated from *S. turris*. [m] Pyridine, imidazole, piperidine, ethylamine, 1,4-diaminobutane, spermidine, spermine, triethylenetetramine, tetraethylenepentamine. [n] TMES, trimethylethoxysilane ($(CH_3)_3SiOCH_2CH_3$), has only one organosilcate bond.

1.3.2 Silicatein, long-chain polyamines (LCPAs), and their model molecules

Silicatein (for silica protein) was extracted from the central protein filament of the spicule of sponges *T. aurantia*[12] and *S. domuncula*.[11] The protein filament can be dissociated to yield three subunits, silicatein-α, -β, and -γ, which have similar molecular weights and amino acid composition.[12] Silicatein-α, the most abundant subunit, is homologous to the members of the cathepsin-L and papain family of proteases.[12] The position of all six cysteine residues forming disulfide bridges has been conserved in silicatein-α as in cathepsin-L while the "catalytic triad" in cathepsin-L, Cys-26/His-165/Asn-184, has been "replaced" by Ser-26/His-165/Asn-184 in silicatein-α. Molecular modeling of cathepsin-L and silicatein has found comparable distances (~6.2Å) between α-C-Ser-26/His-165 of cathepsin-L and α-C-Cys-26/His-165 of silicatein-α. In addition, their secondary conformations did not vary significantly[70], suggesting silicatein may function in an analogous way to the hydrolytic protease in the control of silica synthesis.[12, 17]

Can silicatein precipitate silica *in vitro*? In the presence of insoluble silicatein filaments, silicatein subunits (contains silicatein-α, -β, and -γ), and silicatein-α; silica condensation was observed from the solution of TEOS at pH 6.8 buffered by Tris-HCl at ambient condition.[17] In the absence of these additives, no polymerization of TEOS was observed at neutral pH because catalysis of silica formation by acid or base is usually required.[59] Thus the presence of silicatein-α is sufficient for the catalysis of silica formation *in vitro*. Based on site-directed mutagenesis, Zhou *et al*.[16] confirmed the essentiality of specific Ser-26 and His-165 residues of silicatein-α for the catalysis of siloxane polymerisation. That means the interacting hydroxyl-group of serine and imidazole group of histidine are required for the hydrolytic activity of silicatein-α. Based on this precedent, Cha *et al*.[71] evaluated simpler polypeptides bearing polar functional groups. However these homopolypeptides which lack the structural complexity and polyfunctionality are unable to catalyse silica formation except for poly-$_L$-cysteine.[71] A series of cysteine-lysine block copolypeptides with water soluble domains, water insoluble domains, and potential silica forming catalytic activity was designed and tested. This copolypeptide block was found to self-assemble into structured aggregates that hydrolysed TEOS while simultaneously directing the

formation of ordered silica morphology. This mechanism is similar to that observed in the presence of R5 and R5 truncates which were actively precipitating silica.[25] Silica spheres and packed silica columns were obtained in this study under nitrogen atmosphere and air respectively.[71] Systematic substitution of residues used in the construction of these peptides showed that the rate of catalysis was proportional to the strength of nucleophilicity of the nucleophilic side chain, and that hydrogen bonding was required for efficient catalysis.

By incorporating the features found essential for silicatein's catalysis of hydrolysis at neutral pH in small molecules, Roth *et al*.[4] studied silica formation using a group of analogous small organic molecules bearing a nucleophilic group, such as –SH, -OH, or $–SC_2H_5$, and a hydrogen-bond acceptor group, such as a primary or substituted amine. The criteria used for the small organic molecules selection are proven valid when cysteamine ($HS-(CH_2)_2-NH_2$) and ethanolamine ($HO-(CH_2)_2-NH_2$) turned out to be actively precipitating silica at rates higher than the control reaction.[4]

Matsunaga *et al*. isolated LCPA from marine sponge *A. aculeate*, LCPA-*Aa*, which is believed to be present with phosphate or sulfate.[15] Although both are closely associated with the biosilica structure, LCPA-Aa differs from LCPA of diatoms at least in one of the following factors: chain length, presence of butaneamine unit, or degree of methylation.[15] *In vitro* precipitation of silica in the presence of LCPA-*Aa* was studied using TMOS at pH 6.5, the pH value of sponge cellular fluid. The presence of LCPA-*Aa* was able to precipitate silica where the size and shape of the silica particles are affected by the presence of SO_4^{2-}. At optimum [SO_4^{2-}], the silica particles obtained were remarkably similar to that reported for demosponge biosilica (50-200nm particulates). However when the concentration of SO_4^{2-} was deviated from the optimum level, smaller particulates (20nm) with undefined morphological features were obtained. Therefore the authors believed that LCPA-*Aa* may be one of the factors that aid in the deposition of silica to form sponge spicules *in vivo*.

1.4 Overview of Zinc Oxide (ZnO)

ZnO is a highly researched inorganic material. ZnO is generally being developed for blue/UV optoelectronics,[72-74] semiconductor spintronics,[72] window materials for display and solar cells,[72, 73] dye-sensitized solar cells (DSSCs),[75-77] biomedical applications,[78] photocatalysts,[79] and also other applications such as gas, chemical, and biosensors.[74, 78, 80, 81] The properties of ZnO are closely related to its size, shape/morphology (primary and hierarchical structures), orientation, crystallinity and purity; which in turn determine the application of the ZnO synthesized. Generally ZnO can be synthesized via vapour routes or solution routes. The former has produced a wide range of nanostructures with high level of crystallinity and purity however the cost incurred is high. Thus solution route synthesis with the aid of biomolecules for size/morphology control may be an answer to the realisation of large scale manufacturing of ZnO.

1.4.1 Bulk properties and crystal structure of ZnO

ZnO is a II-VI direct band gap semiconductor with a band gap of 3.437eV[72] which corresponds to the near-UV region. Due to its wide band gap, ZnO is transparent in the visible part of the electromagnetic spectrum hence suitable for short wavelength optoelectronics applications.[72, 73] ZnO has tuneable band gap which can be achieved by substituting the cation (Zn) sites. This has resulted in bandgap value of ~3.0eV and ~4.0eV by Cd-substitution and Mg-substitution on the Zn site in epitaxial films respectively.[73] ZnO also has a high exciton binding energy of 60meV. The exciton is the state at which an electron interacts with a hole via their attractive Coulomb potential; it is the quanta of the excitation in the electronic system of semiconductor. The strong exciton binding energy of ZnO, which is larger than GaN (~25meV), ZnSe (22meV) and ZnS (40meV); and its thermal energy at room temperature (26meV) can ensure efficient excitonic emission at room temperature under low activation energy.[74, 82] Furthermore, ZnO is a piezoelectric material which relates to its crystal structure, and can thus be used as electro-mechanical-coupled sensors and transducer.[83] The basic properties of wurtzite ZnO is summarised in **Table 1.4** below.[73]

Table 1.4. Basic properties of wurtzite ZnO.[73]

Property	Values
Lattice parameters at 300K	
a_0	0.32495 nm
c_0	0.52069 nm
a_0/c_0	1.602 (ideal hexagaonal structure shows 1.633)
u	0.345
Density	5.606 g/cm^3
Stable phase at 300K	Wurtzite
Melting point	1975°C
Thermal conductivity *	0.6, 1-1.2
Linear expansion coefficient (/°C)	a_0: 6.5x10^{-6} c_0: 3.0x10^{-6}
Static dielectric constant	8.656
Refractive index	2.008, 2.029
Energy gap	3.4 eV, direct
Intrinsic carrier concentration	<10^6 cm^{-3} (max n-type doping >10^{20} cm^{-3} electrons; max p-type doping <10^{17} cm^{-3} holes)
Exciton binding energy	60meV
Electron effective mass	0.24
Electron Hall mobility at 300K for low n-type conductivity	200 cm^2/Vs
Hole effective mass *	0.59
Hole Hall mobility at 300K * for low p-type conductivity	5-50 cm^2/Vs

** These values were believed to be influenced by the presence of defects hence they are still debatable.*

ZnO preferentially crystallises in the hexagonal wurtzite type structure (**Figure 1.3a**). This ionic and polar structure of ZnO can be described as hexagonal close packing of oxygen and zinc atoms in space group $P6_3mc$ with zinc atoms in tetrahedral sites. The lattice parameters of ZnO are a=0.3296nm and c=0.52065nm. The hexagonal plane of ZnO crystal perpendicular to the c-axis is polar. An ideal ZnO crystal consists of a positively-charged Zn^{2+}-terminated (0001) plane, a negatively-charged O^{2-}-terminated (000-1) plane; and low index non-polar {10-10} planes parallel to c-axis.[55] The primitive unit cell of ZnO shown in **Figure 1.3b** is ⅓ of the crystal shown in **Figure 1.3a**. Each primitive unit cell contains two formula units of ZnO and the c/a value of the elementary translational vector is around 1.60. The tetragonal coordination of Zn and O atoms in ZnO crystals is a result of a covalent chemical binding with sp^3 hybridization however a substantial fraction of ionic bonding component is present.

Due to the presence of a fraction of ionic component in the chemical binding in ZnO crystals, the lowest unoccupied orbital (LUMO) and the highest occupied orbital (HOMO) are formed essentially from the *4s* level of Zn^{2+} and *2p* level of O^{2-} respectively.

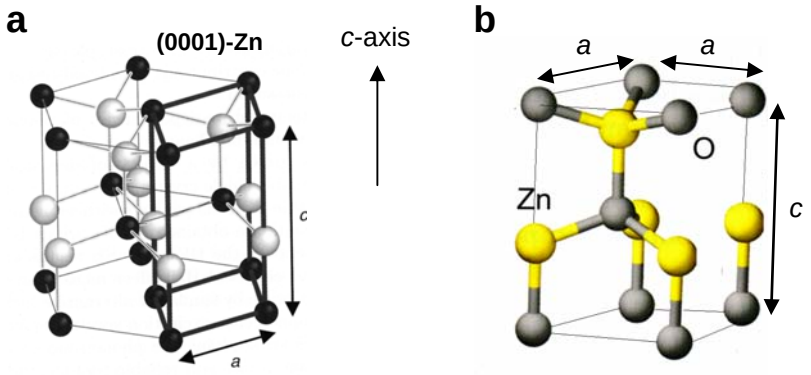

Figure 1.3 The illustration of (a) primitive cell (heavy lines) of the wurtzite-structure lattice placed within a hexagonal prism where *a* and *c* are the lattice constant while the black and grey balls represent Zn^{2+} and O^{2-} respectively,[84] and (b) unit cell of the crystal structure of ZnO. The light grey spheres correspond to oxygen, the dark ones to zinc.[72]

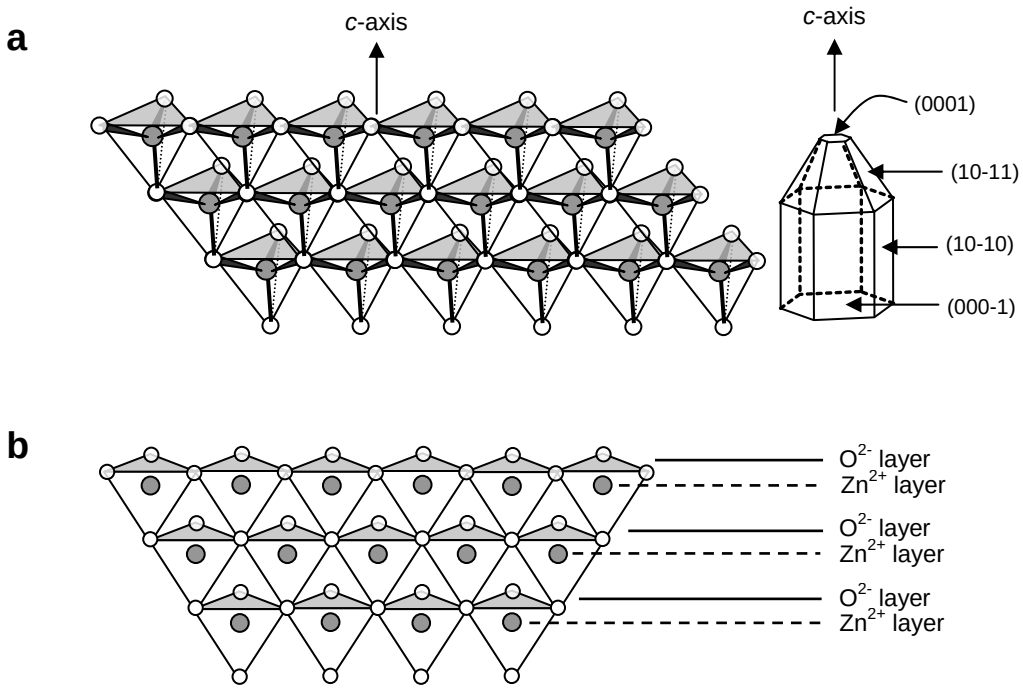

Figure 1.4 Illustration of (a) orientation relation between (0001) plane, (000-1) plane and $[ZnO_4]^{6-}$ tetrahedron, and (b) the asymmetry of Zn^{2+} and O^{2-} layers spacing along *c*-axis of ZnO crystals. White and grey circles correspond to O^{2-} and Zn^{2+} respectively.

In the wurtzite structure, Zn^{2+} is hexagonally close packed where each Zn^{2+} is surrounded by four oxygen atoms to form a $[ZnO_4]^{6-}$ tetrahedron.[85] Every tetrahedron is connected through the corners to form a three-dimensional structure shown in **Figure 1.4a**. One face of the tetrahedron is parallel to the positively-charged Zn^{2+}-terminated (0001) plane while the corner of the tetrahedron normal to the (0001) plane is directed to the negatively-charged O^{2-}-terminated (000-1) plane. As shown in **Figure 1.4b**, the distribution of Zn^{2+} along the *c*-axis is asymmetric and Zn^{2+} is not located in the middle of the two oxygen layers, but nearer to the +*c* direction. Thus, there is no centre of inversion in the wurtzite structure. This intrinsic factor results in ZnO being polar and hence there is an inherent asymmetry along its *c*-axis allowing anisotropic growth along the [0001] direction.[86]

Piezoelectricity refers to a reversible process in which a contraction or elongation is created in the crystal once it is positioned in an electric field. A crystal can only be piezoelectric if it is non-centrally symmetric, ensuring non-compensation among the dipoles in the crystal. In short, piezoelectricity is due to atomic scale polarization. In ZnO crystals, (partial) ionic bonding coupled with the lack of a centre of inversion has resulted in alternating oppositely-charged layers of Zn^{2+} and O^{2-}. These oppositely charged layers create a spontaneous and permanent polarization effect give rise to piezoelectricity to ZnO.[72, 83] The piezoelectric effect is determined by crystal structure therefore it does not reduce or vanish as the dimension of crystal reduces but is preserved or enhanced due to the free boundary for volume expansion/contraction.[87] Since piezoelectric materials are capable of converting a mechanical vibration into an electric signal or vice versa, ZnO can be used in resonators, controlling tip movement in scanning probe microscopy, sensors for vibration waves in air and under sea etc.[87]

1.4.2 Growth habits of ZnO crystal

The growth rate of low index planes of ZnO, determined by their relative surface activities (energy), is given in the following order: (0001)>(10-10)>(10-11)>(000-1).[83, 88-90] Under thermodynamic equilibrium conditions, the morphologies formed tend to maximize the areas of low surface energy planes, such as {10-11} and {10-10}, and minimize the high surface energy planes such as (0001). Thus crystal planes of lower

energy (thermodynamically more stable) tend to grow slower while crystal planes of higher surface energy (thermodynamically less stable) grow faster. As a result ZnO crystals are inherently elongated along its *c*-axis as shown in **Figure 1.4a**. The overall shape and aspect ratio of crystals are determined by the relative growth rates of the crystals planes. The growth rate of a crystal plane is controlled by a combination of internal, structurally-related factors (intermolecular bonding preferences or dislocations), and external factors (supersaturation, temperature, pressure, solvents, and impurities).[91] By controlling the growth kinetics, it is possible to change the growth behaviour of ZnO crystals to promote the formation of different crystal morphologies.

1.4.3 Synthesis routes to ZnO

Vapour route or solution route synthesis can be used to produce bulk ZnO, epitaxial layers and thin films, and large area polycrystalline layers. Depending on the desired type of ZnO, commonly used vapour route techniques are gas transport technique, molecular beam epitaxy (MBE), pulse laser deposition (PLD), metal-organic chemical vapour deposition/metal-organic vapour phase epitaxy (MOCVD/MOVPE), radio-frequency (RF) sputtering, and spray pyrolysis.[72] The structure and quality of vapour route synthesized ZnO depends strongly on the following parameters: composition of ZnO precursor (source material), Zn precursor evaporation temperature, lattice mismatch between ZnO and substrate, substrate temperature, pressure, type of carrier gas, carrier gas flow rate, oxygen concentration, precursor evaporation time period, the use of catalyst, type of catalyst etc. To date, many highly crystalline ZnO nanostructures have been synthesized via the vapour route, i.e. nanorods,[72] nanowires,[92, 93] nanonails,[94] nanocombs,[95] nanobrushes, nanobridges,[94] nanorings,[96] nanohelices/nanosprings,[97] nanobelts/nanoribbons,[98] nanocages,[99] and hierarchical structures such as tetrapods,[100] hierarchical nanowire junction arrays etc.[74] Some of these structures are shown in **Figure 1.5**.

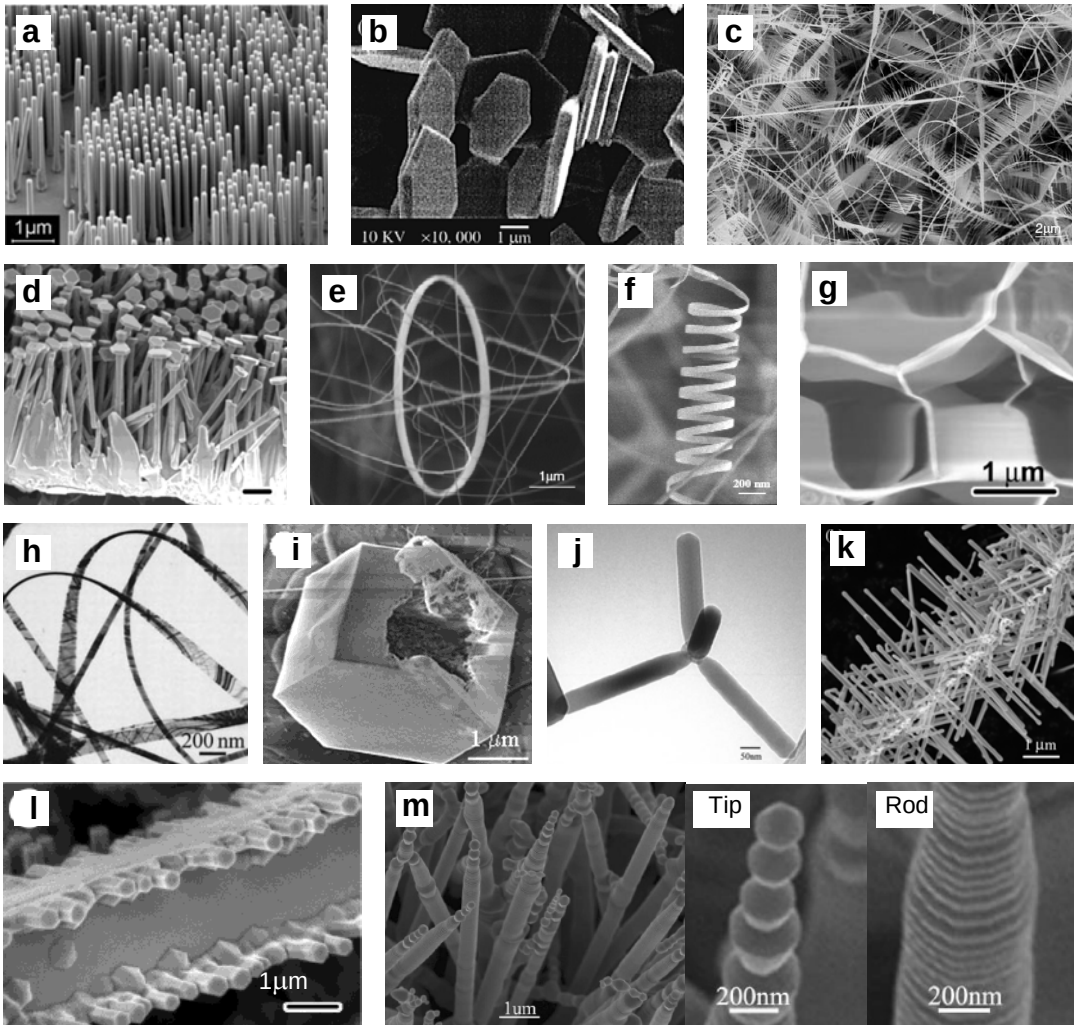

Figure1.5 ZnO nanostructures (scale bar) synthesized via vapour routes: (a) nanorods (1μm),[72] (b) nanodisks (1μm),[101] (c) nanocombs (2μm),[95] (d) nanonails (1μm),[94] (e) nanorings (1μm),[96] (f) nanohelices/nanosprings (200nm),[97] (g) nanowalls (1μm),[102] (h) nanobelts (200nm),[98] (i) nanocage (1μm),[99] (j) tetrapods (50nm),[100] (k) nanowires junction arrays (1μm),[74] (l) nanobridge (1μm),[94] and (m) hierarchical nanorods structures (1μm), the magnifications of the tip (200nm) and the layered middle segment (200nm).[103]

ZnO can be synthesized in solution using a hydrothermal method (closed bath),[83, 104-109] chemical bath deposition (CBD, aqueous solution, open bath),[89, 110-114] sonochemical method,[115-117] microwave-assisted method,[115] and light-assisted method.[118, 119] Solution route synthesis is performed either in an aqueous solution or in an organic solvent, typically at a temperature below 200°C. Since the CBD method has been use in this study, its solution chemistry is summarised as follows. In the presence of aqueous medium, Zn^{2+} species are solvated by water giving rise to $[Zn(H_2O)_n]^{2+}$, the aquo-ions. Since the Zn-OH_2 bond is polarised, it is capable of facilitating the deprotonation of the

coordinated water. In dilute solutions, a range of monomeric species, $[Zn(OH)]^{+}$, $[Zn(OH)_2]$, $[Zn(OH)_3]^{-}$, and $[Zn(OH)_4]^{2-}$ are present (water molecules have been omitted from the formula) where $[Zn(OH)_3]^{-}$ and $[Zn(OH)_4]^{2-}$ are soluble while $[Zn(OH)_4]^{2-}$ is the most stable among the hydroxo species.[120] The formation of polynuclear species occurs via condensation reactions, olation and oxolation.[121] Olation involves the nucleophilic attack of a negatively charged OH group onto a positively charged metal cations and leads to the departure of an aquo ligand from the coordination sphere of the metal. This leads to the formation of an "ol" bridge as follows:

$$M\text{-}OH \quad + \quad M\text{-}OH_2 \quad \rightarrow \quad M\text{-}OH\text{-}M \quad + \quad H_2O$$

Such a process is only possible with aquo-precursors having their maximum coordination numbers. Oxolation occurs when two hydroxo groups react together forming a water molecule and an "oxo" bridge. The reaction starts with the nucleophilic addition of OH groups onto metal ions and is followed by a 1,3-proton transfer within the transition state (M-(OH)----M-OH) so that water molecules can be removed easily. The reaction is shown as follows:

$$2\ M\text{-}OH \quad \rightarrow \quad M\text{-}(OH)\text{----}M\text{-}OH \quad \rightarrow \quad M\text{-}O\text{-}M \quad + \quad H_2O$$

Since reacting species are OH groups in both cases, the condensation reaction does not occur before the formation of stable hydroxylated precursors in aqueous solution.

In CBD, the generation of metal particles can be generated by raising the temperature of the reaction solution (forced hydrolysis) to produce a supersaturated solution.[89, 122] The crystal morphology of ZnO crystals formed by CBD depends on the level of supersaturation, ligands present in solution, counter ions of zinc used, presence of complexing agents, substrates, reaction temperature, and reaction pH.[89] Similar to vapour route synthesis, ZnO of diverse morphologies has been produced by solution route synthesis and some of the morphologies obtained are shown in **Figure 1.6**.

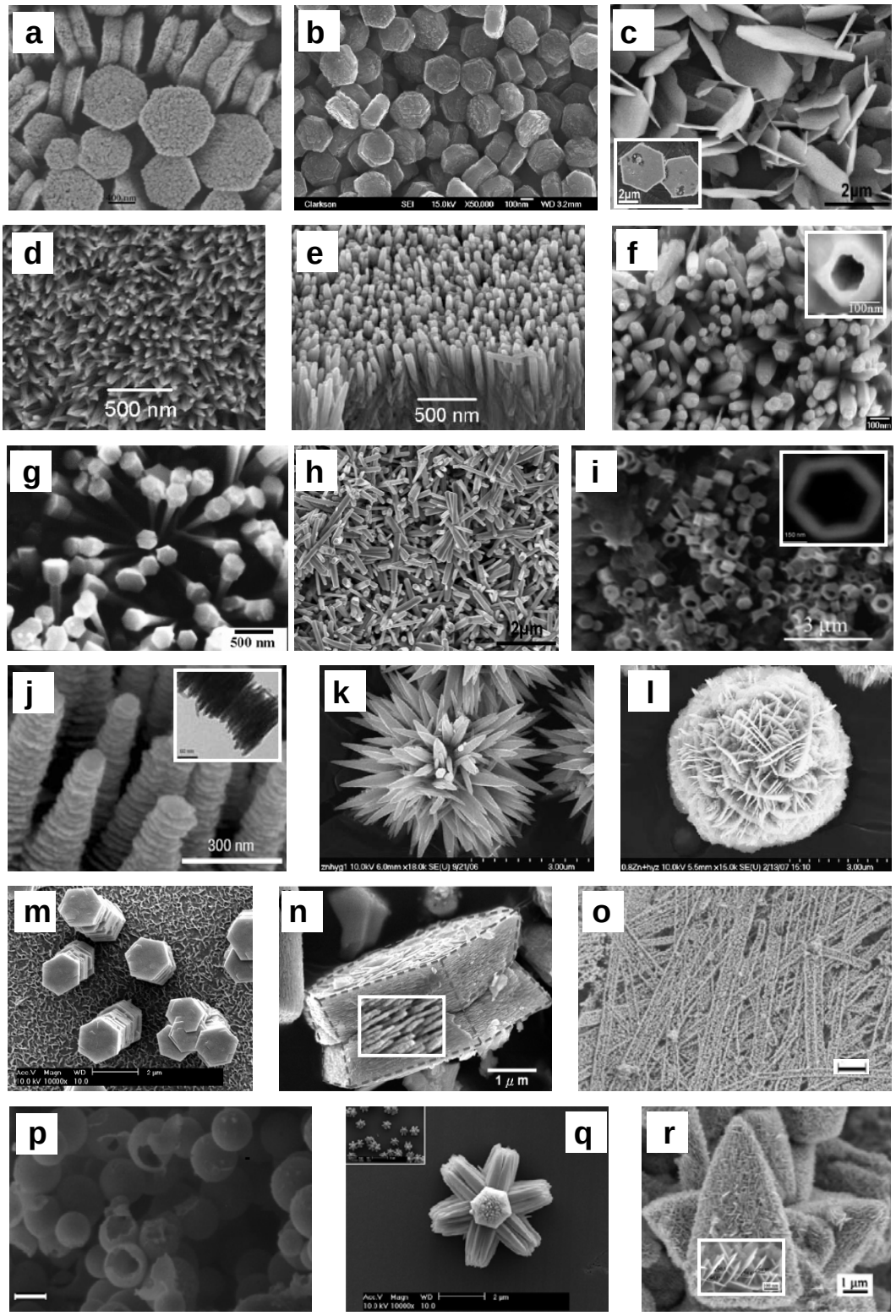

Figure 1.6 ZnO nanostructures (scale bar) synthesized via solution routes: (a) twinned nanodisks,[123] (b) nanodisks (100nm),[124, 125] (c) nanoplates[126] (d) aligned nanoneedles,[127] (e) aligned nanorods,[127] (f) aligned closed-end nanotubes (inset: 100nm),[128] (g) nanonails,[129] (h) nanorods,[126] (i) nanorings (inset: 150nm),[123] (j) oriented nanocolumns and plates (inset: 60nm),[130] (k) and (l) flowerlike ZnO,[131] (m) stacked nanoplates,[132] (n) twinned disk from nanoplates,[5] and (o) porous nanobelts (1μm),[133] (p) hollow spheres (1μm),[75] (q) high surface area floral,[132] and (r) nanosheets on hexagonal based pyramid.[79]

The synthesis of ZnO via the vapour route can produce high quality single crystalline ZnO crystals.[134] However this approach is cost intensive due to the use of elevated temperature (450-900°C), controlled atmospheric systems, more expensive reactants (volatile precursors such as diethyl zinc requires special packaging), and of course safety gauges for risk control. In contrast, the solution approach is simple, straight forward, requires low temperature, and has great potential for scaling up.[134] The solution approach especially the 'green route' (non-organic solvent) allows the combination of biotechnology with ZnO synthesis to improve the nanoparticles assembly capabilities, thus providing diversity in respect of morphology and interfaces.[5, 135] The use of stabilizing agents for size and aggregation control,[136, 137] and capping agents for morphology control are also possible with the use of water and organic as solvent.[79, 132, 138-141] Doping of ZnO can be difficult in aqueous systems due to the potential interactions between the dopant species and water. However this can be overcome by applying a reducing potential to the growth substrate that favours doping over metal-aquo complex formation[142, 143] or by using organic solvents as the reaction medium. The latter option has been shown to be feasible for the incorporation of manganese, iron, and copper as dopant into nanowires. Some ZnO nanostructures synthesized via the solution route have been tested for their potential applications.[3-7, 78, 79, 144]

1.5 Effects of Biomolecules on ZnO Formation

The investigation of biomolecule-mineral, -metal and/or their precursor interactions is not new for silica,[10, 14, 17, 18, 20, 47, 145] titania,[21, 22, 146-148] zirconia,[21] gallium oxide,[149] calcium carbonate,[150-152] aluminium,[153] gold,[42, 48, 154-156] and silver.[7] Inspired by biomineralisation, the synthesis of ZnO and/or its precursors have been studied using amino acids and/or dipeptides,[157-160] polypeptides,[161] ZnO-binding peptides,[41, 162, 163] spider-silk peptides,[164] silk fibroin (SF),[165] gelatine,[5, 166] Arabic gum,[125] whey protein isolates (WPI),[167] eggshell membrane (ESM),[168] genetically modified (GM) collagen,[163] and carbohydrates such as pectin.[169] When these biomolecules are introduced into ZnO-forming systems or stable $Zn(OH)_2$ systems; four general effects

have been reported in the literature (**Figure 1.7**): (i) modification of ZnO morphology,[6, 157, 158, 162, 166, 168, 170] (ii) formation of nanocomposites,[167, 169] (iii) suppression of ZnO formation,[157, 158] and (iv) catalysis of ZnO formation.[41, 163, 164]

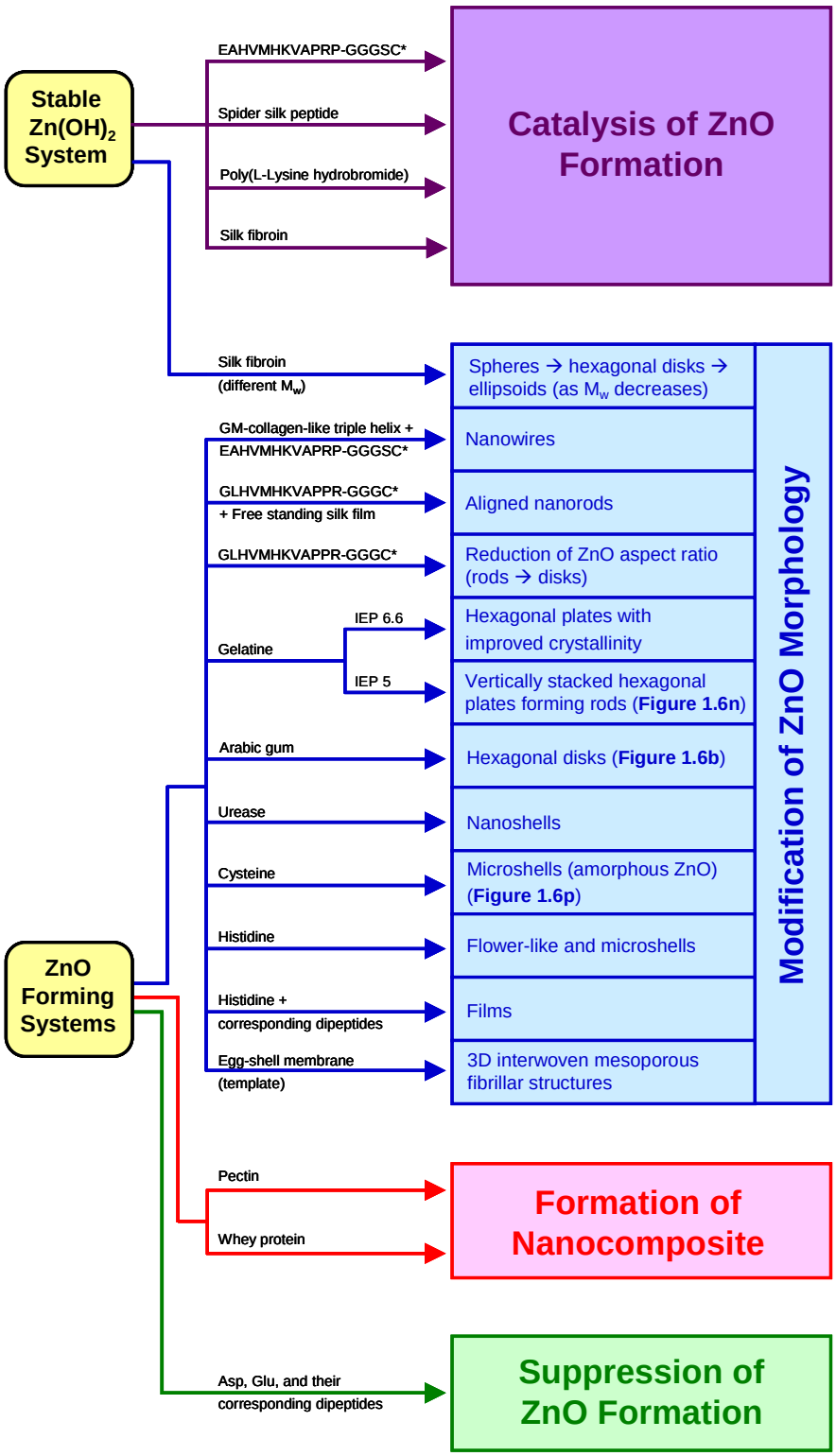

Figure 1.7 The effects of biomolecules on ZnO forming systems and stable $Zn(OH)_2$ systems. Tagged ZnO-BPs are marked with an asterisk. IEP is the abbreviation for isoelectric point.

1.5.1 Modification of ZnO morphology

The presence of GLHVMHKVAPPR-GGGC (GT-16),[162] gelatine,[5, 166] urease,[170] Arabic gum,[125] genetically-modified collagen-like helical structures,[163] egg shell membrane (ESM),[168] silk fibroin (SF),[165] amino acids such as histidine[6, 157, 158] and cysteine,[171] and the dipeptides of histidine (Gly-His, His-Gly, His_2),[157, 158] modified ZnO morphology in different ways (with respect to their controls). To date, the use of some biomolecules has been shown to (i) affect the aspect ratio of ZnO crystals, (ii) facilitate the formation of films, (iii) produce hollow structures, (iv) induce porosity, and (v) template the formation of one- or three dimensional structures.

Twinned/untwinned hexagonal plates formed in the presence of GT-16, gelatine and Arabic gum were very similar to those obtained by the use of DMAB (dimethylamineborane),[75] PAM-COOH (carboxyl-modified polyacrylamide),[123] and citrate ions.[104, 130, 172, 173] In the presence of gelatine and GT-16, a reduction of crystal aspect ratio (L/D) with respect to the controls (without biomolecules) was observed. In the presence of a gelatine sol (<1wt%, random coil, isoelectric point IEP 6.6), Bauermann *et al.* observed the formation of twinned hexagonal plates (L/D~0.1) instead of untwined cylindrical nanodisks (L/D~0.5) in their absence.[166] Based on the detection of gelatine **only** at the twinned plane of these plates, the authors proposed the electrostatic interactions between negatively-charged gelatine (at pH 8) and the Zn^{2+}-water complex was responsible for the twinned plate formation and a concomitant drastic improvement in crystallinity. The improved crystallinity was judged by the increase of crystallite domain size from 20nm (Scherrer equation, XRD) to 460nm (TEM) but the change of morphology was not discussed.[166] The ability of gelatine to induce ZnO crystallization even when immobilized was confirmed.

In another study using gelatine (IEP 5) as the structure directing agent (SDA), Tseng *et al*. produced nacre-like hierarchical twinned hexagonal plates at pH 6.4 (**Figure 1.6n**).[5] Three levels of structural organisation mediated by the adsorption of the COO^- of gelatine on the (0001) plane of ZnO crystals were proposed: (i) oriented attachment of nanoparticles to form hexagonal nanoplates (20nm thick); (ii) stacking of nanoplates to form a mesocrystals (aided by the formation of interlayer bridges); and (iii) the twinning of mesocrystals as proposed by Bauermann *et al*..[166] The adsorption of

gelatine was supported by a 12% weight loss (TGA) assignable to the decomposition of gelatine. These mesocrystals show a whispering gallery mode (WGM) of optical emission when light was confined in the hexagons by total internal reflection giving it great potential to be used for nanoscale fabrication of optoelectronic devices.[5]

GT-16 (GLHVMHKVAPPR-GGGC) is a tagged ZnO-BP used by Tomczak *et al*.[39] in a biotemplating study where the original ZnO-BP isolated was G-12, GLHVMHKVAPPR. In GT-16's presence, L/D value was reduced from ~9 for the control to <0.5 when 0.5mg/mL of GT-16 was used. It was proposed that GT-16 inhibits *c*-axis growth of ZnO by selectively adsorbing on the (0001) plane via its glycine (G) and cysteine (C) residues.[162] This proposal was supported by four observations: (i) GT-16 addition reduced the L/D of ZnO crystals, (ii) the reduction of L/D increased with GT-16 concentration, (iii) a flat and well defined (0001) plane was formed in GT-16's presence instead of bypyramidal ZnO crystals (Control), and (iv) GT-16 did not affect the diameter growth of ZnO crystals. When coupled with a silk film as a biotemplate, GT-16 was found to bind onto free standing silk film and directed the ordered growth of nanorods (normally to the silk film) to form aligned nanorods.[39] The great difference in morphology modification induced by GT-16 in the absence and presence of the silk film is not yet known.

The addition of Arabic gum produced hexagonal disks (**Figure 1.6b**) as opposed to irregular agglomerated particles in its absence.[125] The formation of hexagonal disks occurs via two steps: rapid aggregation of nanosize precursors into larger uniform spheres followed by a slow rearrangement process via dissolution/reprecipitation. Therefore the presence of Arabic gum may have facilitated the rearrangement of constituent particles to regular geometric shape by improving the solubility of the constituent particles. The exact role of this additive, a complex mixture of saccharides and glycoprotein, has not been identified however the L/D of hexagonal disks formed was found to be dependent on the concentration of the zinc precursor and the counterions of zinc salt used.

According to Gerstel *et al*., amino acids having side chain functionality that interact electrostatically with Zn^{2+} in solution or on a crystal seed interface would impose a strong influence on the morphology of the deposits formed.[157, 158] This allows some

amino acids to tune the morphology of ZnO from grain-like (discrete) to two-dimensional (film), and up to three-dimensional features (indirectly). In the absence of Zn^{2+} complexing functions on their side chains, weak interactions of citruline, proline, glycine, and glycylglycine with Zn^{2+} produced micrometric ZnO crystals comparable to those obtained in their absence.[157, 158] In contrast, the strong and direct interactions of imidazole histidine and its dipeptides (His, Gly-His, His-Gly, His_2) with Zn^{2+} species generated smooth ZnO films.[157, 158] The proposed role of histidine is supported by the positive correlation between film thickness and histidine concentration present in the crystallizing system.[157]

Besides ZnO film formation, histidine has been shown to produce a range of ZnO structures; prism-like crystals, floral crystals and microshells (both crystalline and non-crystalline).[6] According to Wu *et al.*,[6] this ZnO structure modulation is driven by competitive coordination between histidine and OH^- to Zn^{2+} to form $Zn(OH)_n$ or $Zn(His)_n^{2+}$ complexes respectively. Depending on the relative concentrations of OH^- Zn^{2+} and histidine ($[OH^-]$), $[Zn^{2+}]$, and [His]), the majority complex species formed would adsorb on the surfaces of ZnO nuclei to direct crystal growth. At higher $[OH^-]/[Zn^{2+}]$ where $Zn(OH)_n$ complexes are the majority, the natural anisotropic growth of ZnO dominates to produce prism-like crystals. At lower $[OH^-]/[Zn^{2+}]$ and/or higher [His], some histidine molecules adsorbed on the surfaces of ZnO nuclei to produce floral crystals and nanoparticles. Extensive coverage of nanoparticles by histidine may have affected the "oriented" aggregation of nanoparticles thus non-crystalline microspheres were obtained (at higher [His]) in opposed to crystalline microspheres when [His] was relatively lower. All three types of ZnO crystals formed showed photocatalytic activity for the reversible reaction of formaldehyde and carbon dioxide (CO_2).

Micro/nanoshells are also produced by exploiting Zn-cysteine interactions[171] and using urease[170] as a nanoreactor. In the presence of R-(+)-cysteine, spherical amorphous ZnO microshells with shell wall thickness of 50nm were produced. The incorporation of cysteine and NO_3^- (from $Zn(NO_3)_2$ precursor) was confirmed (FTIR and TGA). The thermal decomposition of the amorphous microshells produced crystalline ZnO which retained the morphology of its amorphous counterpart. The formation of the amorphous phase was believed to be caused by the complexation of cysteine with Zn^{2+}.

Urease is an enzyme that facilitates the hydrolysis of urea to form ammonia, and it has high affinity for metal ions. Utilising the ability of local pH control, de la Rica and Mitsui used urease to catalyse and template the formation of highly crystalline ZnO nanoshells.[170] The use of an enzymatic approach to produce ZnO nanoshells is very exciting because it offers mild reaction conditions and controllable core diameter via the use of catalytically active isozymes of urease available in various sizes.[174] The catalysis of urea to NH_3 by urease created a local chemical environment of high pH within the vicinity of urease surface, favourable for ZnO formation. Furthermore negatively charged urease (IEP 4.9) at pH 9 is capable of pre-concentrating the Zn precursor on its surface via electrostatic interactions. The catalytic and templating roles of urease, suggested by its chemical and structural properties, were validated when the use of denatured urease did not yield ZnO, even in the presence of externally added ammonia.

Silk fibroin (SF) is one the most extensively research biomaterials because of its good biodegradability and biocompatibility. SF obtained after degumming of *B. mori* silk is made up of two polypeptide chains linked by a disulfide bridge. The major residue in the SF were hydrophobic glycine, alanine, serine with hydroxyl-side chain and aspartic acid.[165] Yan *et al.*[165] used SF of different molecular lengths (thus different M_w) to catalyse and template heterogeneous nucleation of ZnO from a $Zn(OH)_2$ sol. As the M_w of SF was decreased, the dominant morphology of ZnO crystals obtained is given in the following order: globular, plates, and ellipsoidal crystals. Special primary structure of SF and the presence of many charged amino acids allow electrostatic adsorption of Zn^{2+} and OH^- to SF. The further condensation of adsorbed species forms ZnO particles. The presence of SF on the surface of ZnO particles was detected however the distinct morphology obtained from SF with different M_w was not discussed. Antibacterial tests performed showed that the ellipsoid ZnO crystals were non-toxic, cytocompatible and able to penetrate the bacteria studied (*S. aureus*, *E. coli*, and *S. agalactiae*). This is possibly due to the SF-coating on its surface. Thus, the potential application of these ZnO particles in a bio-optical detector could be envisioned.

ZnO synthesis biotemplated by genetically modified-collagen-like triple helix peptide (GM-collagen)[163] and egg shell membrane (ESM)[168] produced one dimensional nanowires and three dimensional interwoven mesoporous fibrillar structures (formed

by nanoparticles of 5-6nm) respectively. ESM is a non-mineralized, collagen-based matrix consisting of type I, V, and X collagen and surrounded by a soluble glycoprotein mantle.[175] Based on the explanation by Dong *et al*., ESM interacts with the zinc precursor ($Zn(NO_3)_2$) via its soluble glycoprotein mantle.[168] When ESM is exposed to zinc nitrate solution, Zn^{2+} ions are transported onto the self-assembled hydrophilic group of the glycoprotein while the short chain amino acids of the glycoprotein function as a capping agent to stabilize nanocrystallites as the building blocks. The final oxide efficiently retained the hierarchical structure of the biotemplate as the biotemplate was burned off. Similar templating effect was observed in PdO and Co_3O_4 formation.[168]

The GM-collagen tailored by Bai *et al*.[163] to produce ZnO nanowires is different from wild collagen in two aspects. Firstly, mechanical rigidity was increased by the repeating $(Gly\text{-}Pro\text{-}Pro)_n$ sequence around the 63 residues of collagen while the enhancement on the rigidity was achieved by inserting a pair of cysteine residues.[176] The rigidity modification of the template also ensures its survival at high reaction pH, confirmed by a higher denaturation temperature (by 5°C) as compared to wild type collagen.[176] Secondly, a tagged ZnO-BP ET-17 (EAHVMHKVAPPR-GGGSC) confirmed to be catalytic in ZnO formation at room temperature was attached on the surface of the triple helix via hydrogen bonding.[41] In the absence of ET-17 and/or the GM-collagen biotemplate, no crystalline ZnO but amorphous zinc hydroxide aggregates were grown. Hence GM-collagen (with reinforced rigidity) and attached catalyst catalysed ZnO formation and templated the formation of nanowires.

1.5.2 Formation of nanocomposites

Biomolecule-coated nanocrystalline ZnO nanocomposites were formed in the presence of pectin[169] and whey protein isolates (WPI).[167] The formation mechanism of pectin-ZnO nanocomposite was not shown but the higher decomposition temperature (by 20°C) of the pectin shell in this nanocomposite was believed to have arisen from the strong interactions between ZnO and pectin. Being a by-product of cheese manufacturing, WPI contains β-lactoglobulin as its major component. Under a reaction

condition of pH 8, β-lactoglobulin with IEP of 5.2 was anionic. Thus rationally the formation of WPI-ZnO nanocomposite was proposed to be directed by electrostatic interactions between Zn^{2+}-aquo complexes and the carboxylic groups of β-lactoglobulin, and/or the primary amino groups or sulfhydryl group of WPI.[167] Coupled with WPI which has been obtained as a drug carrier for oral administration, it is believed that the WPI-coated ZnO nanoparticles will survive the gastric environment and become available in the intestine and be readily adsorbed due to their nanoscale. This makes WPI-coated ZnO nanoparticles a candidate for the form of a Zn fortified element usable in foodstuff however the toxicity of ZnO nanoparticles present in biological systems is still under study.

1.5.3 Suppression of ZnO formation

Among many researchers working on biomolecules-directed ZnO formation, Gerstel *et al*. studied the effects of smaller biomolecules on ZnO formation. As mentioned in **Section 1.5.1**, the selection of the "right" amino acids in accordance with their side chain reactivity with Zn^{2+} would allow the tuning of ZnO morphology to produce a wide spectrum of ZnO structures. Low IEP residues such as aspartic acid and glutamate acid (and their corresponding dipeptides) have been shown to suppress ZnO formation due to their anionic nature under the reaction conditions used. Gerstel *et al*. proposed that the anionic aspartic acid and glutamate acid intercalated between the brucite layers of the layered basic zinc salts (LBZS) by electrostatic interaction hence stabilizing this intermediate compound.[158] The intercalation of aspartic acid and glutamate acid was confirmed by the increase of the LBZS interlayer spacing by XRD. The stabilization effect of the solid phase intermediate compound via complexation with Zn^{2+} was further confirmed when the use of aspartic acid and glutamate acid at higher concentrations produced soluble complexes as a result of a greater stabilization effect.[158]

1.5.4 Catalysis of ZnO formation

The presence of some biomolecules modified ZnO morphology while others form nanocomposites with it. The diversity of effects seen in the presence of biomolecules has been further demonstrated when acidified spider-silk peptides (with adsorbed ZnO nanoparticles),[164] poly($_L$-lysine hydrobromide) (PLL),[161] and EAHVMHKVAPRP-GGGSC[41] (ET-17), were found to catalyse ZnO formation from a stable $Zn(OH)_2$ sol. Huang *et al*. used peptides acidified from spider silk, from *Uloborus walckenaerius Latreille*, to catalyse ZnO formation and produced spindle-like ZnO (described as olivary by the authors).[164] Spider silk peptides obtained from the hydrolysis of spider silk have typical M_w of 45~64kDa, resembling peptides with ~16 amino acid residues. The resulting peptides are amphiphilic chains with aspartic acid, glutamate acid, and lysine. As proposed by Huang *et al*., the catalysis of spindle-like ZnO formation occurred via aggregation driven mineralization. When ZnO nanoparticles immobilized on a peptide chain was exposed to zinc nitrate solution at pH 7.5~8, $Zn(OH)_2$ gel particles formed were coated by the ZnO nanoparticles immobilized peptide chain. The peptide chain then catalysed the condensation of $Zn(OH)_2$ into ZnO nanoparticles which then organised into spindle-like microparticles.

The catalytic effect shown by Umetsu *et al*.[41] using ET-17 was rather interesting. The cysteine residue at the C-terminus of the peptide sequence was added for the immobilization of the peptide on a gold-coated polypropylene plate via its thiol group. In addition, a GGGS linker was added to increase the flexibility of the peptide when immobilized. The addition of ET-17 into a stable $Zn(OH)_2$ sol (stable after a month) induced the formation of flower-like ZnO crystals. Umetsu *et al*. did not confirm if the use of EAHVMHKVAPRP (E-12) alone would induce a similar effect, however they did show that neither a mixture of free amino acids found in ET-17, the GGGSC-tag, nor ET-17 with a serine-substituted C-terminus (EAHVMHKVAPRP-GGGSS), could precipitate ZnO. Hence the presence of EM-12 and the GGGSC-tag were both proposed to be necessary for the condensation of the $Zn(OH)_2$ sol to ZnO. According to them, the cysteine-mediated $Zn(OH)_2$ dehydration was made possible by the microenvironment defined by the EM-12 segment.

At near neutral pH and at room temperature, the use of a cationic poly($_L$-lysine hydrobromide (PLL, 150kDa) and also poly(acrylic hydrochloride) (PAH) has catalysed ZnO formation to produce similar spindle-like ZnO crystals as Huang *et al*.[164] reported.[161] Begum *et al*. suggested that the electrostatic interaction between NH_3^+ of the additives and the surface oxygen atoms of Zn-OH groups was responsible for the nucleation (catalysis) of ZnO formation.[161] PLL (pK_a≈9-11) being positively-charged at ~pH 7.5 is able to adsorb on the surface of $Zn(OH)_2$ via its NH_3^+. The accumulation of many NH_3^+ groups in a confined space initiates the dehydration of hydroxides to form ZnO. The role of electrostatic interaction was verified by the retardation of ZnO formation by increasing the ionic strength of the solution through KNO_3 addition. Apparently the formation of an electrical double layer is able to suppress the electrostatic interactions and hence the electrostatic interaction is essential for ZnO mineralization.

1.6 Project Aims and Scope

The studies of peptide-mineral interactions presented in this thesis aimed to identify and understand the effect(s) induced by peptides/selected motif on mineral formation through the study of two model systems: amorphous silica forming system and crystalline ZnO forming system. The study of biomolecule-silica interactions was motivated by the intricate hierarchical structures of biosilica which serve diverse biological and functional roles. The formation of biosilica involves interesting chemistry such as, benign environment, undersaturated precursor concentration, superior precursor recognition capability, and high structure reproducibility. The ZnO model system was selected because it has only one crystal phase at atmospheric pressure and thus would not complicate the study by going through phase transformation. Furthermore, silica and ZnO are technologically useful materials and the latter has properties and applications which are closely related to its size and morphology. Imidazole-silica interactions has been selected mainly due to the presence of histidine as one of the "catalytic triad" in silicatein[12] which is highly identical to that of cathepsin-L; and also the abundance of histidine residues in SiO_2-BPs identified.[45]

Two ZnO-BPs, EAHVMHKVAPRP[41] and GLHVMHKVAPPR,[39] have been chosen for the study of ZnO formation. These two ZnO-BPs were identified from phage display libraries using ZnO targets of 1μm in diameter and a nanopowder respectively. These ZnO-BPs have highly similar amino acid sequences but the effects imposed on ZnO formation were very different. This suggests that slight difference in their sequences will result in significant changes in the physical and chemical properties of the peptides.

The investigations of the effect of selected biomolecules on these model systems were preceded with a thorough study of the model systems in the absence of any additives. The reaction kinetics were studied using the molybdenum blue assay and Inductively Coupled Plasma Optical Emission Spectrometry (ICP-OES, to quantify $[Zn^{2+}]$ in solution) for silica and ZnO respectively. The silica and ZnO precipitated were characterised using Scanning Electron Microscopy (SEM), Fourier Transform Infrared Spectroscopy (FTIR), Thermogravimetric Analysis (TGA), and also X-Ray Diffraction (XRD) for ZnO. The adsorption of ZnO-BPs on different ZnO surfaces was also studied using ZnO films with single crystal orientation. Computational studies have also been performed by Dr. Olivier Deschaume to complement the findings of this study. The ultimate goal of this peptide-mineral study is two-fold; to explore the phenomenal complexity of the behaviour of imidazole/peptides in (bio)mineralising systems, and to exploit the ground rules in their interactions (with species in (bio)mineralising systems) for the synthesis of novel nanomaterials with properties tailored for specific applications.

References

1 S. Mann, *Biomineralization: principles and concepts in bioinorganic materials chemistry*. (Oxford University Press, New York). 2001.

2 M. B. Dickerson, K. H. Sandhage, and R. R. Naik, *Chem. Rev.* **108**, 4935-4978 (2008).

3 L. L. Brott, R. R. Naik, D. J. Pikas, S. M. Kirkpatrick, D. W. Tomlin, P. W. Whitlock, S. J. Clarson, and M. O. Stone, *Nature* **413**, 291-293 (2001).

4 K. M. Roth, Y. Zhou, W. Yang, and D. E. Morse, *J. Am. Chem. Soc.* **127**, (1), 325-330 (2005).

5 Y.-H. Tseng, H.-Y. Lin, M.-H. Liu, Y.-F. Chen, and C.-Y. Mou, *J. Phys. Chem. C* **113**, 18053-18061 (2009).

6 Q. Wu, X. Chen, P. Zhang, Y. Han, X. C. Y. Yan, and S. Li, *Cryst. Growth Des.* **8**, (8), 3010-3018 (2008).

7 R. R. Naik, S. J. Stringer, G. Agarwal, S. E. Jones, and M. O. Stone, *Nature* **1**, 169-172 (2002).

8 C. C. Harrison, and f. Perry), *Phytochemistry* **41**, (1), 37-42 (1996).

9 N. Kröger, R. Deutzmann, and M. Sumper, *J. Biol. Chem.* **276**, (28), 26066-26070 (2001).

10 N. Kröger, R. Deutzmann, C. Bergsdorf, and M. Sumper, *PNAS* **97**, (26), 14133-14138 (2000).

11 A. Krasko, B. Lorenz, R. Batel, H. C. Schröeder, I. M. Müller, and W. E. G. Müller, *Eur. J. Biochem.* **267**, 4878-4887 (2000).

12 K. Shimizu, J. Cha, G. D. Stucky, and D. E. Morse, *Proc. Natl. Acad. Sci. U. S. A.* **95**, 6234–6238 (1998).

13 C. C. Perry, and T. Keeling-Tucker, *Chem. Commun.* **23**, 2587–2588. (1998).

14 C. C. Perry, and T. K. Tucker, *Colloid Polym Sci* **281**, 652-664 (2003).

15 S. Matsunaga, R. Sakai, M. Jimbo, and H. Kamiya, *ChemBioChem* **8**, 1729-1735 (2007).

16 Y. Zhou, K. Shimizu, J. N. Cha, G. D. Stucky, and D. E. Morse, *Angew. Chem. Int. Ed.* **38** (6), 779-782 (1999).

17 J. N. Cha, K. Shimizu, Y. Zhou, S. C. Christiansen, B. F. Chmelka, G. D. Stucky, and D. E. Morse, *Proc. Natl. Acad. Sci. USA* **96**, 361-365 (1999).

18 N. Kröger, R. Deutzmann, and M. Sumper, *Science* **286**, 1129-1132 (1999).

19 M. Sumper, and N. Kröger, *J. Mater. Chem.* **14**, 2059-2065 (2004).

20 M. N. Tahir, P. Theato, W. E. G. Muller, H. C. Shroder, A. Janshoff, J. Zhang, J. Huth, and W. Tremel, *Chem. Commun.*, 2848-2849 (2004).

21 M. N. Tahir, P. Théato, W. E. G. Müller, H. C. Schröder, A. Borejko, S. Faiss, A. Janshoff, J. Huth, and W. Tremel, *Chem. Commun.*, (44), 5533-5535 (2005).

22 M. N. Tahir, M. Eberhardt, H. A. Therese, U. Kolb, P. Théato, W. E. G. Müller, H. C. Schröder, and W. Tremel, *Angew. Chem. Int. Ed.* **45**, (29), 4803-4809 (2006).

23 M. Sarikaya, C. Tamerler, A. K.-Y. Jen, K. Schulten, and F. Baneyx, *Nature Materials* **2**, 577-585 (2003).

24 P. J. Lopez, C. Gautier, J. Livage, and T. Coradin, *Current Nanoscience* **1**, (1), 73-83 (2005).

25 M. R. Knecht, and D. W. Wright, *Chem. Commun.*, 3038-3039 (2003).

26 D. Belton, S. V. Patwardhan, and C. C. Perry, *Chem. Commun.*, 3475-3477 (2005).

27 S. V. Patwardhan, and S. J. Clarson, *Mater. Sci. Eng., C* **23**, 495-499 (2003).

28 M. M. Tomczak, D. D. Glawe, L. F. Drummy, C. G. Lawrence, M. O. Stone, C. C. Perry, D. J. Pochan, T. J. Deming, and R. R. Naik, *J. Am. Chem. Soc.* **127**, 12577-12582 (2005).

29 D. Belton, S. V. Patwardhan, and C. C. Perry, *J. Mater. Chem.* **15**, 4629-4638 (2005).

30 R. R. Naik, L. L. Brott, F. Rodriguez, G. Agarwal, S. M. Kirkpatrick, and M. O. Stone, *Prog. Org. Coat.* **47**, 249-255 (2003).

31 D. Belton, G. Paine, S. V. Patwardhan, and C. C. Perry, *J. Mater. Chem.* **14**, 2231-2241 (2004).

32 D. J. Belton, S. V. Patwardhan, V. V. Annenkov, E. N. Danilovtseva, and C. C. Perry, *PNAS* **105**, (16), 5963-5968 (2008).

33 T. Coradin, and J. Livage, *Colloids Surf., B: Biointerfaces* **21**, 329-336 (2001).

34 K. E. Cole, A. N. Ortiz, M. A. Schoonen, and A. M. Valentine, *Chem. Mater.* **18**, (19), 4592-4599 (2006).

35 C. Gautier, P. J. Lopez, J. Livage, and T. Coradin, *J. Colloid and Int. Sci.* **309**, 44-48 (2007).

36 U. Kriplani, and B. K. Kay, *Curr. Opin. Biotechnol.* **16**, 470-475 (2005).

37 C. K. Thai, H. Dai, M. S. R. Sastry, M. Sarikaya, D. T. Schwartz, and F. Baneyx, *Biotechnol. Bioeng.* **87**, 129-137 (2004).

38 K. Kjærgaard, J. K. Sørensen, M. A. Schembri, and P. Klemm, *Appl. Environ. Microbiol.* **66**, (1), 10-14 (2000).

39 M. M. Tomczak, M. K. Gupta, L. F. Drummy, S. M. Rozenzhak, and R. R. Naik, *Acta Biomater.* **5**, (3), 876-882 (2009).

40 M. M. Tomczak, J. M. Slocik, M. O. Stone, and R. R. Naik, *Biochem. Soc. Trans.* **35**, 512-515 (2007).

41 M. Umetsu, M. Mizuta, K. Tsumoto, S. Ohara, S. Takami, H. Watanabe, I. Kumagai, and T. Adschiri, *Adv. Mater.* **17**, 2571-2575 (2005).

42 S. Brown, *Nat. Biotechnol.* **15**, 269-272 (1997).

43 S. R. Whaley, D. S. English, E. L. Hu, P. F. Barbara, and A. Belcher, *Nature* **405**, 665-668 (2000).

44 S. V. Patwardhan, G. Patwardhan, and C. C. Perry, *J. Mater. Chem.* **17**, 2875-2884 (2007).

45 R. R. Naik, L. L. Brott, S. J. Clarson, and M. O. Stone, *J. Nanosci. Nanotech.* **2**, (1), 95-100 (2002).

46 E. Eteshola, L. J. Brillson, and S. C. Lee, *Biomolecular Engineering* **22**, 201-204 (2005).

47 P. Roach, D. Farrar, and C. C. Perry, *J. Am. Chem. Soc.* **128**, 3939-3945 (2006).

48 H. S. Mandal, and H.-B. Kraatz, *J. Am. Chem. Soc.*, est 1.9 (2007).

49 C. F. Barbas, J. S. Rosenblum, and R. A. Lerner, *Proc. Natl. Acad. Sci. U. S. A.* **90**, 6385-6389 (1993).

50 B. L. Vallee, and D. S. Auld, *Biochemistry* **29**, (24), 5647-5659 (1990).

51 I. Bertini, H. B. Gray, E. I. Stiefel, and J. S. Valentine, *Biological Inorganic Chemistry: Structure and Reactivity*. University Science Book: California, 2007.

52 S. V. Patwardhan, S. J. Clarson, and C. C. Perry, *Chem. Commun.*, 1113-1121 (2005).

53 D. E. Morse, *Tibtech* **17**, 230-232 (1999).

54 C. W. P. Foo, J. Huang, and D. Kaplan, *Trends in Biotechnology* **22**, (11), 577-585 (2004).

55 S. Mann, *Angew. Chem. Int. Ed.* **39**, 3392-3406 (2000).

56 N. Kröger, S. Lorenz, E. Brunner, and M. Sumper, *Science* **298**, 584-586 (2002).

57 M. Sumper, E. Brunner, and G. Lehmann, *FEBS Letters (Federation of European Biochemical Society)* **579**, 3765-3769 (2005).

58 N. Poulsen, M. Sumper, and N. Kröger, *Proc. Natl. Acad. Sci. U. S. A.* **100**, 12075-12080 (2003).

59 R. K. Iler, *The Chemistry of Silica*. John Wiley & Sons: New York, 1979.

60 C. C. Perry, and T. K. Tucker, *J. Biol. Inorg. Chem.* **5**, 537-550 (2000).

61 S. V. Patwardhan, N. Mukherjee, and S. J. Clarson, *J. Inorg. And Organomet. Polymers* **11**, (3), 193-197 (2002).

62 X.-d. Zhang, Y.-y. Sun, J.-q. Zhuang, and W.-s. Yang, *Chem. Res. Chinese U.* **22**, (3), 368-370 (2006).

63 S. V. Patwardhan, R. Maheshwari, N. Mukherjee, K. L. Kiick, and S. J. Clarson, *Biomacromolecules* **7**, 491-497 (2006).

64 T. Coradin, O. Durupthy, and J. Livage, *Langmuir* **18**, 2331-2336 (2002).

65 K. M. Delak, and N. Sahai, *J. Phys. Chem. B* **110**, (36), 17819-17829 (2006).

66 K. M. Delak, and N. Sahai, *Chem. Mater.* **17**, (12), 3221-3227 (2005).

67 M. Sumper, S. Lorenz, and E. Brunner, *Angew. Chem. Int. Ed.* **42**, 5192-5195 (2003).

68 E. Brunner, K. Lutz, and M. Sumper, *Phys. Chem. Chem. Phys.* **6**, 854-847 (2004).

69 S. V. Patwardhan, and S. J. Clarson, *J. Inorg. Organomet. Polym.* **13**, (1), 49-53 (2003).

70 G. Croce, A. Franche, M. Milanesio, L. Marchese, M. Causà, D. Viterbo, A. Barbaglia, V. Bolis, G. Bavestrello, C. Cerrano, U. Benatti, M. Pozzolini, M. Giovine, and H. Amenitsh, *Biophys. J* **. 86**, (1), 526-534 (2004).

71 J. N. Cha, G. D. Stucky, D. E. Morse, and T. J. Deming, *Nature* **403**, 289-292 (2000).

72 C. F. Klingshirn, *ChemPhysChem* **8**, 782-803 (2007).

73 S. J. Pearton, D. P. Norton, K. Ip, Y. W. Heo, and T. Steiner, *Prog. Mater Sci.* **50**, 293-340 (2005).

74 Z. L. Wang, *J. Phys.: Condens. Matter.* **16**, R829-R858 (2004).

75 T. P. Chou, Q. Zhang, G. E. Fryxell, and G. Cao, *Adv. Mater.* **19**, 2588-2592 (2007).

76 M. Law, L. E. Greene, J. C. Johnson, R. Saykally, and P. Yang, *Nature Materials* **4**, 455-459 (2005).

77 C.-H. Ku, H.-H. Yang, G.-R. Chen, and J.-J. Wu, *Cryst. Growth Des.* **8**, (1), 283-290 (2008).

78 O. Taratula, E. Galoppini, R. Mendelsohn, P. I. Reyes, Z. Zhang, Z. Zhong, and Y. Lu, *Langmuir* **25**, 2107-2113 (2009).

79 F. Lu, W. Cai, and Y. Zhang, *Adv. Funct. Mater.* **18**, 1047-1056 (2008).

80 H.-Y. Park, H.-Y. Go, S. Kalme, R. S. Mane, S.-H. Han, and M.-Y. Yoon, *Anal. Chem.* **81**, 4280-4284 (2009).

81 J.-Y. Ye, Z.-Y. Huang, S.-R. Pan, and D.-H. Chen, *Biomed. Mater.* **4**, 055004-055009 (2009).

82 Y. Chen, D. M. Bagnall, H.-j. Koh, K.-t. Park, K. Hiraga, Z. Zhu, and T. Yao, *J. Appl. Phys.* **84**, 3912-3918 (1998).

83 R. S. Yadav, and A. C. Pandey, *Physica E* **40**, (3), 660-663 (2008).

84 K. Ellmer, A. Klein, and B. Rech, *Transparent Conductive Zinc Oxide: Basics and Applications in Thin Film Solar Cells*. Springer: 2008.

85 Y. Liu, J.-e. Zhou, A. Larbot, and M. Persin, *J. Mater. Process. Technol.* **189**, 379-383 (2007).

86 L. Vayssieres, K. Keis, A. Hagfeldt, and S.-E. Lindquist, *Chem. Mater.* **13**, (12), 4395-4398 (2001).

87 Z.-L. W. Min-Hua Zhao, Scott X. Mao, *Nano Lett.* **4**, (4), 587-590 (2004).

88 R. A. Laudise, and A. A. Ballman, *J. Phys. Chem.* **64**, 688-691 (1960).

89 K. Govender, D. S. Boyle, P. B. Kenway, and P. O'Brien, *J. Mater. Chem.* **14**, 2575-2591 (2004).

90 W.-J. Li, E.-W. Shi, W.-Z. Zhong, and Z. W. Yin, *J. Cryst. Growth* **203**, 186-196 (1999).

91 B. Cheng, and E. T. Samulski, *Chem. Commun.*, 986-987 (2004).

92 S.-Y. Pung, K.-L. Choy, X. Hou, and C. Shan, *Nanotechnology* **19**, 435609-435614 (2008).

93 J.-H. Park, Y.-J. Choi, and J.-G. Park, *J. Cryst. Growth* **280**, 161-167 (2005).

94 J. Y. Lao, J. Y. Huang, D. Z. Wang, and Z. F. Ren, *Nano Lett.* **3**, (2), 235-238 (2003).

95 Z. L.Wang, X. Y. Kong, and J. M. Zuo, *Phys. Rev. Lett.* **91**, (18), 185502-185504 (2003).

96 X. Y. Kong, Y. Ding, R. Yang, and Z. L. Wang, *Science* **303**, 1348-1351 (2004).

97 X. Y. Kong, and Z. L. Wang, *Nano Lett.* **3**, (12), 1625-1631 (2003).

98 Z. W. Pan, Z. R. Dai, and Z. L. Wang, *Science* **291**, 1947-1949 (2001).

99 P. X. Gao, and Z. L. Wang, *Science* **125**, (37), 11299-11305 (2003).

100 W. D. Yu, X. M. Li, and X. D. Gao, *Appl. Phys. Lett.* **84**, (14), 2658-2660 (2004).

101 C. X. Xu, X. W. Sun, Z. L. Dong, and M. B. Yu, *Appl. Phys. Lett.* **85**, (17), 3878-3880 (2004).

102 J. Y. Lao, J. Y. Huang, D. Z. Wang, Z. F. Ren, D. Steeves, B. Kimball, and W. Porter, *Phys. Lett. A* **78**, 539-542 (2004).

103 Y. Yan, L. Zhou, Q. Xue, and Y. Zhang, *J. Phys. D: Appl. Phys.* **41**, 195402-195407 (2008).

104 C.-L. Kuo, T.-J. Kuo, and M. H. Huang, *J. Phys. Chem. B* **109**, (43), 20115-20121 (2005).

105 B. G. Wang, E. W. Shi, and W. Z. Zhong, *Cryst. Res. Technol.* **33**, (6), 937-941 (1998).

106 H. Xu, H. Wang, Y. Zhang, S. Wang, M. Zhu, and H. Yan, *Cryst. Res. Technol.* **38**, (6), 429-432 (2003).

107 A. Sugunan, H. C. Warad, M. Boman, and J. Dutta, *J. Sol-Gel Sci. Technol.* **39**, 49-56 (2006).

108 Z. Li, X. Huang, J. Liu, Y. Li, and G. Li, *Mater. Lett.* **62**, (10-11), 1503-1506 (2008).

109 B. Liu, and H. C. Zeng, *J. Am. Chem. Soc.* **125**, (15), 4430-4431 (2003).

110 M. Kokotov, A. Biller, and G. Hodes, *Chem. Mater.*, (2008).

111 B. Cao, and W. Cai, *J. Phys. Chem. C* **112**, 680-685 (2008).

112 M. S. Ghamsari, and M. Vafaee, *Mater. Lett.* **62**, (12-13), 1754-1756 (2008).

113 M. S. Ghamsari, and M. Vafaee, *Mater. Lett.* **61**, 3265-3268 (2007).

114 M. S. Tokumoto, S. H. Pulcinelli, C. V. Santilli, and V. Briois, *J. Phys. Chem. B* **107**, 568-574 (2003).

115 X.-L. Hu, Y.-J. Zhu, and S.-W. Wang, *Mater. Chem. Phys.* **88**, 421-426 (2004).

116 R. Wahab, S. G. Ansari, Y.-S. Kin, H.-K. Seo, and H.-S. Shin, *Appl. Surf. Sci.* **253**, 7622-7626 (2007).

117 R. S. Yadav, P. Mishra, and A. C. Pandey, *Ultrason. Sonochem.* **15**, 863-868 (2008).

118 M. Izaki, *Chem. Commun.*, 467-477 (2002).

119 S. Chada, and M. Yan, *Soft Matter* **4**, (11), 2164-2167 (2008).

120 C. F. Baes, and R. E. Mesmer, *The hydrolysis of cations*. John Wiley & Sons 1976.

121 J. P. Jolivet, *Metal Oxide Chemistry and Synthesis: From Solution to Oxide*. John Wiley and Sons Ltd.: England, 2000.

122 E. Matijević, *Acc. Chem. Res.* **14**, 22-29 (1981).

123 Y. Peng, A.-W. Xu, B. Deng, M. Antonietti, and H. Colfen, *J. Phys. Chem. B* **110**, (7), 2988-2993 (2006).

124 F. Li, Y. Ding, P. Gao, X. Xin, and Z. L. Wang, *Angew. Chem. Int. Ed.* **43**, 5238-5242 (2004).

125 M. Jitianu, and D. V. Goia, *J. Colloid and Int. Sci.* **309**, 78-85 (2007).

126 Y.-J. Lee, T. L. Sounart, J. Liu, E. D. Spoerke, B. McKenzie, J. W. P. Hsu, and J. A. Voigt, *Cryst. Growth Des.* **8**, (6), 2036-2040 (2008).

127 X. Wu, H. Bai, C. Li, G. Lu, and G. Shi, *Chem. Commun.*, 1655-1657 (2006).

128 J. Duan, X. Huang, and E. Wang, *Mater. Lett.* **60**, 1918-1921 (2006).

129 S. Kar, A. Dev, and S. Chaudhuri, *J. Phys. Chem. B* **110**, 17848-17853 (2006).

130 Z. R. Tian, J. A. Voigt, J. Liu, B. Mckenzie, M. J. Mcdermott, M. A. Rodriguez, H. Konishi, and H. Xu, *Nature Materials* **2**, 821-826 (2003).

131 R. Wahab, S. G. Ansari, Y.-S. Kim, G. Khang, and H.-S. Shin, *Appl. Surf. Sci.* **254**, (7), 2037-2042 (2008).

132 T. Zhang, W. Dong, M. Keeter-Brewer, S. Konar, R. N. Njabon, and Z. R. Tian, *J. Am. Chem. Soc.* **128**, (33), 10960-10968 (2006).

133 R.-Q. Song, A.-W. Xu, B. Deng, Q. Li, and G.-Y. Chen, *Adv. Funct. Mater.* **17**, 296-306 (2007).

134 L. E. Greene, B. D. Yuhas, M. Law, D. Zitoun, and P. Yang, *Inorg. Chem.* **45**, (19), 7535-7543 (2006).

135 C. M. Niemeyer, *Angew. Chem. Int. Ed.* **40**, 4128-4158 (2001).

136 A. Taubert, D. Palms, O. Weiss, T. Piccini, and D. N. Batchelder, *Chem. Mater.* **14**, (6), 2594-2601 (2002).

137 S. Xu, Z.-H. Li, Q. Wang, L.-J. Cao, T.-M. He, and G.-T. Zou, *J. Alloys Compd.* **465**, 56-60 (2008).

138 T. Du, and O. J. Ilegbusi, *J. Mater. Sci. Lett.* **39**, 6105-6109 (2004).

139 J. Zhang, H. Liu, Z. Wang, N. Ming, Z. Li, and A. S. Biris, *Adv. Funct. Mater.* **17**, 3897-3905 (2007).

140 R. C. Hoffmann, S. Jia, L. P. H. Jeurgens, J. Bill, and F. Aldinger, *Mater. Sci. Eng., C* **26**, 41-45 (2006).

141 A. Taubert, G. Glasser, and D. Palms, *Langmuir* **18**, 4488-4494 (2002).

142 J. Cui, and U. J. Gibson, *J. Phys. Chem. B* **109**, 22074-22077 (2005).

143 J. B. Cui, and U. J. Gibson, *Appl. Phys. Lett.* **87**, 133108-133110 (2005).

144 Y. Liu, L. He, A. Mustapha, H. Li, Z. Q. Hu, and M. Lin, *J. Appl. Microbiol.* **107**, 1193-1201 (2009).

145 P. Roach, D. Farrar, and C. C. Perry, *J. Am. Chem. Soc.* **127**, 8168-8173 (2005).

146 M. N. Tahir, M. Eberhardt, P. Théato, S. Faiss, A. Janshoff, T. Gorelik, U. Kolb, and W. Tremel, *Angew. Chem. Int. Ed.* **45**, (6), 908-912 (2006).

147 J. L. Sumerel, W. J. Yang, D. Kisailus, J. C. Weaver, J. H. Choi, and D. E. Morse, *Chem. Mater.* **15**, (25), 4804-4809 (2003).

148 H. Chen, X. Su, K.-G. Neoh, and W.-S. Choe, *Langmuir* **24** 6852-6857 (2008).

149 D. Kisailus, J. H. Choi, J. C. Weaver, W. Yang, and D. E. Morse, *Adv. Mater.* **17**, (3), 314-318 (2005).

150 E. Dalas, A. Chalias, D. Gatos, and K. Barlos, *J. Colloid Interface Sci.* **300**, 536-542 (2006).

151 D. Rautaray, A. Ahmad, and M. Sastry, *J. Am. Chem. Soc.* **125**, 14656-14657 (2003).

152 D. B. Oliveira, and R. A. Laursen, *J. Am. Chem. Soc.* **119**, 10627-10631 (1997).

153 O. Deschaume, A. Fournier, K. Shafran, and C. C. Perry, *New J. Chem.* **32**, 1346-1353 (2008).

154 G. Iucci, C. Battocchio, M. Dettin, R. Gambaretto, C. D. Bello, F. Borgatti, V. Carravetta, S. Monti, and G. Polzonetti, *Surf. Sci.* **601**, 3843-3849 (2007).

155 S. Brown, M. Sarikaya, and E. Johnson, *J. Mol. Biol.* **299**, 725-732 (2000).

156 S. Brown, *Nano Lett.* **1**, (7), 391-394 (2001).

157 P. Gerstel, R. C. Hoffmann, P. Lipowsky, L. P. H. Jeurgens, J. Bill, and F. Aldinger, *Chem. Mater.* **18**, (1), 179-186 (2006).

158 P. Gerstel, P. Lipowsky, O. Durupthy, R. C. Hoffmann, P. Bellina, J. Bill, and F. Aldinger, *J. Ceram. Soc. Jpn.* **114**, (11), 911-917 (2006).

159 S. P. Newman, T. D. Cristina, P. V. Coveney, and W. Jones, **18**, 2933-2939 (2002).

160 S. Aisawa, S. Takahashi, W. Ogasawara, Y. Umetsu, and E. Narita, *J. Solid State Chem.* **162**, 52-62 (2001).

161 G. Begum, S. V. Manorama, S. Singh, and R. K. Rana, *Chem. Eur. J.* **14**, 6421-6427 (2008).

162 M. M. Tomczak, M. K. Gupta, L. F. Drummy, S. M. Rozenzhak, and R. R. Naik, *Acta Biomater.* **5**, (3), 876-882 (2008).

163 H. Bai, F. Xu, L. Anjia, and H. Matsui, *Soft Matter* **5**, 966-969 (2009).

164 Z. Huang, D. Yan, M. Yang, X. Liao, Y. Kang, G. Yin, Y. Yao, and B. Hao, *J. Colloid and Int. Sci.*, (2008).

165 D. Yan, G. Yin, Z. Huang, M. Yang, X. Liao, Y. Kang, Y. Yao, B. Hao, and D. Han, *J. Phys. Chem. B* **113**, (17), 6047-6053 (2009).

166 L. P. Bauermann, A. d. Campo, J. Bill, and F. Aldinger, *Chem. Mater.* **18**, (8), 2016-2020 (2006).

167 L. Shi, J. Zhou, and S. Gunasekaran, *Mater. Lett.* **62**, 4383-4385 (2008).

168 Q. Dong, H. Su, F. Song, D. Zhang, and N. Wang, *J. Am. Ceram. Soc.* **90**, (2), 376-380 (2007).

169 L. Shi, and S. Gunasekaran, *Nanoscale Res. Lett.* **3**, 491-495 (2008).

170 R. d. l. Rica, and H. Matsui, *Angew. Chem. Int. Ed.* **47**, 5415-5417 (2008).

171 D. Weinzierl, D. Touroud, A. Lecker, A. Pfitzner, and W. Kunz, **43**, 62-67 (2008).

172 Z. R. Tian, J. A. Voigt, J. Liu, B. Mckenzie, and M. J. Mcdermott, *J. Am. Chem. Soc.* **124**, 12954-12955 (2002).

173 J. Liang, J. Liu, Q. Xie, S. Bai, W. Yu, and Y. Qian, *J. Phys. Chem. B* **109**, (19), 9463-9467 (2005).

174 W. N. Fishbein, C. L. Spears, and W. Scurzi, *Nature* **223**, 191-193 (1969).

175 M. T. Hincke, U. J. Gautron, M. Panheleux, J. Garcia-Ruiz, M. D. McKee, and Y. Nys, *Matrix Biol.* **19**, 443-453 (2000).

176 H. Bai, K. Xu, Y. Xu, and H. Matsui, *Angew. Chem. Int. Ed.* **46**, 3319-3322 (2007).

Chapter 2
Experimental Methods

2.1 Scanning Electron Microscopy (SEM)[1]

In electron microscopy, a stream of electrons generated by heated filament (cathode), tungsten or LaB_6, is focused towards the optic axis by the Wehnelt cap. The generated parallel electron beams with monochromatic electrons are then accelerated towards a sample by the applied positive electrical potential on the anode. Depending on the depth of penetration by the incident electron beam on the sample, a series of interactions can occur which can be measured and interpreted to provide information about the sample, **Figure 2.1**.

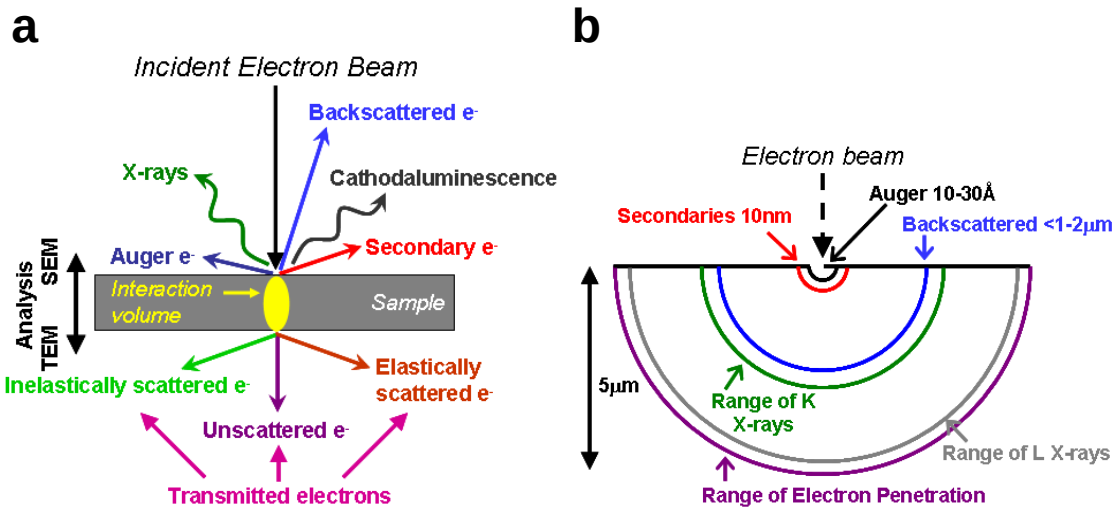

Figure 2.1 Principle interactions involved in electron microscopy (a) and depth of penetration (b).

High energy incident electrons may transfer part of their energies for the ionization of lower energy electrons in the specimen atom. The ionized electrons that leave the atom with a reduced kinetic energy are called 'secondary electrons'. Each incident electron can produce several secondary electrons and only secondary electrons that are near-surface (<10nm depth) can exit and thus be collected. As a result, any topographical

changes in the sample that are more than this sampling depth will change the yield of secondary electrons as the beam is scanned across the sample surface in a raster fashion, making SEM a useful tool to examine surface morphology. The spatial resolution of SEM depends on electron spot size and the extent to which the material interacts with the electron beam. Since the spot size and the interactive volume are both large compared to the distances between atoms, the resolution of the SEM is not high enough to image individual atoms, as is possible in the shorter wavelength (i.e. higher energy) transmission electron microscope (TEM). Depending on the specification of the instrument, the resolution can fall somewhere between less than 1nm and 20nm.

Although not being able to image individual atoms, SEM has the advantage of being able to image a comparatively large area and materials in the bulk phase as well as there being a variety of analytical modes for specimen composition and properties measurement. For example, the relaxation of a sample atom (an electron from an outer orbital moves to fill a now unfilled orbital of lower energy) following the release of secondary electrons usually discharges X-rays to balance the total energy of the atom. The X-rays emitted from the atom have a characteristic energy that is unique to the element and hence these can be used for elemental analysis (EDXA, energy dispersive X-ray analysis).

2.2 Fourier Transform Infrared Spectroscopy (FTIR)[2]

Infrared (IR) spectroscopy is a spectroscopic technique that uses the infrared region (14000-10cm^{-1}) of the electromagnetic spectrum for compound identification and composition analysis. The mid-IR region (4000-400cm^{-1}) is commonly used for the study of organic molecules because its radiation energy induces vibrations and associated rotational transitions of covalently bonded molecules. In IR spectroscopy, the sample is irradiated with mid-IR wavelengths and the intensity of absorbance and its corresponding wavelength are recorded. However, only vibrational modes associated with permanent dipole changes are IR-active. The exact frequency at which

a given vibration occurs is determined by the specific strength and dipole nature of the bond. Thus the frequency of vibration can be associated with a particular bond type or functional group, allowing the inference of molecular structure of the sample. In general the stronger the bond the higher the frequency of the vibration, although this is complicated by the mass of the interacting atoms at either end of the bond, while the greater the electronegativities of the atoms the greater the absorbance.

Instead of using a monochromator to vary IR frequency in conventional IR spectroscopy, FTIR spectroscopy uses a Michelson interferometer to split the beam into two parts, making one part of the beam travel a longer path using a movable fully reflecting mirror. The variation of path difference between the two beams changes the interference patterns which form upon beam recombination. The interferogram arising from changes in interference patterns can be treated mathematically by the Fourier transform method to convert the waveform from time domain to frequency domain. Since FTIR spectroscopy measures the absorbance of the entire spectrum simultaneously, the rapid data acquisition allows multiple sample collection for sensitivity improvement (better signal-to-noise ratio).

Two sampling techniques were used in this study, namely transmission IR spectroscopy and single bounce-attenuated total reflectance (single bounce-ATR). In transmission IR spectroscopy, the IR beam is directly passed through a disc pressed from small fraction of ground sample in ground potassium bromide (KBr, for mid-IR wavelength), or cesium iodide (CsI, for far-IR). This technique produced signals with high intensity and good signal-to-noise ratios when the sample absorbs adequately. The ATR technique enables the study of both solid and aqueous samples because the beam is not transmitted through the sample but reflected by a series of mirrors through a crystal termed an internal reflection element (IRE), **Figure 2.2**. As the beam bounces through the crystal a standing wave is established at the crystal face. The tail of the standing wave which penetrates through the crystal into the sample is called an evanescent wave. The depth of penetration is controlled by the radiation wavelength, the angle of incidence of the IR beam, and the refractive index of both the crystal and the external media. Since the penetration depth into the sample is usually less than 1 micron for most crystals, only a small volume of the sample closely confined to the crystal surface is sampled, minimizing the IR absorption by water in an aqueous

sample. No pre-measurement preparation is required for liquid sample measurement using ATR. However the grinding of solid samples may be required for good contact between the sample and the crystal surface.

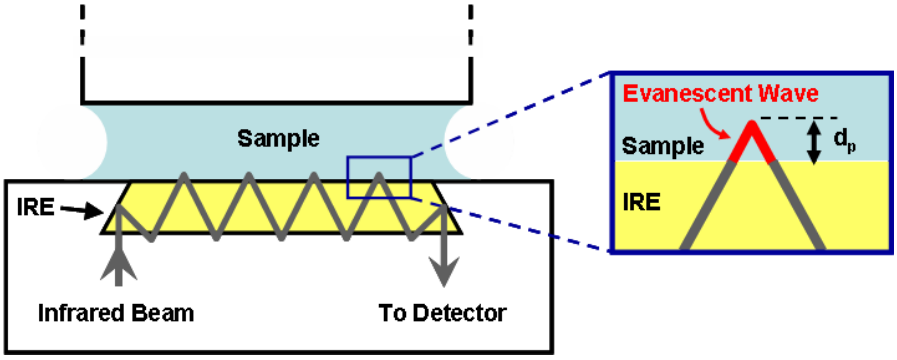

Figure 2.2 Schematic of the generation of evanescent wave from an attenuated total reflectance crystal.[2]

2.3 Thermogravimetric Analysis (TGA)[3] and Differential Scanning Calorimetry (DSC)[4]

Themogravimetric analysis (TGA) is an analytical technique for the study of the thermal stability of materials. As the specimen is heated (and cooled) at a pre-determined rate in air or in an inert atmosphere, the weight of the specimen is monitored and recorded as a function of temperature. The selection of environment in which the sample is analysed depends on the type of material and the thermal transformation expected in the reaction studied. A TGA equipment typically comprises of a microbalance for sample weighing, programmable furnace and computer software for data processing. In this study, TGA was used to detect the presence and to determine the amount of incorporated polymer/peptide in the precipitates collected. For selected silica-polymer composites, the onset temperature for the decomposition of organic phase was determined using differential scanning calorimetry (DSC) synchronized with TGA. The main application of DSC is for the study of phase transitions, such as melting, glass transitions, or exothermic decomposition. DSC is used to detect (with great sensitivity) the energy changes or heat capacity changes involved in the transition process studied. A reference sample with well-defined heat

capacity over the range of temperature to be scanned is used. In the course of the analysis, the difference in the amount of heat required to increase the temperature of a sample and the reference are measured as a function of temperature.

2.4 Inductively Coupled Plasma-Optical Emission Spectrometry (ICP-OES)[5]

Inductively coupled plasma-optical emission spectrometry (ICP-OES), also known as inductively coupled plasma-atomic emission spectrometry (ICP-AES), is widely used as an analytical technique for the identification and determination of trace elements. In this technique, an argon-supported inductively coupled plasma (ICP) is used as the thermal source, **Figure 2.3**. The highly energetic ICP is able to dissociate not only almost any type of sample but also to excite and/or ionize the atoms for atomic and ionic emission. Once the atoms or ions are in their excited states, they will decay to lower states through thermal or radiative (emission) energy transitions. The intensity of the electromagnetic radiation emitted is used to determine the concentrations of the elements of interest while the element(s) present can be identified from their characteristic emission wavelength within the UV-Vis region (160-800nm).

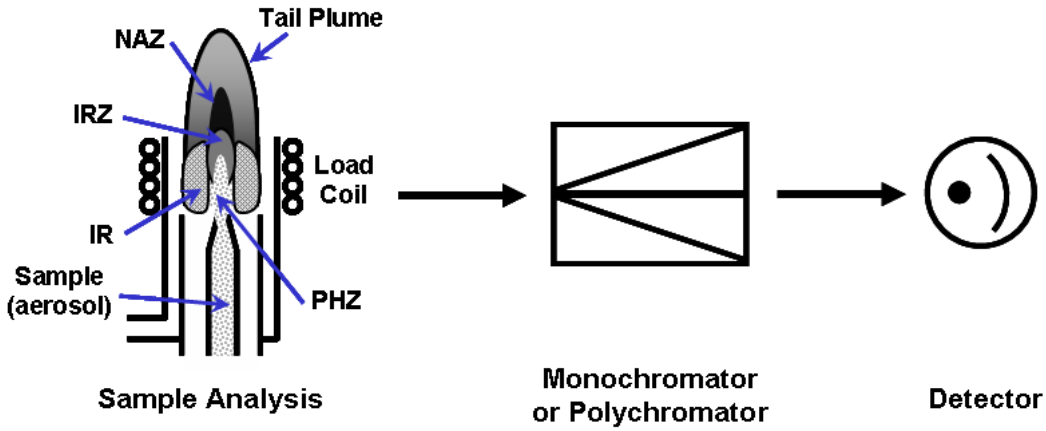

Figure 2.3 ICP-OES system. IR – Induction Region, PHZ – Preheating Zone, IRZ – Initial Radiation Zone, NAZ – Normal Analytical Zone.[5]

The use of high temperature sources in OES enables simultaneous measurement of emission wavelengths from more than one element however interferences may arise from emission lines that are too close in wavelength to be measured separately. While ICP-OES can be used for the detection of over 70 elements in the μg/l (ppb) range, some elements and molecules are usually not determined at trace levels by ICP-OES. These include Argon and carbon dioxide (CO_2) that are naturally entrained into the plasma from sources other than the original sample; halogens with very high excitation energy requirements (Cl, Br, I), and man-made highly radioactive elements with short-lives.

2.5 Nitrogen Gas Adsorption/Desorption Analysis[6-9]

The surface area and pore structure of a material can be determined using nitrogen gas adsorption/desorption analysis. Samples for such analysis are first degassed at suitable temperatures under vacuum to remove water and adsorbed contaminants. Degassed samples are evacuated and thermally equilibrated at the boiling point of nitrogen gas by immersing the sample tube in liquid nitrogen. After equilibration, a small measured amount of nitrogen gas is admitted into the sample tube until a predetermined partial pressure, P/P_0, is reached and the total nitrogen gas admission required to reach this partial pressure is determined. An adsorption isotherm is constructed by increasing the P/P_0 values from 0 to 1, while the desorption isotherm is constructed by the stepwise reduction of P/P_0 by the application of vacuum. The shape of the isotherm reflects the sample surface area, porosity, and energy of nitrogen adsorption. According to Brunauer, Deming, Deming, and Teller (BDDT),[7] these isotherms can be classified into five types, **Figure 2.4**.

Type I isotherms, also known as Langmuir isotherms, arise from microporous solids having low surface area. The amount of adsorbate reaches a limiting value when accessible micorpores are “covered”. The Type II isotherm is normally observed for non-porous and macroporous materials. The plateau indicates the completion of monolayer coverage while the increase of adsorbed amount as P/P_0 increases is a result

of multi-layer adsorption. Type III isotherms are quite rare and are observed when the adsorbate-adsorbate interactions are higher than the adsorbate-adsorbent interactions. The initial part of Type IV isotherms follows the same path as Type II isotherms while the steep slope at higher P/P_0 is associated with capillary condensation in mesopores. The uncommon Type V isotherms correspond to Type III isotherms except that pores in the mesopore range are present.

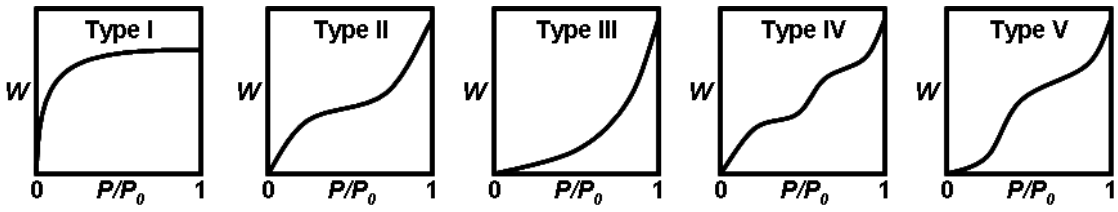

Figure 2.4 Isotherm types (classified by BDDT). W = mass of adsorbate, P/P_0 = partial pressure.[7]

The surface area of a sample is determined based on the BET[9] method where monolayer coverage by nitrogen as adsorbate is determined from the P/P_0 range of 0.05-0.35. It is the characteristics of porous materials to exhibit hysteresis, where the desorption profiles do not follow the path of the adsorption isotherms. de Boer has identified five types of hysteresis loops (**Figure 2.5**) and correlated them with various pore shapes: cylindrical pores (Type A), slit-shaped pores (Type B), wedge-shaped pores with open ends (Type C), wedge-shaped pores with narrow necks at one or both open ends (Type D), and "ink-bottle" pores (Type E). Total pore volume is determined by the amount of vapour adsorbed at P/P_0~1 and the average pore size is estimated from the total pore volume.

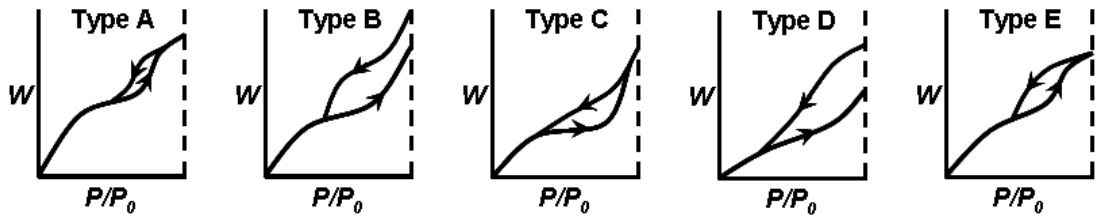

Figure 2.5 Hysteresis types according to deBoer.[10]

2.6 X-Ray Diffraction (XRD)[11]

X-ray diffraction (XRD) is a non-destructive technique for the identification of crystalline phases and crystalline film orientation because every crystalline material has its own characteristic diffraction pattern. As illustrated in **Figure 2.6** X-rays produced from an X-ray tube are directed onto the sample at an incident angle (θ). When the X-ray beam strikes the sample it is scattered by the crystal planes present. The constructive interference of the scattered beams from crystal planes of the same crystal orientation produce a diffracted beam which is detected by the detector placed at 2θ away from the incident beam. By directing X-ray beams onto the sample at the range of incident angles of interest, a diffraction pattern of the sample can be obtained. The condition for constructive interference of the beam at angle θ is given by Bragg's equation, $n\lambda=2d\sin\theta$, with n an integer; λ, the wavelength of X-rays; d, the inter-planar distance in the crystal and θ, the incident angle of X-ray radiation.

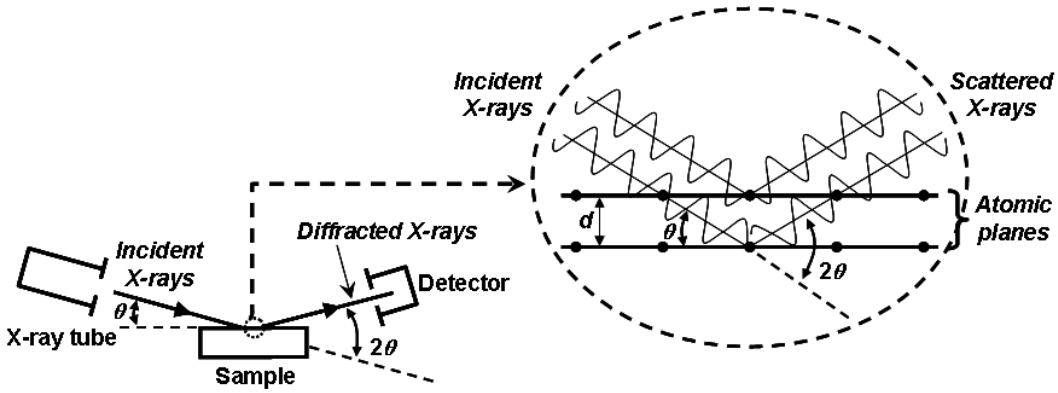

Figure 2.6 Crystallinity study using X-ray diffraction technique. d=atomic spacing.[11]

Powder diffraction and thin film diffraction techniques were used in this study. Powder diffraction is a technique generally used for the characterisation of crystallographic structure, determination of crystallite size (Scherrer equation), and the identification of preferred orientation.[11] Powder diffraction is also a common method for determining strains in crystalline materials because besides the reduction in crystallite size, the presence of strain is also known to induce peak-broadening. Similar to powder diffraction, thin film diffraction can be used to characterise the crystallographic

structure and preferred orientation of substrate-anchored thin films. In this study powder diffraction was used for the characterisation of ZnO and layered basic zinc acetate (LBZA) obtained while the orientation of ZnO film deposited on silicon wafers was confirmed using film diffraction.

2.7 Ultraviolet-Visible (UV-Vis) Spectroscopy[12]

The Beer-Lambert law states that the absorbance of a solution (A) is directly proportional to the concentration of the absorbing species in the solution, c, and the path length, L:

$$A = \epsilon cL = - \text{Log}_{10}[I / I_0] = -\text{Log}_{10}T$$

where ϵ is the molar absorptivity or the extinction coefficient, I is the intensity of light passing through a sample, I_0 is the intensity of light before it passes through the sample, and T is the transmittance. Thus, for a fixed path length, UV-Vis spectroscopy can be used to determine the concentration of a chemical in solution if the chemical contains functionalities that absorb in the 200-800nm region. The functionalities that absorb in this region are known as chromophores and include aromatics, heterocyclics, coordination compounds, and compounds with multiple bonds.

UV-Vis spectroscopy is an easy and fast technique which requires small amounts of sample and minimum sample preparation. It has medium sensitivity and relatively high precision however interferences may arise from the presence of foreign metal ions, anions and other chromophores that are not of interest. The Unicam UV2 UV/Vis spectrometer used in this study has wavelength accuracy of ±0.5nm at 500-1100nm. Its photometric range is -0.3 to 6A with photometric accuracy at 1A, 2A and 3A being ±0.004A, ±0.006A and ±0.012A respectively. It was used to determine the concentration of monosilicic acid and peptides in solution. The analysis of ZnO precipitates was also performed using a JASCO V-670 spectrophotometer for the determination of direct energy band gap.

2.8 The Molybdenum Blue Method[13-15]

The molybdenum blue method can be used to determine the concentration of monosilicic acid ($Si(OH)_4$) in aqueous solution. This method has a low detection limit (as low as 0.1ppm), thus is ideal for the study of $Si(OH)_4$ concentration changes during the initial stage of silica formation. The two reagents used are the molybdic acid reagent and the reducing agent. The former is prepared from ammonium molybdate (VI) tetrahydrate and hydrochloric acid, while the latter contains oxalic acid dihydrate, 4-methylaminophenol sulphate, sodium sulphite (hydrated), and sulphuric acid. The reactions are simplified in **Figure 2.7**.

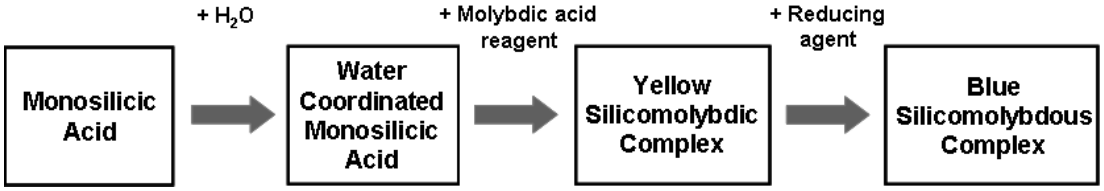

Figure 2.7 Simplified reactions for the molybdenum blue method.

Each monosilicic acid present in aqueous solution (the sample) first coordinates with two water molecules to form water-saturated monosilicic acid:

$$Si(OH)_4 + 2H_2O \longrightarrow H_8SiO_6$$

When added into the molybdic acid reagent, the fully water-saturated monosilicic acid reacts with the acidified molybdate ions to form the yellow silicomolydate complex which has an absorbance maximum of around 400nm:

$$H_8SiO_6 + 12MoO_4^{2-} + 24H^+ \longrightarrow H_8[Si(Mo_2O_7)_6] + 12H_2O$$

The silicomolybdic acid complex, $H_8[Si(Mo_2O_7)_6]$, has a cage structure formed by twelve MoO_6 octahedra made up of four groups of three where each of the three groups of octahedra share an oxygen atom which also forms one corner of a central tetrahedron to which the central silicon atom coordinates. The geometry of the cage is

such that only one silicon atom can reside in the cavity. Thus the formation of the yellow complex is possible only between the molybdic acid reagent and monosilicic acid (monomer) present, or the monomers formed from the rapid dissociation of oligomeric species. At 293K, the formation of this yellow complex completes within 75 seconds while the complete dissociation of disilicic acid to monomer requires approximately 10 minutes.[13] Being carried out at low pH (~1.5), the interference from the dissolution of any particulate silica (larger than oligomeric species) present in the condensing system is minimized.

The reduction of the silicomolybdic acid complex produces the blue silicomolybdous acid complex within 90 minutes which is stable for at least 48 hours at room temperature. The blue silicomolybdous acid complex has an absorbance maximum at 810nm with a greater extinction coefficient than the silicomolybdic acid complex, making it more sensitive and able to provide reliable quantitative data at concentrations of monosilicic acid as low as 0.1ppm.

2.8.1 Kinetic analysis

The addition of reducing agent is carried out 15 minutes after addition of sample into the molybdic acid reagent. Thus the observed changes in the absorbance at 810nm of the molybdenum blue assay are a result of the loss of both monomer and dimer from the condensing system. During the early stage of condensation this is due solely to the formation of the trimer, so the apparent net loss of monomers is equivalent to three molecules of $Si(OH)_4$:

$$Si(OH)_4 + Si(OH)_3OSi(OH)_2O^- \longrightarrow [Si(OH)_3OSi(OH)_2OSi(OH)_2O]^- + 2H_2O$$

As the reaction appears termolecular, involving three molecules of monosilicic acid, the reaction and the reduced normal rate expression are as follows:[15]

$$A + B + C \longrightarrow \text{Products}$$

$$\frac{dx}{dt} = k(a-x)^3 \qquad (1)$$

where a is the concentration of reactant at time t=0, while x is the concentration of product at time t. Rearranging and integrating gives:

$$\frac{1}{2(a-x)^2} = kt + c \qquad (2)$$

where c is a constant value. When t=0 and x=0 the constant reduces to $1/2a^2$ as in (3). The rearrangement of (3) is shown in (4), where (a - x) represents the measured $[Si(OH)_4]$ at time t. So a plot of $1/[Si(OH)_4]^2$ against time should give a straight line of gradient $2k$ when third order kinetics are observed.

$$kt = \left(\frac{1}{2(a-x)^2}\right) - \left(\frac{1}{2a^2}\right) \qquad (3)$$

$$\frac{1}{2(a-x)^2} = kt + \frac{1}{2a^2} \qquad (4)$$

After this (predominantly) trimerisation stage, further reduction in monosilicic acid concentration is the result of condensation of monomer onto increasingly larger oligomers, a process which is reversible as some of the oligomers redissolve. This stage can be represented as follows with k_+ and k_-, the rate constants for the forward and reverse processes respectively, which are both assumed to be first order:[15]

$$A \rightleftharpoons B \quad [k_+, k_-]$$

The rate expression is given in (5), where the rate of change in the concentration of A is the difference between its rate of consumption via the forward process and its rate of production via the reverse process.

$$\text{Rate} = -d[A]/dt = k_+[A] - k_-[B] \qquad (5)$$

If the initial concentration of B, $[B]_0$, is zero, then at any point during the process, $[B] = [A]_0 - [A]$. So the equation becomes:

$$-d[A]/dt = (k_+ + k_-)[A] - k_-[A]_0 \qquad (6)$$

This can be integrated, but the resulting expression will not be linear. To eliminate the $k_-[A]_0$ term, let $[A]_\infty$ represent the equilibrium concentration of A,

$$-d[A]_\infty/dt = (k_+ + k_-)[A]_\infty - k_-[A]_0 \qquad (7)$$

Subtracting (7) from (6) which eliminates the $k_-[A]_0$ term is given as (8) where $k = (k_+ + k_-)$, the sum of forward and reverse rate constants.

$$-d([A] - [A]_\infty)/dt = (k_+ + k_-)([A] - [A]_\infty) = k([A]-[A]_\infty) \qquad (8)$$

The integration of (8) in the variable of $[A] - [A]_\infty$, which is the *deviation* of the concentration of A from the equilibrium value, gives (9):

$$\ln ([A] - [A]_\infty) = - kt \qquad (9)$$

Thus (9) shows that in a reversible first-order process, the approach to equilibrium is governed by first-order kinetics. A plot of $\ln([A] - [A]_\infty)$ against t will be linear, with slope $-k$ being the sum of the forward and reverse rate constants. The equilibrium constant, K is given by (10) where p_∞ is the concentration of silica and a_∞ is the concentration of monosilicic acid, both at equilibrium.

$$K = \frac{k_+}{k_-} = \frac{p_\infty}{a_\infty} \qquad (10)$$

Rearranging (10) gives:

$$k_+ = \frac{p_\infty k_-}{a_\infty} \qquad (11)$$

Substituting in to slope = $-k = k_+ + k_-$ gives:

$$Slope = \left(\frac{p_\infty}{a_\infty} + 1 \right) k_- \qquad (12)$$

The rate constants, k_3, k_+ and k_-, determined by the molybdenum blue assay provide information on the consumption rate of monosilicic acid during the initial stage of silica formation. In order not to affect the reaction while studying its reaction kinetics, 10mL of reaction solution was prepared and only 10μl of aliquots were taken at selected sampling times. The experimenter skill-dependent nature of this assay and the small volume of aliquot used have subjected the rate constants to errors. Therefore all reactions to be studied, if possible, should be carried out in triplicate. While studying the effect of an additive on the reaction kinetics, the individual rate constants are normalised to the average of their counterparts from the blank (obtained in the absence of additive) before a statistical analysis is performed. The details of the statistical analysis are shown in the experimental section of **Chapter 3**.

2.9 Solid Phase Peptide Synthesis (SPPS)[16]

SPPS is a method whereby a peptide chain is constructed on an amino acid pre-loaded insoluble solid support (resin or bead) step-by-step in solutions containing amino acids. The amino acid sequence of the peptide is determined by the sequence in which the amino acid solutions are exposed to the preloaded-resin. The major advantages of SPPS are easy removal of excess reactants in the solution phase and minimum physical loss of peptide as the peptide remains attached to the resin throughout the synthesis. However by-products from incomplete reactions, side reactions, or impure reactants will accumulate on the resin during chain assembly and can contaminate the final product. The purification of the "contaminated"-final product is difficult because these contaminants are, by their nature, very similar to the desired peptide.

The principle of SPPS is illustrated in **Figure 2.8** where the C-terminal amino acid residue of the target peptide is attached to the resin via its carboxyl group. Any functional groups in amino acid side-chains must be masked with permanent protecting groups (Y in **Figure 2.8**) that are not affected by the reaction conditions employed during peptide chain assembly (coupling) which involves the temporary N-terminus protecting group (X in **Figure 2.8**).

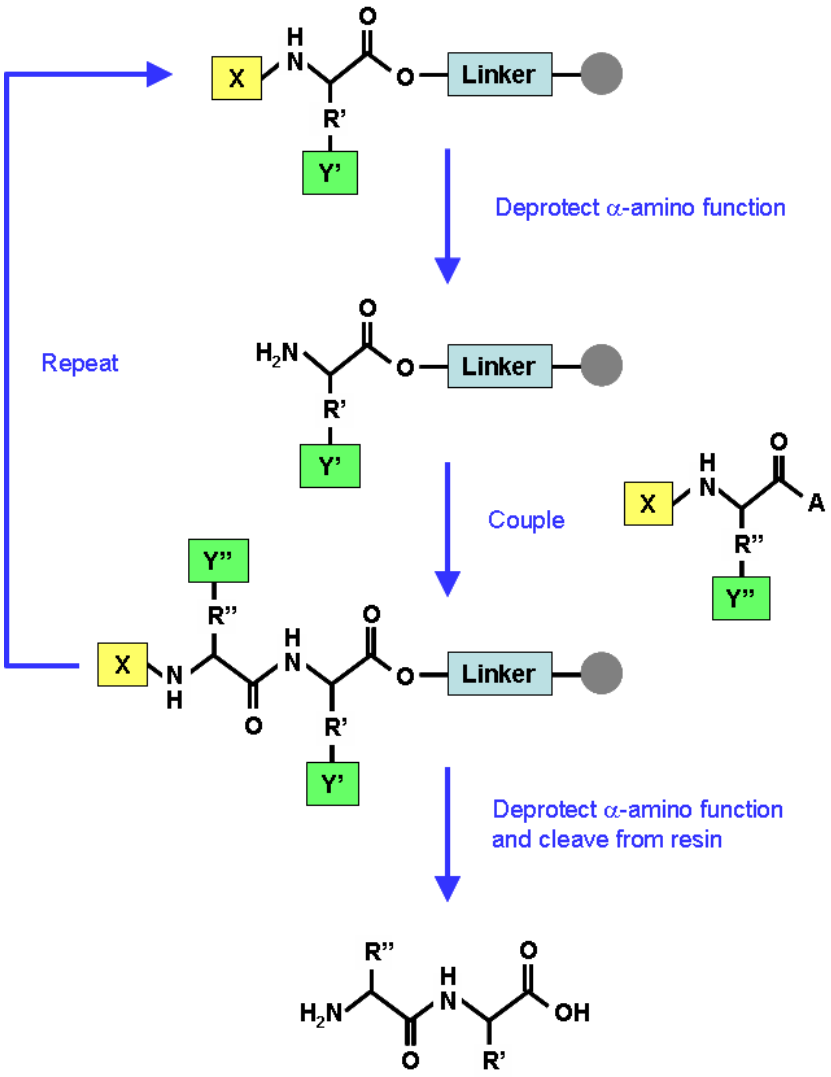

Figure 2.8 The SPPS principle. X is the temporary amino protecting group, Y is the permanent side-chain protecting group, A is the carboxyl activating group, and the grey circle is the resin.

The most commonly used X and Y in SPPS are 9-flurenylmethyl carbamate (Fmoc) and a tertiary butyl-based side chain protection group (*t*Bu), respectively. The temporary protecting group masking the α-amino group is removed (deprotected)

during the initial loading. An excess of the second amino acid is introduced, with the carboxyl group of this amino acid being activated for amide bond formation through generation of an activated ester or by reaction with a coupling agent. After coupling, excess reagents are removed by washing and the protecting group is removed from the N-terminus of the dipeptide (on-resin), prior to addition of the third amino acid residue. This process is repeated until the desired peptide sequence is assembled. Prior to detaching the peptide from the resin, the protecting group at the N-terminal is removed (final deprotection).

In the final step, the peptide is released from the resin and the side chain protecting groups are removed by the use of a cleavage mixture. Generally, the side-chain protecting groups and resin linkage are chosen such that the side-chain protection groups and resin linkage are released under the same conditions. The cleavage mixture typically contains 90-95%v/v trifluoroacetic acid (TFA). During the cleaving process, highly reactive cationic species are generated from the protecting groups and resin linkers. These cationic species, unless trapped, will react with and modify those amino acids containing electron-rich functional groups: tyrosine, tryptophan, methionine, and cysteine. For this reason, various nucleophilic reagents, known as scavengers, such as water, 1,2-ethanedithiol (EDT), thioanisole, phenol, etc.; are added to the TFA to quench these ions. The cleaved peptides in the cleavage mixture are reprecipitated in chilled-diethyl ether as white precipitates. The peptide obtained is washed with chilled-diethyl ether before drying. The diethyl ether in peptide can be removed by using a vacuum oven at low temperature, by bubbling nitrogen into the chilled diethyl ether, or by lyophilisation.

2.10 X-Ray Photoelectron Spectroscopy (XPS)[2]

XPS, also called electron spectroscopy for chemical analysis (ESCA), measures the elemental composition, empirical formula, chemical state and electronic state of the elements on the surface of a sample analysed based on the photoelectric effect. It is a widely used surface characterisation method due to its high information content and

flexibility in addressing a wide variety of sample forms. Usually ten to twenty atomic layers of the surface will be probed.

The surface to be analyzed is placed in an ultra-high vacuum (UHV) environment and when irradiated with photons of X-ray energy range, one of three events may occur: (i) the photon can pass through with no interaction; (ii) the photon can be scattered by an atomic orbital electron leading to partial energy loss; and (iii) the photon may transfer all of its energy to the core level electron of the surface atoms resulting in electron emission, **Figure 2.9(b)**. The emitted electrons are subsequently separated according to energy and counted. The kinetic energy (KE) of the photoelectrons measured is used to determine the electron binding energy (E_B). The E_B value, related to the atomic and molecular environment from which they originated, is described by the Einstein equation as follows:

$$E_B = h\nu - KE$$

where $h\nu$ is the energy of the X-ray source. The number of electrons emitted is related to the concentration of the emitting atom in the sample.

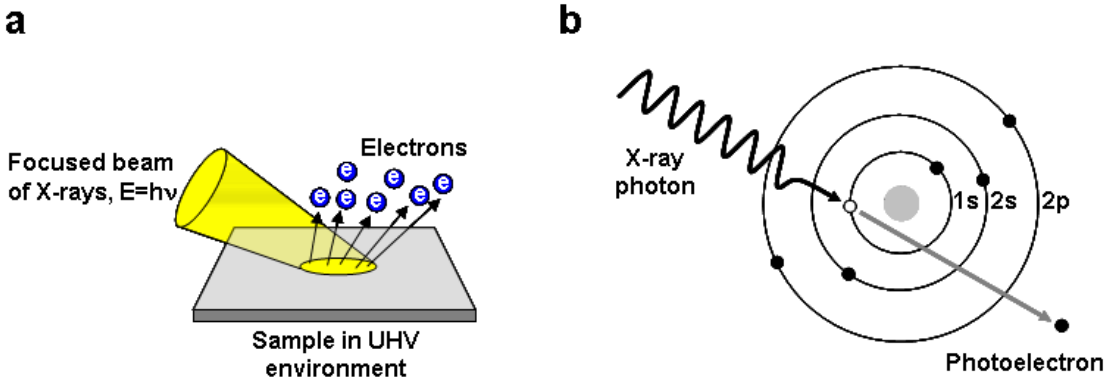

Figure 2.9 The principle of XPS.[2] (a) A surface irradiated by a photon source of X-ray energy range will emit electrons. (b) The X-ray photon transfers its energy to a core-level electron imparting enough energy for the electron to leave the atom.

The most basic XPS analysis of a surface will provide qualitative and quantitative information on all the elements present (except H and He). More sophisticated

applications of XPS, summarised in **Table 2.1**, is able to provide much detailed information about the chemistry, organization, and the morphology of a surface. The detection limits of most of the elements are in the parts-per-thousand range. The detection limit can be improved by a surface concentration approach or by increasing the collection time.[2]

Table 2.1 Information derived from an XPS experiment.[2]

In the outer most 10nm of a surface, XPS can provide:
▪ Identification of all elements (except H and He) present at concentrations > 0.1 atomic %
▪ Semiquantitative determination of the approximate elemental surface composition (error <±10%)
▪ Information about the molecular environment (oxidation state, bonding atoms, etc.)
▪ Information about aromatic or unsaturated structures from $\pi^* \rightarrow \pi$ transition
▪ Identification of organic groups using derivatization reactions
▪ Non-destructive elemental depth profiles 10nm into the sample and surface heterogeneity assessment using (i) Angular-dependent XPS studies and (ii) Photoelectrons with differing escape depth
▪ Destructive elemental depth profiles several hundred nanometers into the sample using ion etching (for inorganics)
▪ Lateral variation in surface composition (spatial resolution of 8-150μm, depending upon the instrument)
▪ 'Fingerprinting' of materials using valence band spectra and identification of bonding orbitals
▪ Studies on hydrated (frozen) surface

2.11 Computational Simulations: Molecular Dynamics (MD) and Adsorption Locator (AL)[17]

2.11.1 Molecular dynamics (MD)

Accurate simulation of atomic and molecular systems generally involves the application of quantum mechanical theory and hence solving the Schrödinger equation. Born and Oppenheimer proposed an approximation to reduce the complexity of the Schrödinger equation by decoupling the motion of the electrons from the nuclei to give

two separate equations. The first equation, the equation of electronic motion or the potential energy surface, depends only parametrically on the positions of the nuclei while the second equation is the equation for nuclear motion on the potential energy surface.

The solution of the potential energy surface (first equation) requires extremely large effort, so usually an empirical fit to the potential energy surface, commonly called a forcefield, is used. A forcefield describes the potential energy hypersurface on which the atomic nuclei move and it contains all the necessary elements for calculation of energy and force. The choice of forcefield, which depends on the type of structure that is being investigated, has great impact on the accuracy of molecular properties prediction. When a forcefield is combined with the coordinates of a structure, an energy expression which describes the potential energy surface of the structure as a function of its atomic coordinates is created. The potential energy of the system is expressed as a sum of three components: valence, cross terms, and non-bonded interaction and their sub-components are described in **Table 2.2**. The spatial configuration of interacting particles is described by four geometrical measures: distance, angle, dihedral angle, and inversion angle.

Table 2.2 Components of the potential energy of a system.[17]

Components	Descriptions of Sub-components
Valence	Bond stretching (bond), valence angle bending (angle), dihedral angle torsion (torsion), inversion / out of plane interactions (oop), Urey-Bradley / interactions between atom pairs involved in 1-3 configurations (UB). $E_{valence} = E_{bond} + E_{angle} + E_{torsion} + E_{oop} + E_{UB}$
Cross Terms	Bond or angle distortion caused by nearby atoms. Important for the determination of the dynamic properties of molecules. Cross terms can include the following: stretch-stretch, stretch-bend-stretch, bend-bend, torsion-stretch, torsion-bend-bend, bend-torsion-bend, stretch-torsion-stretch.
Non-bonded	van der Waals (vdW), electrostatic (Coulomb), and hydrogen bond (hbond) $E_{non\text{-}bond} = E_{vdW} + E_{Coulomb} + E_{hbond}$

Nuclei are relatively heavy objects (compared to electrons) so quantum mechanical effects are often insignificant. Thus, Newton's equation of motion is used to describe the motion of the nuclei, replacing the second equation from the Born-Oppenheimer approximation. The solution of Newton's equation of motion, using an empirical fit to the potential energy surface, is called molecular dynamics (MD). Molecular mechanics ignores the time evolution of the system and instead focuses on finding particular geometries and associated energies or other static properties. This includes finding equilibrium structures, transition states, relative energies, and harmonic vibrational frequencies.

2.11.2 Adsorption Locator (AL)

AL software from Materials Studio®4.3 is used to simulate a substrate loaded with an adsorbate or an adsorbate mixture of a fixed composition. Designed to study individual systems, it allows the identification of low energy adsorption sites on both periodic and nonperiodic substrates or to investigate the preferential adsorption of mixtures of adsorbate components. The protocol is summarised in **Figure 2.10**.

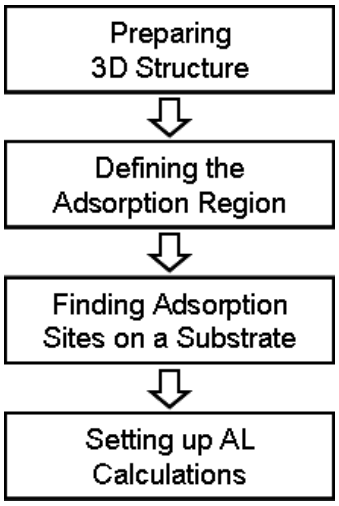

Figure 2.10 Simplified protocol for Adsorption Locator (AL).

The procedure to obtain the adsorption sites of an adsorbate on a substrate is generally as follows. To begin, the three-dimensional structure of the substrate is constructed and

the optimized structure of the adsorbate is generated using MD. It is important to optimize the geometry of the structures and assign charges accordingly. Secondly, the adsorption region can be defined using a bounding box, a target atom set, or fields or field segregates. Thirdly, the simulated annealing task in AL is used to simulate a substrate loaded with an adsorbate or an adsorbate mixture of fixed composition. A low energy adsorption site is identified by carrying out a Monte Carlo search of the configuration space of the heated substrate-adsorbate system as the temperature is slowly decreased (simulated annealing method) so that at any given time, it is approximately in thermodynamic equilibrium.[18] This process is repeated to identify further local energy minima. It is important to note that during the course of simulation, adsorbate molecules are randomly rotated and translated around the substrate. The configuration that results from one of these steps is accepted or rejected according to the selection rules of the Metropolis Monte Carlo method.[19] The Metropolis Monte Carlo method assumes that the adsorbate molecules do not have a high degree of torsional flexibility and ignores any internal degrees of freedom that the adsorbate components may possess on the substrate surface. Lastly the adsorption energy of the final configuration is extracted.

Reference:

1 J. Goldstein, D. E. Newbury, P. Echlin, D. C. Joy, A. D. R. Jr, C. E. Lyman, C. Fiori, and E. Lifshin, *Scanning electron microscopy and X-ray microanalysis: a text for biologists, materials scientists, and geologists*. Plenum: New York 1981.

2 B. Ratner, and D. Castner, *Surface Analysis - The principal techniques*. John Wiley & Sons: West Sussex, 1997.

3 *Mettler Toledo STARe System, Operation Manual TGA/SDTA851e*

4 D. A. Skoog, D. M.West, and F. J. Holler, *Fundamentals of analytical chemistry*. 6th ed.; Saunders College Pub.: Philadelphia, 1992.

5 C. B. Boss, and K. J. Fredeen, *Concepts, Instrumentation, and Techniques in Inductively Coupled Plasma Optical Emission Spectrometry* Second ed.; The Perkin Elmer Corporation: 1997.

6 *Quantasorb, NOVAWin2 / 2-P Ver. 2.1 Operation Manual P/N 05079*,

7 S. Brunauer, L. S. Deming, W. E. Deming, and E. Teller, *J. Am. Chem. Soc.* **62**, 1723-1732 (1940).

8 S. Brunauer, P. H. Emmett, and E. Teller, *J. Am. Chem. Soc.* **60**, (2), 309-319 (1938).

9 E. P. Barrett, L. G. Joyner, and P. P. Halenda, *J. Am. Chem. Soc.* **73**, (1), 373-380 (1951).

10 J. H. deBoer, *The Structure and Properties of Porous Materials*. Butterworths: London, 1958.

11 H. P. Klug, and L. E. Alexander, *X-ray difraction procedures: for polycrystalline and amorphous materials* John Wiley and Sons New York, 1974.

12 D. A. Skoog, and J. Leary, *Principles of Instrumental Analysis*. Fort Worth: Saunders, 1992.

13 R. K. Iler, *The Chemistry of Silica*. John Wiley & Sons: New York, 1979.

14 D. J. Belton, in, Nottingham Trent University: Nottingham, 2005; Vol. PhD (Chemistry).

15 C. C. Harrison, and N. Loton, *J. Chem. Soc. Faraday Trans.* **91**, (23), 4287-4297 (1995).

16 W. C. Chan, and P. D. White, *Fmoc Solid Phase Peptide Synthesis*. Oxford university Press: New York, 2000.

17 *Material Studio® 4.3 Manual*.

18 S. Kirkpatrick, C. D. Gelatt, and M. P. Vecchi, *Science* **220**, 671-680 (1983).

19 N. Metropolis, A. W. Rosenbluth, M. N. Rosenbluth, A. H. Teller, and E. Teller, *J. Chem. Phys.* **21**, 1087 (1953).

Chapter 3
Imidazole Catalysed Silica Synthesis: Progress towards Understanding the Role of Histidine in (Bio)silicification

3.1 Introduction

The intricate and highly repeatable biosilica structures exhibited by marine organisms demonstrate the magnificence of construction control exerted by life. Studies of these organisms have revealed that organic biomolecules including proteins are associated with the growth of biosilica structures however the role(s) of these biomolecules at the molecular level are not yet fully understood. Silicatein proteins extracted from sponges, such as *T. aurantia* and *S. domuncula*, have high sequence homology with cathepsin-L which shows a hydrolytic function in the lysosome.[1, 2] The major subunit of silicatein, silicatein-α, proved to be sufficient to accelerate the polymerisation of silica from tetraethoxysilane (TEOS) at neutral pH[3] while a site-directed mutagenesis study of silicatein-α has shown that the hydroxyl of Ser-26 and imidazole of His-165 residues present at its active site are necessary for the catalysis of TEOS.[4] The necessity for the two functionalities, nucleophilic side chain of serine/cysteine and the imidazole nitrogen of histidine, to be in close proximity, ca. 6.2Å,[5] has been shown by an *in vitro* study using bifunctional small molecules such as cysteamine ($HS–(CH_2)–NH_2$) and ethanolamine ($HO–(CH_2)–NH_2$).[6]

On the basis of the above results, it was hypothesized that hydrogen bond formation between the hydroxyl group of Ser-26 and the imidazole of histidine-165 is important in silicification.[4, 6, 7] This hypothesis has been corroborated by an *ab initio* density functional theory (DFT) study using a gas-phase model which has shown that the free to rotate imidazole group of His-165 is able to form a hydrogen bond with the –OH of Ser-26.[5] When a similar simulation was performed in the presence of monosilicic acid,

the binding energy (BE) and formation energy (FE) values obtained showed that polycondensation between monosilicic acid molecules was energetically favourable in the presence of silicatein,[5] thus further supporting the importance of the hydrogen-bonding ability of histidine in silica formation. In other studies of silica formation, combinatorial phage display methods have been used to identify silica-binding peptides (SiO_2-BPs).[8] Many of the SiO_2-BPs identified that were also capable of facilitating silica formation, contain high numbers of histidine residues.[8, 9] Based on the studies reviewed above, it is highly likely that the presence of histidine-containing biomolecules in a silica-forming reaction environment is simply not fortuitous. However, no direct evidence has been presented which shows that histidine catalyses the condensation of silicic acid molecules. Furthermore model studies of silica formation in the presence of polyhistidine (P-His) have generated conflicting results; one *in vitro* study at neutral pH using tetramethoxysilane (TMOS)[10] has precipitated silica in the presence of P-His whereas in another study where TEOS was used as the silica precursor, P-His alone did not show activity.[7]

Although silicatein proteins have been used to generate a range of different materials including silica (natural and recombinant silicatein),[3, 11] zirconia (recombinant silicatein),[12] titania (natural and recombinant silicatein)[12-14] and gallium oxide (natural silicatein),[15] they are expensive to produce and therefore not suitable for the mass production of novel materials. In order to apply and build upon the knowledge learned from the studies of silicatein and its sub-components; the exploration of the role(s) of its active sites via the study of molecules with limited functionality may be a more practical approach to pursue. Moreover molecules with single functionality may be more ideal for the study of the influence of non-bonded interactions (hydrogen bond and electrostatic interactions) on silica formation. Polyvinylimidazole (PVI) and P-His both have imidazole as their side chain functionality but with different backbones. The chemical structures of imidazole, PVI and P-His are shown in **Figure 3.1**. The pK_a values of the most accessible ring nitrogen are, 6.14 for histidine monomer (calculated);[16] 6.79 for vinylimidazole monomer (calculated),[16] and 3.6~4.9 for PVI (empirical).[17-20] In this study, PVI and P-His have been used to probe the ability of imidazole in catalysing silica formation from monosilicic acid. The effect of PVI chain length and the influence of backbone were also investigated.

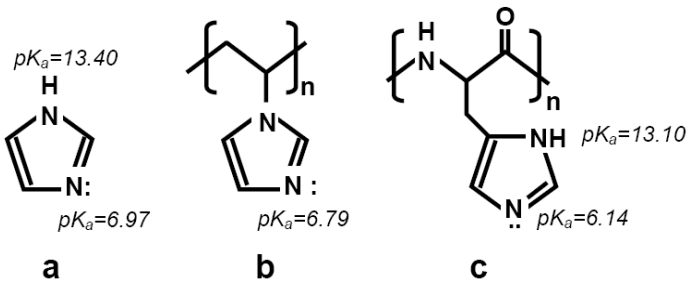

Figure 3.1 Chemical structures of (a) imidazole, (b) PVI and (c) P-His. pK_a values shown were determined from their corresponding monomeric units using Marvin pK_a calculator at 298K.[16]

3.2 Experimental

3.2.1 Reagents

Dipotassium silicon triscatecholate ($K_2[Si(C_6H_4O_2)_3]\cdot 2H_2O$, 97%), anhydrous sodium sulphite (Na_2SO_4, 97%), potassium bromide (KBr, FTIR grade) and poly histidine (39kDa) were purchased from Sigma Aldrich Chemicals; ammonium molybdate tetrahydrate ($H_{24}Mo_7N_6O_{24}\cdot 4H_2O$), hydrochloric acid (HCl, 37%) and sulfuric acid (H_2SO_4, 98%) were purchased from Fisher Scientific; oxalic acid ($C_2H_2O_4\cdot 2H_2O$, 99%) and 4-methylamino phenol sulfate ($C_{14}H_{18}N_2O_2\cdot H_2SO_4$, 99%) were purchased from Acros Organics and standard silicate solution (1000ppm SiO_2) was purchased from BDH. Dipotassium silicon triscatecholate was purified by dissolution in methanol followed by filtration to remove undissolved impurities. Methanol was removed by evaporation at 60°C and the sample was vacuum-dried at 40°C. All other chemicals were used without further treatment unless specified. Deionised-distilled water (ddH_2O) with conductivity less than 1 μScm^{-1} was used to prepare all solutions and to wash precipitates.

The synthesis of PVI and its fractionation was carried out by Dr. Elena N. Danilovtseva and Dr. Vadim V. Annenkov from the Limnological Institute of Siberian Branch of Russian Academy of Sciences according to methods previously reported.[21] The

molecular masses (MM) of these fractions were determined by viscosity measurement.[22] PVI-7, PVI-14, PVI-48, PVI-106, PVI-240 and PVI-530 were prepared and used in this study where the numbers indicate the average MM in kDa. P-His with MM of 39kDa was used as a reference material for comparison. The degree of polymerization (DP) of the PVI fractions relative to P-His is summarized in **Table 3.1**.

Table 3.1 Degree of polymerization (DP) of PVI fractions relative to P-His.

Polymer-MM in kDa	DP	Relative DP*
PVI-7	74	0.33
PVI-14	149	0.66
PVI-48	511	2.26
PVI-106	1128	4.99
PVI-240	2553	11.30
PVI-530	5638	24.90
P-His-39	226	1.00

** Relative DP=DP of PVI / DP of P-His*

3.2.2 Silica synthesis

The effect of imidazole functionality on silica synthesis and its reaction kinetics was studied using 30mM dipotassium silicon triscatecholate (K_2SiCat_3) at 25±1°C adjusted to pH 6.8±0.05 using HCl. K_2SiCat_3 is readily hydrolysed to monosilicic acid and thus is suitable for the investigation of siloxane bond formation activity in the presence of PVI or P-His. The concentration of PVI and P-His with respect to the imidazole group (the monomeric heterocyclic unit) was maintained at 5.3mM for all additives studied, keeping the silicon-to-imidazole ratio at 6:1. All reactions were studied using routinely prepared reactants of 10ml. PVI fractions or P-His were dissolved in 3ml of ddH_2O and a known amount of 0.1M HCl was added to adjust the solution to pH 6.8±0.05. The required amount of K_2SiCat_3 was dissolved in ddH_2O and the hydrolysis reaction was initiated by the addition of a predetermined amount of 2M HCl at time zero (t=0). pH-adjusted PVI or P-His solution was added at a time when the sample contained the highest concentration of monosilicic acid, i.e. 30 seconds after hydrolysis had been started (**Appendix 3.1**). Precipitated silica was collected by centrifugation at 3000rpm after 1 hour (only for some samples due to limited quantities of some of the PVI fractions), 4 hours (near-equilibrium levels of monosilicic acid) and 7 days (following maturation of samples and to allow comparison with materials generated in other

studies).[23] Collected samples were washed at least three times with ddH_2O before being lyophilised at -70°C using a Virtis-110 freeze-dryer. Experiments conducted in the presence of PVI-48, PVI-106, PVI-530, and P-His were performed in duplicate.

3.2.3 Kinetic studies

Condensation reactions were studied by measuring the change in monosilicic acid concentration with time by a modification of the molybdenum blue colorimetric method.[24-26] The composition of the two reagents used, the molybdic acid reagent and the reducing agent, are shown in **Table 3.2**.

Table 3.2 Composition of molybdic acid reagent and reducing agent.

Reagent	Chemical	Amount
Molybdic acid reagent	Ammonium molybdate (VI) tetrahydrate	20g
	Hydrochloric acid	60ml
	ddH_2O	940ml
Reducing agent	Oxalic acid dihydrate	20g
	4-methylaminophenol sulphate	6.7g
	Sodium sulphite	4g
	Sulphuric acid	100ml
	ddH_2O	900ml

At a sampling point, a 10µl aliquot was drawn from the reaction pot and dispensed into a sample pot containing 15ml of the molybdic acid reagent. After 15 minutes, 8ml of reducing agent was added into the same sample pot where the blue silicomolybdous complex was formed. The formation of the blue complex was left to equilibrate at room temperature for 24 hours before the intensity of the blue silicomolybdous complex at 810 nm was measured using a Unicam UV2 UV-VIS spectrometer. The apparent third order rate constant (k_3) (formation of trimers probably from a dimer and a monomer of silicic acid), first order rate constant for oligomer formation (k_+), and oligomer dissolution (k_-) were determined according to **Section 2.8**. The transition from third order kinetics (predominantly trimer formation) to first order kinetics (oligomerisation process) occurs when the $1/[Si(OH)_4]^2$ vs time plot deviates from linearity, **Figure 3.2**. The concentration of monosilicic acid present in solution was also measured at this time of transition.

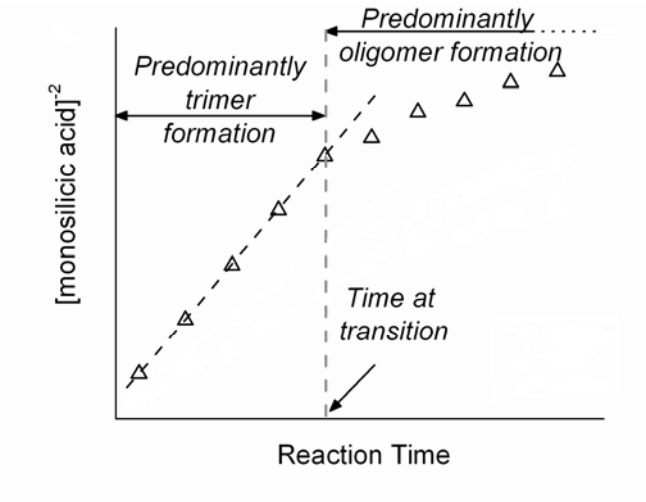

Figure 3.2 Illustration of the transition from third order kinetics (predominantly trimer formation) to first order kinetics (oligomerisation). The gradient of the graph before the transition time was used to derive k_3.

The apparent rate constants obtained from PVI or P-His-added reactions were normalized with respect to the values obtained from the blank system (no additive). The reaction kinetics of the blank system was studied using 4 samples run in parallel with experiments performed with PVI or P-His added. The confidence level of 95%, corresponding to α (significance level) of 0.05, were determined for k_3, k_+ and k_- of the blank. Any corresponding data obtained from systems with additives (PVI or P-His) lying outside these envelopes has a 95% probability of being statistically significant. The confidence interval (CI) for a small dataset (<30 samples) was calculated by $CI=\bar{x} \pm t_x \hat{\sigma}_x$ where, $\hat{\sigma}_x = s/\sqrt{n}$ is the standard error of the mean, $\bar{x}$ is the mean of the 4 samples, t_x is the Student t value obtained for given degrees of freedom x, α is the significance level (1-Confidence level), and s is the standard deviation. The CI was normalized against the respective rate constants obtained for the blank system before being presented in the graphs as error bars.

3.2.4 Titration of polyvinylimidazole (PVI) and polyhistidine (P-His)

Potentiometric titration of PVI and P-His solutions was performed using a Radiometer Autotitrator TitraLab 865 (Radiometer analytical) with TitraMaster 85 PC software

equipped with a Red Rod combined gas-electrode and PT100 temperature sensor. Solutions of the same molarity used for the silicification experiments (5.3mM) were acidified with 1M HCl to pH 2 and then titrated from pH 2 to pH 12 using 100mM KOH. The pK_a value and percentage of protonated species at pH 6.8 were determined from the titration curves obtained. Theoretical modelling of the pK_a values of imidazole and histidine was also performed using Marvin.[16]

3.2.5 Fourier Transform Infrared Spectroscopy (FTIR)

The silica and organic content of the precipitates was determined using a Nicolet Magna IR-750 Fourier Transform Infrared Spectrometer set at 128 scans and 4cm^{-1} resolution. 1mg of sample and 199mg of KBr was ground and pressed with 10 tons weight for 6 minutes into a transparent disk before analysis. A pure KBr disk was scanned as a background before scanning each prepared disk. Spectra were studied by using pure PVI, P-His, and dipotassium silicon triscatecholate as references.

3.2.6 Thermogravimetric Analysis (TGA)

The amount of occluded PVI or P-His was determined using a Perkin-Elmer Pyris 6 TGA. Samples were heated at 10°/min from 30°C to 900°C in air to ensure complete combustion of all organic material. Heating from 30°C-200°C was found to remove both the physisorbed and chemisorbed water molecules. Further heating from 200°C to 900°C removed organic material occluded in the lyophilized precipitates. Any remaining material was assumed to be "pure" silica (i.e. free of water and organics) and identified as such by FTIR spectroscopy. A Mettler Toledo TGA/DSC1 was used to determine the onset temperature for the decomposition of the organic phase in silica-PVI-106 and silica-P-His composites. The samples were run under air at 5°/min from 30°C to 900°C using 70μl aluminium pans and the results were obtained using a blank correction method. The analyses to determine the onset temperature of two samples were performed by Dr. Phil Williams from Mettler Toledo.

3.2.7 Surface area analysis

Precipitate surface area and porosity was obtained using a Quantachrome Nova 3200e surface area and pore size analyzer with all samples being degassed at 130°C overnight under vacuum prior to analysis. Surface areas were determined by the BET[27] method where nitrogen is assumed to have a cross sectional area of 0.16nm^2, over the range of relative pressures (P/P_0=0.05-0.3) at which point the monolayer is assumed to assemble. Pore radii were determined by the BJH[28] method using the desorption branch of the isotherm.

3.2.8 Scanning Electron Microscopy (SEM)

Samples for SEM were prepared by dispersing lyophilized powders on double-sided carbon tape mounted on aluminium stubs, loose aggregates were removed by tapping before gold-coating the sample (Edwards S150B sputter coater; argon plasma at 1.2 kV and 4 mbar pressure for 2.5 minutes). Images were acquired using a JEOL JSM-840A scanning electron microscope at an accelerating voltage of 20 kV and working distance of 15mm.

3.3 Results and Discussion

3.3.1 Catalytic role of imidazole in the early stages of silicic acid condensation

The initial condensation of monosilicic acid generates dimers followed by trimers and tetramers with further condensation to form larger oligomers and condensed particles. For the comparison with other studies in the research group, the silicon-to-imidazole ratio in this study was kept constant at 6:1 for both P-His and PVI-added reactions. The use of lower silicon-to-imidazole ratio, i.e. 3:1, for PVI-added reactions has been

attempted by keeping other reaction conditions constant. However undesirable immediate precipitation of PVI upon reactant mixing was observed (**Appendix 3.2**).

The effect of PVI and P-His on the kinetics of the early stages of the condensation reaction has been monitored. It was found that the addition of molecules with imidazole functionality to the silicifying medium resulted in a statistically significant increase in the apparent third order trimerisation rate constant k_3 (**Figure 3.3a, b**). A similar effect was also found in other previous studies using additives with amine functionality.[25, 29, 30] As shown in **Figure 3.3b**, the normalised k_3 values increased with the DP of PVI to a maximum value of 135% with PVI-106. The k_3 value for the P-His-added system (143%) was significantly higher than the k_3 values of all PVI-added reactions especially when considering the DP of most PVI additives were higher than the DP of P-His (**Table 3.1**). The trend in normalised k_3 rate constant values follows a trend similar to that of PVI coil size as a function of its DP in solution,[21] suggesting that the polymer conformation in solution may directly affect its ability to catalyse silicic acid condensation.

As discussed in the introduction, an additive could cause an increase in condensation kinetics by forming hydrogen bonds and/or by promotion of electrostatic interactions. From the chemical structures (**Figure 3.1**) and ionization properties (pK_a) of P-His[16] and PVI,[17-20, 31] it would appear feasible that these two additives could interact with silicic acid species through hydrogen bonds, and an additional electrostatic attractions by P-His (~50% protonated). The formation of a hydrogen bond between lone pairs of electrons with silanol groups has been demonstrated by infrared studies of the adsorption of gas phase NO_x on silica surfaces.[32] Furthermore in two independent studies on the adsorption of PVI on silica surfaces, the high affinity of PVI for silica surfaces at pH 10, conditions under which PVI is completely uncharged, showed that the adsorption of PVI on silica surfaces can be driven by hydrogen bonding interactions alone.[18, 31] It is, therefore likely that during the initial stage of the silica condensation reaction at pH 6.8 when almost all silicic acid species are uncharged ($Si(OH)_4$ charge $<<1\%$, $pK_a(Si(OH)_4)=9.8$), the presence of polymers containing imidazole functionality could facilitate hydrogen bond formation thereby bringing silicic acid species into close proximity to one another, thus favouring condensation. The higher k_3 value measured for P-His (compared to PVI) could be due to (i) the

larger separation and flexibility of the P-His imidazole side chain to form hydrogen bonds;[5] and (ii) the difference in their pK_a values (**see Section 3.3.3**).

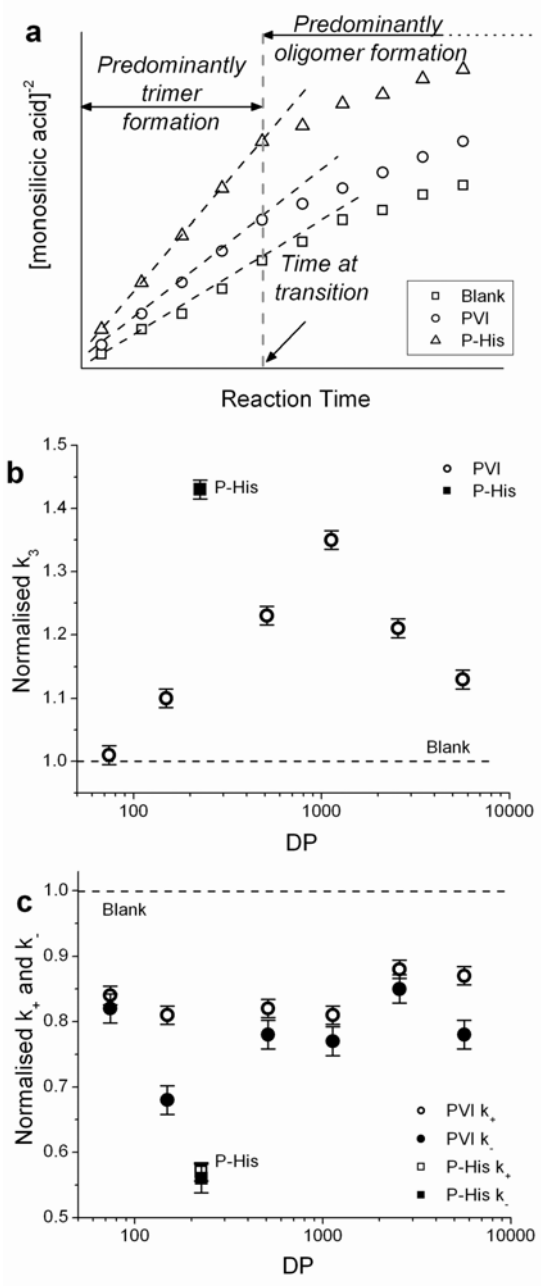

Figure 3.3 (a) Illustration of the effect of additives on the concentration of monosilicic acid at the transition time. The gradient of the linear region of the graphs, used to derive k_3, is not scaled. Reaction kinetics: (b) normalised apparent trimerisation rate constant, k_3, and (c) normalised apparent first order forward oligomerisation rate, k_+ and reverse oligomerisation rate k_-. The normalisation of apparent rate constants was against respective values from the blank system and the error bars represent the 95% confidence level.

In contrast with the increases observed in k_3, the first order rate constants for condensation (k_+) and dissolution (k_-) for PVI and P-His added reactions were lower than the blank, **Figure 3.3c**. Both k_+ and k_- for PVI-added system were reduced to 80-90% and 65-90% respectively, while much lower values were obtained in the presence of P-His (56-57% for both k_+ and k_-). In these reactions, the transition (ca. 4 minutes reaction) between the time period when apparent third order kinetics and first order kinetics was followed, was little affected by the presence of PVI or P-His, as illustrated in **Figure 3.3a**. However, the monosilicic acid concentrations for PVI fractions and P-His-added solutions were all statistically lower than the blank: 3.2-7.9% reduction for the PVI-added reactions and 19.2% reduction for the P-His-added reaction (**Table 3.3**). It is believed that the reduction in the available monosilicic acid for further condensation, at the end of the (predominantly) trimerisation process, has reduced the rate of further reaction (oligomerisation).

Table 3.3 Monosilicic acid concentration, $[Si(OH)_4]$, on the transition time from apparent third order kinetics to first order kinetics.

System / Additive	$[Si(OH)_4]$ on Transition Time (mM)
Blank	20.16 [19.76 to 20.71]*
PVI-7	19.51
PVI-14	19.03
PVI-48	19.41
PVI-106	18.56
PVI-240	19.51
PVI-530	19.03
P-His	16.29

* Average and 95% C.I. (shown in bracket) from 10 sets of blanks.

3.3.2 Modification of materials production rate and materials properties by PVI and P-His

In addition to affecting the very early stages of silicic acid condensation, both PVI and P-His promoted silica precipitation. Immediate turbidity was observed upon the addition of PVI or P-His into hydrolyzed precursor solutions, however, no precipitation was observed in the blank silicifying system (without additive) after more than 24 hours reaction. A pale yellow substance was precipitated upon PVI addition after 90 seconds while a brownish gel-like substance was formed immediately in the presence of P-His. This brownish gel-like substance was indeed similar in appearance to

material that usually is observed to form in the blank system after 1-2 days of reaction, **Figure 3.4a**.

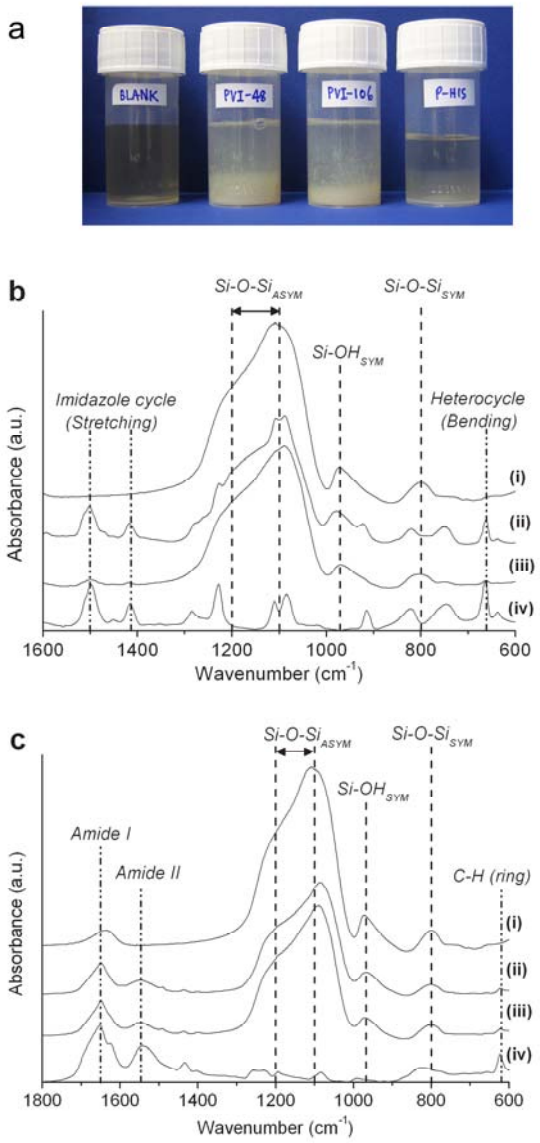

Figure 3.4 (a) Precipitates formed in reaction vessels 90 seconds after addition of PVI or P-His into the hydrolyzed silica precursor. The additives used are labelled on the reaction vessels. (b) FTIR spectra of (i) silica from the blank, (ii) silica-PVI-7 composites (4hours), (iii) silica-PVI-7 composite (7days), and (iv) PVI-7. (c) FTIR spectra of (i) silica from the blank, (ii) silica-P-His composites (4 hours), (iii) silica-P-His composite (7 days), and (iv) P-His. *SYM* and *ASYM* are symmetrical and asymmetrical vibrations respectively.

The composition of the precipitates formed was assessed at 4 hours after the start of the reaction and after 7 days by TGA and FTIR analysis. FTIR analysis confirmed the

presence of the respective polymers (PVI: 1502cm^{-1} and 1418cm^{-1} from imidazole cycle stretching, and 665cm^{-1} from heterocyclic bending; P-His: amide-I and amide-II bands centred at ~1646cm^{-1} and 1548cm^{-1} respectively) and silica (Si-OH at ca. 950cm^{-1}, Si-O-Si$_{sym}$ at 800cm^{-1} and Si-O-Si$_{asym}$ centred at ca. 1100cm^{-1}) within the samples collected, **Figure 3.4b-c**. The FTIR spectra for silica-PVI composites formed from PVI with different MM were comparable (**Appendix 3.3**) hence only spectra from the PVI-7-added reaction are shown in **Figure 3.4b**.

The area ratios of selected peaks from FTIR spectra (**Figure 3.4b-c**) were used as an indication of polymer-to-silica ratio for composites obtained after 4 hours and 7 days. For convenience, distinctive (non-overlapping) peaks were selected, thus the ratios obtained did not represent the absolute weight ratio between polymer and silica of the composites collected. The 1502cm^{-1} band from imidazole cycle stretching, the 1646cm^{-1} band from the amide-I band, and the 800cm^{-1} band from Si-O-Si$_{sym}$ were used to represent PVI, P-His and silica respectively. The results presented in **Table 3.4** imply that the polymer-to-silica peak area ratio was time-dependent for silica-PVI composites but time-invariable for silica-P-His composites.

Table 3.4 Polymer-to-silica peak area ratio determined from FTIR spectra.

Sample	Polymer-to-Silica Ratio
Silica-PVI-7 Composite (4h)	3.16
Silica-PVI-7 Composite (7d)	0.31
Silica-P-His Composite (4h)	2.79
Silica-P-His Composite (7d)	2.68

Remarks: 4h=4 hours, 7d=7 days.

The absolute amount of silica precipitated and the proportions of silica and organic polymer in the precipitates collected after 4 hours and 7 days was determined from TGA. The remaining material after TGA was confirmed to be pure silica by FTIR spectroscopy (**Appendix 3.4**) while the determination of PVI/P-His weight is described in the experimental section. As seen in **Figure 3.5a**, less than 0.01mg of silica was obtained from the blank reaction after 4 hours while ~14mg was produced after 7 days. For all of the samples containing PVI ca. 3-4mg (20-28% that of the blank at 7 days) of silica was generated after 4 hours reaction and, for samples containing P-His; ca 10.2mg of silica was generated after 4 hours reaction which corresponds to 70% of the

amount produced by the blank after 7 days. The addition of P-His or PVI to the reaction medium increased silica precipitation during the early stage of reaction with the effect of P-His being greater than that of PVI additions. There was no significant difference in the yield of silica for any of the samples after 7 days of reaction.

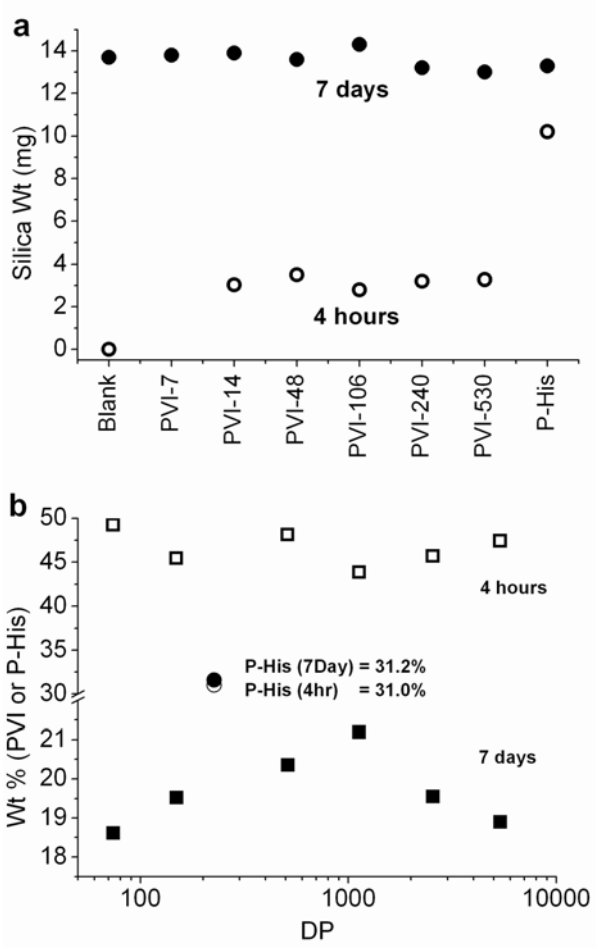

Figure 3.5 The mass of silica (a) and the weight percentage of PVI or P-His (b) precipitated from 10ml reaction after 4 hours and 7 days.

The weight percentage of occluded polymers after 4 hours and 7 days of reaction as assessed by TGA is presented in **Figure 3.5b**. Selected samples (where sufficient polymer was available) were also studied after 1 hour of reaction. After 1 hour reaction the weight percentage of PVI in the silica-PVI composites synthesized in the presence of PVI-48, PVI-106 and PVI-530 were 72wt%, 70 wt% and 65% wt% respectively. After a further 3 hours of reaction the weight percentage was reduced to 45-50wt% and reduced further to 18-21% after 7 days. This trend suggests that PVI incorporation was

more rapid during the initial stage of reaction with the percentage of silica within the precipitated material increasing with time, **Figure 3.5b**. Therefore for reactions involving PVI, the initial precipitate was almost entirely PVI with a decoration of silica, as observed when higher 20mM imidazole was added (**Appendix 3.2**). It is likely that further silica condensation and precipitation occurs on these initial precipitates thereby changing the PVI-to-silica ratio in the material over time. In contrast to the silica-PVI composites, the percentage of occluded P-His (represented by circles in **Figure 3.5b**) did not change between 4 hours and 7 days of reaction (31.0wt% and 31.2wt% respectively). The data indicated that the precipitation of P-His and silica occurred at a fixed ratio throughout the reaction even up to 7 days, as also indicated by the constant silica-to-P-His peak area ratio (calculated from FTIR spectra) presented in **Table 3.4** above.

The effect of PVI and P-His on the morphology of material was studied using SEM. The materials formed in the presence of P-His or PVI have more open, and porous structures compared to those formed in the absence of additives (**Appendix 3.5**). Representative structures of silica-PVI composite, silica-P-His composite, and the Blank are shown in **Figure 3.6** which similar particle sizes were exhibited by these materials although a more condensed structure was shown by the Blank. The typical granular structures observed when other amines have been used as precipitating agents were not observed for these materials.[25, 29, 30]

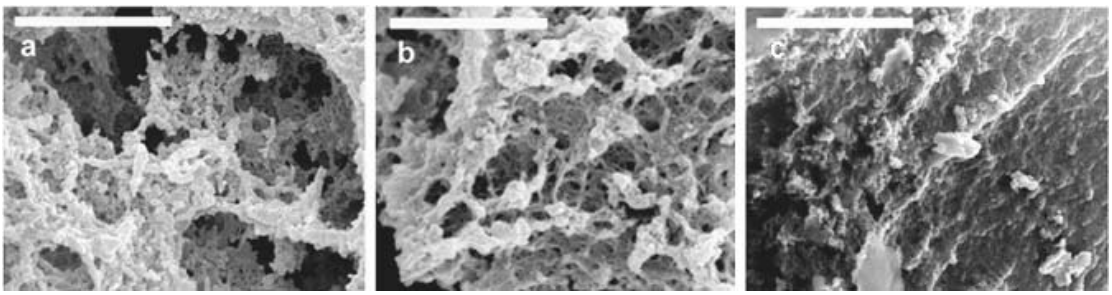

Figure 3.6 SEM of silica-PVI and silica-P-His composites precipitated after 7 days for (a) silica-PVI-106 composite, (b) silica-P-His composite, and (c) the blank (without additive). Scale bars=5μm.

In the absence of additives, the surface area, pore volume and pore radius of the silica produced from the blank were 597m^2/g, 1.33cc/g, and 41.7Å respectively. As shown in

Figure 3.7, the addition of PVI and P-His has reduced the surface area and pore volume of the precipitates obtained. Although the microscopic appearance of these silica-polymer composites were very similar as seen in **Figure 3.6a-b**, the degree of surface area and pore volume reduction was greater for the material made in the presence of P-His (surface area and pore volume of silica-PVI composites; 350-450m^2/g, 0.9-1.2cc/g and silica-P-His composites; 283m^2/g, 1.06cc/g).

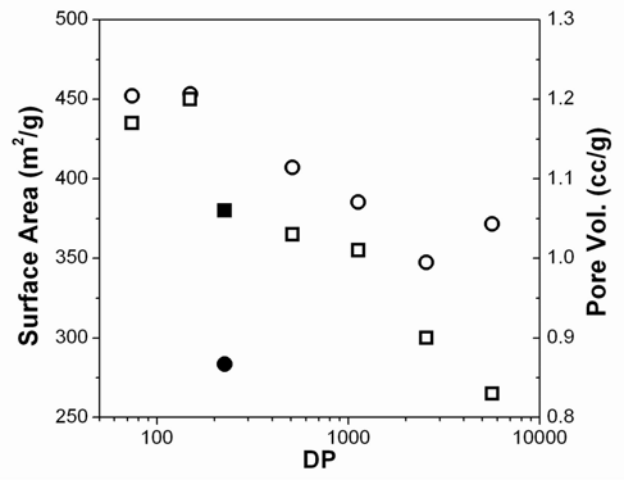

Figure 3.7 Surface area (circle) and pore volumes (square) for precipitates collected after 7 days in the presence of PVI (open symbols) and P-His (filled symbols) as a function of the DP of the polymers.

The results obtained from the reaction kinetics study, FTIR and TGA experiments suggest that (i) the presence of the imidazole functionality is sufficient to increase the apparent rate constant of trimer formation as well as the overall silica precipitation activity; (ii) higher activity was evidenced for P-His; and (iii) the presence of two distinct chemical functional groups in the same molecule is **not** essential for the catalysis of silicic acid condensation, contrary to the hypothesis that the presence of both histidine and serine is essential for the catalysis of silica formation.[6]

3.3.3 The role of electrostatic interactions in the catalysis of silica formation by imidazole

The significant difference in silica precipitating activity within the first 4 hours between P-His (2.55mg/hr) and PVI (0.75-1mg/hr) as compared to their small

difference in the apparent third order rate constant for trimer formation, k_3 (**Figure 3.3b**) suggests, the interaction of PVI or P-His with silicate species other than the smallest oligomers could also play an important role in promoting silica precipitation. The possibility of electrostatic interactions occurring between the reacting species was explored by potentiometric titration of histidine (His), PVI and P-His solutions in the absence of silicon containing species. The pK_a value for the azole nitrogen atom in the various species and the percentage of protonated species were determined and compared with the values obtained from theoretical modelling using Marvin[16] where possible (theoretical calculation of the pK_as for PVI fractions and P-His was not possible due to their very high molecular weights).

The calculated pK_a value of histidine was 6.14, in good agreement with the pK_a value of 6.09±0.01 obtained from the potentiometric study. Based on the results of the potentiometric study alone (**Figure 3.8**), the pK_a of P-His was 6.97 while the pK_a of PVI fractions ranged from 3.84 to 4.03, in good agreement with values obtained by other researchers.[17-20] These pK_a values also implied that at pH 6.8, the pH conditions at which the silicification reaction was studied, about half of the imidazole groups in P-His were protonated (positively-charged) while PVI fractions were almost fully unprotonated (0.1~0.2% protonated), leaving PVI generally uncharged.

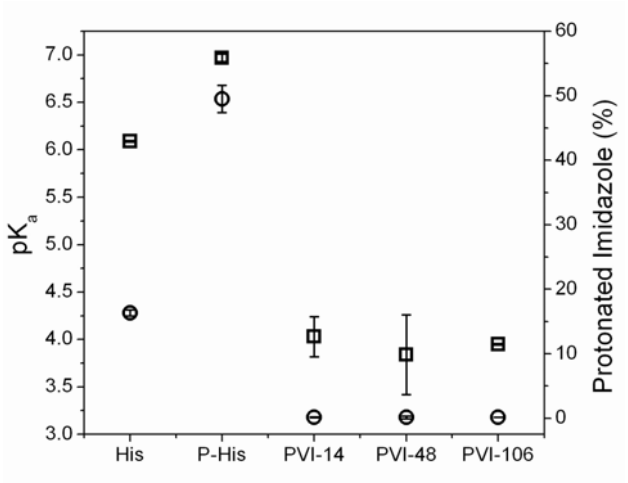

Figure 3.8 pK_a (square) and percentage of protonated imidazole (circle) at pH 6.8 determined from potentiometric titration of 5.3mM solution of histidine, P-His, PVI-14, PVI-48 and PVI-106, with 100mM KOH.

Thus, both PVI and P-His are capable of forming hydrogen bonds with 'Si' containing species in solution that result in increased rates of condensation (k_3) and precipitation. The further enhancement of the silica precipitating activity by P-His relative to all PVI fractions at pH 6.8 could be caused by electrostatic interaction between the protonated P-His species and a range of charged silicic acid oligomers and particles.

3.3.4 Chain length-dependent precipitation and stabilization by PVI

The imidazole functionality possesses both electron withdrawing and electron donating properties. The electron donating property is contributed by the lone electron pair of the azole N atoms while the unsaturated π-system has electron withdrawing capability. The electron donating properties of imidazole in PVI is more prominent than its electron withdrawing property (pK_{BH}^{+}=5-6).[17] In a previous study of silicification using sodium silicate at ≈8mM, the addition of PVI to the reaction system was found to stabilize silicic acid and form soluble complexes by inhibiting silicic acid condensation.[21, 33] The mechanism of silicic acid stabilization by protonated azole cycles probably involves hydrogen bonding. This is supported by quantum chemical calculations that have shown that hydrogen bond formation is energetically favourable.[33] The inhibition of silicic acid condensation was found to be PVI chain length dependent[21]. As chain length increased from PVI-7 through to PVI-530, more basic conditions were needed for silica to precipitate as shown in **Figure 3.9**. The range of pH over which precipitation occurred also reduced as PVI chain length was increased. Long chain PVI samples were proposed to produce stable soluble complexes over a wide range of pH due to their capability to "encapsulate" silicic acid species.

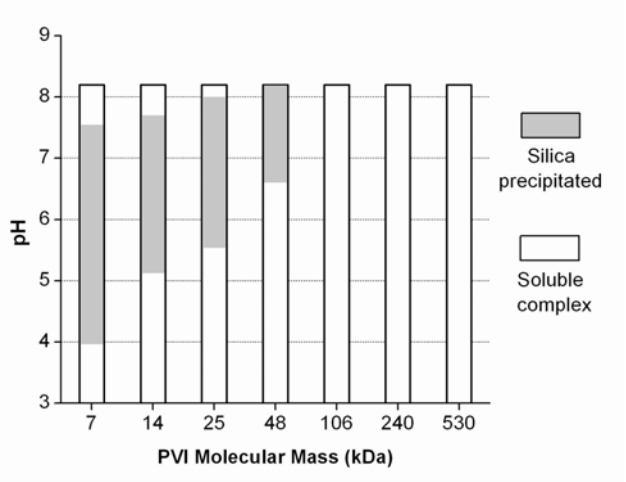

Figure 3.9 The effect of PVI chain length on silica precipitation from sodium silicate (summarised from results presented in ref.[21]).

In contrast, in the present work using 30mM dipotassium silicon triscatecholate as the silicon precursor, the addition of any PVI fraction was able to precipitate silica. In order to verify if the same stabilization effect was related to low precursor concentration employed, an experiment was performed with K_2SiCat_3 of 7.8mM (as used in the study where stabilisation of silicic acid was observed) in the presence of PVI-106, PVI-240, or PVI-530. Although precursor concentration has been reduced to 7.8mM while keeping other reaction conditions constant, immediate precipitation was observed and FTIR analysis confirmed that the precipitates were silica-PVI composites, **Figure 3.10**. Since no stabilized complex was formed upon the reduction of K_2SiCat_3 concentration, we can conclude that the observed formation of precipitates in this study was not caused by the relatively higher concentration of precursor. The difference in behaviour (soluble complex vs precipitation) has to be in part related to the silicon precursor used which requires further investigation.

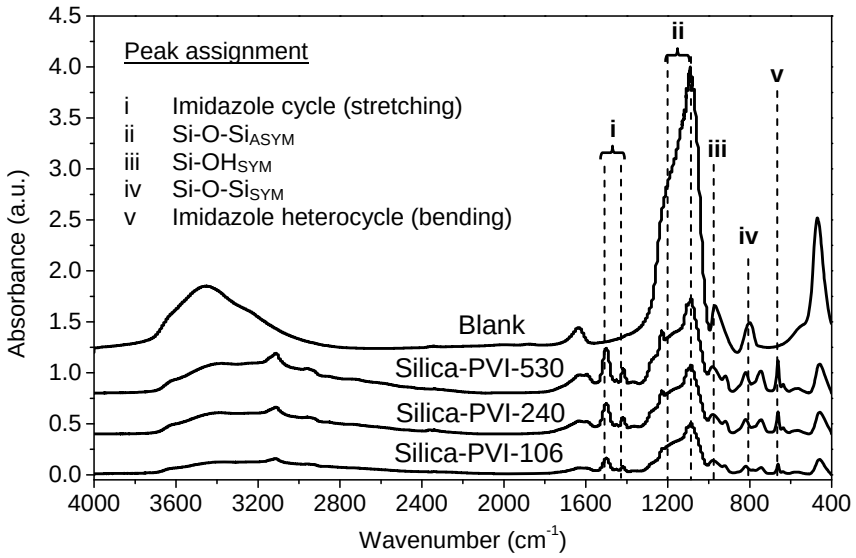

Figure 3.10 FTIR spectra of precipitates obtained from the hydrolysis of 7.8mM of K_2SiCat_3 after 4 hours in the absence of additives (blank) and in the presence of PVI-106, PVI-240, and PVI-530.

3.3.5 Proposed mechanism for the catalysis of silica formation by PVI and P-His

Based on experimental observations and the results obtained in this study, it is proposed that PVI and P-His catalysed silica formation via different mechanisms. As shown in **Scheme 3.1a**, PVI self-precipitates at the initial stage of reaction and subsequently, most probably via heterogeneous catalysis, catalysed silica precipitation on its surface. However when P-His with the same imidazole concentration but higher protonated species was added into the silica precipitating system, homogeneous catalysis occurred, **Scheme 3.1b**. Homogeneous catalysis by P-His was inferred from the co-precipitation of silica with P-His, where the P-His-to-silica ratio remained constant for precipitates obtained at 4 hours and 7 days (**Figure 3.5b**). Calculated from TGA results and the the weights of precipitates collected, it was found that the additives were not completely exhausted after 7 days reaction: ~20wt% and 20-37wt% of added P-His and PVI respectively remained in solution after 7 days (**Table 3.5**).

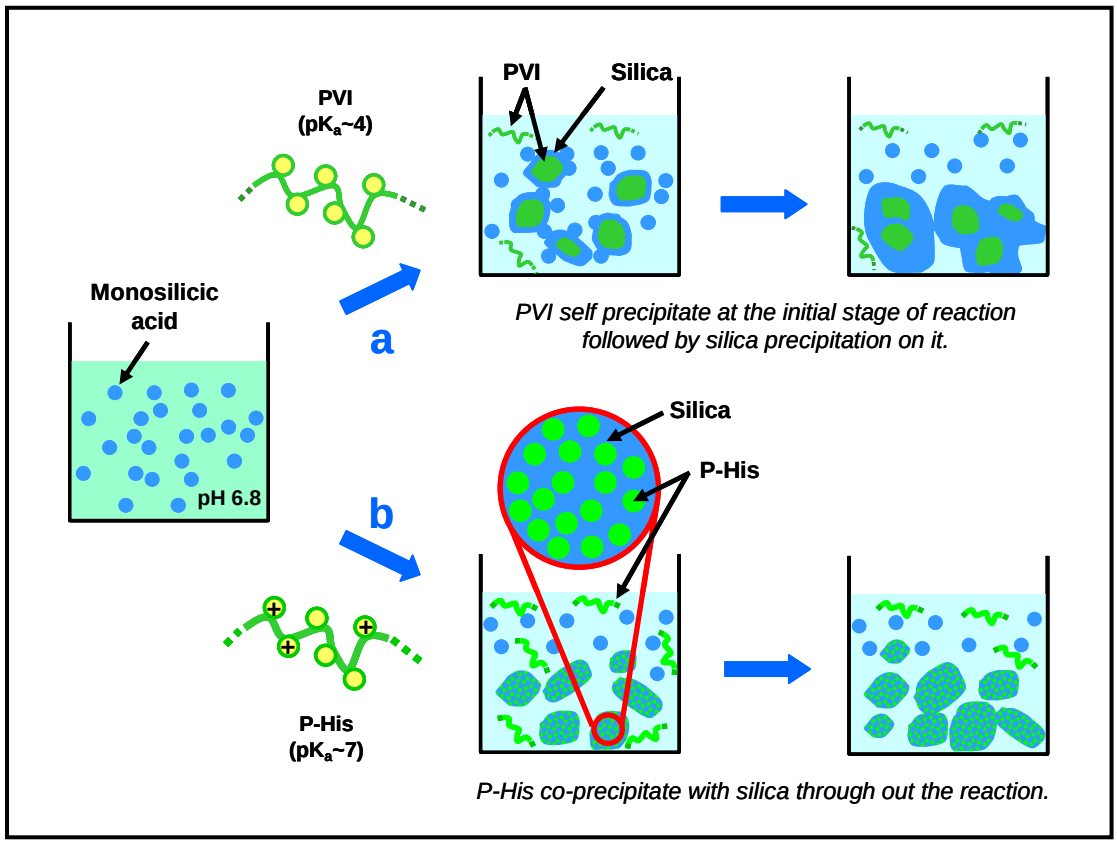

Scheme 3.1 The proposed mechanism for the catalysis of silica formation by (a) PVI and (b) P-His.

Table 3.5 The weight percentage (wt%) of added PVI and P-His remaining in the reaction solution after 7 days reaction with respect to the added weight.

Additives	Additive in solution after 7 days (wt%)
PVI-7	32.3
PVI-14	29.6
PVI-48	23.6
PVI-106	20.1
PVI-240	33.5
PVI-530	36.7
P-His	21.1

The formation of silica-PVI composites starts with the self precipitation of PVI may produce PVI/silica "core-shell" structures. However coprecipitation of silica and P-His was expected to produced uniformly distributed P-His in a silica matrix. The results from synchronized TGA/DSC support this proposal where the onset temperature for the organic phase decomposition was lower by 30°C for silica-P-His composite (260.69°C) compared to silica-PVI-106 composite (291.52°C). The

TGA/DSC results and the TGA curves for all composites are shown in **Appendix 3.6**. The onset temperatures for the decomposition of the organic component of the composites were then compared with the corresponding onset temperature of P-His and PVIs (**Appendix 3.7**). The onset temperature for P-His of and PVIs were 261.0°C and 271-280°C respectively, indicating an increase in the onset temperature for PVI in the form of silica-PVI composite by 11~20°C but not for P-His in the form of silica-P-His composite. This observation supports the proposal of PVI/silica "core-shell" structures in oppose to uniformly distributed P-His in silica-P-His composite.

The verification of structural differences in these composites was attempted by measuring the surface area of these composites before and after calcination. It was anticipated that the calcined silica-P-His composite would have greater increase in surface area compared to the calcined-silica-PVI composite. However a reduction of surface area, pore volume and pore diameter was observed for both samples and the calcined-silica blank (**Figure 3.11**). The surface properties of the calcined samples were believed to be affected by condensation of silanol groups during/after the decomposition of organic phase, thus an increase of surface area was not observed. No significant morphological changes (compared to morphology before calcination, **Figure 3.6**) were observed, **Figure 3.12**.

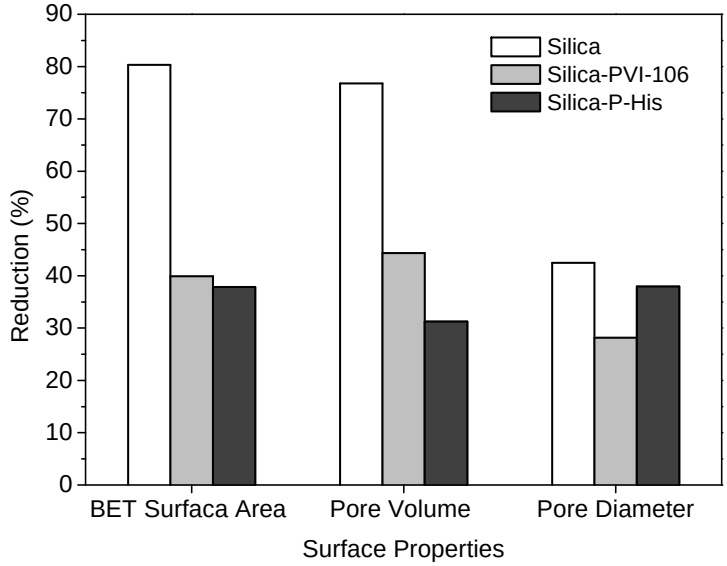

Figure 3.11 Surface area, pore volume and pore diameter reduction (%) for calcined samples with respect to those before calcination.

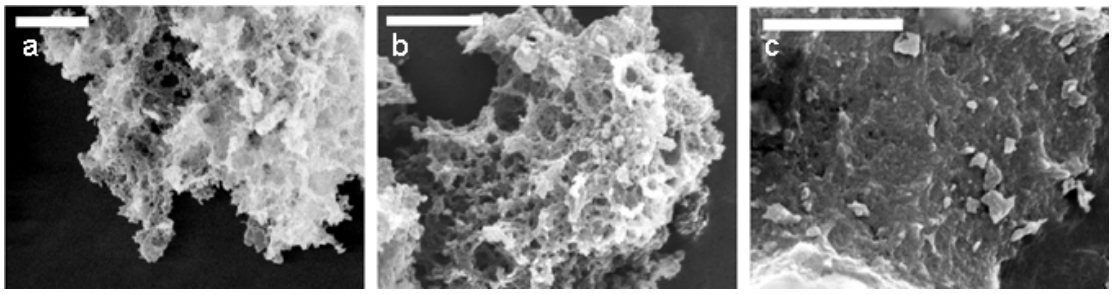

Figure 3.12 SEM of calcined samples precipitated after 7 days: (a) calcined silica-PVI-106 composite, (b) calcined silica-P-His composite, and (c) calcined silica blank (without additive). Scale bars=5μm.

3.4 Conclusions

Histidine is an amino acid present in proteins associated with biosilica formation. It is often found in peptides identified during phage display studies using silica as the target material but its role(s) and the extent of its involvement in the silica precipitation process is not fully understood. Here an *in vitro* silicification study has been conducted using P-His and PVI (with a range of molecular mass) containing the imidazole functionality. It has been shown that the imidazole functionality of PVI and the P-His side chain is able to promote silica condensation and precipitation. It is hypothesized that the imidazole functionality of both P-His and PVI accelerates monosilicic acid condensation by forming hydrogen bonds with monosilicic acid at the early stage of reaction, giving rise to higher apparent trimerisation rate constants, k_3, compared to the blank reaction. During subsequent reaction stages, the protonated imidazole groups (cationic) increased silica precipitation activity via electrostatic interaction with the anionic oligomeric and/or polysilicic acid species. The higher silica precipitation activity of P-His compared to PVI is probably due to the presence of more protonated imidazole groups in P-His at pH 6.8. Although both PVI and P-His mediated silica precipitation and coprecipitated with silica, their time dependent behaviour differed: the P-His-to-silica weight ratio of the precipitates remained constant for the time period from 4 hours to 7 days whereas for reactions performed in the presence of the PVI fractions, initial precipitates were essentially silica decorated PVI polymers that become more silicified with time. It is believed that the results presented herein are of importance in understanding how histidine, a frequently occurring amino acid in

biomolecules associated with silica formation, interacts with different silicic acid species.

References

1 K. Shimizu, J. Cha, G. D. Stucky, and D. E. Morse, *Proc. Natl. Acad. Sci. U. S. A.* **95**, 6234–6238 (1998).

2 A. Krasko, B. Lorenz, R. Batel, H. C. Schröeder, I. M. Müller, and W. E. G. Müller, *Eur. J. Biochem.* **267**, 4878-4887 (2000).

3 J. N. Cha, K. Shimizu, Y. Zhou, S. C. Christiansen, B. F. Chmelka, G. D. Stucky, and D. E. Morse, *Proc. Natl. Acad. Sci. USA* **96**, 361-365 (1999).

4 Y. Zhou, K. Shimizu, J. N. Cha, G. D. Stucky, and D. E. Morse, *Angew. Chem. Int. Ed.* **38** (6), 779-782 (1999).

5 G. Croce, A. Franche, M. Milanesio, L. Marchese, M. Causà, D. Viterbo, A. Barbaglia, V. Bolis, G. Bavestrello, C. Cerrano, U. Benatti, M. Pozzolini, M. Giovine, and H. Amenitsh, *Biophys. J* . **86**, (1), 526-534 (2004).

6 K. M. Roth, Y. Zhou, W. Yang, and D. E. Morse, *J. Am. Chem. Soc.* **127**, (1), 325-330 (2005).

7 J. N. Cha, G. D. Stucky, D. E. Morse, and T. J. Deming, *Nature* **403**, 289-292 (2000).

8 R. R. Naik, L. L. Brott, S. J. Clarson, and M. O. Stone, *J. Nanosci. Nanotech.* **2**, (1), 95-100 (2002).

9 E. Eteshola, L. J. Brillson, and S. C. Lee, *Biomolecular Engineering* **22**, 201-204 (2005).

10 S. V. Patwardhan, and S. J. Clarson, *J. Inorg. Organomet. Polym.* **13**, (1), 49-53 (2003).

11 M. N. Tahir, P. Theato, W. E. G. Muller, H. C. Shroder, A. Janshoff, J. Zhang, J. Huth, and W. Tremel, *Chem. Commun.*, 2848-2849 (2004).

12 M. N. Tahir, P. Théato, W. E. G. Müller, H. C. Schröder, A. Borejko, S. Faiss, A. Janshoff, J. Huth, and W. Tremel, *Chem. Commun.*, (44), 5533-5535 (2005).

13 M. N. Tahir, M. Eberhardt, H. A. Therese, U. Kolb, P. Théato, W. E. G. Müller, H. C. Schröder, and W. Tremel, *Angew. Chem. Int. Ed.* **45**, (29), 4803-4809 (2006).

14 J. L. Sumerel, W. J. Yang, D. Kisailus, J. C. Weaver, J. H. Choi, and D. E. Morse, *Chem. Mater.* **15**, (25), 4804-4809 (2003).

15 D. Kisailus, J. H. Choi, J. C. Weaver, W. Yang, and D. E. Morse, *Adv. Mater.* **17**, (3), 314-318 (2005).

16 Marvin 5.0.0 was used for drawing and characterizing chemical structures and substructures, 40 ChemAxon (http://www.chemaxon.com).

17 N. L. Mazyar, V. V. Annenkov, V. A. Kruglova, S. M. Anabev, E. N. Danilovtseva, A. V. Rokhin, and S. V. Zinchenko, *Russ. Chem. Bull., Int. Ed.* **49**, (12), 2013-2017 (2000).

18 B. Cabot, A. Deratani, and A. Foissy, *Colloids and Surf., A* **139**, 287-297 (1998).

19 T. Roques-Carmes, F. Membrey, M. Kaisheva, C. Filiâtre, and A. Foissy, *J. Colloid Interface Sci.* **299**, 504-512 (2006).

20 B. Popping, A. Deratani, B. Sebille, N. Desbois, J. M. Lamarche, and A. Foissy, *Colloids and Surfaces* **64**, 125-133 (1992).

21 V. V. Annenkov, E. N. Danilovsetva, Y. V. Likhoshway, S. V. Patwardhan, and C. C. Perry, *J. Mater. Chem.* **18**, 553-559 (2008).

22 V. E. Eskin, S. Y. Magarik, U. B. Zhuraev, and G. D. Rudkovskaya, *Vysokomolekulyarnye Soedineniya Seriya A* **20**, (10), 2219-2223. (1978).

23 D. J. Belton, in, Nottingham Trent University: Nottingham, 2005; Vol. PhD (Chemistry).

24 R. K. Iler, *The Chemistry of Silica*. John Wiley & Sons: New York, 1979.

25 D. Belton, G. Paine, S. V. Patwardhan, and C. C. Perry, *J. Mater. Chem.* **14**, 2231-2241 (2004).

26 C. C. Harrison, and N. Loton, *J. Chem. Soc. Faraday Trans.* **91**, (23), 4287-4297 (1995).

27 E. P. Barrett, L. G. Joyner, and P. P. Halenda, *J. Am. Chem. Soc.* **73**, (1), 373-380 (1951).

28 S. Brunauer, P. H. Emmett, and E. Teller, *J. Am. Chem. Soc.* **60**, (2), 309-319 (1938).

29 D. Belton, S. V. Patwardhan, and C. C. Perry, *Chem. Commun.*, 3475-3477 (2005).

30 D. Belton, S. V. Patwardhan, and C. C. Perry, *J. Mater. Chem.* **15**, 4629-4638 (2005).

31 M. R. Böhmer, W. H. A. Heesterbeek, A. Deratani, and E. Renard, *Colloids Surf., A* **99**, 53-64 (1995).

32 G. Ghiotti, E. Garrone, and F. Boccuzzi, *J. Phys. Chem.* **91**, 5640-5645 (1987).

33 V. V. Annenkov, E. N. Danilovtseva, E. A. Filina, and Y. V. Likhoshway, *J. Polym. Sci., Part A: Polym. Chem.* **44**, 820-827 (2006).

Chapter 4
Studies of ZnO Morphology Modification by Zinc Oxide-Binding Peptides via Selective Adsorption

4.1 Introduction

The realisation of the ZnO era in electronics and optoelectronics industries may be possible if the excellent electrical and optical properties of ZnO,[1-3] from micrometer sized crystals to sub-nanometer quantum dots; can be exploited. The challenges ahead can be generally classified into four aspects: crystallinity and purity of ZnO; doping effectiveness and efficiency; size, morphology and functional structure assembly; and, process feasibility and cost. Among them, morphology control has been given much attention because ZnO applications in many instances rely on its shape- and size-dependent properties. Highly crystalline ZnO crystals with diverse nanostructures, from simple to hierarchical, have been produced by vapour route synthesis.[1, 2, 4-12] However, solution route offers a simpler, low scale-up cost, "green", and versatile alternative for ZnO synthesis.

The morphology of ZnO synthesized in solution (aqueous and non-aqueous) is tuned via three approaches: (i) the use of structure-directing agents (SDAs); (ii) the retention of the structure of ZnO precursors, such as layered basic zinc salt (LBZS), by thermal decomposition; and (iii) localised-reaction approach such as sonochemical and microwave-assisted synthesis. Being the most commonly used approach, a wide spectrum of SDAs ranging from simple amines,[13-16] anionic species,[17-21] polymers (DBCP,[22-29] PVP,[30-42] PAM,[29] and PAH[43]) to biomolecules,[44-51] have been shown to affect the morphology of ZnO through imposing effects on nucleation and/or growth of the crystals.

Among these SDAs, biomolecules have been little used in ZnO synthesis because of their complexity, high cost, and sensitivity to reaction conditions. However, the use of biomolecules to direct ZnO synthesis is attractive for a number of reasons. The first is the potential of biomolecules to direct ZnO formation under mild, energy-saving and "green" reaction conditions.[52] Secondly, some biomolecule-directed syntheses have been shown to impose exquisite controls on ZnO morphology/structure;[44-48] improve ZnO crystallinity;[50] catalyse ZnO formation;[53, 54] and also suppress ZnO formation.[44, 45] These diverse effects can be used to tune ZnO properties and thus possibly its applications. Thirdly, biomolecules show remarkable recognition capabilities, functional specificity and multi-functional characteristics which may contribute to high efficiency and accuracy in structure tailoring. Finally, there is a large reservoir of biomolecules with highly diverse functionalities that can be explored and discovered.[52]

Some biomolecules have been shown to be capable of influencing ZnO morphology as demonstrated by the changes/transformation induced and the structural variety of the materials formed. In the presence of histidine and/or its dipeptides, ZnO films instead of discrete particles were formed on substrates[44, 45] while the change of reactant concentrations, including the concentration of histidine, generated ZnO particles in the form of microrods, flowers, and microshells.[48] ZnO microshells were also produced by the use of cysteine[55] while the use of urease[47] has been shown to produce nanoshells with potentially tuneable diameters. The transformation of ZnO particles from spheres to hexagonal plates and ellipsoids has been achieved by reducing the chain length of silk fibroins added.[56] Hexagonal plates have also been synthesized using gelatine[50, 51] and Arabic gum[57] from reactions where hexagonal pellets and irregularly-shaped crystals respectively were more usually formed. In addition to one- and two-dimensional structures, a three-dimensional interwoven mesoporous fibrillar structure has been obtained using eggshell membrane as a template.[49]

With the exception of amino acids and dipeptides, biomolecules used for the study of ZnO formation are mainly complex macromolecules and, for some, their reactivity is determined by their multiple active sites and secondary/tertiary conformations. Thus many of the "wonders" that occur in their presence are created in a "black box". An alternative approach is to use combinatorial display method to identify short peptides (7-mer or 12-mer) that have affinity to the surface of metal or metal oxides. Although

there are limitations in this method,[58] quite a number of metal-binding peptides[59-62] and metal oxide-binding peptides[46, 54, 63-67] have been identified that were either proven to have affinity for the surface on which they were isolated from or have shown influence on the growth of their respective metal or metal oxide.

The identification of ZnO-binding peptides (ZnO-BPs) and understanding how they adhere to the surface of a material is useful for the construction of artificial biomaterials, medical implants, and biosensors where biocompatibility is required. The peptide could also be used to control crystal growth, producing ZnO with high surface to volume ratio for applications such as solar cells, catalysts and sensors.[1-3, 68] Using combinatorial phage display method, a ZnO-BP, EAHVMHKVAPRP (EM-12), has been identified by Umetsu *et al.* whereby EAHVMHKVAPRP-GGGSC (ET-17) was found to catalyse ZnO formation from a stable $Zn(OH)_2$ sol.[54] The use of this ZnO-BP was further demonstrated when Bai *et al.* attached ET-17 via hydrogen bonds onto a GM-collagen template to yield ZnO nanowires.[69]

Independently, Tomczak *et al*. isolated a ZnO-BP that has 67% sequence similarity to EM-12; GLHVMHKVAPPR (G-12).[46] Tomczak *et al*. have shown that a transformation of ZnO from hexagonal rods to hexagonal plates can take place by increasing the concentration of GLHVMHKVAPRP-GGGC (GT-16) in a zinc nitrate-hexamethylenetetramine ($Zn(NO_3)_2$-HMTA) reaction.[46] They proposed that GT-16 inhibited the growth of ZnO along its *c*-axis by selectively adsorbing on the (0001) plane of ZnO.[46] This was deduced from three observations: (i) the reduction of the aspect ratio of ZnO which was GT-16 concentration-dependent, (ii) the (0001) plane of ZnO crystal was flat and well-defined, and (iii) GT-16 had no effect on the diameter of ZnO.

Hitherto, the ability of biomolecules to tune ZnO morphology was evidenced from the use of single amino acids,[44, 45, 48, 55] short peptides,[44, 45, 54, 70] to complex macromolecules such as proteins.[47, 50, 51, 53, 69, 71] However the focus of researches in this area has been generally application-driven and, a description of biomolecule-mediated ZnO formation remains incomplete. It is well accepted that the suppression of ZnO growth along its *c*-axis by biomolecules (also by many synthetic polymers/molecules) may be due to the adsorption of growth-inhibiting additives on

the (0002) plane of ZnO via electrostatic interactions[13, 18-20, 46, 50, 72] or growth-promoting additives on complementary planes.

Recently Muthukumar developed a theory of competitive adsorption-nucleation to explain changes of ZnO aspect ratio in the presence of polypeptides.[73] According to this theory, the adsorption of polypeptides on the (0002) plane of ZnO would reduce the surface energy of the (0002) plane which in turn reduces the aspect ratio of ZnO crystals formed. The aspect ratio-polypeptide concentration relationship calculated fitted extremely well with the experimental data from Tomczak *et al.*.[46] However, no empirical direct evidence has been provided to prove the adsorption of biomolecules (that have altered ZnO morphology in their presence) on the crystal plane(s) of ZnO. The adsorption of alanine on the (10-10) plane and the adsorption of glycine on the (0002) plane have been studied by Gao *et al.*[74] and Irrera *et al.*,[75] respectively. Based on XPS[74] and computational results,[74, 75] they found that the anionic form of these amino acids adsorbed via a bidentate mode on these surfaces. However the significant effect of glycine and alanine on ZnO morphology/growth is yet to be identified.[45] The interaction of tryptophan,[76] bovine serum albumin,[77] and plasma proteins[78] with ZnO have been studied experimentally. These experiments were conducted using ZnO nanoparticles mainly characterised in terms of size,[76, 78] shape,[76, 78] and zeta potential.[78] Crystallographic information relating to the surfaces of these nanoparticles exposed to biomolecules was not provided.

A fundamental understanding of biomolecule-mediated ZnO synthesis is essential for two reasons: sensitivity of ZnO and cost. The conductivity of ZnO is highly sensitive to impurities incorporated into ZnO lattices because they may be contributing to compensating electrons.[3] As for the cost point of view, biomolecules are 'practically too expensive' for the mass production of ZnO hence it is essential to understand the mechanism involved so that a substitute can be identified.

The aim of this study was to seek direct evidence to prove that selective adsorption of ZnO-BP on ZnO crystal plane(s) was the cause of the morphological changes observed. A thorough study of ZnO formation in $Zn(NO_3)_2$-HMTA reaction, both in the absence and presence of G-12 and GT-16 has been conducted. The selective adsorption of G-12 and GT-16 on (0002) and (10-10) crystal planes were studied using

oriented-ZnO films grown by Atomic Layer Deposition technique (ALD). In addition, the motifs of G-12 and GT-16 responsible for the selective adsorption on ZnO crystal planes were predicted using a combination of molecular dynamics (MD) simulations from GROMACS and Adsorption Locator (AL) from Materials Studio®4.3. The essentiality of the GGGC-tag to induce the preferential growth of ZnO was also studied by comparing the effects shown by G-12 and GT-16 on the formation of ZnO crystals.

4.2 Experimental

4.2.1 Reagents

Zinc nitrate hexahydrate ($Zn(NO_3)_2 \cdot 6H_2O$), hexamethylenetetramine (HMTA, $C_6H_{12}N_4$), sodium monophosphate (NaH_2PO_4), sodium phosphate dibasic (Na_2HPO_4), sodium chloride (NaCl), piperazine ($C_4H_{10}N_2$), N,N-Diisopropylethylamine (DIPEA, $C_8H_{19}N$), trifluoroacetic acid (TFA, $C_2HF_3O_2$), thioanisole (C_7H_8S), 3,6-Dioxa-1,8-octanedithiol (DODT, $C_6H_{14}O_2S_2$), 1M hydrochloric acid (HCl), and Zinc atomic absorption standard solution (1000ppm), were purchased from Sigma-Aldrich; N,N-dimethylformamide (DMF), Dichloromethane (DCM), N-methyl-2-pyrrolidinone (NMP), and diethyl ether were purchased from Fisher Scientific; O-Benzotriazole-N,N,N',N'-tetramethyl-uronium-hexafluoro-phosphate (HBTU) and all Fmoc-protected amino acids required for peptide synthesis were purchased from CEM Corporation while the arginine- and cysteine-preloaded Wang resins were obtained from Novabiochem®. All chemicals were used without further treatment. ddH_2O with conductivity less than $1\mu Scm^{-1}$ was used as the solvent for all ZnO synthesis reactions.

4.2.2 Solid Phase Peptide Synthesis (SPPS)

GLHVMHKVAPPR (G-12) and GLHVMHKVAPPR-GGGC (GT-16) were synthesized in house using a microwave-assisted solid phase synthesis apparatus (CEM

Corporation). Wang resins preloaded with Fmoc-protected arginine (for G-12) or Fmoc-protected cysteine (for GT-16) were swelled in equal volumes of DMF and DCM for 20 minutes. Swollen resins were rinsed with DMF before N-terminal deprotection (twice) using piperazine in DMF. Again the resins were thoroughly rinsed with DMF before coupling with the subsequent amino acid. During amino acid coupling, HBTU (in DMF) and DIPEA (in NMP) were used as activator and activator base respectively. The 'deprotection(2x)-rinse-coupling-rinse' step was repeated until all amino acids had been coupled. At the end of the synthesis, the N-terminus of the resin-bound peptide was final-deprotected, rinsed with DCM, and cleaved with a mixture of TFA and scavengers (TFA/Thioanisole/water/DODT solution having v/v% ratio of 91.7/1.0/2.4/4.9). The cleaved peptide was re-precipitated in 100ml chilled diethyl ether, washed three times with chilled diethyl ether prior to lyophilisation at -70°C (Virtis-110 freeze-dryer).

The purity of lyophilised G-12 and GT-16 was determined as 95% and 88% respectively by Dr. David Belton. A peptide solution at 1mg/ml was prepared in 50/50 acetonitrile/water and analysed with a Dionex high performance liquid chromatography equipped with a UV detector (set at 214nm) and a Jupiter 4u Proteo 90A C_{12} Reverse Phase column (Phenomenex). A binary solvent system was used for gradient elution where mobile phase A and B were 5% acetonitrile/95% water/0.1% TFA and 95% acetonitrile/5% water/0.1% TFA respectively. The peptide solutions were eluted with the binary solvent system at a linear gradient of 100% A to 100% B over first 20 minutes, isocratic 100% B for the next 40 minutes, and flow rate of 4ml/min at 25°C. The molecular weights (M_w) of the peptides synthesized were measured by Clare Coveney (Proteomics group, The John Van Geest Cancer Research Centre) using Bruker UltraflexIII TOF/TOF mass spectrometer and analysed with Daltonics flexAnalysis software. The M_w of G-12 and GT-16 were confirmed to be on target where the calculated M_w for G-12 and GT-16 were 1341.6g/mol and 1615.9g/mol respectively while their measured M_w were 1341.7g/mol and 1615.8g/mol respectively.

4.2.3 ZnO synthesis and kinetic studies

100mM $Zn(NO_3)_2 \cdot 6H_2O$, 100mM HMTA, 30mM G-12, and 30mM GT-16 were prepared as stock solutions for this study. Prior to each reaction, equal volumes of $Zn(NO_3)_2 \cdot 6H_2O$ and the HMTA stock solution were mixed and predetermined volumes of G12 or GT-16 stock solutions were added immediately to obtain final [G-12] or [GT-16] of 0mM, 0.03mM, 0.15mM and 0.30mM, respectively. The pH of the solutions prepared were pH 6.9±0.1 regardless of the presence of additives. Prepared solutions incubated at 20°C for 24 hours (±1 minute) were then transferred to a 65°C water bath for another 72 hours (±1 minute).[46] During the course of reaction, samples were taken from the reaction vessels at selected times (±1 minute). The control reaction was performed in triplicate in a single run. Collected samples were centrifuged at 13000rpm for 3 minutes to separate any precipitate from the supernatant. The supernatant was drawn carefully using a pipette and re-centrifuged using the same conditions. Only ~80% of the supernatant was drawn from the vial although no precipitates were observed at the bottom of the vial. This supernatant was used to determine the Zn^{2+} concentration, $[Zn^{2+}]$, using ICP-OES.

The precipitates collected were washed three times with ddH_2O. For each washing, the volume of ddH_2O used was two times the sample volume taken from the reaction vessel. Cleaned precipitates were lyophilised at -70°C using a Virtis-110 freeze-dryer. Selected lyophilised precipitates were characterised using SEM, FTIR, TGA, XRD, and solid phase UV spectrophotometry. Direct measurement of peptide concentration in the supernatant was attempted by UV-VIS spectrometer (at 214nm) and fluorescamine assay. The former was unsuccessful due to $Zn(NO_3)_2$, HMTA, and peptides all absorbing at this wavelength (**Appendix 4.1**). The use of a dilution approach to reduce the concentration (absorbance) of one or more of the adsorbing components was not useful since the peptide concentration in the reaction solution was much lower (and also absorbing more weakly than HMTA) compared to other components. The failure of the fluorescamine assay to quantify peptide concentration in the supernatant was related to the working pH for the fluorescamine assay.[79] The phosphate buffer saline (PBS) used to buffer the peptide calibration samples (~pH 3

without buffer) was found to interact with $Zn(NO_3)_2$ to form immediate precipitates which interfered with the assay.

4.2.4 Peptide adsorption studies

The selective adsorption of G-12 and GT-16 on the (0002) and (10-10) planes of ZnO was studied using ZnO films (~9cm^2) grown on silicon wafers by the atomic layer deposition (ALD) technique. ZnO films were grown by S. Y. Pung (University of Nottingham) using conditions reported.[80] The film crystal orientation is controlled by its deposition temperature: 280°C and 165°C being used for the (0002) and (10-10) planes respectively. The as-grown ZnO films were annealed at 800°C (1 hour) to improve film crystallinity followed by confirmation of crystal orientation by XRD.

For the adsorption test, ZnO films (on silicon wafers), silicon wafers, and glass slides were cleaned with acetone, dried in air, and placed into 12ml peptide solution prepared in PBS (Phosphate buffer saline, 50mM phosphate and 150mM NaCl, pH 7.0). As calculated, the planar zinc atomic density for (0002) and (10-10) plane are 10.94 atoms/nm^3 and 5.91 atoms/nm^3 respectively (**Appendix 4.2**).[81] The peptide solutions contained ca. 5 times the estimated number of Zn atoms present on ZnO films used (Peptide:Zn=5). At predetermined incubation times (t=0, 5 hours), 650µl aliquots were sampled from the peptide solution and dispensed into 2ml vials, followed by the addition of an equal volume of Micro-BCA (Bicinchoninic acid) working reagent into the aliquots. The Micro-BCA working reagent was prepared as per protocols provided by the manufacturer (Thermo Fisher Scientific).

The sample and the Micro-BCA working reagent mixture was incubated in a water bath at 60°C for 1 hour then cooled to room temperature. The absorbance of the cooled solution in a disposable polystyrene cuvette (10mm path length) was measured at 562nm using a Unicam UV2 UV-VIS spectrometer. The net absorbance of the sample was determined by subtracting the absorbance of the blank (PBS only) from the absorbance of the sample. The net absorbance was compared against a series of calibration peptide solutions (0-10.5µM), prepared by the same medium (**Appendix**

4.3). Adsorption tests were performed three times in separate runs. At the end of the adsorption studies, the ZnO films were cleaned with ddH_2O and air-dried at room temperature. The first ten to twenty atomic layers of the ZnO films were analysed by XPS using a Kratos AXIS ULTRA with a monochromated Al-K_α X-rays source (1486.6eV) operated at 10mA emission current and 10kV anode potential (100W). The pressure of the analysis chamber was $3x10^{-9}$ torr. A wide scan (10 minutes) and high resolution scans (10, 5, 20 and 5 minutes for Zn, O, N, and C respectively) were performed on each sample where the latter was charge-corrected to the main C1s peak of hydrocarbon (285eV) and then quantified to compare the amounts of relevant element present, using Kratos sensitivity factors. The pass energy for wide scan and high resolution scan were 80eV and 20eV respectively. Fresh ZnO films (not exposed to peptide solution), G-12, and GT-16 were also analysed and used as references.

4.2.5 X-Ray Diffraction (XRD)

The lyophilised precipitates were ground (if necessary) before packing into an aluminium sample holder, scanned for 2θ from 5° to 70° using a PANalytical X'Pert PRO X-Ray diffractometer ($CuK_{\alpha 1}$ radiation with wavelength of 1.54056Å.) at 45kV accelerating voltage, 40mA filament current, and using scan speed of 0.02°/s at room temperature. Diffraction patterns were analysed using X'Pert-HighScore Plus (Version 2.0a) programme for diffractogram manipulation, background determination and peak identification.

4.2.6 Scanning Electron Microscopy (SEM) and ZnO crystal dimension studies

The morphology of ZnO crystals was examined using a SEM (JEOL JSM-840A) at an accelerating voltage of 20kV. Lyophilised precipitates were redispersed in ethanol by sonication (15 minutes) before dispensing onto aluminium sample holders, air-drying then gold-coating (Edwards S150B sputter coater; argon plasma at 1.2kV, 4mbar pressure, 2.5 minutes). The dimensions of ZnO crystals obtained from SEM images

were measured using ImageJ 1.37v software.[82] A minimum of 50 ZnO crystals were measured from samples obtained after 48 hours and 25 hours. However, due to overlapping of the ZnO crystals, only 30 ZnO crystals were suitable for both length and diameter measurements from the 25 hours precipitate formed in the presence of 0.30mM of G-12. A single length measurement was performed for each measurable crystal due to high length uniformity. The diameter of each (measurable) crystal was determined from the average of their maximum and minimum diameters. The aspect ratio (L/D_{Avg}=length/average diameter) of individual crystals was also calculated. 95% CI of crystal length, average diameter and aspect ratio was calculated for comparison.

4.2.7 Fourier Transform Infrared Spectroscopy (FTIR)

FTIR was used to detect the presence of ZnO and non-ZnO components, such as peptide, in lyophilised precipitates. 1mg of sample and 199mg of KBr was ground and pressed into a transparent disk (10 tons weight for 6 minutes) before analysing using a Nicolet Magna IR-750 Fourier Transform Infrared Spectrometer (256 scans at $2cm^{-1}$ resolution). A pure KBr disk was scanned as a background before scanning each prepared disk.

4.2.8 Thermogravimetric Analysis (TGA)

A Mettler Toledo TGA/SDTA 851^e was used to determine the amount of non-ZnO components in the precipitates collected. Samples were heated at 10°/min from 30°C to 900°C in air to ensure complete combustion of all organic material.

4.2.9 Inductively Coupled Plasma-Optical Emission Spectroscopy (ICP-OES)

A Perkin Elmer Inductively Coupled Plasma Optical Emission Spectrometer Optima 2100DV was used to quantify $[Zn^{2+}]$ remained in the supernatant at different reaction time. At predetermined times, 100µl aliquots of supernatant were drawn and added to

9.9ml of acidified ddH_2O, prepared with a known volume of 1M HCl. For each acidified sample prepared, three aliquots were analysed and the average value was used for the determination of [Zn^{2+}] in the samples based on a [Zn^{2+}] calibration curve. The [Zn^{2+}] calibration curve was obtained from the measurement of a set of standard solutions of Zn^{2+} with known concentrations, prepared in triplicate. Since the Blank (without additive) reaction was performed in triplicate (single run), the average and standard deviation of [Zn^{2+}] at different reaction times for the Blank was calculated. The standard deviation value of [Zn^{2+}] was presented as error bars in the [Zn^{2+}] vs time plot.

4.2.10 Molecular dynamics (MD) and Adsorption Locator (AL)

A MD simulation tool, GROMACS,[83] was used to determine the stable configurations of G-12 and GT-16 in water computationally. The energy of the peptides was minimised in explicit single point charge (SPC) water at 300K with a time step of 2fs and total time of 2ns using the OPLS-AA-(L)-all atom force field. The visualisation of the stable molecular configurations was achieved using 1.8.6 VMD software.[84] VMD software also allowed comparison of G-12 and GT-16 stable configurations by using the multiseg VMD extension. Using the stable configurations obtained from MD simulations, the interactions of G-12 and GT-16 with the (0002) and (10-10) planes of ZnO was studied using the Materials Studio®4.3 AL module based on the Metropolis Monte Carlo algorithm.[85] The adsorption modes and adsorption energies of G-12 and GT-16 on these ZnO planes were studied and the segments/moieties of peptides responsible for adsorption were identified. The computational work was performed by Dr. Olivier Deschaume.

4.2.11 Solid State Ultraviolet-Visible (UV-Vis) Spectroscopy

The optical properties of the lyophilised precipitates collected in the presence of G-12 or GT-16 was studied using JASCO V-670 spectrophotometer. The UV emission of the precipitates was studied from a wavelength of 200nm to 1000nm using a scan speed of

400nm/min. The UV-Vis and Near-IR band width were 5nm and 20nm respectively while data pitch was 1.0nm. The direct bandgap (E_g) of these samples were determined.

4.3 Results and Discussion

4.3.1 Anisotropic growth of ZnO in $Zn(NO_3)_2$-HMTA reaction at 65°C

ZnO crystallises in the hexagonal wurtzite structure with space group $P6_3mc$. The absence of a centre of inversion in the wurtzite structure results in ZnO having inherent asymmetry along its *c*-axis.[1] In order to understand the effect(s) of ZnO-BPs on ZnO formation, the $Zn(NO_3)_2$-HMTA reaction in the absence of ZnO-BPs was thoroughly studied and the crystals formed were carefully characterised. A small quantity of gel-like precipitate was formed after 24 hours incubation at 20°C. FTIR (**Figure 4.1a-c**) and XRD (**Figure 4.2a**) analyses confirmed that the gel-like precipitate collected was neither ZnO nor pure $Zn(NO_3)_2 \cdot 6H_2O$ (**Appendix 4.4**).

As shown in **Figure 4.1c**, the ZnO stretching mode typically in the 430-550cm^{-1} region was absent from the spectrum of the gel-like precipitate, while a broad and strong water band centred at 3408cm^{-1} was observed. Three absorption peaks from this intermediate compound, 1384cm^{-1} (marked with asterisk in **Figure 4.1c**), 1351cm^{-1}, and 830cm^{-1}, coincided with strong peaks observed from $Zn(NO_3)_2 \cdot 6H_2O$ (**Figure 4.1b**) at 1391cm^{-1}, 1355cm^{-1} and 829cm^{-1}, assignable to the asymmetric stretching and bending of NO_3^- respectively.[44, 55, 86, 87] The absence of the C–N tertiary amine absorption peak of HMTA at 1006cm^{-1} (**Figure 4.1a**) from the intermediate compound suggested that HMTA remained soluble at 20°C.

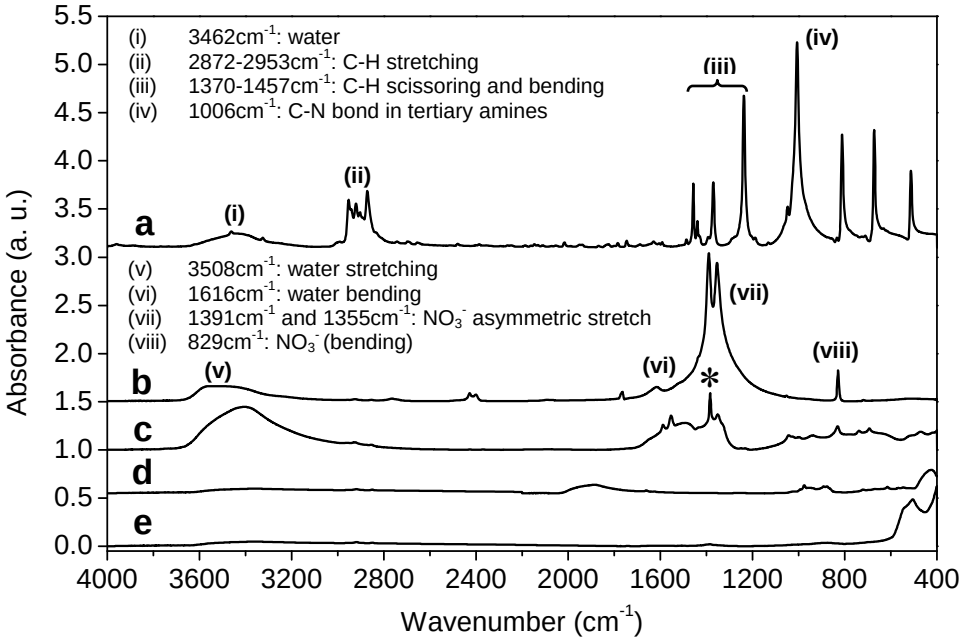

Figure 4.1 FTIR-KBr of (a) HMTA, (b) $Zn(NO_3)_2{\cdot}6H_2O$, and precipitates collected from the control reaction (without additive) after (c) 24 hours ($t_{20°C}$=24hr), (d) 25 hours ($t_{20°C}$=24hr, $t_{65°C}$=1hr), and (e) 48 hours ($t_{20°C}$=24hr, $t_{65°C}$=24hr).

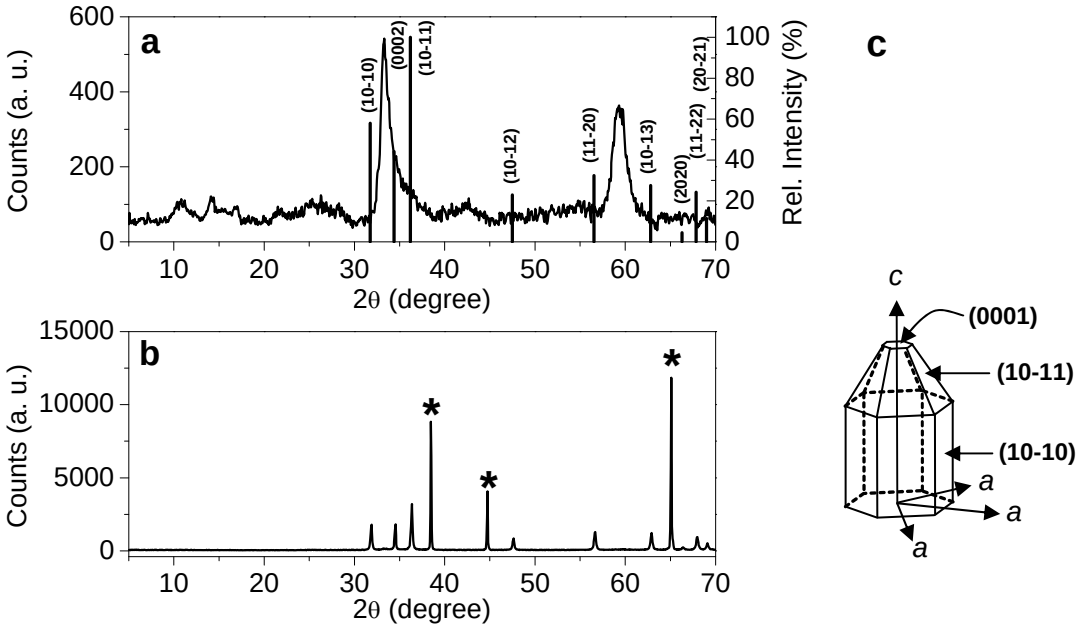

Figure 4.2 X-ray diffraction pattern of precipitates collected from the control reaction (without additive) after (a) 24hours ($t_{20°C}$=24hr), (b) 25 hours ($t_{20°C}$=24hr, $t_{65°C}$=1hr), and (c) representation of low index planes and axes of ZnO crystal. Stick plot in (a) shows the diffraction pattern of wurtzite ZnO while the diffraction peaks from the aluminium holder are marked with asterisks in (b).

When the reaction temperature was increased to 65°C for a duration of one hour ($t_{20°C}$=24hr, $t_{65°C}$=1hr), all diffraction peaks from the precipitate (**Figure 4.2b**) can be indexed to wurtzite structure of ZnO[88] (**Appendix 4.5**) except for peaks at 38.47°, 44.72°, and 64.93° (marked with asterisks) arising from the aluminium sample holder used. The lattice parameters, *a* and *c*, for this sample were 3.237Å and 5.1872Å respectively hence the axial *c*/*a* ratio was 1.602, in good agreement with published data (*a*=3.2489Å and *c*=5.2053Å, *c*/*a*=1.602)[88]. No impurity was observed in the diffractogram indicating that ZnO was the only crystalline phase present. Although FTIR detected the presence of impurities besides ZnO from the 25 hours-precipitate (**Figure 4.1d**), the impurity diminished as the reaction was extended to 48 hours ($t_{20°C}$=24hr, $t_{65°C}$=24hr) (**Figure 4.1e**). The detection of ZnO in the early stages of ZnO growth implies that ZnO formation occurred as early as 1 hour after the adjustment of reaction temperature from 20°C to 65°C.

The growth of ZnO at 65°C as a function of time was studied using SEM and the measurement of the [Zn^{2+}] in solution. Although no turbidity was observed after up to 2 hours of incubation at 20°C, a 5~10% reduction of [Zn^{2+}] was detected after 30 minutes (first data point in **Figure 4.3a**) which remained stable up to 24 hours. When the temperature of the reaction studied was adjusted to 65°C, Zn^{2+} was consumed steadily before equilibrium was reached after 168hr ($t_{20°C}$=24hr, $t_{65°C}$=144hr) where 39.7±1.3% Zn^{2+} was left in the reaction solution. The change in the percentage of Zn^{2+} reacted with time also suggested that ZnO formation occurred only when reaction temperature was increased to 65°C however the driving force of the reaction remained debatable. Two mutually exclusive roles of HMTA in ZnO formation have been proposed in the literature. Some researchers claim that the thermal dissociation of HMTA could provided OH^- for the dehydration of $Zn(OH)_4^{2-}$ to form ZnO,[89] while one team showed that the dissociation of HMTA would not occur at 65°C (by FTIR) hence HMTA did not supply OH^- but was responsible for the anisotropic growth of ZnO by its adsorption onto the (10-10) plane of ZnO.[90]

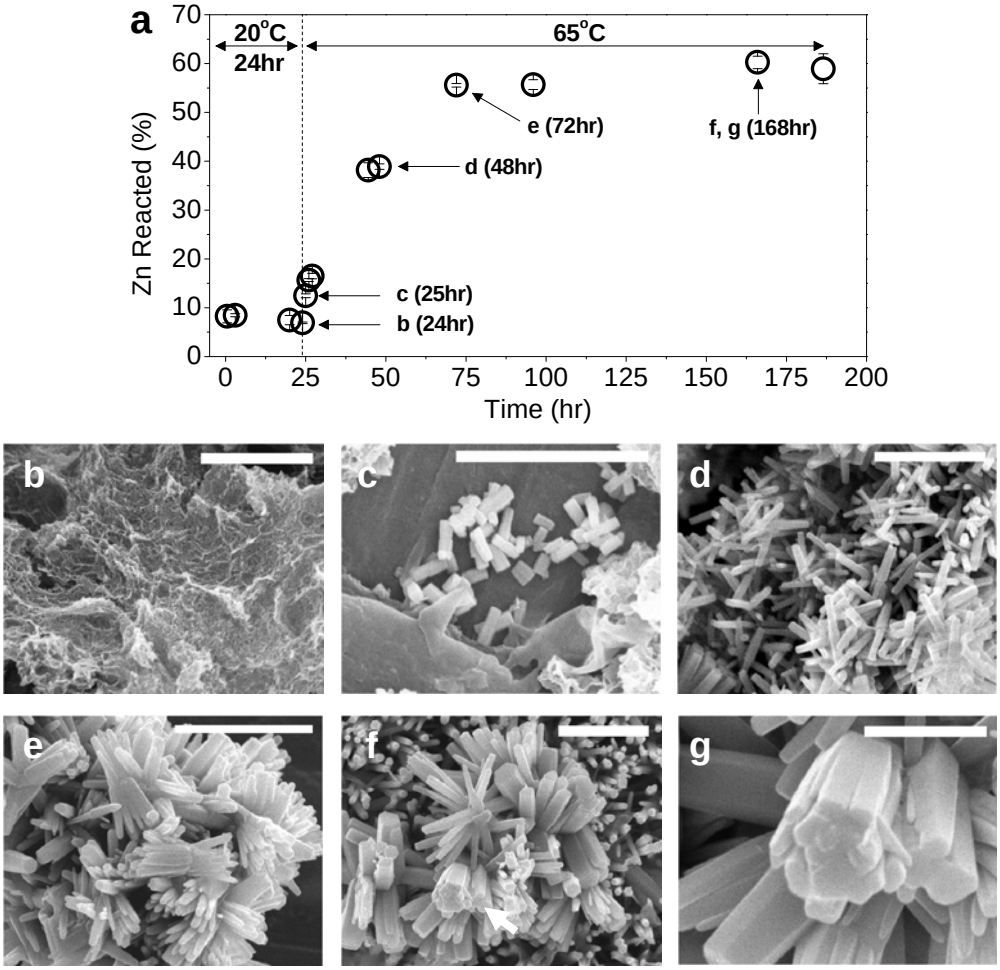

Figure 4.3 (a) Percentage of Zn^{2+} consumed as a function of reaction time and SEM images for precipitates collected from control reaction after (b) 24 hour ($t_{20°C}$=24hr), (c) 25 hour ($t_{20°C}$=24hr, $t_{65°C}$=1hr), (d) 48 hours ($t_{20°C}$=24hr, $t_{65°C}$=24hr), (e) 72 hours ($t_{20°C}$=24hr, $t_{65°C}$=48hr), (f) 168 ($t_{20°C}$=24hr, $t_{65°C}$=144hr) hours, and (g) is the higher magnification of white arrow-pointed region of (h). Scale bars: 5μm for (b-f) and 2μm for (g). Standard deviation bars in (a) were obtained from 3 samples.

From the morphology study, the non-ZnO gel-like precipitate appeared to be continuous sheets with rough-surfaces (**Figure 4.3b**), similar to layered basic zinc acetate (LBZA) formed in the $Zn(CH_3COO)_2$-NaOH reaction at 25°C with $[OH^-]/[Zn^{2+}]<2$ (**Appendix 4.6**). Hexagonal ZnO rods with aspect ratio (L/D_{Avg}) of ~2.7 and the rough-surfaced continuous sheets were both present in the precipitate collected after 25 hours ($t_{20°C}$=24hr, $t_{65°C}$=1hr) (**Figure 4.3c**). However at 48 hours ($t_{20°C}$=24hr, $t_{65°C}$=24hr), only hexagonal ZnO rods with L/D_{Avg}~11.4 were seen (**Figure 4.3d**). This drastic increase of L/D_{Avg} from the extension of reaction from 25 to 48 hours implied an anisotropic growth of ZnO along its *c*-axis. As reaction was prolonged to ≥72 hours

($t_{20°C}$=24hr, $t_{65°C}$=48hr), large numbers of ZnO rods attached to each other along their *c*-axes forming rod bundles were observed (**Figure 4.3e-g)**. The oriented attachment of ZnO rods in a coplanar manner via the (10-10) plane has also been described in other reports however the cause of this which is reaction-dependent, is still debated.[39, 90-94] According to Li *et al*.[93], the oriented attachment of ZnO crystals is driven by surface energy reduction while Sugunan *et al*.[90] and Wang *et al*.[95] suggest HMTA-driven oriented attachment. The formation of ZnO rods bundles at ≥72 hours has rendered the accurate determination of crystal aspect ratio impossible.

In short, ZnO crystals were found to grow anisotropically from the $Zn(NO_3)_2$-HMTA reaction, producing slightly tapered hexagonal ZnO rods (L/D_{Avg}~11.4 after 48 hours ($t_{20°C}$=24hr, $t_{65°C}$=24hr)) as opposed to bipyramidal hexagonal crystals showed by Tomczak *et al*..[46] ZnO crystal formation did not start during the room temperature incubation period as confirmed by the high and stable [Zn^{2+}] in solution (**Figure 4.3a**) and non-detection of ZnO by FTIR (**Figure 4.1**), XRD (**Figure 4.2a**), and SEM (**Figure 4.2b**). The formation of ZnO occurred as early as one hour ($t_{20°C}$=24hr, $t_{65°C}$=1hr) after the elevation of reaction temperature to 65°C while extensive oriented attachment was observed when reaction was prolonged to 72 hours ($t_{20°C}$=24hr, $t_{65°C}$=48hr). At equilibrium, ~20mM of Zn^{2+} (40% of 50mM) remained in the reaction solution. The $Zn(NO_3)_2$-HMTA reaction is not a perfect system for the study of ZnO-BP effects on ZnO formation because HMTA may interfere with the adsorption of ZnO-BPs on ZnO crystals, and affect the quantification of ZnO-BP concentration in the course of reaction. However, the effect of GT-16 on ZnO aspect ratio reduction reported by Tomczak *et al*.,[46] which suggested adsorption-driven morphology tuning by GT-16, makes the system an interesting one to explore. Furthermore the effect of HMTA adsorption, if present, can be taken care of by careful comparison of results obtained in the absence and presence of additives.

4.3.2 Reduction of ZnO aspect ratio by G-12 and GT-16

GT-16 was derived from G-12 by the addition of a GGGC-tag at its C-terminus. In the presence of G-12 and GT-16, ZnO was detected after 25 hours ($t_{20°C}$=24hr, $t_{65°C}$=1hr)

(**Figure 4.4**) and beyond (**Appendix 4.7**) by XRD. The addition of these peptides into $Zn(NO_3)_2$-HMTA reaction also did not alter the Zn^{2+} consumption rate with respect to the control (**Figure 4.5**) throughout the 7 day study. Therefore the presence of G-12 and GT-16 did not alter the $[Zn^{2+}]$ at equilibrium.

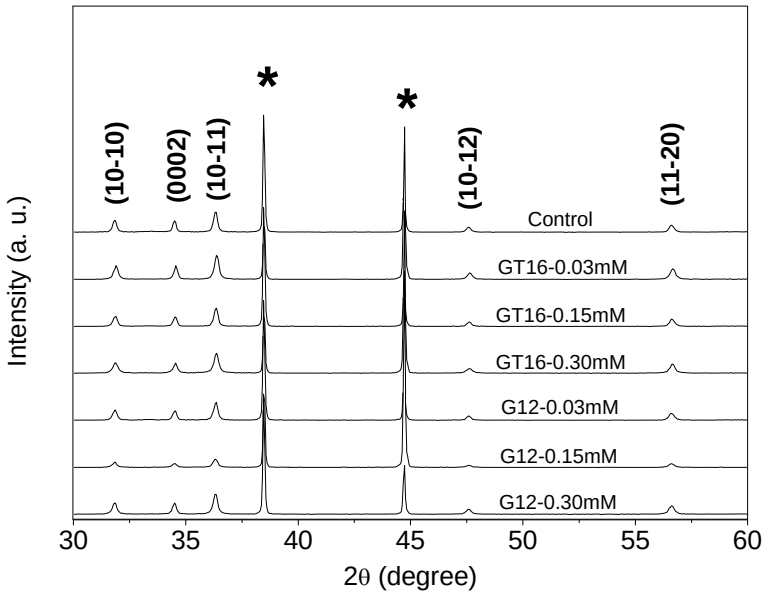

Figure 4.4 XRD patterns of ZnO formed after 25 hours ($t_{20°C}$=24hr, $t_{65°C}$=1hr) in the presence and absence of different concentrations of GT-16 and G-12. The diffraction peaks from the aluminium sample holder are marked with asterisks.

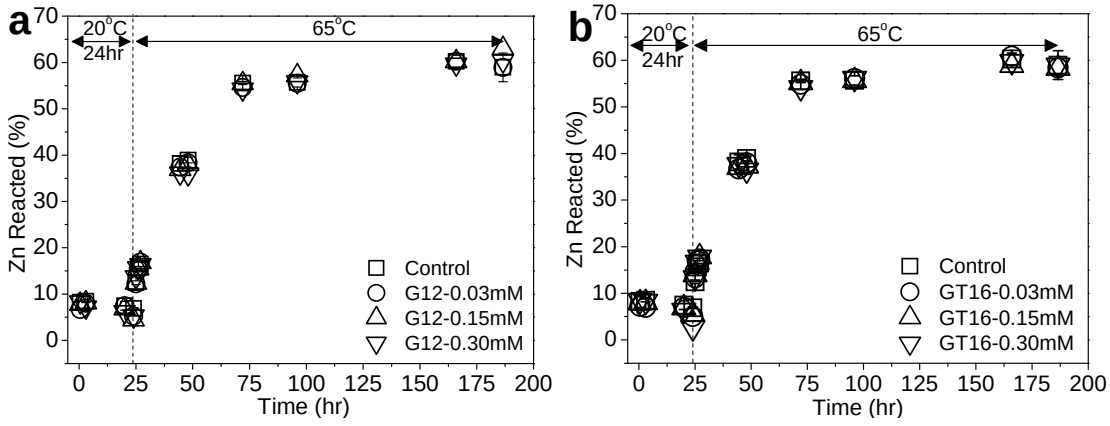

Figure 4.5 The percentage of Zn^{2+} reacted as a function of reaction time for (a) G-12-added reactions and (b) GT-16-added reactions. The standard deviation for the control was based on three samples.

The modification of morphology by G-12 and GT-16 was studied using SEM. As reported by Tomczak *et al*.,[70] the aspect ratio reduction of ZnO crystals as a function of peptide concentration was observed (**Figure 4.6a**). The SEM images for precipitates from G-12 and GT-16 added reactions are shown in **Figure 4.6b-g**.

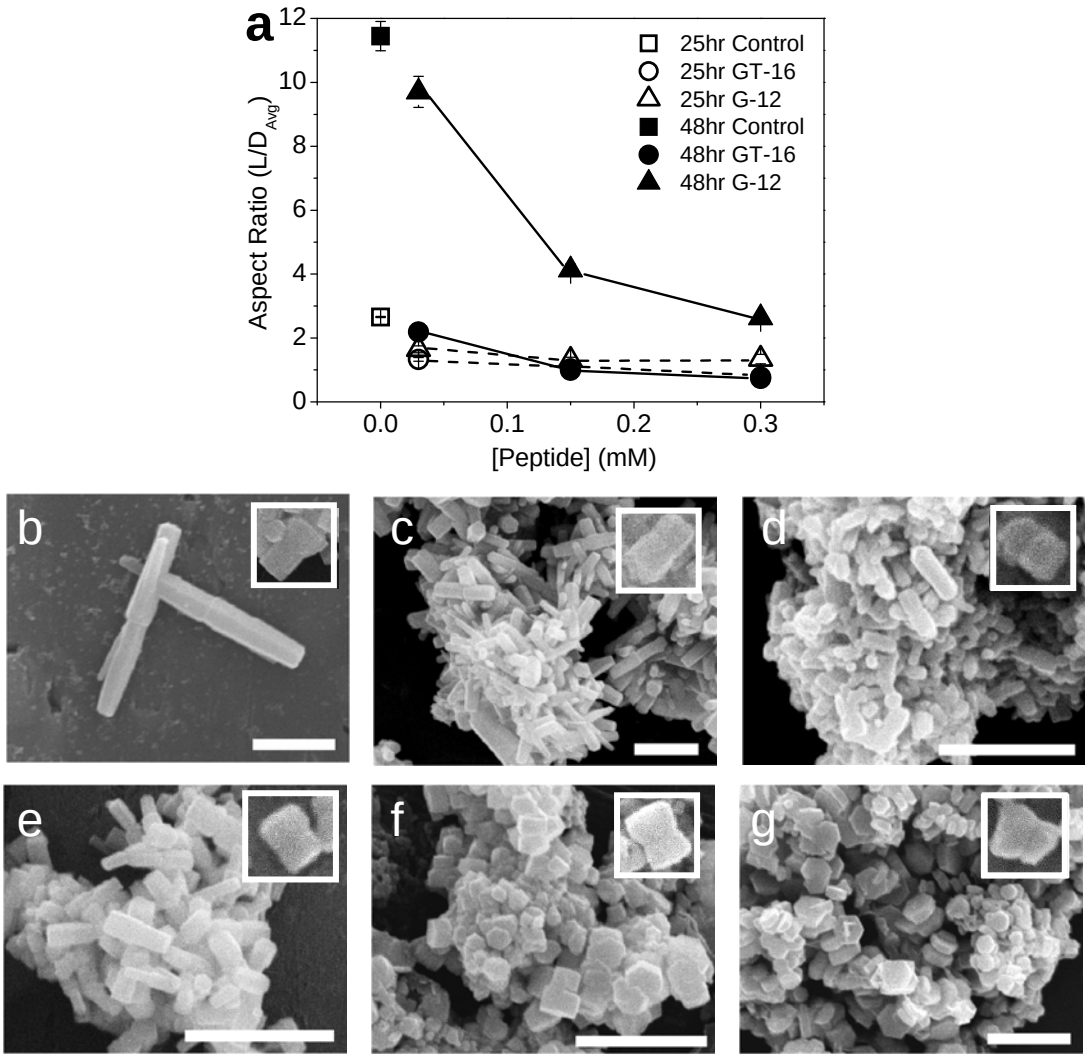

Figure 4.6 (a) The average and 95% CI of ZnO aspect ratio (L/D_{Avg}) as a function of peptide concentration, and ZnO crystals formed in the presence of G-12 (b-d) or GT-16 (e-g) after 48 hours ($t_{20°C}$=24hr, $t_{65°C}$=24hr) with peptide concentrations of 0.03mM (b and e), 0.15mM (c and f), and 0.30mM (d and g). The scale bars shown are 2μm and the insets are ZnO crystals formed after 25 hours ($t_{20°C}$=24hr, $t_{65°C}$=1hr).

At 25 hours ($t_{20°C}$=24hr, $t_{65°C}$=1hr), the L/D_{Avg} for all peptide-added reactions was 1.0~1.7 compared to 2.7 for the control reaction, **Figure 4.6a**. When reaction was extended to 48 hours ($t_{20°C}$=24hr, $t_{65°C}$=24hr), the L/D_{Avg} of crystals formed in the

presence of the peptides reduced drastically. Thus the difference of the L/D_{Avg} values between the control reaction and peptide-added reactions was increased. Apparently, in the presence of G-12 and GT-16, the reduction of ZnO crystal aspect ratio has started from the early stage of crystal formation. Although the L/D_{Avg} values of GT-16 and G-12 were comparable at 25 hours, GT-16 showed a more prominent effect on the aspect ratio after 48 hours (L/D_{Avg}: 0.7~2.2 for GT-16, 2.6~9.7 for G-12, and ~11.4 for control). GT-16 was able to induce a greater extent of reduction even with the lowest dose of GT-16 (0.03mM). The reduction of aspect ratio implied that G-12 and GT-16 were able to reduce the *c*-axis/*a*-axes relative growth rate of the crystals, tuning the crystal morphology from hexagonal rods to hexagonal plates.

4.3.3 Incorporation of G-12 and GT-16 with ZnO precipitates

Rationally, organic additives that tune crystal morphology via adsorption/templating should be detectable in/on the precipitate if the collection procedures did not involve the use of high temperature. The characteristic ZnO peaks at 450-550cm^{-1} region, amide-I band (1600-1700cm^{-1}), amide-II band (1500-1600cm^{-1}), and asymmetric stretching of NO_3^- at 1384cm^{-1} were detected by FTIR from precipitates produced in the presence of peptides. Since all precipitates were washed thoroughly before lyophilisation, the results thus confirmed that peptides and nitrate have strongly adsorbed on or are well entrained in the precipitates collected (**Figure 4.7**).

A peak area analysis was performed to obtain more insights about the co-precipitation of peptide with ZnO. As shown in **Figure 4.8a**, the normalised area under the amide bands (with respect to the control) which represents the amount of peptide present, was strongly correlated with peptide concentration, further confirming the incorporation of peptides. A blue-shift of amide-I band from the precipitates relative to pure peptides was observed (**Table 4.1**), likely to be due to the absorption of peptides on the crystal surface which altered the energy of vibration.[96] Besides the band shifts, a new peak at 1590-1594cm^{-1} (not seen from pure peptides or ZnO from the blank) appeared in the spectra of precipitates from the peptide-added reactions. Its presence can be associated with the ν_{as}(bound COO^-) from the C-terminus, the only COOH-group present in the

peptides.[40, 97] The absence of tertiary amine adsorption peak (~1006cm^{-1}) suggested the absence of HMTA from precipitates.

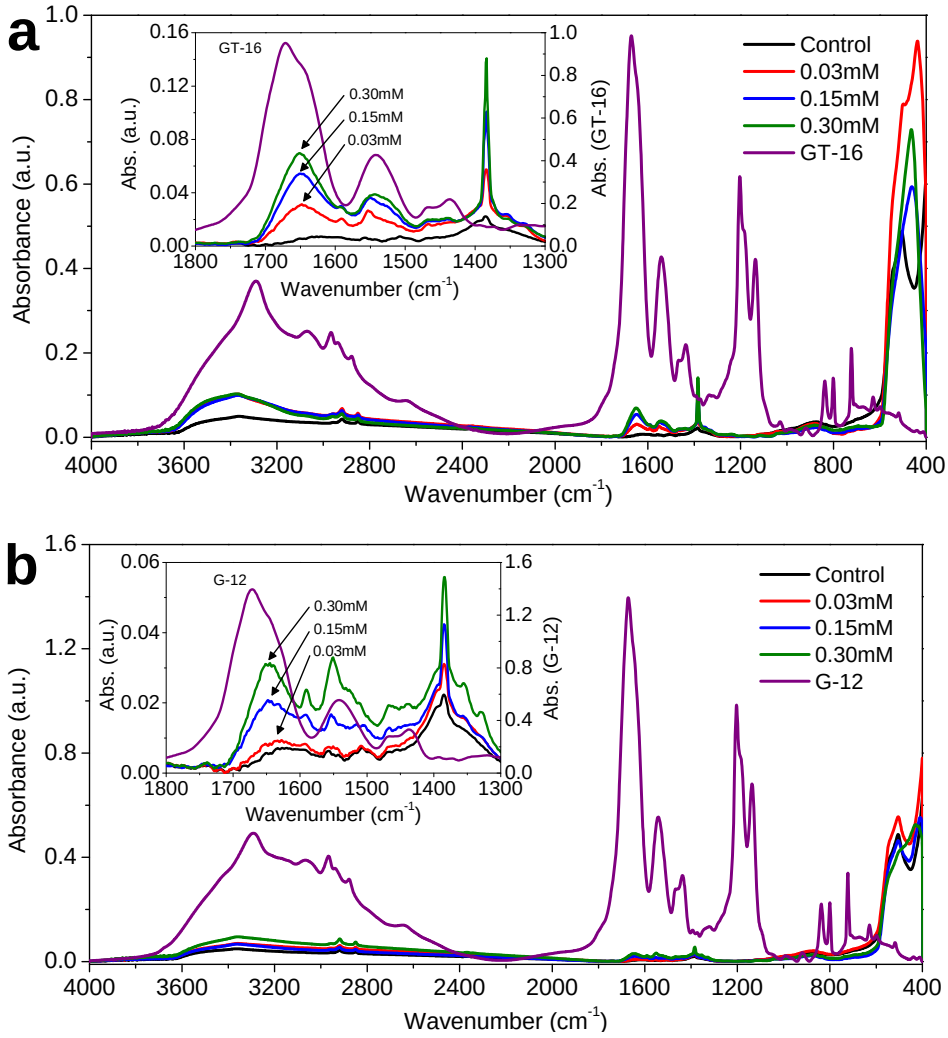

Figure 4.7 FTIR spectra of precipitates obtained after 48 hours ($t_{20°C}$=24hr, $t_{65°C}$=24hr) from (a) GT-16-added reactions, the control, and pure GT-16, and (b) G-12-added reactions, the control, and pure G-12.

Table 4.1 Amide-I and amide-II bands from precipitates produced in the presence of GT-16 and G-12 (48hours).

Sample	**Wavenumber (cm^{-1})**		
	Amide-I	----------	**Amide-II**
GT-16	1671.5	-	1542.4
Precipitates from 0.03mM GT-16	1648.1	1591.3	1553.3
Precipitates from 0.15mM GT-16	1650.5	1592.4	1550.4
Precipitates from 0.30mM GT-16	1651.4	1593.6	1543.2
G-12	1671.7	-	1541.9
Precipitates from 0.03mM G-12	1635.7	1593.4	1558.5
Precipitates from 0.15mM G-12	1647.9	1591.8	1553.6
Precipitates from 0.30mM G-12	1645.4	1590.6	1550.7

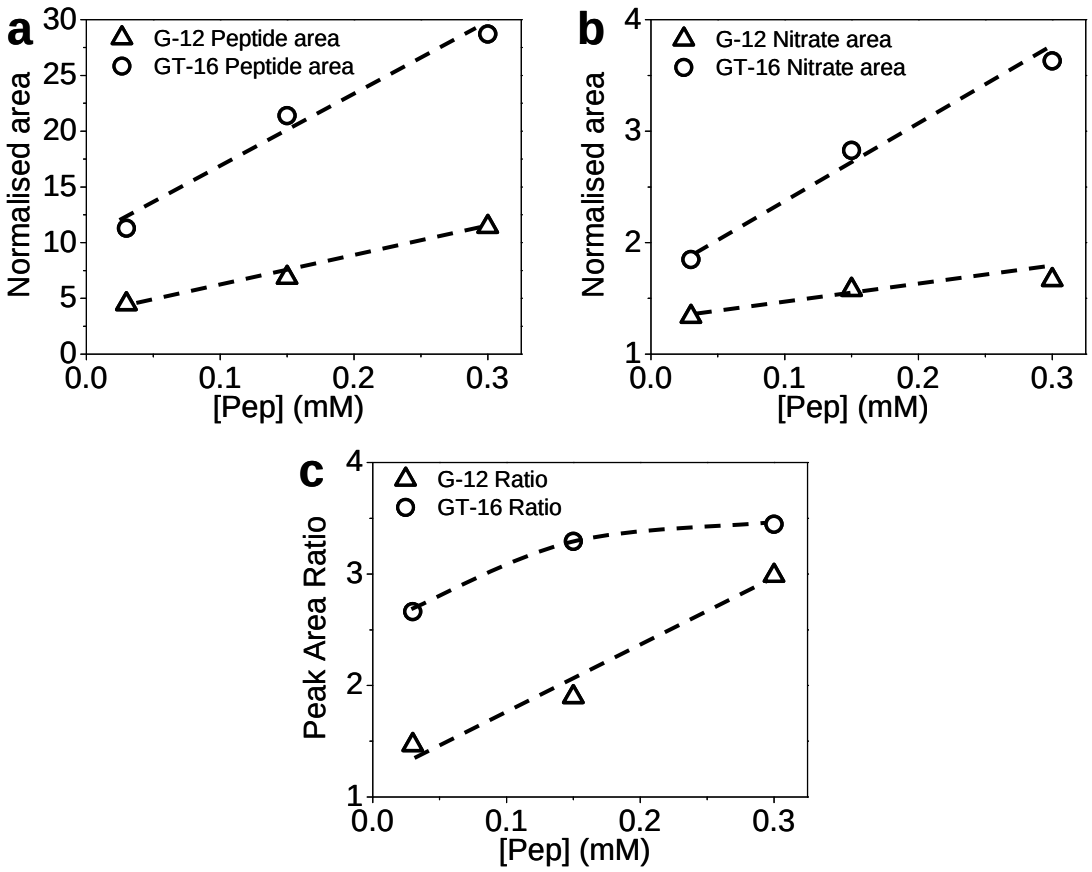

Figure 4.8 FTIR normalised peak area (with respect to the control) for spectra in **Figure 4.7** (48-hour precipitates) for: (a) peptide absorbing region (amide-I and amide-II bands) and (b) NO_3^- absorption peak at 1384cm^{-1}. Peptide and NO_3^- regions were taken from 1480-1730cm^{-1} and 1360-1427cm^{-1} respectively. (c) Peak area ratio of amide-I and amide-II bands to NO_3^- (1384cm^{-1}).

A very sharp adsorption peak at 1384cm^{-1} was identified in all precipitates including the control (insets of **Figure 4.7**), and the gel-like compound produced after 24 hours ($t_{20°C}$=24hr) from the Blank (**Figure 4.1c**). The normalised area of this peak corresponding to the asymmetric stretching of NO_3^-,[44, 55, 86, 87] appeared much stronger than the control and increased linearly as a function of peptide concentration, **Figure 4.8b**. This suggests that NO_3^- may have formed a complex with, possibly, the cationic moieties of the peptide and co-precipitated with ZnO when peptides adsorbed on ZnO surfaces. A non-constant peak area ratio of amide-I and II bands to NO_3^- (1384cm^{-1}) calculated from FTIR spectra suggests that not all cationic moieties of each peptide molecule have reacted with NO_3^-, **Figure 4.8c**.

According to the residue side chain pK_a values calculated using Marvin,[98] G_1, H_3 and K_7 residues of both G-12 and GT-16 are expected to be cationic (>50% protonated) at pH 6.9±0.1 (**Appendix 4.8**) thus the formation of peptide-nitrate salts is possible. Although the co-precipitation of NO_3^- with ZnO has been reported in literature,[55, 87] the insignificance of NO_3^- interacting with Zn^{2+} on (0002) plane in this study was shown by the low peak absorbance at 1384cm^{-1} for the control. Considering the fact that these peptides were able to modify ZnO morphology, it would appear plausible that the peptide-nitrate salt which probably formed during the incubation period (24 hours, 20°C) adsorbed on the surfaces of ZnO crystals (formed at 65°C) before being collected during sampling.

Using TGA, the co-precipitation of peptide with ZnO was again substantiated. Based on the TGA curves of ZnO precipitates and peptides (**Appendix 4.9**), the component weight losses was assigned as follows: (i) 30-100°C, the release of physisorbed water, (ii) 100-200°C, the removal of chemisorbed water, and (iii) 200-600°C, decomposition of organic phase. Precipitates obtained from the control experiment after 48 hours ($t_{20°C}$=24hr, $t_{65°C}$=24hr) have shown an organic phase weight loss of 1.96±0.17wt% (**Figure 4.9**). The organic weight loss percentage of 48 hour-precipitates from peptide-added reactions was significantly higher than the control, and the weight loss percentage increases with peptide concentration. Furthermore, the organic fraction of precipitates from reactions with GT-16 was higher than those with G-12. Due to the lower M_w of NO_3^- (62g/mol) compared to the M_w of G-12 (1341.64g/mol) and GT-16 (1615.93g/mol), the presence of NO_3^- as part of the organic component in the precipitate would not alter the trend showed in **Figure 4.9** significantly. Assuming every peptide molecule would form complexes with three NO_3^- as suggested by the calculated pK_a values of side chain functionalities, the organic weight loss contributed by NO_3^- would be 12.2% and 10.3% for G-12 and GT-16 respectively.

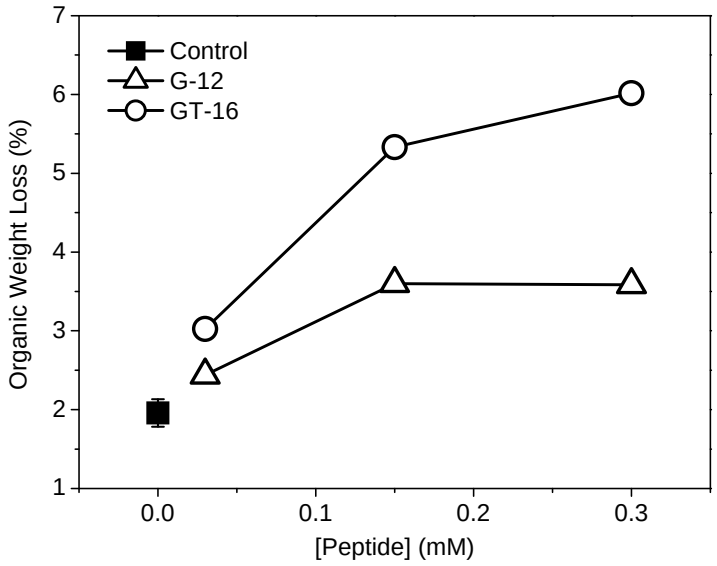

Figure 4.9 Weight loss attributed to the loss of organic component from precipitates obtained after 48 hours ($t_{20°C}$=24hr, $t_{65°C}$=24hr) of reaction where the standard deviation (error bar) for the control (0mM peptide) was obtained from three sets of blanks.

GT-16 which induced a greater extent of crystal aspect ratio reduction had a higher organic weight fraction in its corresponding precipitates, which may imply more adsorbed peptide molecules. Therefore, the number of moles of "co-precipitated" peptides was estimated from the net organic weight loss (excluded organic weight loss from the control) and by considering weight loss caused by NO_3^- as 12.2% and 10.3% for G-12 and GT-16 respectively. It was found that for a comparable added amount (in moles), more GT-16 molecules were adsorbed compared to G-12 (**Figure 4.10a**) and peptide added was in excess for both peptides and for the range of peptide concentration studied, **Figure 4.10b**. The weight loss attributed to physisorbed and chemisorbed water was less than 0.7% for all samples (**Appendix 4.10**).

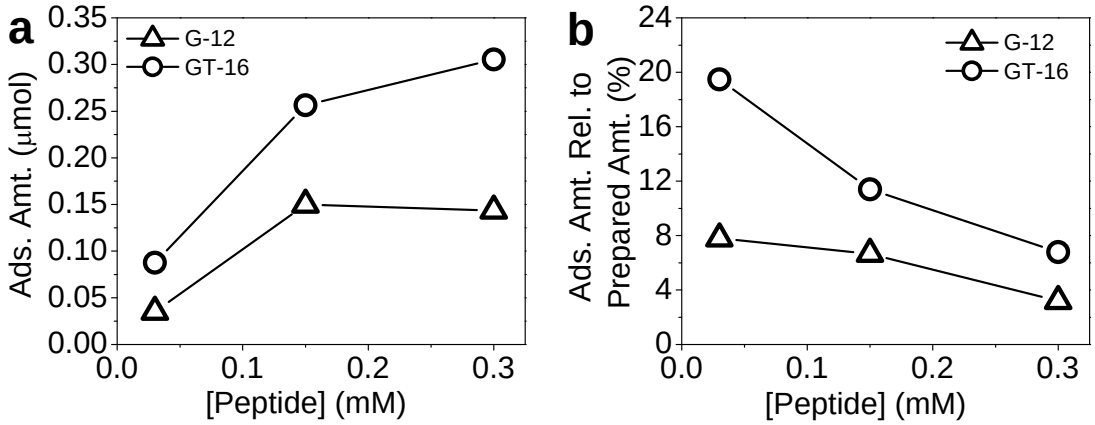

Figure 4.10 The estimated (a) amount of peptide co-precipitated with ZnO from a 15ml reaction solution, and (b) percentage of the amount of adsorbed peptide with respect to the added amount. Estimation was based on TGA data and assuming every molecule of peptide interacts with three NO_3^-.

4.3.4 ZnO growth rate modification by G-12 and GT-16

While reducing the relative growth rate between the *c*-axis and the *a*-axes of ZnO crystals, G-12 and GT-16 were incorporated into the ZnO precipitates formed. In order to understand how ZnO growth has been affected and how the additional GGGC-tag of GT-16 has enhanced the aspect ratio reduction; the growth rates of individual crystal dimensions were calculated and plotted as a function of peptide concentration, namely $\Delta L/\Delta t$ for length along the *c*-axis and $\Delta D_{Avg}/\Delta t$ for the average diameter along the *a*-axes (**Figure 4.11**).

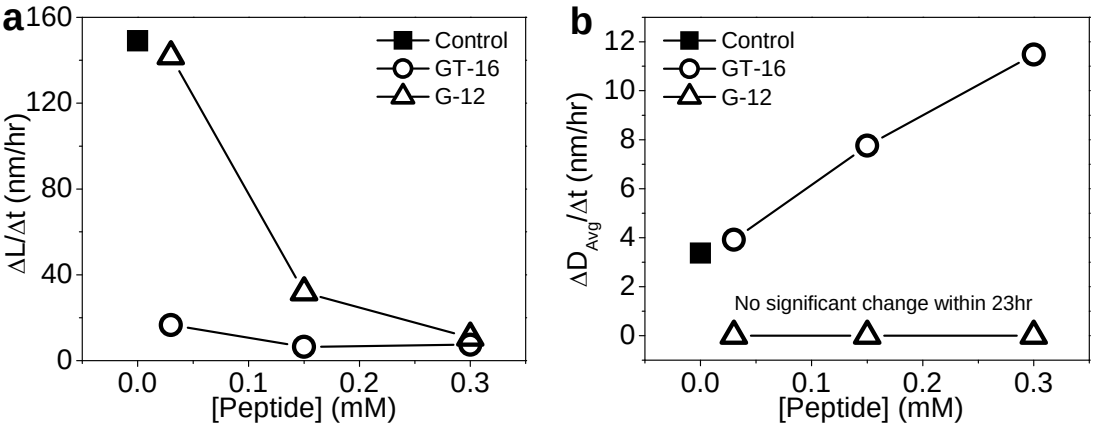

Figure 4.11 The growth rate of (a) length ($\Delta L/\Delta t$) and (b) average diameter ($\Delta D_{Avg}/\Delta t$) of ZnO crystals within 23 hours at 65°C; from 25 hours ($t_{20°C}$=24hr, $t_{65°C}$=1hr) to 48 hours ($t_{20°C}$=24hr, $t_{65°C}$=24hr) of reaction.

In the absence of peptide, $\Delta L/\Delta t$ and $\Delta D_{Avg}/\Delta t$ were 149nm/hr and 3.4nm/hr respectively. The addition of 0.03mM G-12 reduced the $\Delta L/\Delta t$ to 142nm/hr, a reduction of 4.7% relative to the control. A further increase of G-12 concentration resulted in a further reduction of the $\Delta L/\Delta t$ value to 31.8nm/hr (78.7% reduction) and 10.7nm/hr (92.8% reduction) for 0.15mM and 0.30mM G-12 addition respectively. Compared to G-12, the suppression of the growth of length by GT-16 was greater, with ca. 89% reduction ($\Delta L/\Delta t$=16.6nm/hr) being observed even for the lowest GT-16 concentration. At the highest amount of GT-16 addition (0.30mM), the $\Delta L/\Delta t$ was only 7.4nm/hr (95% reduction). Although the overall reduction of $\Delta L/\Delta t$ was more drastic for GT-16, the $\Delta L/\Delta t$ value for G-12 and GT-16 were comparable at 0.30mM. The growth suppression along the *c*-axis would normally enhance the growth of other planes/axes. This was clearly demonstrated by the linearly increasing $\Delta D_{Avg}/\Delta t$ as a function of GT-16 concentration (circles in **Figure 4.11b**). However, in the presence of G-12, D_{Avg} remained unchanged within the 23 hours of this study regardless of G-12 concentration added (triangles in **Figure 4.11b**). It is notable that the D_{Avg} of ZnO crystals formed in the presence of G-12>0.03mM were comparable with the D_{Avg} of ZnO crystals from the control reaction at 25 hours.

In many instances where capping agents such as DBCP,[22-25] citrate ions,[19, 20, 72] hydroxyl ions[13] etc. have been involved in ZnO growth, the reduction of crystal aspect ratio observed was hypothesized to be a consequence of the additives adsorption on the (0002) plane of ZnO crystals. Since (0002) is a Zn-terminated plane, the capping agents that have affected ZnO morphology and/or are proposed to adsorb on the (0002) plane are generally anionic. Based on this generally accepted rationalization, the inhibition of diameter growth ($\Delta D_{Avg}/\Delta t \sim 0$) in the presence of G-12 but not with GT-16 would lead to three possible speculations. Firstly, besides adsorbing on (0002), G-12 molecules were able to adsorb onto the (10-10) plane of ZnO crystals, possibly via a different adsorption mechanism. Secondly, GT-16 selectively adsorbed onto the (0002) planes of ZnO crystals. Thirdly, the plane selectivity of GT-16 was attributable to the GGGC tag not present in G-12. To unravel the cause(s) of these interesting findings, the adsorption behaviour of G-12 and GT-16 was studied.

4.3.5 Peptide adsorption-driven morphological changes and plane selectivity by GT-16

The adsorption behaviour of G-12 and GT-16 on ZnO planes was studied using ZnO films with different crystal orientation grown by the ALD technique. (0002) and (10-10) films of ZnO were grown by controlling the deposition temperature and the orientations were confirmed as such by XRD (**Figure 4.12**). The use of oriented-ZnO films aimed to eliminate any uncertainties arising from using ZnO crystals with more than one surface crystallographic plane. However the small surface area of ZnO films (compared to particles), constrained the concentrations and volume of the peptide solution that could be used. Moreover, the Micro-BCA assay (higher sensitivity) was used after failed attempts to establish linear fluorescence/absorbance-peptide concentration correlations within the concentration range of interest by using fluorescamine, Bradford, and BCA assays.

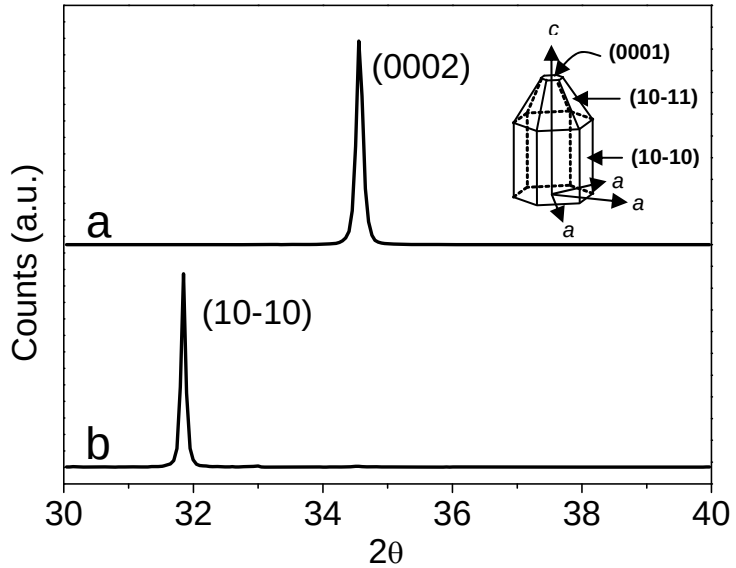

Figure 4.12 Diffractograms of ALD-grown ZnO films: (a) (0002) plane and (b) (10-10) plane were grown at deposition temperature of 280°C and 165°C respectively. Inset shows the representation of low index planes and axes of ZnO crystal.

ZnO(0002), ZnO(10-10), Si-wafer(100), and glass slide were exposed to peptide solutions for 5 hours. The amount of peptide adsorbed was determined from the change of peptide concentration. As shown in **Figure 4.13a**, 1.4~4.3nmol of peptides were

found to adsorb on ZnO films (~9cm^2) while the amount adsorbed on Si(100) and glass slides was <0.50nmol and <0.37nmol respectively (also on ~9cm^2), comparable to the blank (without substrate). This implied that G-12 and GT-16 were being selective towards ZnO over the Si-wafer and the glass slide.

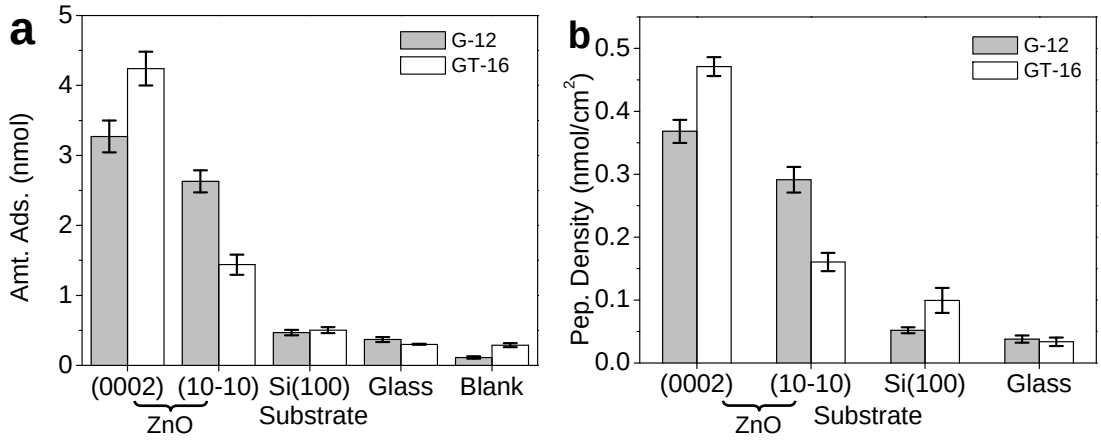

Figure 4.13 (a) The amount of peptide adsorbed, and (b) peptide density after 5 hours of exposure to different substrates (area ~9cm^2). The error bars shown are the standard deviation obtained from three separate sets of experiments.

Figure 4.13b revealed that peptide density was typically higher on ZnO(0002) compared to Zn(10-10) and the inter-plane density difference was 0.31nmol/cm^2 for GT-16 as compared to 0.08nmol/cm^2 for G-12. The "preferential" adsorption of GT-16 on the (0002) plane of ZnO supported the observation – reduction of the growth rate of the crystals along the *c*-axis but no reduction of growth rate of the crystal *a*-axes, **Figure 4.11**. The lower G-12 density on ZnO(0002) and its weaker plane selectivity were demonstrated by the lower extent of ZnO aspect ratio reduction in its presence. FTIR-ATR and XPS were used to detect the presence of peptide on ZnO films used in the binding experiment. FTIR-ATR failed to detect the presence of peptides due to sensitivity limitations (**Appendix 4.11**). XPS analysis confirmed the presence of peptide by the detection of nitrogen with binding energy of ~400eV (N1s) although the results did not quantitatively coincide entirely with the adsorption results, **Figure 4.14** (**Appendix 4.12**).

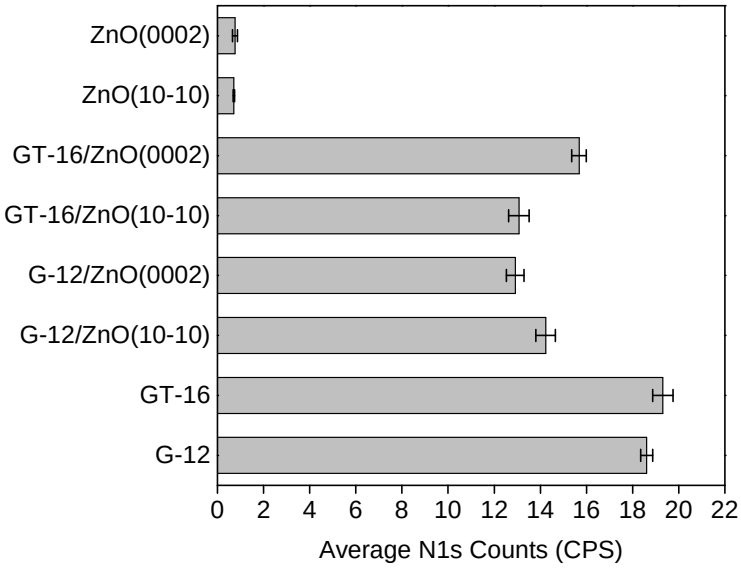

Figure 4.14 Average N 1s counts at binding energy of ~400eV from 3 areas on samples. The standard deviation is shown as an error bar.

To our knowledge, this is the first study to provide unambiguous and direct quantitative experimental evidence, by the use of ALD-grown single orientation ZnO films, to prove (selective and non-selective) adsorption-driven ZnO morphology modification by biomolecules and ZnO-BP identified from phage display libraries. FTIR and TGA are frequently used for the detection of "incorporated" organic additives that shown to affect ZnO morphology or growth.[21, 23, 34] However no binding information is provided by TGA while the identification of a frequency-shift of the adsorbed species from the FTIR spectra is highly dependent on the quality of the spectra (purity of the precipitates, fraction of the adsorbed species, etc.). The addition of water-soluble graft polymers[25] and diblock copolymers (DBCPs)[23, 24, 26] has shown to alter the morphology, size, and size distribution of ZnO crystals. The adsorption of DBCPs on the basal plane, (0002) plane, was proposed and proved qualitatively by the use of fluorescence microscopy by Taubert *et al*.[23] while Wegner *et al*.[25] "showed" the evidence of P(PEO_{31}-MA)-co-$VS_{0.3}$ adsorption on the (0002) plane of ZnO through the presence and multiplication of growth spirals on the basal plane of ZnO crystals observed under SEM. The adsorption of a ZnO-BP, EM-12 (EAHVMHKVAPRP), on ZnO particles was studied by exposing peptide immobilized on Au-coated surface to fluorescent ZnO particles suspension.[54] Qualitative results were obtained however the required modifications may have altered the surface chemistry of ZnO and the

reactivity of peptide studied. In fact, the authors have shown that the catalysis reactivity of GGGSC tagged-EM-12 and GGGSS tagged-EM-12 were different.[54] Furthermore, the plane(s) involved in the binding process cannot be identified.

The findings from binding experiments confirmed the adsorption of G-12 and GT-16 being the cause of ZnO morphology modification however the energetic information and the binding sites involved were not obtained from such a study. To complement the experimental findings, computational approach was employed to provide (calculated) energetic data and prediction of binding moieties. Using computational approach, the adsorption of G-12 and GT-16 on ZnO planes was found to be energetically favourable, **Figure 4.15**. When exposed to ZnO surfaces in vacuum, the adsorption modes and adsorption energy (E_{Ads}) of stable configurations of G-12 and GT-16 (simulated in water by MD) were determined. In good agreement with the trend of peptide density from the adsorption test (**Figure 4.13b**), GT-16 showed a higher preference towards the (0002) plane as opposed to the (10-10) plane with an inter-plane E_{Ads} difference of 288kJ/mol. This value is much higher than the inter-plane difference of E_{Ads} for G-12, 100kJ/mol.

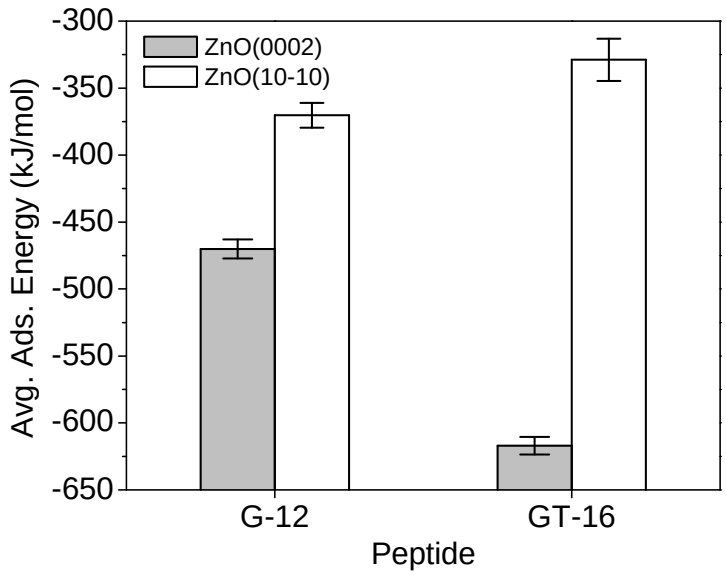

Figure 4.15 The average adsorption energy and standard deviation of G-12 and GT-16 on (0002) and (10-10) planes of ZnO. The standard deviation was less than 5% (n=10).

Based on (i) peptide density calculated from the results of the adsorption test, (ii) the confirmation of peptides' presence on the ZnO films by XPS, and (iii) the computed adsorption energies; the following deduction can be made. Firstly, G-12 and GT-16 suppress ZnO crystal growth along its *c*-axis by adsorbing onto the (0002) plane because the process is more energetically favourable compared to their binding onto the (10-10) plane. Secondly, greater *c*-axis growth suppression by GT-16 (relative to G-12), leading to hexagonal plates formation, can be attributed to the high specificity (lower adsorption energy) of GT-16 for the (0002) plane. Finally, the retardation of diameter growth by G-12, but not by GT-16 addition, is due to a competition in binding arising from the (small) difference in the energies of adsorption between the two planes. This results in an additional limitation of growth along the *a*-axes by the addition of G-12 to the crystallising medium.

4.3.6 GGGC-tag and the preferential adsorption of GT-16 on the (0002) plane

The plane-dependent binding behaviour of GT-16 on ZnO surfaces may be caused by the GGGC-tag at its terminus. The moiety(ies) of GT-16 engaging with the ZnO surfaces was studied computationally where stable conformation of G-12 and GT-16 obtained using a MD tool (in water) was exposed to a constructed ZnO surface. Since the identification of engaging moiety(ies) was studied in vacuum, the results obtained was mainly used as reference.

As seen in **Figure 4.16**, the polar side chains of H_3 and K_7 of G-12 were close to the surface of both (0002) and (10-10) planes while the amino acids toward the negative-termini of G-12 moved away from the surfaces. When exposed to the (0002) plane, H_6, K_7 and G_1 of GT-16 (**Figure 4.17a**) appear to have engaged with the surface. At pH 6.9±0.1, the side chain of H_3 and K_7 of G-12, and K_7 and G_1 of GT-16 would be cationic based on the pK_a values obtained (**Appendix 4.8**). It was unexpected to find these cationic moieties being the most favourable anchor points onto the generally accepted as positively-charged (0002) plane of ZnO.[29, 99] There was also evidence that NO_3^- formed complexes with both G-12 and GT-16 and "co-precipitated" with ZnO (discussed in **Section 4.3.3**) which suggests that, it is quite likely that the cationic

moieties of peptides (such as K_7 and H_3) were not available for the interaction with (0002) plane of ZnO. Therefore a refinement of the model may be required due to the presence of anionic species in the reaction solution having a tendency to interact with the peptides themselves.

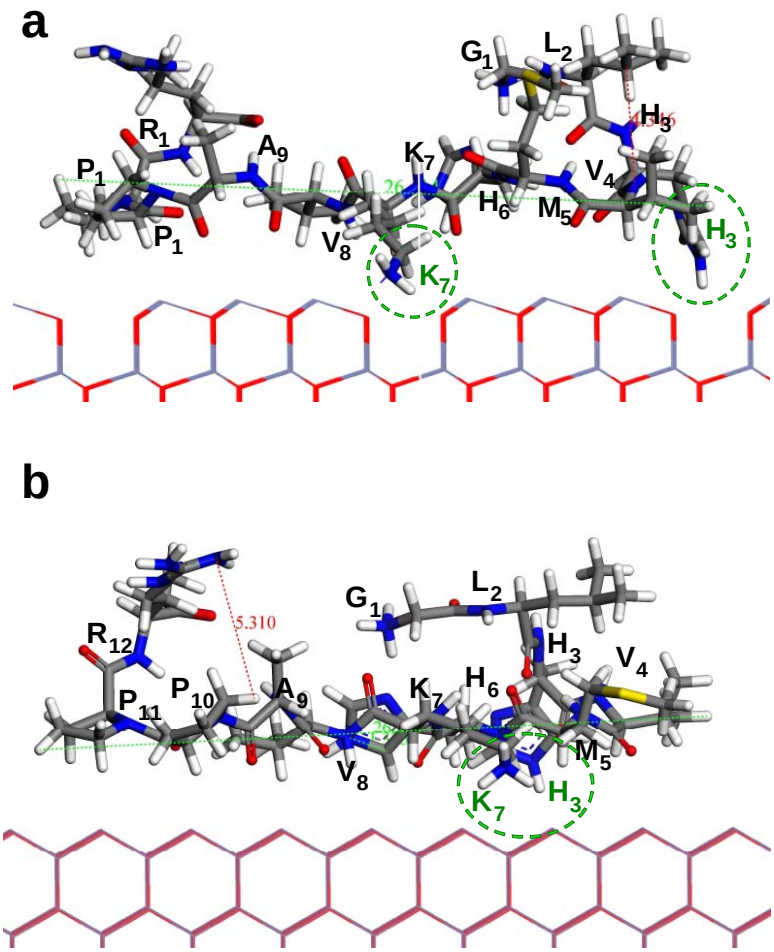

Figure 4.16 The side view of G-12 adsorbing on (a) (0002) plane and (b) (10-10) plane of ZnO. The peptide sequence was numbered from the N-terminus to the C-terminus using the standard single letter abbreviation. The side chains of residues predicted to adsorb on ZnO surfaces are marked with dash-lined circles.

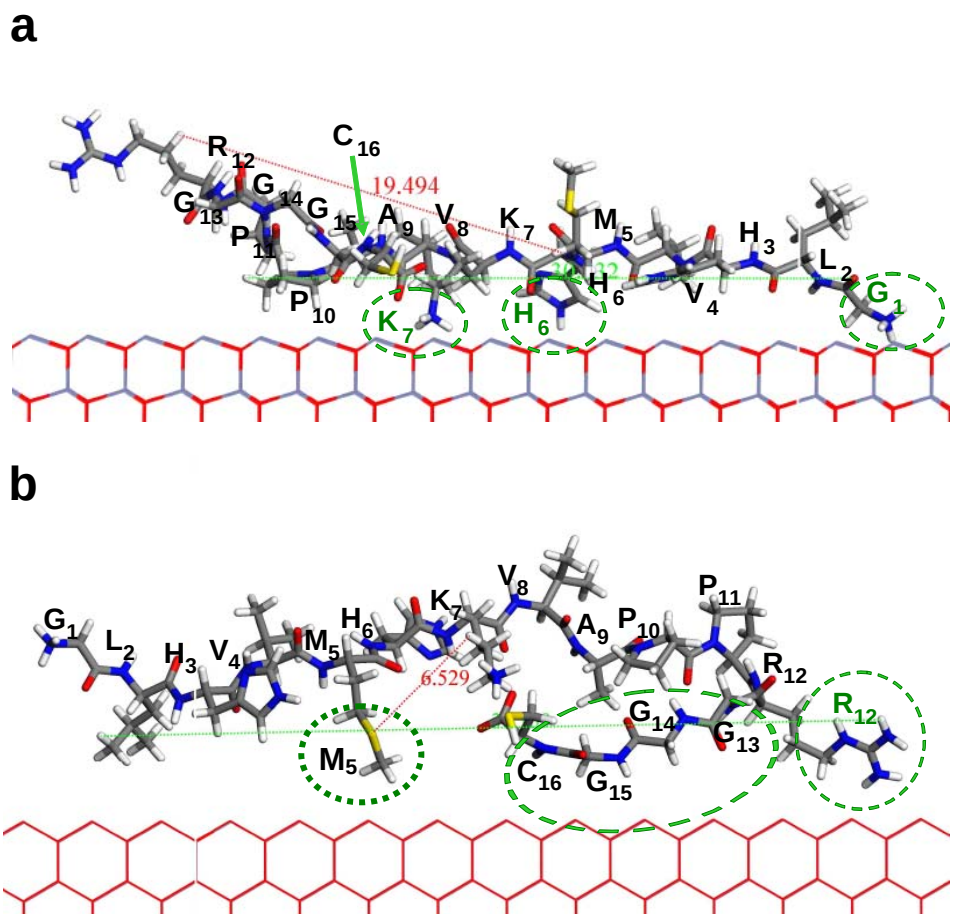

Figure 4.17 The side view of GT-16 adsorbing on (a) (0002) plane and (b) (10-10) plane of ZnO. The peptide sequence was numbered from the N-terminus to the C-terminus using the standard single letter abbreviation. The side chains of residues predicted to adsorb on ZnO surfaces are marked with dash-lined circles.

If cationic H_3 and K_7 of G-12 were free to react with ZnO surfaces, their adsorption on the (10-10) plane would be feasible via electrostatic interaction/hydrogen bonding due to the presence of oxygen on the (10-10) plane. As for GT-16, when interacting with the (10-10) plane, the side chains of R_{12}, M_5, and the GGGC-tag of GT-16 lie close to the surface. This (predicted) interaction may be arise through hydrogen bonding (neutral R_{12} with O^{2-}), electrostatic interactions (anionic C_{16} with Zn^{2+}) and reinforced in water by hydrophobic interactions via M_5 and the GGG-segment. Since the prediction of GT-16-(10-10) interaction only involved non-cationic moieties, it should not be affected by complexation of the peptide with NO_3^-. It is speculated that the difference in adsorption behaviour between GT-16 and G-12 may be related to the

additional GGGC-tag on GT-16. The difference in the nature of the groups engaging with the (10-10) plane: polar for G-12 (H_3 and K_7) and non-polar in the majority for GT-16 (M_5, R_{12}, GGGC-tag) has shown the significance of the GGGC-tag in contributing to the discriminative adsorption of GT-16 on ZnO planes. Inferred from this difference, the presence of GGGC-tag may have lowered the GT-16 density on the (10-10) plane due to a weaker hydrophobic adsorption contribution.

4.3.7 Direct band gap energy of ZnO formed

The determination of direct band gap energy of ZnO crystals formed in the absence and presence of G-12 and GT-16 does not contribute to the understanding of the mechanism of morphology modification induced by these ZnO-BPs. The direct band gap measurement aimed to compare the optical properties of ZnO produced in the absence and presence of morphology modifier under comparable conditions. This comparison is perceived as an indication of the feasibility of biomimetic approach in producing "useable" ZnO crystal with tuneable morphology. The UV absorption of lyophilised precipitates from the control and 0.30mM peptide-added reactions was measured. The post-TGA sample from the control reaction was also measured for comparison. **Figure 4.18** shows the room temperature UV-Vis absorption of these ZnO samples and the direct band gap energies (E_g) calculated on the basis of the corresponding absorption edges are showed in the inset of **Figure 4.18**. The calculated direct band gap energies are 3.220±0.001eV for the controls, 3.193eV for the calcined control and, 3.231eV and 3.253eV for ZnO produced in the presence of 30mM G-12 and 30mM GT-16 respectively. These values are comparable to the values of bulk ZnO reported in the literature, 3.437eV.[1] Therefore the use of biomimetic approach in solution route synthesis which provides great flexibility in morphology tuning also produces ZnO of comparable qualities, generally.

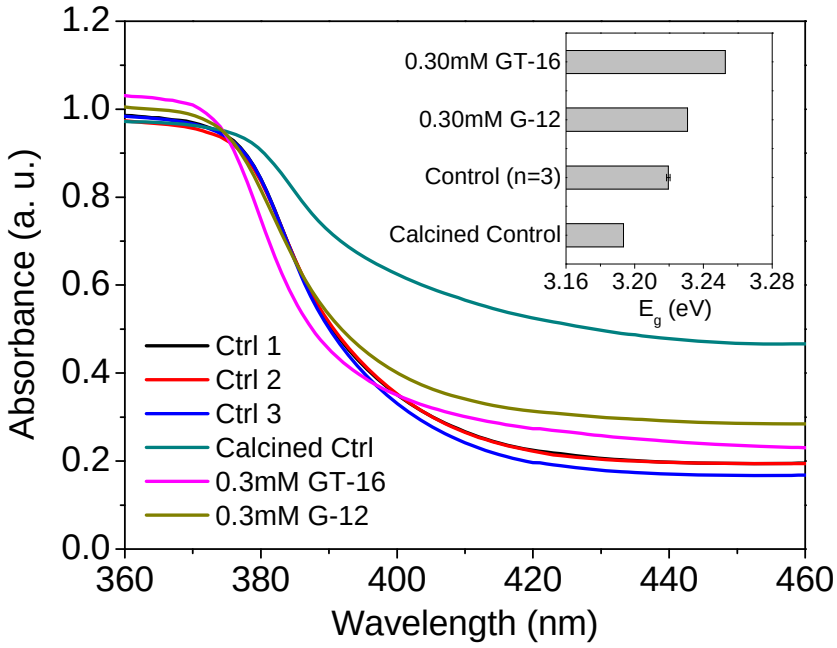

Figure 4.18 UV absorbance of ZnO precipitates from the control reactions and reactions in the presence of 0.30mM G-12 or GT-16. Inset shows the direct band gap for samples where the average value is shown for the control sample with the standard deviation represented by an error bar.

4.3.8 Proposed mechanism of adsorption-driven morphology modification of ZnO by ZnO-BPs

The addition of G-12 and GT-16 into ZnO forming reaction at pH 6.9±0.1 has been shown to reduce the aspect ratio of the crystals through the alteration of growth rates at both the *c*-axis and *a*-axes of ZnO crystals. The effects of these peptides on ZnO growth and morphology were determined by the measurement of ZnO crystal dimensions at different stages of formation using SEM. As illustrated in **Scheme 4.1**, the presence of G-12 reduced the growth rate of ZnO crystal along both the *c*-axis and the *a*-axes while the presence of GT-16 only reduce the crystal growth rate along the *c*-axis. The reduction of the *c*-axis growth rate by GT-16 was compensated by the increase of the *a*-axes growth rate.

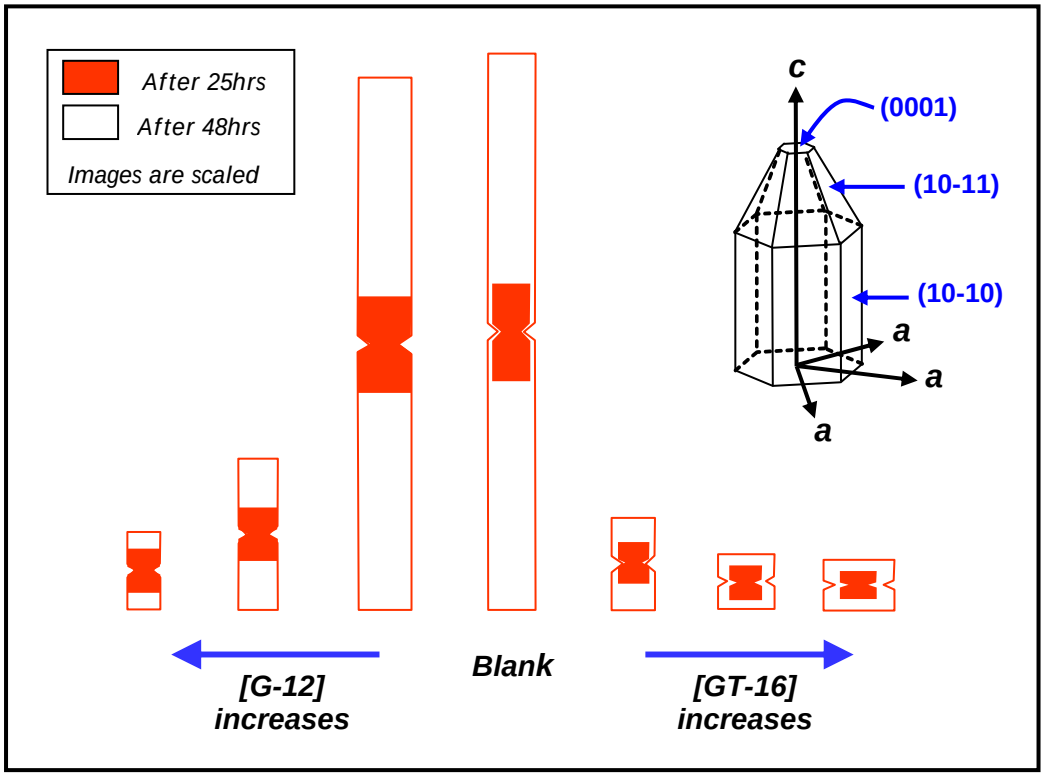

Scheme 4.1 The representation of the effect of G-12 and GT-16 on the growth and morphology of ZnO crystals using scaled images of ZnO crystals formed after 25 hours ($t_{20°C}$=24hr, $t_{65°C}$=1hr) and 48 hours ($t_{20°C}$=24hr, $t_{65°C}$=24hr) of reaction.

Based on (i) the confirmation of peptide adsorbing on ZnO crystal planes (XPS), (ii) the detection of peptide concentration-dependent organic weight fraction in precipitates collected (FTIR and TGA), and (iii) the differences in peptide density, strongly related to the type of peptide and ZnO crystallographic planes (adsorption test); the effects of G-12 and GT-16 on ZnO aspect ratio is explained by a peptide adsorption-growth inhibition mechanism, as shown in **Scheme 4.2**. The adsorption of G-12 on both (0002) and (10-10) planes, and the preferential adsorption of GT-16 on (0002) plane lowered the surface energy of the adsorbed plane and leading to the reduction/inhibition of crystal growth along the direction perpendicular to the adsorbed planes. Up to this point what remained unclear is the peptide moiety(ies) which bind(s) the corresponding surface planes of ZnO crystals. Many literatures have reported/proposed electrostatic interaction/coordination between the Zn^{2+} of the (0002) plane and the additives (DBCP,[23, 24, 100] citrate,[19, 20] phosphate,[17] TEA,[15, 101] etc) being responsible for the adsorption of additive on the (0002) plane of ZnO which in turn

modified the ZnO morphology. If the complexation of NO_3^- with cationic moieties of G-12 and GT-16 (G_1, H_3, and K_7) has taken place, as inferred from the FTIR data and side chain pK_a value of peptides; the side chain residues of ZnO-BPs left to bind with ZnO surfaces (Zn^{2+} of (0002), and Zn^{2+} and O^{2-} of (10-10)) are namely, COO^- at C-terminus,[102] the neutral side chain imidazole nitrogens,[102] and the sulphur atoms of M_5 and C_{16},[102-104] and probably the hydrophobic GGG of the tag segment.

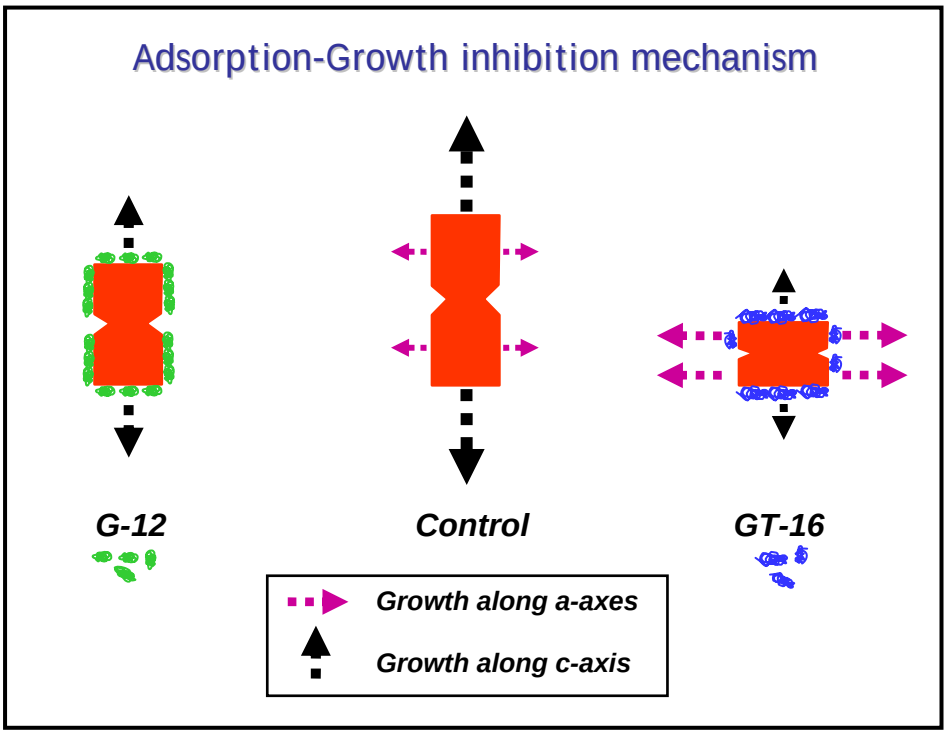

Scheme 4.2 Peptide adsorption-growth inhibition mechanism. The length and thickness of growth arrows reflects the growth rate of the crystal along the respective axis.

Based on these possible binding centres and in conjunction with the peptide density pattern of both peptides on the (0002) and (10-10) planes of ZnO, the adsorption moieties on ZnO planes were proposed as follows. In the absence of cationic residues in G-12 and GT-16, pure carboxylate coordination with (0002) plane via their C-termini results, R_{12} for G-12 and C_{16} for GT-16 respectively.[102] However the coordination of Zn^{2+} of (0002) with the sulphur of M_5 is also possible.[104] Stronger binding by GT-16, demonstrated by higher peptide density and greater reduction in crystal length, may be caused by higher percentage of unprotonated H_6 which is able to bind (0002) plane for GT-16 compared to G-12, and the possibility of C_{16} and M_5 of

GT16 to bind (0002). However, the affinity between Zn-S of cysteine has been shown higher compared to Zn-N of histidine and Zn-S of methionine based on the calculation of stability constants (of Zn-short peptide complexes) using potentiometric titration data.[105] In addition to the coordination between Zn^{2+} and the C-terminus of peptides on the (10-10) plane, secondary interactions (hydrogen bond, hydrophobic interaction or Van der Waals) are possible between the peptide residues and oxygen on this plane. The complete suppression of *a*-axes growth by G-12 as opposed to increased growth along the *a*-axes in the presence of GT-16 may be due to stronger hydrogen bonding between G-12 with oxygen on the (10-10) plane compared to weaker hydrophobic interactions between the GGGC-tag of GT-16 with this ZnO plane.

4.4 Conclusions

The effect of G-12 (a ZnO-BP) and its derivative (GT-16) on crystal morphology was probed by varying their concentrations in a $Zn(NO_3)_2$-HMTA crystallization reaction. Compared to the control reaction, the presence of both G-12 and GT-16 reduced the growth rate along the *c*-axis of the crystal, with the effect being more prominent with GT-16. For the first time, peptide adsorption on ZnO surfaces has been studied quantitatively using ALD-grown ZnO films. In conjunction with confirmation by XPS, this study has provided direct evidence for adsorption-driven ZnO morphology modification showed by G-12 and GT-16. The adsorption of these peptides has led to growth reduction/inhibition on the adsorbed planes. The correlation of peptide adsorption behaviours with their effects on ZnO morphology verified the preferential binding (discriminative behaviour) of GT-16 on the (0002) plane over the (10-10) plane. Such discriminative behaviour was not evidenced for G-12 which lacked the GGGC-tag. Therefore the GGGC-tag present on GT-16 was not essential for aspect ratio reduction, but provided GT-16 with crystal plane-specific adsorption behaviour. The calculated adsorption energies (by computational approach) of G-12 and GT-16 on different ZnO planes were in agreement with the level of plane-selectivity shown by these peptides. The tuning of ZnO morphology by G-12 and GT-16 was a complex phenomenon. The solution chemistry of amino acid residues, the nature of zinc salt

counterions, the surface chemistry of ZnO planes, and peptide sequences were found to play a part and influence the reaction. The total elucidation of this complex phenomenon would require more extensive studies. However it is believe that the findings reported in this thesis provide evidence for ZnO morphology-tuning via the adsorption of biomolecules on specific crystal plane(s) of ZnO crystals. The ultimate goal of such a study is to identify and understand the specific role(s) of participating functionalities of a biomolecules in ZnO morphology tuning. By doing so, the specificity and multifunctionality of biomolecules in affecting ZnO morphology can be learned and manipulated to tailor-make ZnO with novel properties for specific applications.

References

1 C. F. Klingshirn, *ChemPhysChem* **8**, 782-803 (2007).

2 Z. L. Wang, *J. Phys.: Condens. Matter.* **16**, R829-R858 (2004).

3 S. J. Pearton, D. P. Norton, K. Ip, Y. W. Heo, and T. Steiner, *Prog. Mater Sci.* **50**, 293-340 (2005).

4 C. X. Xu, X. W. Sun, Z. L. Dong, and M. B. Yu, *Appl. Phys. Lett.* **85**, (17), 3878-3880 (2004).

5 Z. L.Wang, X. Y. Kong, and J. M. Zuo, *Phys. Rev. Lett.* **91**, (18), 185502-185504 (2003).

6 J. Y. Lao, J. Y. Huang, D. Z. Wang, and Z. F. Ren, *Nano Lett.* **3**, (2), 235-238 (2003).

7 X. Y. Kong, Y. Ding, R. Yang, and Z. L. Wang, *Science* **303**, 1348-1351 (2004).

8 Z. W. Pan, Z. R. Dai, and Z. L. Wang, *Science* **291**, 1947-1949 (2001).

9 P. X. Gao, and Z. L. Wang, *Science* **125**, (37), 11299-11305 (2003).

10 X. Y. Kong, and Z. L. Wang, *Nano Lett.* **3**, (12), 1625-1631 (2003).

11 W. D. Yu, X. M. Li, and X. D. Gao, *Appl. Phys. Lett.* **84**, (14), 2658-2660 (2004).

12 Y. Yan, L. Zhou, Q. Xue, and Y. Zhang, *J. Phys. D: Appl. Phys.* **41**, 195402-195407 (2008).

13 B. Cao, and W. Cai, *J. Phys. Chem. C* **112**, 680-685 (2008).

14 Y. Masuda, N. Kinoshita, and K. Koumoto, *Electrochim. Acta* **53**, 171-174 (2007).

15 R. Xie, D. Li, H. Zhang, D. Yang, M. Jiang, T. Sekiguchi, B. Liu, and Y. Bando, *J. Phys. Chem. B* **110**, (39), 19147-19153 (2006).

16 F. Lu, W. Cai, and Y. Zhang, *Adv. Funct. Mater.* **18**, 1047-1056 (2008).

17 H. Imai, S. Iwai, and S. Yamabi, *Chem. Lett.* **33**, (6), 768-769 (2004).

18 Z. R. Tian, J. A. Voigt, J. Liu, B. Mckenzie, and M. J. Mcdermott, *J. Am. Chem. Soc.* **124**, 12954-12955 (2002).

19 J. Liang, J. Liu, Q. Xie, S. Bai, W. Yu, and Y. Qian, *J. Phys. Chem. B* **109**, (19), 9463-9467 (2005).

20 C.-L. Kuo, T.-J. Kuo, and M. H. Huang, *J. Phys. Chem. B* **109**, (43), 20115-20121 (2005).

21 T. Zhang, W. Dong, M. Keeter-Brewer, S. Konar, R. N. Njabon, and Z. R. Tian, *J. Am. Chem. Soc.* **128**, (33), 10960-10968 (2006).

22 M. Öner, J. Norwig, W. H. Meyer, and G. Wegner, *Chem. Mater.* **10**, (2), 460-463 (1998).

23 A. Taubert, D. Palms, O. Weiss, T. Piccini, and D. N. Batchelder, *Chem. Mater.* **14**, (6), 2594-2601 (2002).

24 A. Taubert, G. Glasser, and D. Palms, *Langmuir* **18**, 4488-4494 (2002).

25 G. Wegner, P. Baum, M. Müller, J. Norwig, and K. Landfester, *Macromolecules Symp.* **175**, 349-355 (2001).

26 A. Taubert, C. Kubel, and D. C. Martin, *J. Phys. Chem. B* **107**, (12), 2660-2666 (2003).

27 R. C. Hoffmann, S. Jia, J. C. Bartolomé, T. M. Fuchs, Joachim Bill, P. C. J. Graat, and F. Aldinger, *J. Eur. Ceram. Soc.* **23**, 2119-2123 (2003).

28 R. C. Hoffmann, T. M. Fuchs, T. P. Niesen, J. Bill, and F. Aldinger, *Surf. Interface Anal.* **34**, 708-711 (2002).

29 Y. Peng, A.-W. Xu, B. Deng, M. Antonietti, and H. Colfen, *J. Phys. Chem. B* **110**, (7), 2988-2993 (2006).

30 J. Zhang, H. Liu, Z. Wang, N. Ming, Z. Li, and A. S. Biris, *Adv. Funct. Mater.* **17**, 3897-3905 (2007).

31 L. Guo, and S. Yang, *Chem. Mater.* **12**, 2268-2274 (2000).

32 N. Lepot, M. K. V. Bael, H. V. d. Rul, J. D'Haen, R. Peeters, D. Franco, and J. Mullens, *Mater. Lett.* **61**, 2624-2627 (2007).

33 K. Biswas, B. Das, and C. N. R. Rao, *J. Phys. Chem. C* **112**, 2404-2411 (2008).

34 J. Zhang, H. Liu, Z. Wang, and N. Ming, *J Cryst. Growth* **310**, 2848-2853 (2008).

35 M. Bitenc, M. Marinšek, and Z. C. Orel, *J. Eur. Ceram. Soc.* **28**, 2915-2921 (2008).

36 R. Viswanatha, and D. D. Sarma, *Chem. Eur. J.* **12**, 180-186 (2006).

37 D. Tao, W. Qian, Y. Huang, and F. Wei, *J Cryst. Growth* **273**, 353-357 (2004).

38 L. Guo, J. X. Cheng, X.-Y. Li, Y. J. Yan, S. H. Yang, C. L. Yang, J. N. Wang, and W. K. Ge, *Mater. Sci. Eng., C* **16**, 123-127 (2004).

39 C. Pacholski, A. Kornowski, and H. Weller, *Angew. Chem. Int. Ed.* **41**, (7), 1188-1191 (2002).

40 R.-Q. Song, A.-W. Xu, B. Deng, Q. Li, and G.-Y. Chen, *Adv. Funct. Mater.* **17**, 296-306 (2007).

41 S. Musić, A. Šarić, and S. Popović, **448**, 277-283 (2008).

42 S. Lee, S. Jeong, D. Kim, B. K. Park, and J. Moon, *Superlattices Microstruct.* **42**, 361-368 (2007).

43 G. Begum, S. V. Manorama, S. Singh, and R. K. Rana, *Chem. Eur. J.* **14**, 6421-6427 (2008).

44 P. Gerstel, R. C. Hoffmann, P. Lipowsky, L. P. H. Jeurgens, J. Bill, and F. Aldinger, *Chem. Mater.* **18**, (1), 179-186 (2006).

45 P. Gerstel, P. Lipowsky, O. Durupthy, R. C. Hoffmann, P. Bellina, J. Bill, and F. Aldinger, *J. Ceram. Soc. Jpn.* **114**, (11), 911-917 (2006).

46 M. M. Tomczak, M. K. Gupta, L. F. Drummy, S. M. Rozenzhak, and R. R. Naik, *Acta Biomater.* **5**, (3), 876-882 (2008).

47 R. d. l. Rica, and H. Matsui, *Angew. Chem. Int. Ed.* **47**, 5415-5417 (2008).

48 Q. Wu, X. Chen, P. Zhang, Y. Han, X. C. Y. Yan, and S. Li, *Cryst. Growth Des.* **8**, (8), 3010-3018 (2008).

49 Q. Dong, H. Su, F. Song, D. Zhang, and N. Wang, *J. Am. Ceram. Soc.* **90**, (2), 376-380 (2007).

50 L. P. Bauermann, A. d. Campo, J. Bill, and F. Aldinger, *Chem. Mater.* **18**, (8), 2016-2020 (2006).

51 Y.-H. Tseng, H.-Y. Lin, M.-H. Liu, Y.-F. Chen, and C.-Y. Mou, *J. Phys. Chem. C* **113**, 18053-18061 (2009).

52 M. B. Dickerson, K. H. Sandhage, and R. R. Naik, *Chem. Rev.* **108**, 4935-4978 (2008).

53 Z. Huang, D. Yan, M. Yang, X. Liao, Y. Kang, G. Yin, Y. Yao, and B. Hao, *J. Colloid and Int. Sci.*, (2008).

54 M. Umetsu, M. Mizuta, K. Tsumoto, S. Ohara, S. Takami, H. Watanabe, I. Kumagai, and T. Adschiri, *Adv. Mater.* **17**, 2571-2575 (2005).

55 D. Weinzierl, D. Touroud, A. Lecker, A. Pfitzner, and W. Kunz, **43**, 62-67 (2008).

56 D. Yan, G. Yin, Z. Huang, M. Yang, X. Liao, Y. Kang, Y. Yao, B. Hao, and D. Han, *J. Phys. Chem. B* **113**, (17), 6047-6053 (2009).

57 M. Jitianu, and D. V. Goia, *J. Colloid and Int. Sci.* **309**, 78-85 (2007).

58 S. V. Patwardhan, G. Patwardhan, and C. C. Perry, *J. Mater. Chem.* **17**, 2875-2884 (2007).

59 S. Brown, M. Sarikaya, and E. Johnson, *J. Mol. Biol.* **299**, 725-732 (2000).

60 S. Brown, *Nat. Biotechnol.* **15**, 269-272 (1997).

61 S. Brown, *Nano Lett.* **1**, (7), 391-394 (2001).

62 R. R. Naik, S. J. Stringer, G. Agarwal, S. E. Jones, and M. O. Stone, *Nature* **1**, 169-172 (2002).

63 C. K. Thai, H. Dai, M. S. R. Sastry, M. Sarikaya, D. T. Schwartz, and F. Baneyx, *Biotechnol. Bioeng.* **87**, 129-137 (2004).

64 K. Kjærgaard, J. K. Sørensen, M. A. Schembri, and P. Klemm, *Appl. Environ. Microbiol.* **66**, (1), 10-14 (2000).

65 R. R. Naik, L. L. Brott, S. J. Clarson, and M. O. Stone, *J. Nanosci. Nanotech.* **2**, (1), 95-100 (2002).

66 E. Eteshola, L. J. Brillson, and S. C. Lee, *Biomolecular Engineering* **22**, 201-204 (2005).

67 H. Chen, X. Su, K.-G. Neoh, and W.-S. Choe, *Langmuir* **24** 6852-6857 (2008).

68 T. P. Chou, Q. Zhang, G. E. Fryxell, and G. Cao, *Adv. Mater.* **19**, 2588-2592 (2007).

69 H. Bai, F. Xu, L. Anjia, and H. Matsui, *Soft Matter* **5**, 966-969 (2009).

70 M. M. Tomczak, M. K. Gupta, L. F. Drummy, S. M. Rozenzhak, and R. R. Naik, *Acta Biomater.* **5**, (3), 876-882 (2009).

71 L. Shi, J. Zhou, and S. Gunasekaran, *Mater. Lett.* **62**, 4383-4385 (2008).

72 Z. R. Tian, J. A. Voigt, J. Liu, B. Mckenzie, M. J. Mcdermott, M. A. Rodriguez, H. Konishi, and H. Xu, *Nature Materials* **2**, 821-826 (2003).

73 M. Muthukumar, *J. Chem. Phys.* **130**, 161101-161105 (2009).

74 Y. K. Gao, F. Traeger, O. Shekhah, H. Idriss, and C. Wöll, *J. Colloid and Int. Sci.* **338**, 16-21 (1009).

75 S. Irrera, D. Costa, and P. Marcus, *J. Mol. Struct.* **903**, 49-58 (2009).

76 G. Mandal, S. Bhattacharya, and T. Ganguly, *Chem. Phys. Lett.* **472**, 128-133 (2009).

77 M. Bardhan, G. Mandal, and T. Ganguly, *J. Appl. Phys.* **106**, 034701-034705 (2009).

78 Z. J. Deng, G. Mortimer, T. Schiller, A. Musumeci, D. Martin, and R. F. Minchin, *Nanotechnology* **20**, 455101-455109 (2009).

79 S. Udenfriend, S. Stein, P. Böhleń, W. Dairman, W. Leimgruber, and M. Weigele, *Science* **178**, 871-872 (1972).

80 S.-Y. Pung, K.-L. Choy, X. Hou, and C. Shan, *Nanotechnology* **19**, 435609-435614 (2008).

81 C. H. Liu, M. Yan, X. Liu, E. Seelig, and R. P. H. Chang, *Chem. Phys. Lett.* **355**, 43-37 (2002).

82 W. S. Rasband, *National Institute of Health, Bethesda, Maryland, USA* **http://rsb.info.nih.gov/ij/**, (1997-2004).

83 *GROMACS is a free software available under the GNU General Public License*.

84 W. Humphrey, A. Dalke, and K. Schulten, *J. Mol. Graphics* **14**, 33-38 (1996).

85 N. Metropolis, A. W. Rosenbluth, M. N. Rosenbluth, A. H. Teller, and E. Teller, *J. Chem. Phys.* **21**, 1087 (1953).

86 S. Aisawa, E. Ishida, S. Takahashi, H. Hirahara, and E. Narita, *Chem. Lett.* **34**, (5), 630-631 (2005).

87 S. Aisawa, S. Takahashi, W. Ogasawara, Y. Umetsu, and E. Narita, *J. Solid State Chem.* **162**, 52-62 (2001).

88 H. Sawada, R. Wang, and A. W. Sleight, *J. Solid State Chem.* **122**, 148-150 (1996).

89 K. Govender, D. S. Boyle, P. B. Kenway, and P. O'Brien, *J. Mater. Chem.* **14**, 2575-2591 (2004).

90 A. Sugunan, H. C. Warad, M. Boman, and J. Dutta, *J. Sol-Gel Sci. Technol.* **39**, 49-56 (2006).

91 Z. Zhang, M. Lu, H. Xu, and W.-S. Chin, *Chem. Eur. J.* **13**, 632-638 (2007).

92 B. Liu, and H. C. Zeng, *J. Am. Chem. Soc.* **125**, (15), 4430-4431 (2003).

93 Q. Li, V. Kumar, Y. Li, H. Zhang, T. J. Marks, and R. P. H. Chang, *Chem. Mater.* **17**, (5), 1001-1006 (2005).

94 S.-C. Liou, C.-S. Hsiao, and S.-Y. Chen, *J. Cryst. Growth* **274**, 438-446 (2005).

95 H. Wang, C. Xie, D. Zeng, and Z. Yang, *J. Colloid and Int. Sci.* **297**, 570-577 (2006).

96 A. Barth, *Prog. Biophys. Mol. Biol.* **74**, 141-173 (2000).

97 O. Deschaume, A. Fournier, K. Shafran, and C. C. Perry, *New J. Chem.* **32**, 1346-1353 (2008).

98 Marvin 5.0.0 was used for drawing and characterizing chemical structures and substructures, 40 ChemAxon (http://www.chemaxon.com).

99 C. Wöll, *Prog. Surf. Sci.* **82**, 55-120 (2007).

100 K. Gorna, R. Muñoz-Espí, F. Gröhn, and G. Wegner, *Macromol. Biosci.* **7**, 163-173 (2007).

101 Y.-S. Fu, X.-W. Du, J. Sun, Y.-F. Song, and J. Liu, *J. Alloys Compd.* **461**, 527-531 (2008).

102 M. Rombach, M. Gelinsky, and H. Vahrenkamp, *Inorg. Chim. Acta* **334**, 25-33 (2002).

103 U. Brand, M. Rombach, J. Seebacher, and H. Vahrenkamp, *Inorg. Chem.* **40**, (24), 6151-6157 (2001).

104 I. Bertini, H. B. Gray, E. I. Stiefel, and J. S. Valentine, *Biological Inorganic Chemistry: Structure and Reactivity*. University Science Book: California, 2007.

105 P. Gockel, M. Gelinsky, R. Vogler, and H. Vahrenkamp, *Inorg. Chim. Acta* **272**, 115-124 (1998).

Chapter 5
Studies of the Delayed Formation of ZnO via the Complexation of Zn^{2+} with ZnO-Binding Peptide

5.1 Introduction

The identification of biomineral-associated biomolecules has shed light on how biominerals are formed in living organisms. This has also led to the use of the bioinspired/biomimetic approach for materials synthesis, even for non-biologically produced minerals such as ZnO. Due to the absence of ZnO in living organisms, ZnO-binding motifs have been identified from combinatorial phage display libraries. To date, more than twenty ZnO-binding peptides (ZnO-BPs) have been identified from either cell surface display[1, 2] or phage display libraries[3, 4] but only two 12-mer peptides, GLHVMHKVAPPR[3] (G-12) and EAHVMHKVAPRP[4] (EM-12), have been thoroughly studied and confirmed to impact ZnO formation. These two ZnO-BPs display 67% sequence similarity and were identified by two independent studies. GGGC-tagged G-12[3] and G-12 (**Chapter 4**) were found to alter ZnO crystal morphology by inhibiting the growth of the plane onto which they adsorbed while the addition of GGGSC tagged-EM-12 (named as ET-17 hereafter) into stable $Zn(OH)_2$ sol catalysed ZnO formation. Umetsu *et al*.[4] also confirmed that the use of neither a mixture of amino acids present ET-17 nor EAHVMHKVAPRP-GGGSS showed a similar catalytic effect. The catalytic effect of ET-17 was further confirmed by Bai *et al*.[5] when its attachment to a collagen-like triple helix template via hydrogen bonds was able to generate ZnO nanowires.

For living organisms, the complexation of Zn^{2+} with proteins is very important for the structural stability and functionality of proteins, as evidenced in metalloproteins such as metallothionine and zinc fingers of DNA-binding proteins.[6] The coordination of

Zn^{2+} with proteins occurs at specific domain(s) via the side chain of amino acid residues namely; sulphur atoms of cysteine (C) and methionine (M), nitrogen atoms of histidine (H), and oxygen atoms of aspartic acid (D) and glutamate acid (E).[6] Despite high sequence similarity between G-12 and EM-12, the presence of glutamate acid (E_1) as an additional Zn^{2+} binding residue, besides histidine (H_3 and H_6) and methionine (M_5), suggests the possibility of Zn^{2+}-EM-12 complexation, which may led to very different effects on ZnO formation compared to the addition of G-12. Furthermore, Gerstel *et al*. demonstrated that the presence of aspartic acid, glutamate acid, and their corresponding dipeptides in $Zn(NO_3)_2$-HMTA reaction produced layered basic zinc salts (LBZS) instead of ZnO.[7] They also observed the formation of soluble complexes when higher concentrations of these additives were used. Thus, Zn^{2+}-additives complexation via electrostatic interaction was proposed to be responsible for LBZS or soluble complex formation.

Intrigued by the small but believed to be significant difference between EM-12 and G-12, the effect of EM-12 on ZnO-formation was studied using a $Zn(CH_3COO)_2$-NH_3 reaction. The kinetics of reaction was studied by monitoring Zn^{2+} concentration in the reaction solution with time. The role of EM-12 in affecting ZnO formation was also explored by the characterisation of precipitates and the analysis of components present in solutions at different reaction time. The complexation process of EM-12 and Zn^{2+} was probed by studying EC-12, EAHVCHKVAPRP. EC-12 was obtained by replacing methionine (M_5) with cysteine (C_5). Due to the presence of deprotonable sulphur atom, cysteine has stronger complexation capability with Zn^{2+} compared to methionine. In this study, no tag has been added onto EM-12 and EC-12 so that the effect of 12-mer peptides on ZnO formation can be studied using peptide (and its mutant) that was originally found to bind to ZnO during the original biopanning process.

5.2 Experimental

5.2.1 Reagents

Zinc acetate ($Zn(CH_3COO)_2$), piperazine ($C_4H_{10}N_2$), N,N-Diisopropylethylamine (DIPEA, $C_8H_{19}N$), trifluoroacetic acid (TFA, $C_2HF_3O_2$), thioanisole (C_7H_8S), 3,6-Dioxa-1,8-octanedithiol (DODT, $C_6H_{14}O_2S_2$), 1M hydrochloride acid (HCl), Zinc atomic absorption standard solution (1000ppm), 1M potassium hydroxide volumetric standard (KOH), and sodium chloride (NaCl) were purchased from Sigma-Aldrich; ammonia solution (NH_3, 35%), N,N-dimethylformamide (DMF), Dichloromethane (DCM), N-methyl-2-pyrrolidinone (NMP), and diethyl ether were purchased from Fisher Scientific; O-Benzotriazole-N,N,N',N'-tetramethyl-uronium-hexafluoro-phosphate (HBTU) and all Fmoc-protected amino acids required for peptide synthesis were purchased from CEM Corporation while the proline-preloaded-TGT resins were obtained from Novabiochem®. All chemicals were used without further treatment. ddH_2O with conductivity less than $1\mu Scm^{-1}$ was used as the solvent for all ZnO synthesis reactions.

5.2.2 Solid Phase Peptide Synthesis (SPPS)

EM-12 and EC-12 were synthesized in house using a microwave-assisted solid phase synthesis apparatus (CEM Corporation) according to procedures reported in **Section 4.2.2** with the use of a TGT resin preloaded with Fmoc-protected proline. The purity of EM-12 and EC-12 determined using HPLC (as detailed in **Section 4.2.2**) by Dr. David Belton were 88% and 93% respectively. The molecular weights (M_w) of the peptides synthesized were measured by Clare Coveney (Proteomics group, The John van Geest Cancer Research Centre) using Bruker UltraflexIII TOF/TOF mass spectrometer and analysed with Daltonics flexAnalysis software. The M_w of EM-12 and EC-12 were confirmed to be on target where the calculated M_w for EM-12 and EC-12 were 1371.6g/mol and 1343.6g/mol respectively while their measured M_w were 1371.7g/mol and 1343.8g/mol respectively.

5.2.3 ZnO synthesis and kinetic studies

30mM of $Zn(CH_3COO)_2$ (labelled hereafter $ZnAc_2$) in 50°C water, 31.25mM of NH_3, 30mM of EM-12, and 30mM of EC-12 were prepared as stock solutions for this study. Freshly made 31.25mM NH_3 stock solution used in this study was prepared from a 5% NH_3 solution (~2M, stored in a refrigerator). To avoid the variation of the concentration of NH_3 stock solution caused by evaporation, prior to stock solution preparation, the concentration the 5% NH_3 solution was determined by back titrating a mixture of 2ml 5% NH_3 and 10ml 1M HCl with 1M KOH volumetric standard. A series of 1ml peptide solutions with peptide concentrations of 5mM, 10mM, 15mM and 25mM were prepared by diluting known volume of peptide stock solutions with ddH_2O. Prior to each reaction, 24ml of 31.25mM NH_3 stock solution at room temperature was vigorously stirred into a 25ml of 30mM $ZnAc_2$ solution (at 50°C) followed by the addition of the 1ml peptide solutions prepared; giving rise to final peptide concentrations of 0.1mM, 0.2mM, 0.3mM and 0.5mM respectively. For the blank reaction, in the absence of peptide, 1ml ddH_2O was added into the $ZnAc_2$-NH_3 mixture to replace the 1ml of peptide solution. The pH of the reaction solutions were pH 7.0±0.1 regardless of the type of peptides and the concentrations of the peptide used.

The mixtures were placed into a water bath set at 50°C for periods of up to 168 hours. During the course of reaction, samples were taken from the reaction vessels at selected times (±2 minutes). Collected samples were centrifuged at 13000rpm for 3 minutes to separate any precipitate from the supernatant. Supernatant was drawn carefully by a pipette and re-centrifuged using the same condition. Only ~80% of the supernatant was drawn from the vial although no precipitates were observed at the bottom of the vial. This supernatant was used for the determination of $[Zn^{2+}]$ using ICP-OES while peptide concentration in the supernatant was measured at 214nm using UV-Vis spectrophotometer. The precipitates collected were washed three times with ddH_2O. For each washing, the volume of ddH_2O used was two times of the sample volume taken from the reaction pot. Cleaned precipitates and selected set of supernatants (collected after 48 hours) were lyophilised at -70°C using a Virtis-110 freeze-dryer. Selected lyophilised precipitates (after 24 hours and 48 hours) were characterised using

SEM, FTIR-ATR, TGA and XRD while the lyophilised supernatants were analysed using FTIR-ATR.

5.2.4 Quantification of retained peptides in the supernatant by UV spectroscopy

200µl supernatant was diluted ten times with ddH_2O, placed in a quartz cuvette (10mm path length), and scanned at 214nm using a Unicam UV2 UV-VIS spectrophotometer. For this reaction system, $ZnAc_2$, NH_3 and the peptides all absorbed at 214nm. However the absorbance of $ZnAc_2$ and NH_3 were much lower than the peptides and the absorbance of NH_3 was constant within the range of concentration studied as shown in the calibration curves (**Appendix 5.1**). Therefore the absorbance of EM-12 or EC-12 in the supernatant was determined by subtracting the absorbance arising from $ZnAc_2$ and NH_3 from the absorbance of the supernatant shown as follows: $Abs_{Peptide} = Abs_{Supernatant} - Abs_{Zinc\ Acetate} - Abs_{Ammonia}$. The absorbance of $ZnAc_2$ at 214nm was estimated from the calibration curve for $ZnAc_2$ absorbance using Zn^{2+} concentration measured by ICP-OES while a constant value was deducted for NH_3.

5.2.5 X-Ray Diffraction (XRD)

As described in **Section 4.2.5**.

5.2.6 Scanning Electron Microscopy (SEM) and ZnO crystal dimension studies

The morphology of selected precipitates was examined using a scanning electron microscope (JEOL JSM-840A) at an accelerating voltage of 20kV. Lyophilised precipitates were redispersed in ethanol and sonicated for 15 minutes before dispensing onto aluminium sample holders, air-drying then gold-coating (Edwards S150B sputter coater; argon plasma at 1.2kV, 4mbar pressure, 2.5 minutes). The dimensions of ZnO crystals from selected samples were measured using ImageJ 1.37v software.[8] At all

instances, both length and diameter of the same crystal were measured for the determination of crystal aspect ratio (L/D_{Avg}=length/average diameter). The 95% CI (Confidence Interval) of crystal length, average diameter and aspect ratio was calculated for comparison when applicable.

5.2.7 Fourier Transform Infrared Spectroscopy (FTIR)

The presence of the acetate group, amide-I and amide-II bands of peptides, and ZnO in the lyophilised precipitates and supernatants was determined using the ATR mode of a Perkin Elmer Spectrum 100 FTIR Spectrometer with Diamond/KRS-5 crystal. Spectra were averaged over 32 scans at $2cm^{-1}$ resolution with air as background. All samples were ground prior to analysis for good contact with the crystal.

5.2.8 Thermogravimetric Analysis (TGA)

As described in **Section 4.2.8**.

5.2.9 Inductively Coupled Plasma-Optical Emission Spectroscopy (ICP-OES)

As described in **Section 4.2.9**.

5.3 Results and Discussion

5.3.1 Layered basic zinc acetate, LBZA, as the intermediate compound for ZnO formation in the $ZnAc_2$-NH_3 reaction

In this study of the $ZnAc_2$-NH_3 reaction at pH 7.0±0.1 and 50°C, twinned hexagonal ZnO rods[9] were produced after 24 hours and the amount of Zn^{2+} consumed with time was studied using ICP-OES. The percentage of Zn^{2+} remained in solution with respect to the initial amount was calculated and presented as $^{\%}Zn^{2+}$ in this report. As shown in **Figure 5.1**, $^{\%}Zn^{2+}$ rapidly reduced to a minimum of 34.5% after 2 hours followed by a gradual increase of $^{\%}Zn^{2+}$ which stabilized at ~43% after 24 hours. Based on these results, it was deduced that ZnO formation in $ZnAc_2$-NH_3 reaction occurred via the formation of an intermediate compound. This intermediate compound which was consumed for the formation of ZnO has lower activation energy and lower stability than ZnO formed.

To ascertain what the intermediate compound was, the characterisation of precipitates obtained at different reaction times was performed using XRD, SEM, FTIR and TGA. Precipitates collected after 30 minutes, 4 hours, 7 hours, 16 hours, 24 hours, 48 hours, and selected samples after 72 hours, 96 hours, 168 hours were inspected using SEM. The major component of precipitates collected from 30 minutes to 7 hours (described as early stage precipitates hereafter) appeared chunky with irregular shapes was believed to be the intermediate compound, **Figure 5.2a-c**. It is notable that ZnO crystals were present in all the precipitates, including that obtained after 30 minutes. The number of ZnO crystals in precipitates was found to increase with reaction time and ZnO eventually became the major component at 16 hours and beyond, **Figure 5.2d-f**. Anisotropic growth of ZnO crystals in this reaction was also demonstrated by the increase of crystal aspect ratio (L/D_{Avg}) from 2~3 after 24 hours to 5~7 after 72 hours. The aspect ratio values were determined from 30 crystals for each precipitates.

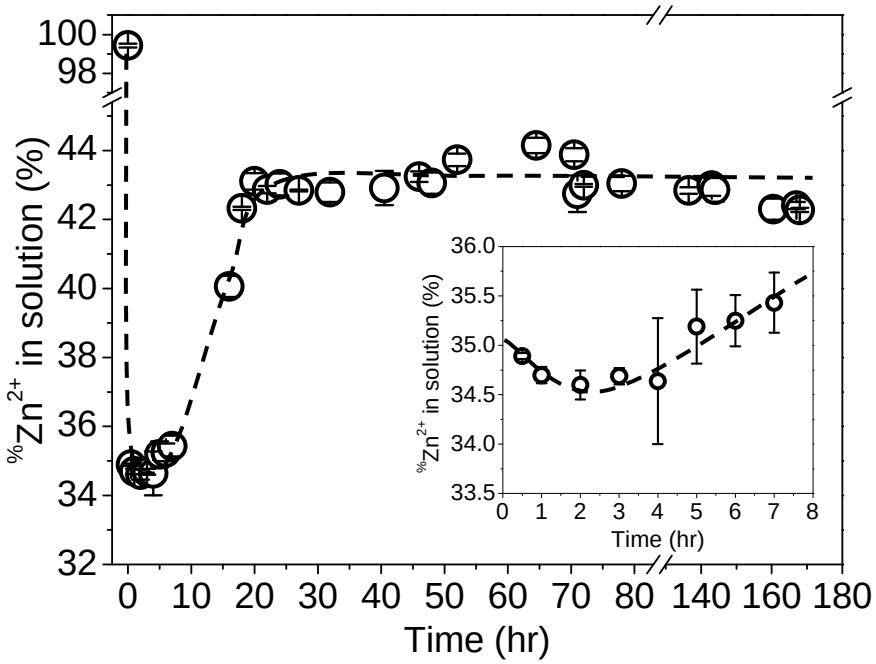

Figure 5.1 $^{\%}Zn^{2+}$, the percentage of Zn^{2+} in solution with respect to the prepared amount, as a function of reaction time.

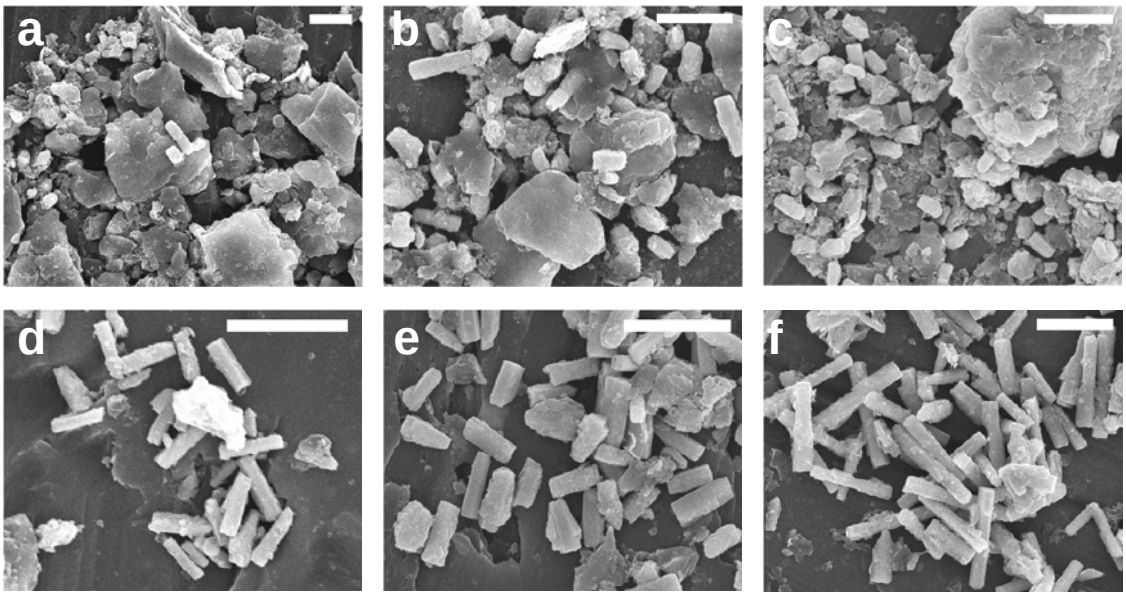

Figure 5.2 SEM of blank precipitates collected after different reaction times: (a) 30 minutes, (b) 4 hours, (c) 7 hours, (d) 16 hours, (e) 24 hours, and (f) 48 hours. All scale bars are 5μm.

From the characterisation of precipitates using SEM, two observations can be made: (i) early stage precipitates were a mixture of non-ZnO compound and ZnO with the former being the major component, and (ii) ZnO became the major component at later

stages of precipitation by the consumption of the non-ZnO component; this was clearly reflected in the XRD, FTIR, and TGA results.

As shown by XRD analysis in **Figure 5.3**, the characteristic diffraction peaks of ZnO at 31.98°, 34.63°, and 36.48°, corresponding to (10-10), (0002), and (10-11) planes of ZnO respectively, and other characteristic peaks within 2θ of 40-70° were detected in all precipitates (30 minutes to 72 hours). The peak intensity of ZnO characteristic peaks increased with reaction time and, at 16 hours and beyond, only ZnO was detected by XRD. Besides diffraction peaks from ZnO, a series of diffraction peaks spaced by 2θ of ~6° at 2θ<20° was observed for early stage precipitates. The non-ZnO diffraction pattern agrees with that of layered basic zinc acetate, LBZA.[10-13] The strongest peak from the early precipitates (at 6.864±0.025°) corresponded to an interlayer spacing of 12.87±0.05Å was originated from the (001) plane of LBZA (12~15Å).[10-14]

From FTIR (**Figure 5.4**) a broad absorption peak in the 3000-3600cm^{-1} region can be assigned to the O-H group of hydroxide or intercalated water. The absorbance of O–Zn–O at 430-530cm^{-1} region was observed for all precipitates collected but only became prominent for precipitates collected at 16 hours and beyond. The inset in **Figure 5.4** shows the absorption region of acetate while the peak assignments are shown in the upper left corner in the same figure. The average and standard deviation of peak position was calculated (using data from all precipitates) for the detection of significant shifts in the peak position with respect to the scanning resolution used. The presence of acetate was confirmed by peaks at 1555cm^{-1} and 1392cm^{-1} corresponding to asymmetric stretching (ν_{as}) and symmetric stretching (ν_s) modes of COO^- respectively.[13, 15-20] The absorption peaks caused by $–CH_3$ bending (1338cm^{-1}) and $–CH_3$ rocking (1045cm^{-1} and 1019cm^{-1}) of acetate were also observed. The shift of peak position with time was observed for peak arisen from $\nu_{as}(COO^-)$ and the peak at 1507cm^{-1} (not assigned). The former shifted from 1551cm^{-1} (at 30 minutes) to 1556cm^{-1} (at 24 hours) and vanished when the reaction was prolonged while the latter shifted from 1514cm^{-1} (at 30 minutes) to 1506cm^{-1} (at 72 hours).

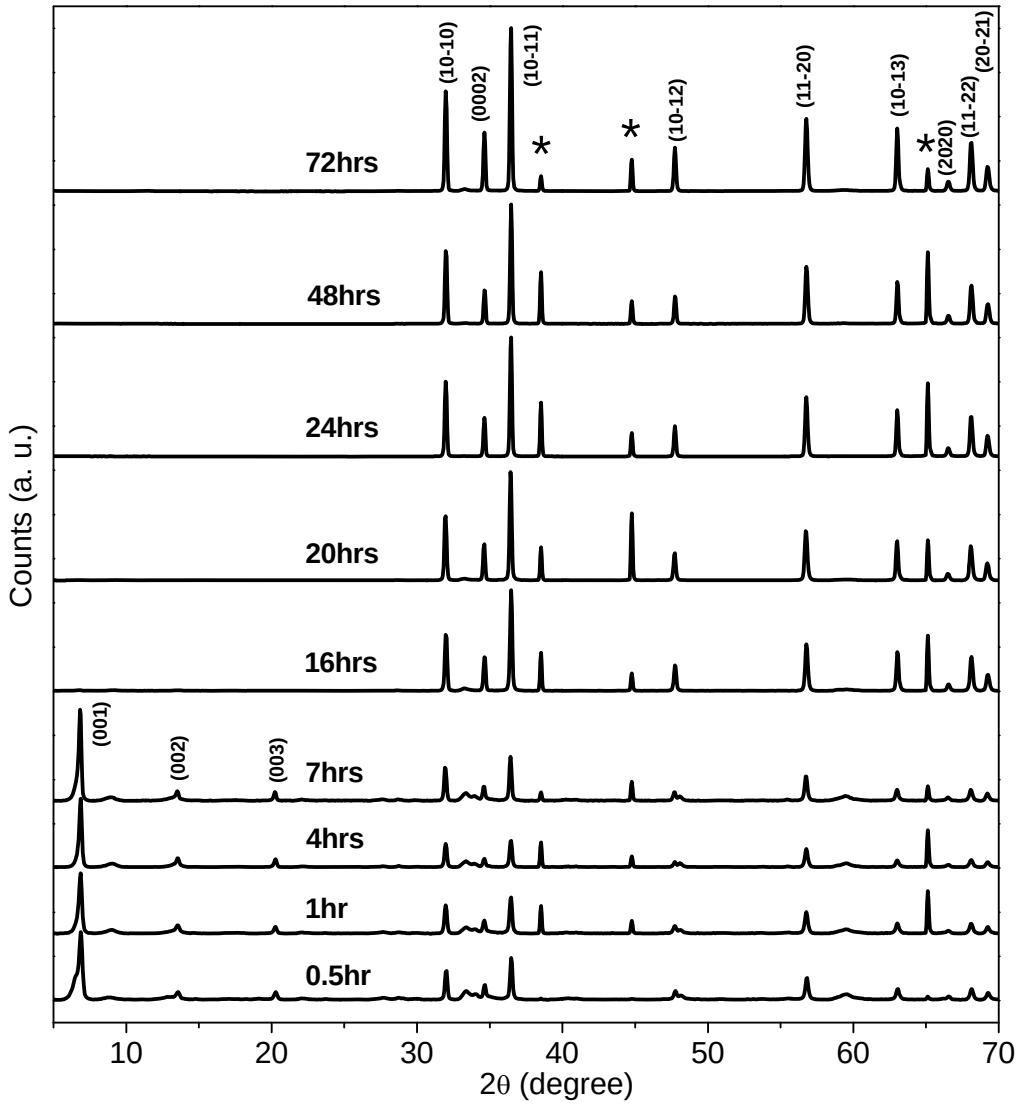

Figure 5.3 XRD diffractograms of precipitates collected at 30 minutes, 1 hour, 4 hours, 7 hours, 16 hours, 20 hours, 24 hours, 48 hours and 72 hours. The positions of diffraction peaks originating from aluminium sample holder are marked with asterisks. Four-digit and three-digit Miller indices were assignable to crystal planes of ZnO and LBZA respectively.

The coordination mode of acetate ions to metal ions, either by monodentate, bidentate chelating, or bidentate bridging is reflected by the $\Delta\nu_{as\text{-}s}$ values,[15, 19] the difference between $\nu_{as}(COO^-)$ and $\nu_s(COO^-)$. The $\Delta\nu_{as\text{-}s}$ value for precipitates (up to 24 hours) was ~163cm^{-1}. This $\Delta\nu_{as\text{-}s}$ value was very closed to both the experimentally determined $\Delta\nu_{as\text{-}s}$ for an ionic complex of metal ion-acetate ions[15] and the calculated $\Delta\nu_{as\text{-}s}$ for acetate ion acting as a bridging ligand[19] for Zn^{2+} ions. Although LBZA was not detected by XRD from precipitates at 16 hours and beyond, FTIR has shown the

presence of trace amounts of acetate in these precipitates even though the major component was ZnO.

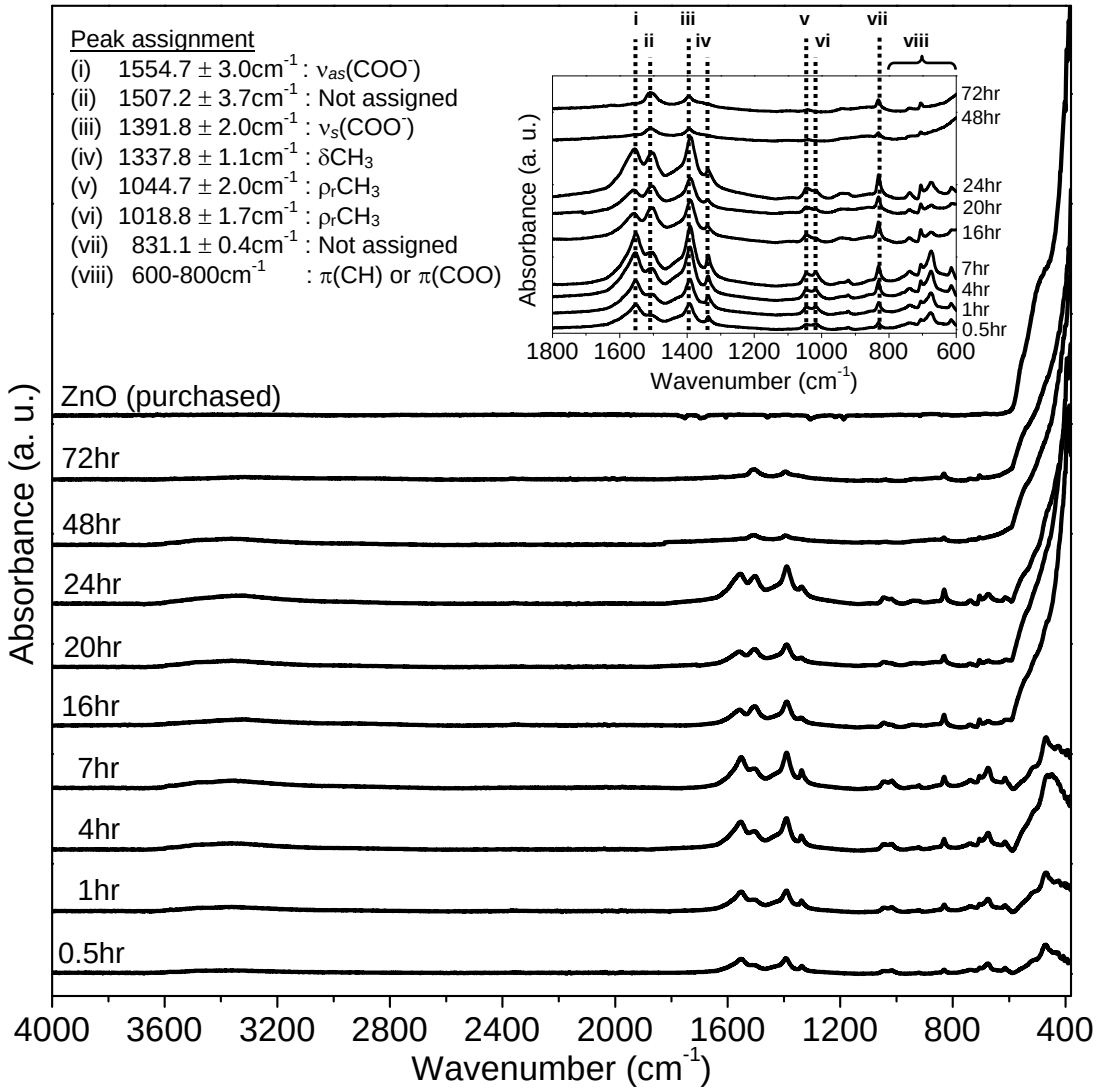

Figure 5.4 FTIR spectra of precipitates collected after 30 minutes, 1 hour, 4 hours, 7 hours, 16 hours, 20 hours, 24 hours, 48 hours and 72 hours. ZnO purchased from Sigma Aldrich was used as reference and inset magnifies the absorption region of 600-1800cm^{-1}. Abbreviations used are ν, stretching; δ, in-plane bending or deformation; ρ_r, rocking; and π, out-of-plane bending while subscripts *as* and *s* denote asymmetric and symmetric modes respectively. Peak assignment shows the average wavenumber ± standard deviation for all samples shown in this figure.

Subjecting the precipitates to thermal decomposition (TGA) resulted in three stages of weight loss (**Appendix 5.2**). The release of intercalated water occurred up to 100°C followed by dehydroxylation of the zinc hydroxide in LBZA to form ZnO (100°C-

168°C) while the decomposition of acetate occurred at higher temperature (168°C-700°C).[10, 12, 21, 22] As shown in **Figure 5.5**, for precipitate collected at 30 minutes, the 31% weight loss observed was very close to the results shown in the literature.[10, 23] Based on a study by Tokumoto *et al*., a complete conversion of LBZA (determined as $Zn_5(OH)_8Ac_2{\cdot}2H_2O$) to ZnO results in a 34wt% loss.[23] This finding supported the argument that LBZA was the major component of the 30 minutes-precipitate, and the small fraction of non-thermally decomposable material was ZnO. The reduction of precipitate weight loss with reaction time was caused by the reduction of LBZA fraction and the increase of ZnO fraction in the precipitate with time. The stable weight loss percentage from 48 hours onwards indicating equilibrium state of LBZA conversion to ZnO was reached.

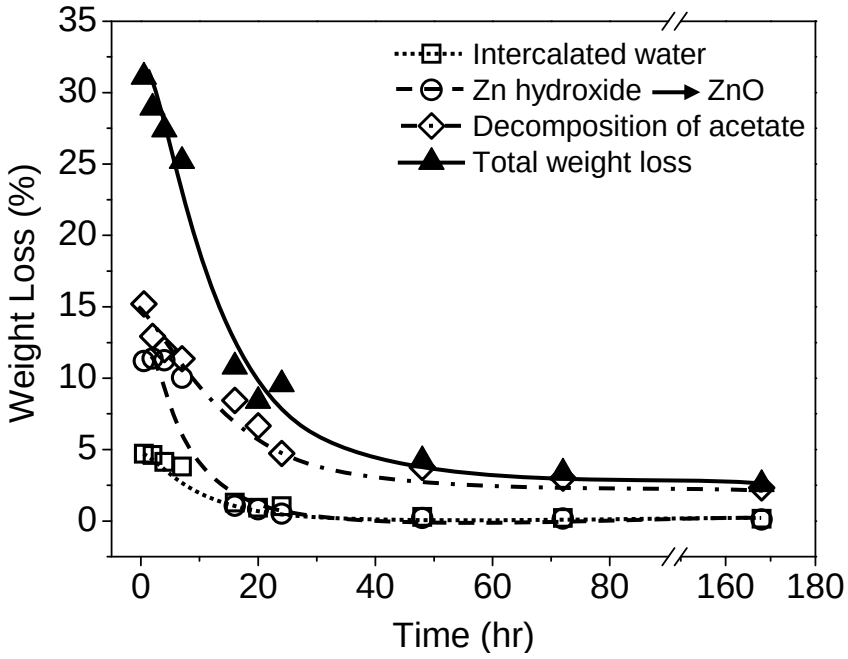

Figure 5.5 Weight loss caused by thermal decomposition (TGA) plotted by component weight loss and total weight loss as a function of reaction time (from 30 minutes to 168 hours).

XRD, FTIR, TGA and SEM results confirmed that the formation of ZnO from the $ZnAc_2$-NH_3 reaction at 50°C occurred via the formation of LBZA as the intermediate compound. LBZA is a layered single metal hydroxide (LSMH) or layered double hydroxide (LDH) with disordered lattice consisting of a main layer with Zn^{2+} ions in octahedral coordination and intermediate layers of tetrahedrally-coordinated Zn^{2+}.[14, 24,

[25] The interlayer spacing of the intermediate compound, determined as 12.87±0.05Å, was typical for LBZA, 12Å~15Å.[10-14] Since acetate ions are a good complexant for Zn^{2+},[26] these zinc hydroxide layers are held together by acetate ions and water molecules intercalated in between the layers. The $\Delta\nu_{as\text{-}s}$ value for the stretching vibration mode of COO^- of ~163cm^{-1} implied these acetate ions held the layers together either by the formation of ionic complexes[15] or by being a bridging bidentate ligand.[19] However based on the studies of LBZA as an ionic exchange material[11, 14, 27, 28] the intercalated acetate ions are exchangeable with nitrate and organic anions.[11, 28] Therefore the intercalated acetate ions in the LBZA formed were most probably free[12] or bound via the formation of ionic complex with the zinc hydroxide layers. When $ZnAc_2$ and NH_3 were mixed, LBZA was formed and more or less instantaneously, it started to be converted to ZnO based on the detection of ZnO in the 30 minute-precipitate. The amount of ZnO converted from LBZA increased with time and eventually ZnO became the major component of the precipitate at 16 hours. In the presence of acetate ions, the precursors of ZnO formation have been reported to be $Zn_{10}O_4Ac_{12}$,[29, 30] Zn_4OAc_6,[23, 30] or $Zn_5(OH)_5Ac_2{\cdot}2H_2O$.[23] The interlayer spacing from XRD and the weight loss from TGA suggest that the intermediate compound in this study was most probably $Zn_5(OH)_5Ac_2{\cdot}2H_2O$.

5.3.2 Reduction of the rate of LBZA conversion to ZnO by EM-12

In the absence of additives, ZnO was detected as the major component in precipitate collected at 16 hours. Considering the formation of ZnO occurred via LBZA as the intermediate compound, the presence of EM-12 reduced the rate of ZnO formation, leading to the detection of LBZA instead of ZnO as the major component after 24 hours reaction as shown in **Figure 5.6a**. This effect will be referred to as "delayed-formation" hereafter. The delayed-formation of ZnO was EM-12 concentration-dependent. In the presence of 0.1mM EM-12, no significant effect was observed (**Figure 5.6a(i)**). In the presence of 0.2mM and 0.3mM EM-12, LBZA was detected as the major phase at 24 hours, **Figure 5.6a(ii-iii)**, and ZnO detected as the major phase was not observed at 24 hours but at 48 hours, **Figure 5.6b(ii-iii)**. For the highest concentration of EM-12 studied, 0.5mM, LBZA remained as the major phase at 48

hours based on SEM and XRD results (**Figure 5.6b(iv)**), and up to 168 hours based on SEM data (**Figure 5.7**). Precipitates sampled at 72 hours, 96 hours and 168 hours from 0.5mM EM-12 reaction were not sufficient for XRD analysis. The interlayer spacing values of LBZA formed in the presence of EM-12 at 24 hours and 48 hours, shown in **Figure 5.6**, were comparable with those of LBZA formed in the absence of EM-12.

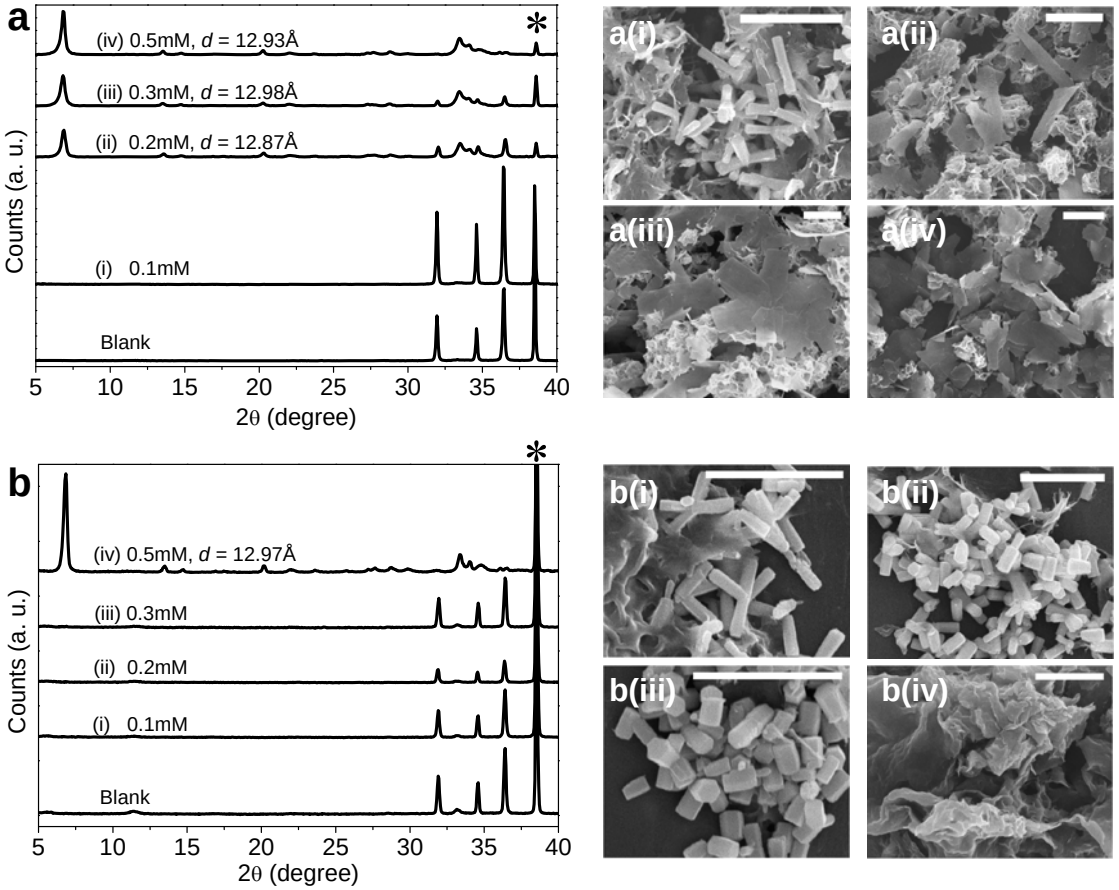

Figure 5.6 XRD diffractograms of precipitates collected in the presence of EM-12 with different concentrations at (a) 24 hours and (b) 48 hours. The diffractograms of the blank was included for comparison and the position of diffraction peak arisen from the aluminium sample holder is marked with asterisk. *d* denotes interlayer spacing of LBZA formed. The SEM images of precipitates in the presence of EM-12 at 24 hours and 48 hours are shown on the right of the their XRD results. All scale bars shown are 5μm and (i) to (iv) correspond to 0.1mM, 0.2mM, 0.3mM and 0.5mM respectively.

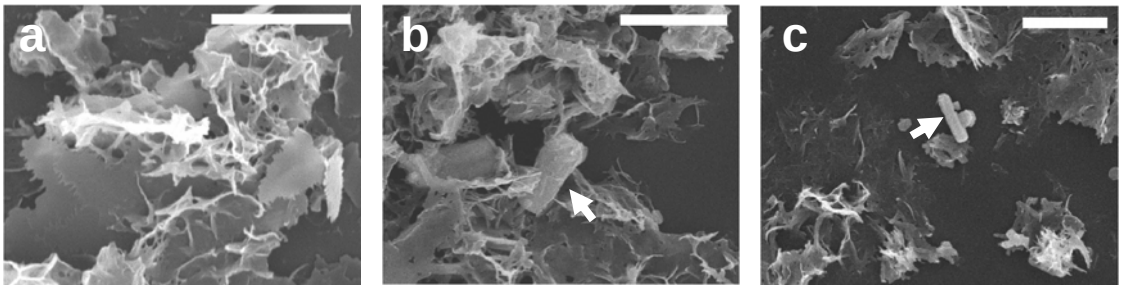

Figure 5.7 The SEM images of precipitates collected in the presence of 0.5mM EM-12 at (a) 72 hours, (b) 96 hours, and (c) 168 hours. All scale bars shown are 5μm. ZnO crystals are indicated by white arrows.

The phenomenon of where LBZA (the intermediate compound) remained stable for longer periods of time in the presence of EM-12 was further supported by TGA results. As shown in **Figure 5.8a**, the 24 hour-precipitates, collected from reactions with EM-12 concentration >0.1mM (marked with asterisks), have a total weight loss of ~34%. The weight loss caused by dehydroxylation for these precipitates was calculated as ~15% (**Figure 5.8b**). Therefore, the major component of these precipitates was LBZA. When a large fraction of LBZA had been converted to ZnO at 48 hours, total weight loss and dehydroxylation weight loss reduced to ~15% and ~2% respectively, **Figure 5.8c**. No significant change in total weight loss and weight loss components for precipitates collected from 0.5mM EM-12 reaction at different times confirming that LBZA remained stable after 168 hours, **Figure 5.8d**. Thus, the addition of EM-12 at low concentration (<0.5mM) into selected ZnO-forming reaction delayed ZnO formation and when higher concentration was added, ZnO formation inhibition (up to 168 hours) took place. The ZnO crystals obtained from the delayed formation were found to be asymmetrical where the asymmetry increased with EM-12 concentration to the extent that un-twinned hexagonal rods were formed instead of twinned hexagonal rods, **Figure 5.6b(ii-iii)**. The effect of EM-12 on ZnO morphology is discussed in **Section 5.3.5** while the cause of the delay of ZnO formation in the presence of EM-12, investigated using ICP-OES, FTIR and the quantification of EM-12 concentration in supernatants, is reported in the following section.

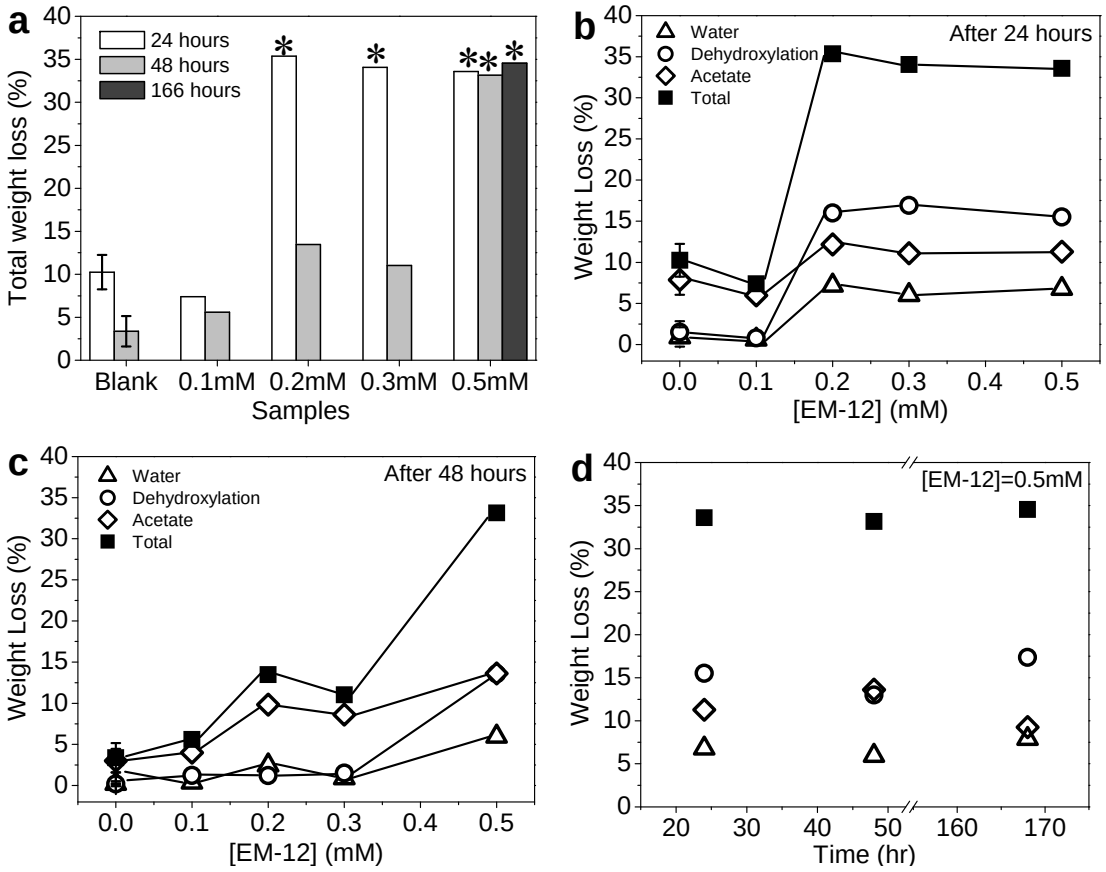

Figure 5.8 Weight loss via thermal treatment (TGA): (a) total weight loss for 24 hours, 48 hours and selected 168 hours precipitates with difference [EM-12] and; total weight loss and weight loss by components for precipitates collected (b) at 24 hours as a function of [EM-12]; (c) at 48 hours as a function of [EM-12]; and (d) for [EM-12]=0.5mM at different reaction time.

5.3.3 Zn^{2+}-EM-12 complexation and the delay/suppression of ZnO formation

The presence of EM-12 extended the period where LBZA was the intermediate phase and hence delayed ZnO formation or suppressed the formation of ZnO completely. According to Gerstel *et al.*,[7] amino acids having side chain functionality that interact electrostatically with Zn^{2+} in solution or on a crystal seed interface would impose a strong influence on the morphology of the deposits formed. The presence of amino acids that could form complexes with Zn^{2+} such as histidine and cysteine, may reduce the amount of free Zn^{2+} in solution. Thus, the delay/suppression of ZnO formation is believed to be closely related to the change of Zn^{2+} concentration in solution when EM-12 was present.

The $^{\%}Zn^{2+}$, the percentage of Zn^{2+} in solution with respect to its prepared amount, was studied as a function of reaction time and showed in **Figure 5.9**. For data analysis, the time point at 1 hour was used to represent the LBZA formation stage while 96 hours was used as the equilibrium state; denoted by $^{\%}Zn^{2+}_{t=1hr}$ and $^{\%}Zn^{2+}_{t=96hr}$ respectively. **Figure 5.9** shows that EM-12 addition increased both the $^{\%}Zn^{2+}_{t=1hr}$ and $^{\%}Zn^{2+}_{t=96hr}$. The increase of $^{\%}Zn^{2+}_{t=1hr}$ and $^{\%}Zn^{2+}_{t=96hr}$ with respect to the Blank was also calculated and shown as $\Delta^{\%}Zn^{2+}_{t=1hr}$ and $\Delta^{\%}Zn^{2+}_{t=96hr}$ respectively (**Figure 5.10a**). Although EM-12 addition increased the $^{\%}Zn^{2+}$ at both stages, the $\Delta^{\%}Zn^{2+}_{t=1hr}$ was directly proportional to EM-12 concentration but not for $\Delta^{\%}Zn^{2+}_{t=96hr}$. This difference suggests that EM-12 formed complexes with Zn^{2+} from the very beginning of the reaction. The inter-stage difference, $\Delta^{\%}Zn^{2+}_{Interstage}=^{\%}Zn^{2+}_{t=1hr}-^{\%}Zn^{2+}_{t=96hr}$, was then calculated. **Figure 5.10b** shows that $\Delta^{\%}Zn^{2+}_{Interstage}$ value reduced slightly from 10.4% as EM-12 concentration was increased. When EM-12 concentration was further increased to 0.5mM, the $\Delta^{\%}Zn^{2+}_{interstage}$ value dropped to ~7%, coincides with when "suppression" of ZnO formation was observed.

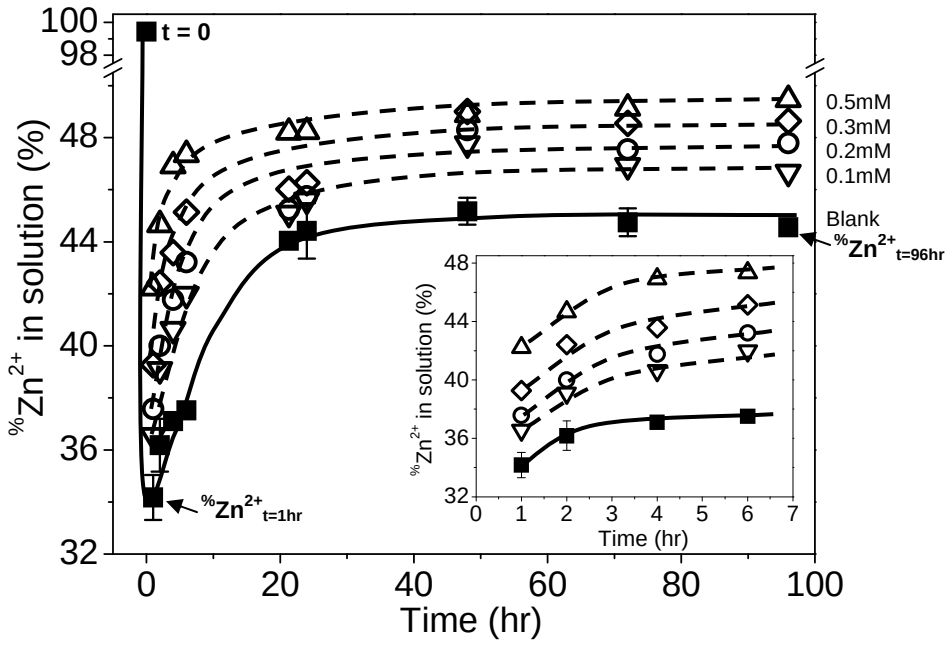

Figure 5.9 $^{\%}Zn^{2+}$, the percentage of Zn^{2+} in solution with respect to the prepared amount, as a function of reaction time for EM-12-added reactions at different concentrations. $^{\%}Zn^{2+}_{t=1hr}$ and $^{\%}Zn^{2+}_{t=96hr}$ correspond to $^{\%}Zn^{2+}$ at the LBZA formation stage and at the equilibrium state respectively.

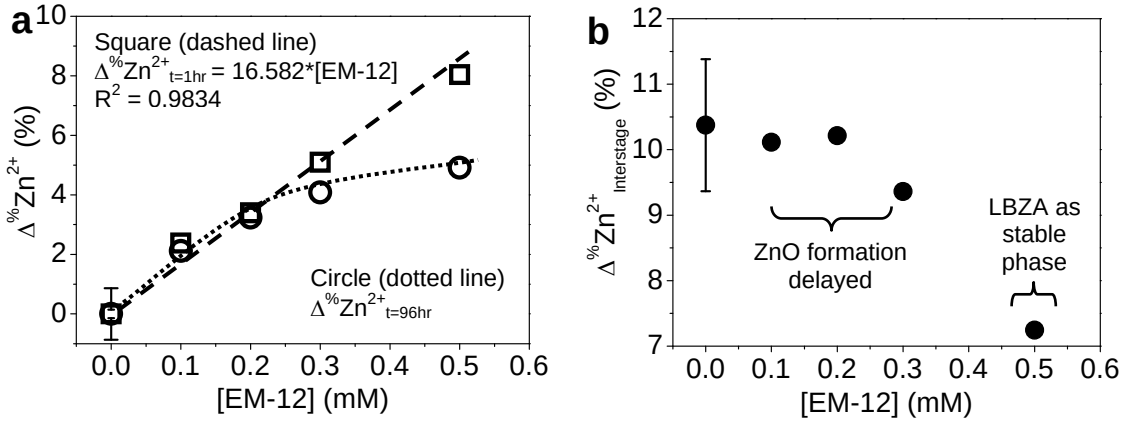

Figure 5.10 The increase of $^{\%}Zn^{2+}$ with respect to the Blank at (a) the LBZA formation stage (square, dashed line), $\Delta^{\%}Zn^{2+}_{t=1hr}={}^{\%}Zn^{2+}_{t=1hr/Sample}-{}^{\%}Zn^{2+}_{t=1hr/Blank}$, and at equilibrium (circle, dotted line), $\Delta^{\%}Zn^{2+}_{t=96hr}={}^{\%}Zn^{2+}_{t=96hr/Sample}-{}^{\%}Zn^{2+}_{t=96hr/Blank}$, and (b) $\Delta^{\%}Zn^{2+}_{Interstage}$, the difference between $^{\%}Zn^{2+}_{t=1hr}$ and $^{\%}Zn^{2+}_{t=96hr}$ for the Blank and reactions with different EM-12 concentrations.

The binding of amino acid residues with Zn^{2+} is a very common phenomenon in biological systems. The complexation of amino acids,[31] peptides,[32-34] or zinc finger binding motifs[6, 35, 36] of proteins has been extensively studied. In general, cysteine (C, Cys), histidine (H, His), glutamate acid (E, Glu), and aspartic acid (D, Asp) have been found to have strong binding affinity to Zn^{2+} via their side chain functions, offering S, N, and O coordination.[6] Quite often bis(cysteinyl) or bis(histidinyl) protein sequences in zinc fingers, such as Cys-$(X)_n$-Cys or His-$(X)_n$-His with very short spacer units ($(X)_n$ is 1-4 amino acids) are the ligating units. Based on this understanding EM-12 having two His residues separated by a two amino acid-spacer and the presence of methionine (M, Met) containing S atom would suggest the possibility of Zn^{2+}-EM-12 binding.

When forming a complex with Zn^{2+} in solution, EM-12 would be retained in the supernatant which was confirmed as such through the measurement of EM-12 concentration in supernatants collected at different reaction times. It is clearly shown in **Figure 5.11**, for 0.1mM to 0.3mM of EM-12, all EM-12 added was retained in solution starting from the early stages of the reaction. This observation, consistent with the linear relationship between $^{\%}Zn^{2+}_{t=1hr}$ and EM-12 concentration in **Figure 5.10a**, suggests immediate "binding" between Zn^{2+} and EM-12; which remained stable throughout the reaction. For 0.5mM of EM-12 where LBZA remained stable throughout the reaction (SEM and TGA), 92~93% (~0.46mM) of the added EM-12

remained in solution within the first 10 hours but the concentration of EM-12 in solution gradually increased thereafter and eventually reached 0.5mM at 72 hours. The amount of EM-12 present in the blank reaction was below the detection limit and is not shown in **Figure 5.11**.

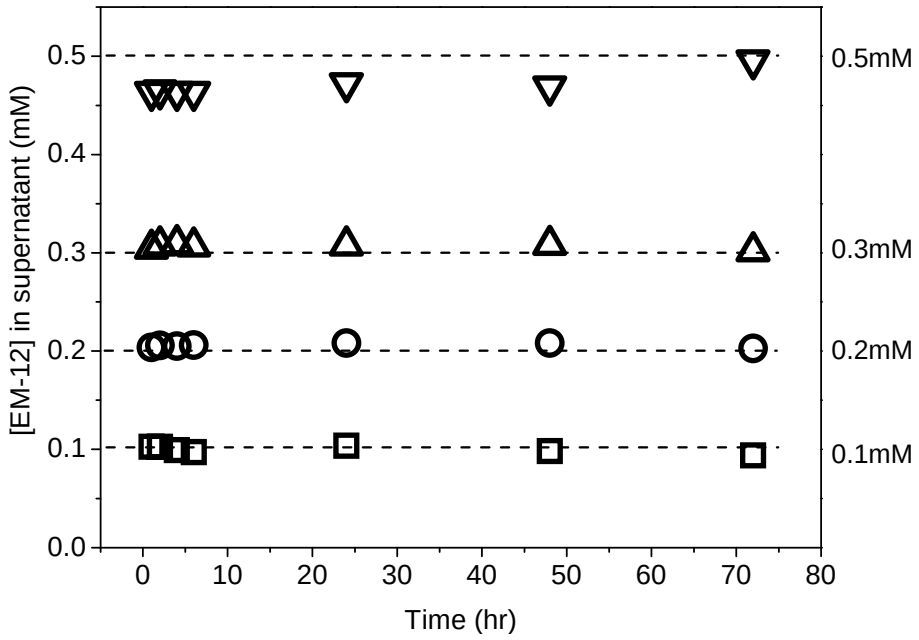

Figure 5.11 EM-12 concentration, [EM-12], in supernatants collected at different reaction time from reactions added with 0.1mM, 0.2mM, 0.3mM, and 0.5mM of EM-12 (shown on the right). The amount of EM-12 present in the blank was below the detection limit of the method used.

Figure 5.12 shows the FTIR spectra for 24 hour-precipitates where spectra typical for LBZA were observed for 0.2mM to 0.5mM of EM-12 while a strong ZnO absorption peak in the 430-530cm^{-1} region was identified for 0.1mM EM-12 and the Blank. Since the COO^- stretching vibration frequency from acetate overlaps with the amide-II band (1500-1600cm^{-1}), the amide-I band (1600-1700cm^{-1}) and C-O stretch (1000-1260cm^{-1}) were used for the identification of EM-12 in precipitates and lyophilised supernatant. The amide-I band and C-O stretch were absent from the 1300-1800cm^{-1} region of the precipitates spectra (inset of **Figure 5.12**) but present in the spectra of lyophilised supernatants collected at 48 hours (**Figure 5.13**). These results provided evidence that EM-12 did not co-precipitate with products but was retained in solution. Therefore the delay/suppression of ZnO formation was a result of Zn^{2+}-EM-12 complexation. In fact, this effect on the reaction speed of ZnO formation has also been observed by others

when PVP was added into ZnO forming reactions.[37] The authors attributed the delay/suppression of ZnO formation effect to the possible coordination between PVP and Zn^{2+}.

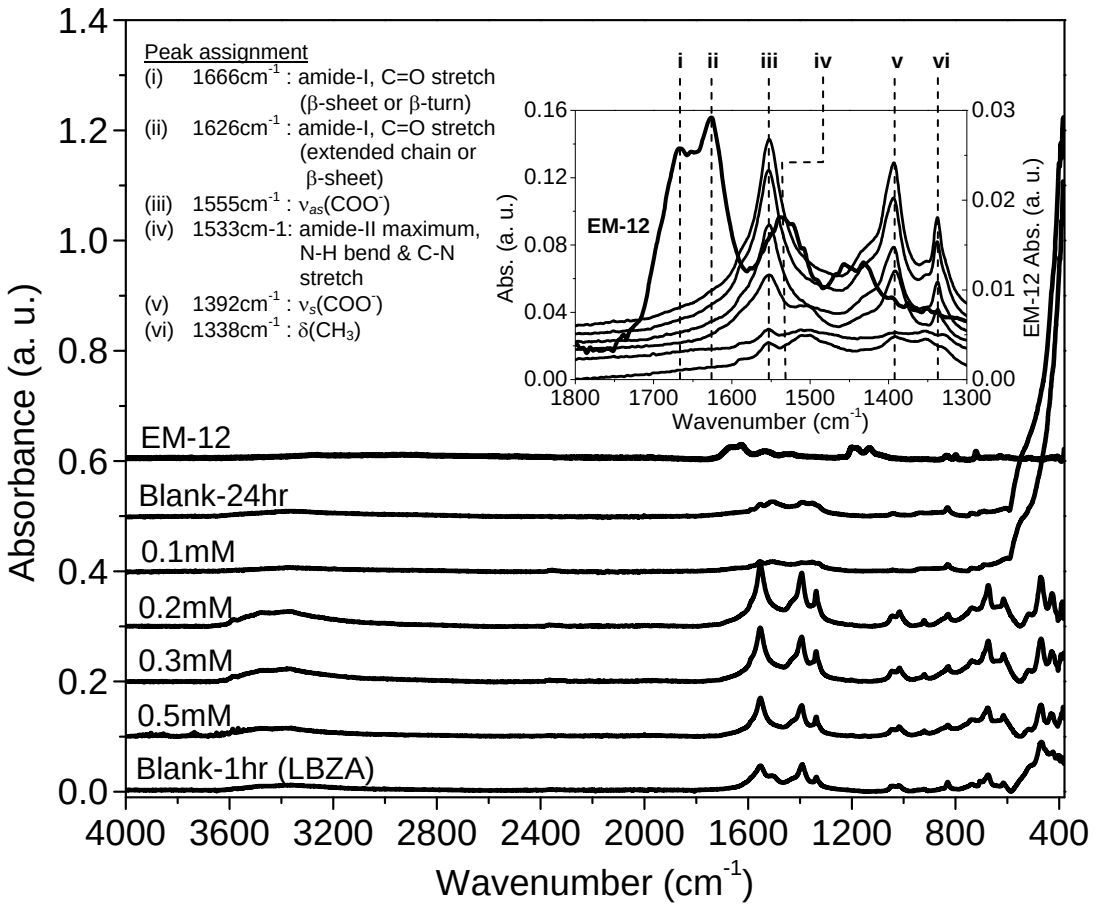

Figure 5.12 FTIR spectra of 24 hour-precipitates in the absence and presence of EM-12. The spectra of EM-12, and the 1 hour-Blank are included for reference. Inset spectra label (from top to bottom at i): EM-12, 0.2mM, 0.3mM, 0.5mM, Blank-1hr (LBZA), 0.1mM, and Blank-24hr. Abbreviations used are ν, stretching; δ, in-plane bending or deformation; while subscripts *as* and *s* denote asymmetric and symmetric modes respectively.

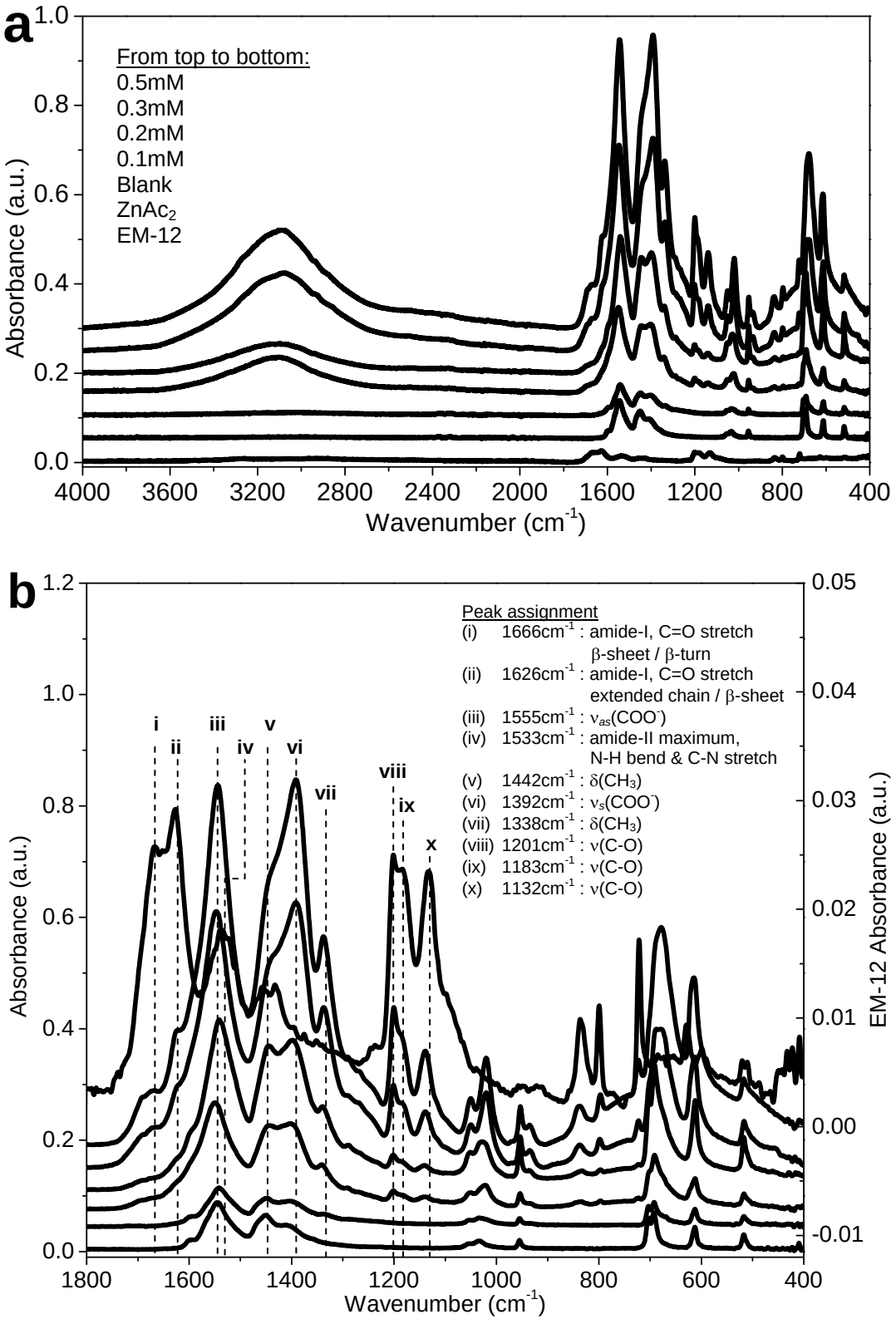

Figure 5.13 FTIR spectra of the lyophilised supernatant collected at 48 hour from reactions in the presence of EM-12: (a) 400-4000cm^{-1} and (b) 400-1800cm^{-1}. The spectra of EM-12 and the Blank are included for comparison. Spectra label for (b) (from top to bottom at i): EM-12, 0.5mM, 0.3mM, 0.2mM, 0.1mM, Blank, and $ZnAc_2$. Abbreviations used are ν, stretching; δ, in-plane bending or deformation; while subscripts *as* and *s* denote asymmetric and symmetric modes respectively.

5.3.4 Comparison with EC-12 with higher complexation capability

Up to this point, the effect of EM-12 on "delaying" or "suppressing" ZnO formation was very different from the ZnO catalytic effect shown by ET-17.[4 5] This difference was believed to be caused by the additional GGGSC tag on ET-17. Based on the side chain pK_a calculation using Marvin,[38] the charges of EM-12 and EC-12 side chains at pH 7.0±0.1 (**Appendix 5.3**) are summarised in **Table 5.1**. At this narrow range of pH, the side chain and termini charges of both peptides are nearly identical and their net charges are the same. Although only E_1 and P_{12} are anionic, residues such as histidine, cysteine, and methionine are able to coordinate with Zn^{2+}.[6, 31, 33] Histidine can bind metal ions through the imidazole Nε2 or Nδ1 and became a bridging ligand when present in its deprotonated state. Although cysteine binds to metal ions most frequently in its deprotonated cysteinate form, a neutral cysteine is able to serve as a ligand in ferrous heme iron while non-deprotonable methionine binds through its sulphur lone pair.[6] Thus it is convincing that these two peptides were able to form complexes with Zn^{2+} thereby holding more Zn^{2+} in solution as demonstrated by EM-12 in **Section 5.3.3**.

Table 5.1 The charges of EM-12 and EC-12 side chain functional groups calculated using Marvin[38] at pH 7.0±0.1 at 298K.

EM-12 Sequence	E_1	A_2	H_3	V_4	M_5	H_6	K_7	V_8	A_9	P_{10}	R_{11}	P_{12}	Net Charge
Side Chain Charge	-		+				+						+
Terminal Charge	+											-	

EC-12 Sequence	E_1	A_2	H_3	V_4	C_5	H_6	K_7	V_8	A_9	P_{10}	R_{11}	P_{12}	Net Charge
Side Chain Charge	-					+	+						+
Terminal Charge	+											-	

At identical reaction conditions, when the M_5 of EM-12 was substituted by C_5 to form EC-12, a greater complexation capability for the latter was anticipated. The change of $[Zn^{2+}]$ in solution with time and its analysis are shown in **Figure 5.14** and **Figure 5.15** respectively. Similar to what was observed with EM-12 (**Figure 5.9**), an increase of $[Zn^{2+}]$ in solution compared to the Blank was observed throughout the reaction, **Figure 5.14**. The $\Delta^{\%}Zn^{2+}_{t=1hr}$ value, difference between sample and the Blank, was 25.5%/mM for reactions with EC-12 (dashed-line gradient in **Figure 5.15a**), much higher than that

caused by EM-12 addition, 16.6%/mM (dashed-line gradient in **Figure 5.10a**). As for $\Delta^{\%}Zn^{2+}_{t=96hr}$, its increase with EC-12 concentration was more or less linear but the $\Delta^{\%}Zn^{2+}_{t=96hr}$-EM-12 concentration relationship clearly showed deviation from linearity.

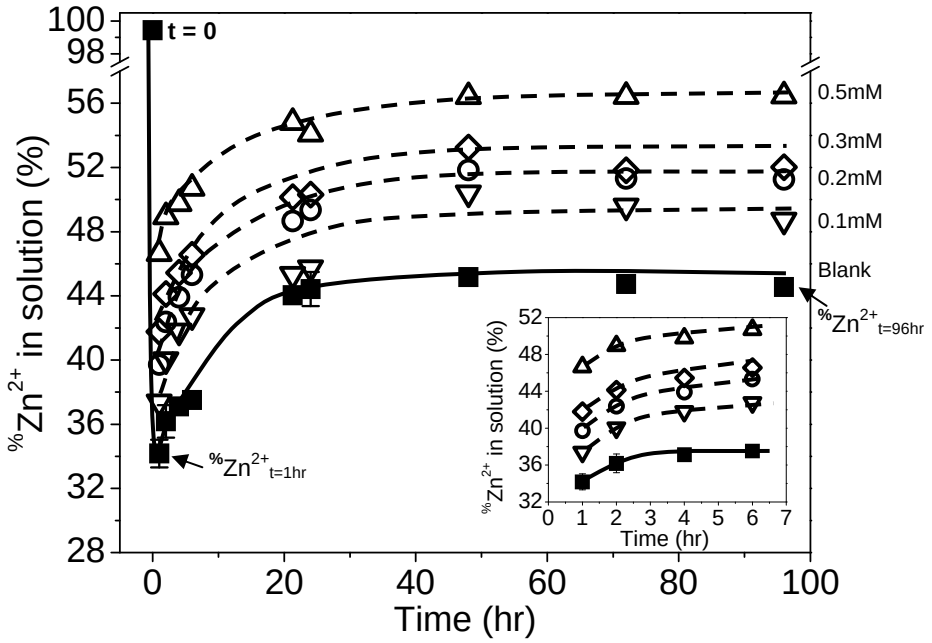

Figure 5.14 The amount of Zn^{2+} in solution (%) as a function of reaction time for reactions in the presence of EC-12 at different concentrations. $^{\%}Zn^{2+}_{t=1hr}$ and $^{\%}Zn^{2+}_{t=96hr}$ correspond to zinc concentration at LBZA formation stage and at equilibrium state respectively.

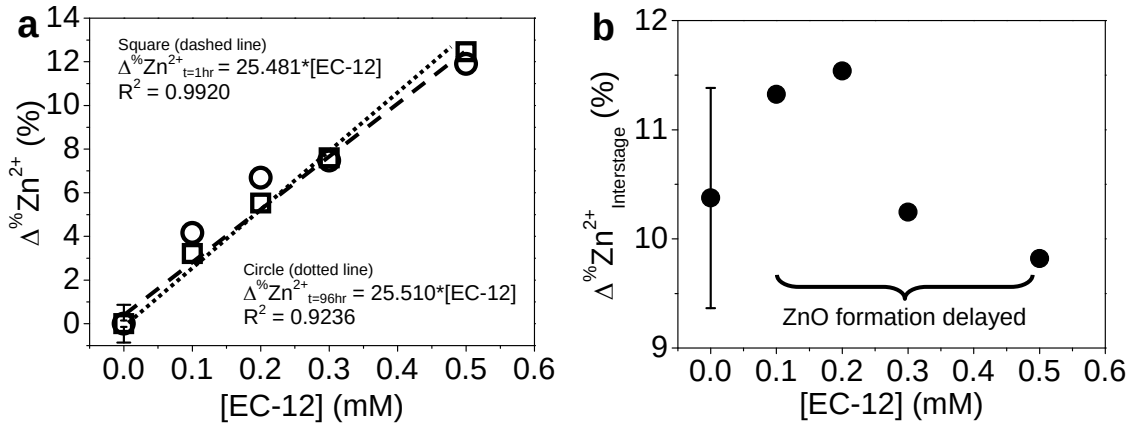

Figure 5.15 The increase of $^{\%}Zn^{2+}$ with respect to the Blank at (a) LBZA formation stage (square, dashed line), $\Delta^{\%}Zn^{2+}_{t=1hr}={}^{\%}Zn^{2+}_{t=1hr/Sample}-{}^{\%}Zn^{2+}_{t=1hr/Blank}$, and at equilibrium (circle, dotted line), $\Delta^{\%}Zn^{2+}_{t=96hr}={}^{\%}Zn^{2+}_{t=96hr/Sample}-{}^{\%}Zn^{2+}_{t=96hr/Blank}$, and (b) $\Delta^{\%}Zn^{2+}_{Interstage}$, the difference between $^{\%}Zn^{2+}_{t=1hr}$ and $^{\%}Zn^{2+}_{t=96hr}$ for the Blank and for reactions with different EC-12 concentrations.

For EM-12, all peptides formed complexes with Zn^{2+} started from the initial stage of reaction (100% detected in supernatant, **Figure 5.11**). However the complete complexation of EC-12 with Zn^{2+} only occurred at least 7 hours after the initiation of reaction as shown in **Figure 5.16** and the time required for complete complexation increased with EC-12 concentration: ~7 hours for 0.1-0.2mM, ~24 hours for 0.3mM, and ~30 hours for 0.5mM. The complexation profile shown by EC-12 was supported by the presence of the amide-I band only in the FTIR spectrum of 24 hour-precipitates collected from reaction in the presence of 0.5mM EC-12, **Figure 5.17**. Therefore, the studies of [Zn^{2+}] with time and complexation profiles revealed that; by retaining more Zn^{2+} in solution using either fewer peptide molecules (t≤24 hours) or comparable numbers of peptide molecules (t>24 hours), EC-12 was a better complexing agent with Zn^{2+} compared to EM-12.

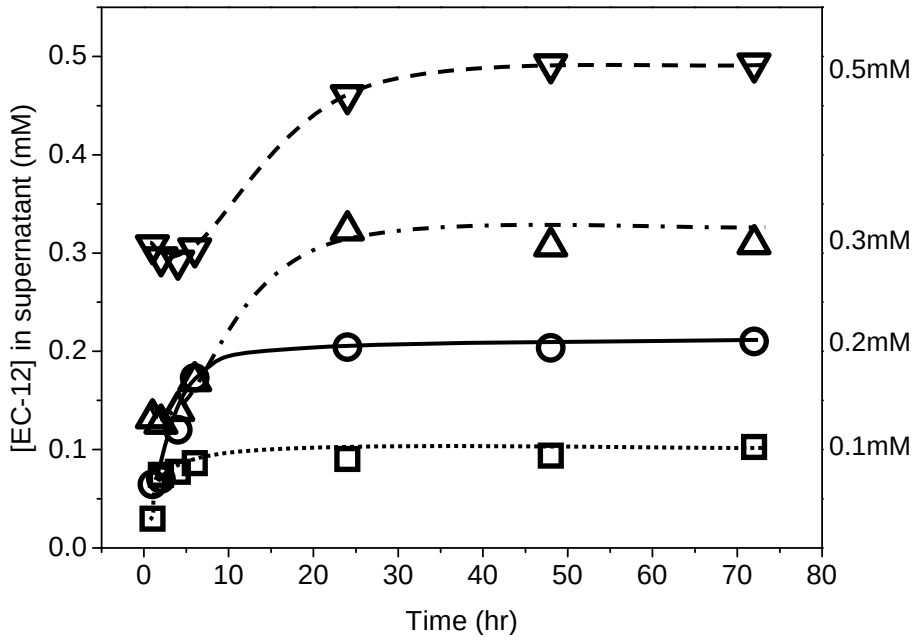

Figure 5.16 EC-12 concentration, [EC-12], in supernatants collected at different reaction times from reactions added with 0.1mM, 0.2mM, 0.3mM and 0.5mM of EC-12. The amount of EC-12 present in the blank was below the detection limit of the method used.

In the presence of EM-12, ZnO formation was delayed or suppressed depending on the concentration of EM-12 used. For EC-12-added reactions, only the delayed formation of ZnO was observed. This was deduced based on (i) all the precipitates collected at 24 hours were a mixture of ZnO and LBZA (FTIR in **Figure 5.17**, XRD in **Figure 5.18**),

and (ii) ZnO was the major phase in all the 48 hour-precipitates (SEM, **Figure 5.19**). In contrast to the action of EM-12, the fraction of LBZA in the 24 hour-precipitates reduced as EC-12 concentration was increased (**Figure 5.18a**). Furthermore EC-12 which was found to retain more Zn^{2+} in solution (**Figure 5.14** and **Figure 5.15**) did not show any instances of ZnO suppression as was observed with 0.5mM EM-12. In order to study the complexation behaviour of EM-12 and EC-12 with Zn^{2+}, $CoCl_2 \cdot 6H_2O$ that absorbs in the visible light region was used as a probe however, the studies were not successful as no tetrahedral complexes (akin to the Zn^{2+} complexes) formed (**Appendix 5.4**).

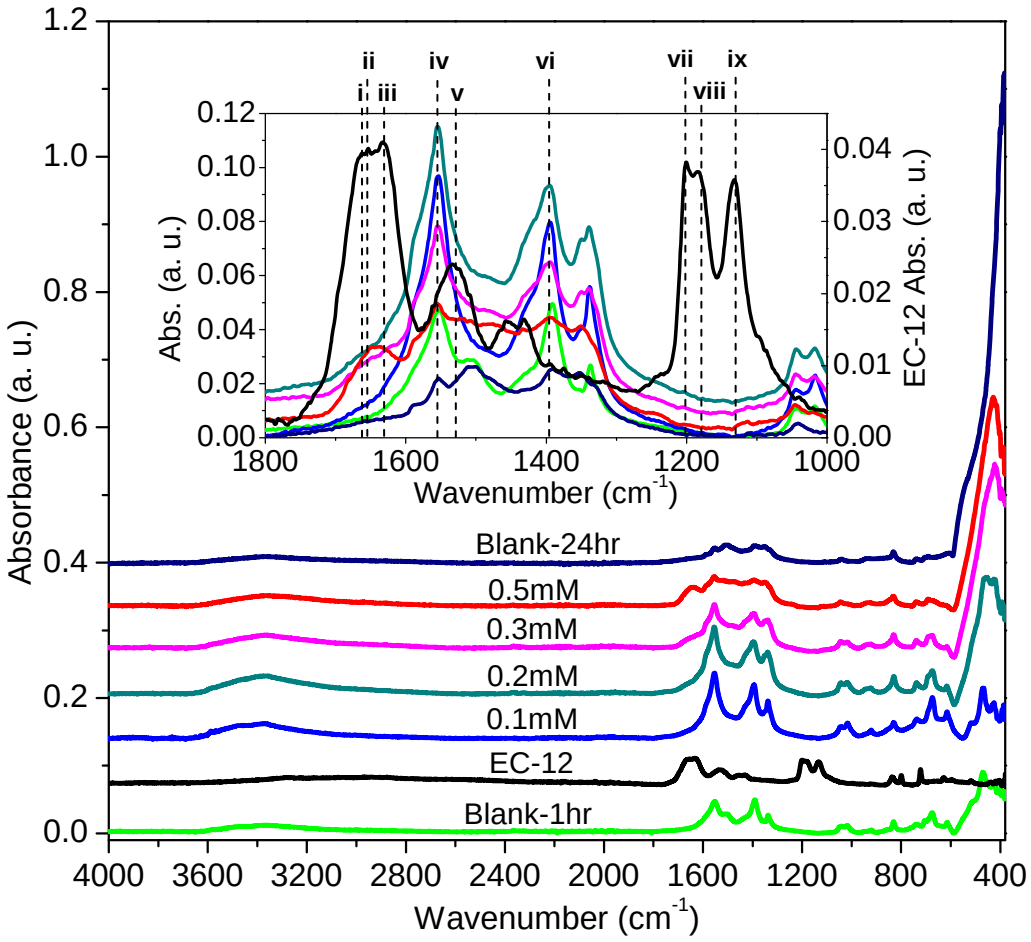

Figure 5.17 FTIR spectra of the lyophilised precipitates collected at 24 hour from reactions in the presence of EC-12 at different concentrations. The spectra of EC-12 and the Blanks are included for comparison. Peak assignments for the inset are (i)-(iii) for amide-I C=O stretch: 1662cm^{-1} (β-sheet/β-turn), 1654cm^{-1} (α-helices), and 1633cm^{-1} (extended chain/β-sheet); (iv) 1547cm^{-1}: $\nu_{as}(COO^-)$; (v) 1536cm^{-1} : amide-II maximum, N-H bend & C-N stretch; (vi) 1399cm^{-1}: $\nu_s(COO^-)$; (vii)-(ix) 1201cm^{-1}, 1183cm^{-1}, and 1132cm^{-1}: ν(C-O). ν represents stretching while subscripts *as* and *s* denote asymmetric and symmetric modes respectively.

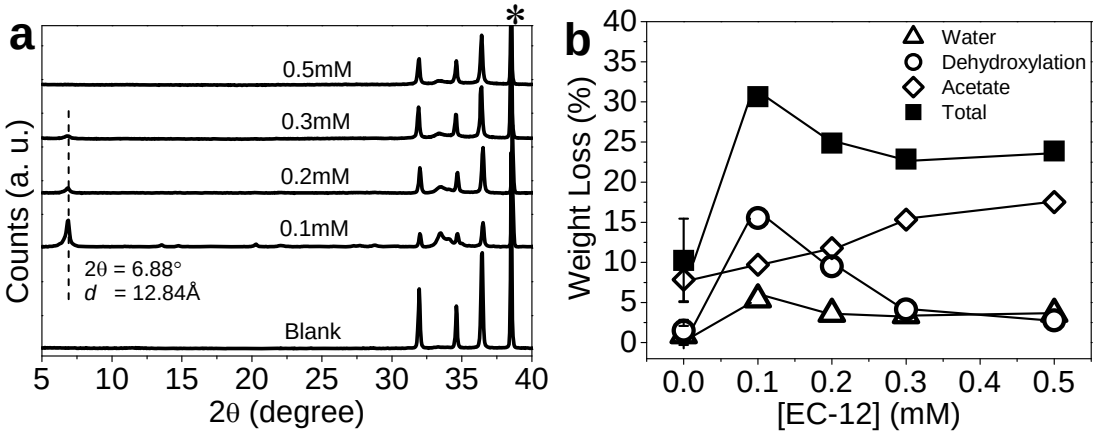

Figure 5.18 Characterisation of 24 hour-precipitates formed in the presence of EC-12 at different concentrations using (a) XRD and (b) TGA techniques. The position of diffraction peaks from aluminium sample holder is marked with an asterisk in (a), and *d* denotes the interlayer spacing of LBZA.

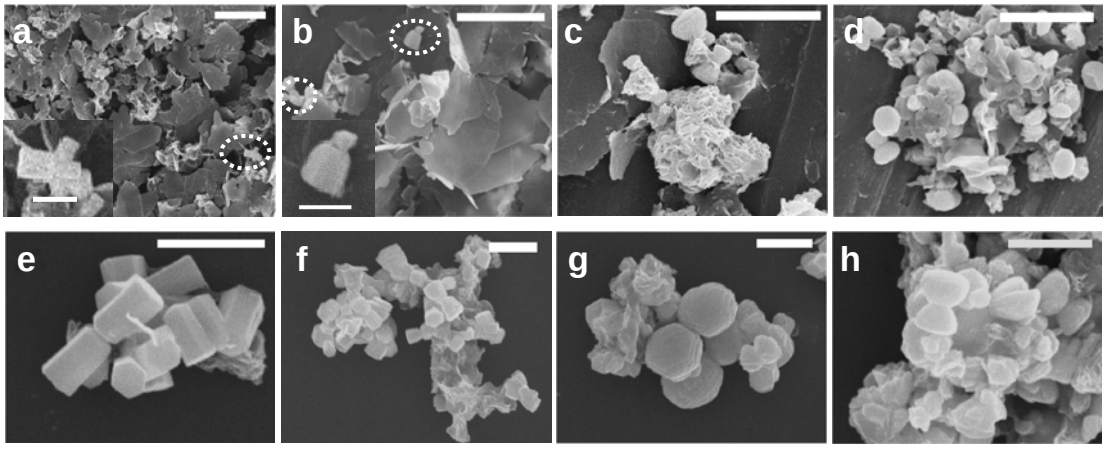

Figure 5.19 SEM images of precipitates collected at (a-d) 24 hours (scale bar 5μm, inset 1μm) and (e-h) 48 hours (scale bar 2μm). EC-12 concentration for SEM images shown are 0.1mM (a) and (e), 0.2mM (b) and (f), 0.3mM (c) and (g) and 0.5mM (d) and (h), respectively.

In respect of crystal morphology, ZnO crystals formed at 24 hours were mostly twinned but asymmetrical. However, crystals formed in the presence of 0.1-0.2mM EC-12 (**Figure 5.19a-b**) have more defined facets compared to those formed at higher concentrations of EC-12. ZnO crystals formed in the presence of 0.3-0.5mM EC-12 assumed the shape of mushrooms, **Figure 5.19c-d**. When reaction was extended to 48 hours, the asymmetrical crystals developed into more symmetrical crystals with smaller diameter at the twinned plane, having either a dumbbell shape (**Figure 5.19e-f)**

or an hourglass-like shape (**Figure 5.19g-h**). It is noticeable that these ZnO crystals were morphologically different from those obtained from the Blank reaction with uniform diameters along their *c*-axes.

5.3.5 Effects of EM-12 and EC-12 on the morphology of ZnO formed

The addition of EM-12 slowed down the conversion of LBZA to ZnO. The ZnO crystals obtained from this reaction (at 48 hours) have an EM-12 concentration-dependent morphology whereby the asymmetry of twinned crystals, in the majority, increased with EM-12 concentration and, in the presence of 0.3mM EM-12, un-twinned crystals were obtained as illustrated in **Scheme 5.1a** (refer to **Appendix 5.5** for SEM images). Due to the presence of branched, asymmetric, and untwined crystals, the dimension statistics of ZnO crystals were compiled according to one side of a twinned hexagonal rod or the entire un-twinned hexagonal rod (inset of **Figure 5.20b**) to allow comparison. From the dimension analysis, **Figure 5.20a**, the distribution of lengths (L) and diameters (D) were bimodal. Increasing EM-12 concentration significantly reduced crystal length and slightly increased its diameter. This trend was observed for both the larger side and smaller side of each crystal. This resulted in the crystal aspect ratio (L/D) reduction showed in **Figure 5.20b**.

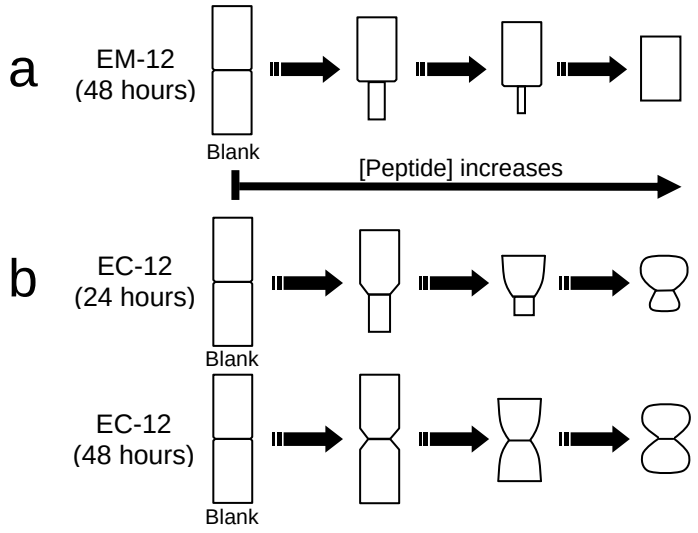

Scheme 5.1 The illustration of ZnO morphology (principal) in the presence of (a) EM-12 at different concentrations (based on 48 hour-precipitates) and, (b) EC-12 at difference concentrations collected after 24 hours and 48 hours. Images were created for morphology comparison only.

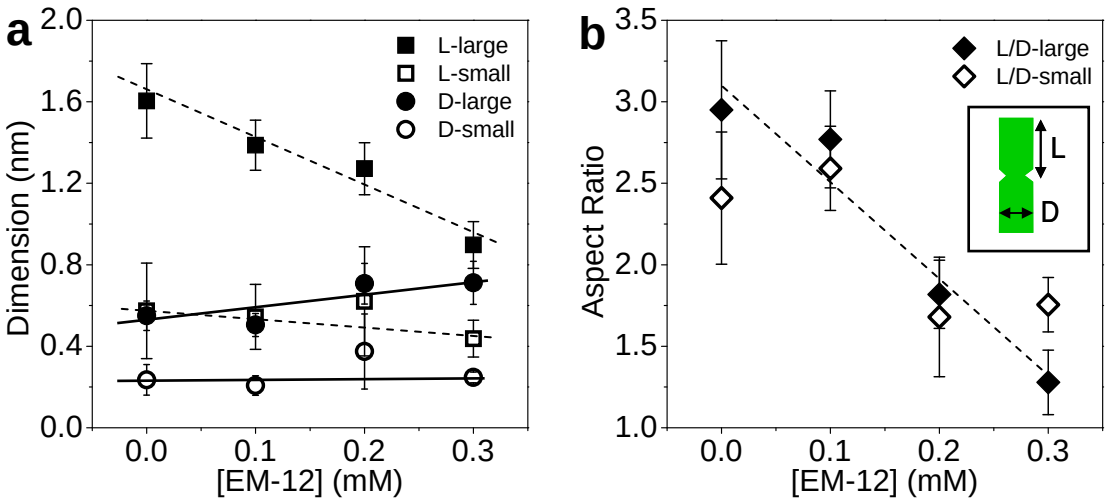

Figure 5.20 Dimension analysis (n>30) of asymmetric ZnO crystals on crystal (a) average length and diameter (L & D), and (b) average aspect ratio (L/D) as a function of EM-12 concentration with the error bar representing the standard deviation. Large and small indicated on the legend represent the larger or smaller crystal on each side of the twin plane. The inset in (b) shows the measurement of L and D.

As shown in **Scheme 5.1b**, the ZnO crystals generated in the presence of EC-12 were different from those obtained in the presence of EM-12 in three aspects; twinning, diameter uniformity along the *c*-axis of crystal, and how well defined the surface plane of the crystals were. There have been proposals that twinned hexagonal rods are formed by the aggregation of two approximately spherical particles.[39] However, the change of ZnO morphology with time in the presence of EC-12 has shown that crystal formation in this reaction occurred via an alternative mechanism. The reported ZnO synthesis in the presence of PVP[37, 40] was stated to have occurred by the formation of the first hexagonal rod (R_{1st}) followed by the growth of the second rod (R_{2nd}) on the first one. It is believed that EM-12-added reactions may have followed the same mechanism. Based on the 100% detection of added EM-12 in solution throughout the reaction (**Figure 5.11**) and its ability to form complex with Zn^{2+}, the increased of EM-12 concentration would reduce the amount of Zn^{2+} available for crystal growth. Therefore, in the presence of 0.3mM EM-12, the crystal growth equilibrated at an earlier crystal formation stage (before the end of R_{1st} growth), giving rise to the formation of untwined ZnO crystals. This was supported by the observation of untwined crystals (0.3mM EM-12) being shorter but have comparable diameters with those (larger side) formed at lower EM-12 concentrations (**Figure 5.20a**).

The cause of the ZnO morphology modification by EC-12 (from dumbbell-shaped hexagonal rods to mushroom-like crystals) remains unclear. During the first few hours of reaction, 40-75% of added EC-12 was absent from solution. These peptides may have modified the ZnO morphology via reversible adsorption on ZnO crystals as reported with PVP.[37] However the reversible adsorption of EC-12 on ZnO cannot be confirmed due to the presence of another solid phase, LBZA.

Two interesting morphology-related observations have been identified but remain unanswered: (i) the cause(s) of the transformation of dumbbell crystals to mushroom-like crystals with increasing EC-12 concenration, and (ii) the effect of EM-12 and EC-12 on the selection of twinning plane for ZnO crystals. The second point was raised because it has been reported that twinned hexagonal/bypiramidal hexagonal rods and dumbbell/mushroom-like crystals have different twinning planes, (000-1) and (0001) respectively.[41] More detailed and extensive studies will be required for the unravelling of the causes of these observations.

5.4 Conclusion

The effect of EM-12 and EC-12 on ZnO formation was explored using a $ZnAc_2$-NH_3 reaction. Detailed study of this reaction (in the absence of additive) revealed that (i) the formation of ZnO occurred via an intermediate compound which has been identified as LBZA, (ii) LBZA formation consumed more Zn^{2+} from solution compared to the equilibrium state of ZnO formation, created a unique $^{\%}Zn^{2+}$ profile (with time), and (iii) ZnO was detected as the major component in precipitates after 16 hours reaction. Depending on the concentration used, the presence of EM-12 in the $ZnAc_2$-NH_3 reaction delayed or suppressed ZnO formation by retaining a fraction of Zn^{2+} in solution (16.6% added Zn^{2+}/mM of EM-12) starting from the early stage of reaction and hence reduced the amount of Zn^{2+} available for ZnO synthesis. The high affinity of EM-12 towards Zn^{2+} was attributable to the presence of Zn^{2+}-binding residues such as histidine, methionine, and glutamate acid in the peptide. EC-12, that was expected to have higher Zn^{2+}-binding affinity, retained more Zn^{2+} in solution (25.5% added Zn^{2+}/

mM of EC-12 at early stages where LBZA was formed). However surprisingly, ZnO suppression was not observed and the delayed formation effect was weaker than that from EM-12 for the same range of peptide concentrations employed. The similarities and differences between these two peptides were reflected in the ZnO morphologies obtained. The increase of EM-12 concentration created a transformation of ZnO morphology from twinned hexagonal rods to untwinned hexagonal rods with reduced aspect ratio. The formation of ZnO crystals in the presence of EM-12 and EC-12 was proposed to occur via a rod-by-rod growth mechanism. Based on this mechanism, the formation of untwinned crystals at higher EM-12 concentration was a result of insufficient Zn^{2+} to initiate the growth of the second rod on the first one. The cause of the conversion of twinned hexagonal rods (the Blank) to dumbbell-shaped crystals which eventually turned to mushroom-like crystals is not understood.

References

1 C. K. Thai, H. Dai, M. S. R. Sastry, M. Sarikaya, D. T. Schwartz, and F. Baneyx, *Biotechnol. Bioeng.* **87**, 129-137 (2004).

2 K. Kjærgaard, J. K. Sørensen, M. A. Schembri, and P. Klemm, *Appl. Environ. Microbiol.* **66**, (1), 10-14 (2000).

3 M. M. Tomczak, M. K. Gupta, L. F. Drummy, S. M. Rozenzhak, and R. R. Naik, *Acta Biomater.* **5**, (3), 876-882 (2009).

4 M. Umetsu, M. Mizuta, K. Tsumoto, S. Ohara, S. Takami, H. Watanabe, I. Kumagai, and T. Adschiri, *Adv. Mater.* **17**, 2571-2575 (2005).

5 H. Bai, F. Xu, L. Anjia, and H. Matsui, *Soft Matter* **5**, 966-969 (2009).

6 I. Bertini, H. B. Gray, E. I. Stiefel, and J. S. Valentine, *Biological Inorganic Chemistry: Structure and Reactivity*. University Science Book: California, 2007.

7 P. Gerstel, P. Lipowsky, O. Durupthy, R. C. Hoffmann, P. Bellina, J. Bill, and F. Aldinger, *J. Ceram. Soc. Jpn.* **114**, (11), 911-917 (2006).

8 W. S. Rasband, *National Institute of Health, Bethesda, Maryland, USA* **http://rsb.info.nih.gov/ij/**, (1997-2004).

9 Y. Masuda, N. Kinoshita, and K. Koumoto, *Electrochim. Acta* **53**, 171-174 (2007).

10 E. Hosono, S. Fujihara, T. Kimura, and H. Imai, *J. Colloid and Int. Sci.* **272**, 391-398 (2004).

11 H. Morioka, H. Tagaya, J.-I. Kadokawa, and K. Chiba, *J. Mater. Sci. Lett.* **18**, 995-998 (1999).

12 L. Poul, N. Jouini, and F. Fiévet, *Chem. Mater.* **12**, 3123-3132 (2000).

13 Q. Cui, K. Yu, N. Zhang, and Z. Zhu, *Appl. Surf. Sci.* **254**, 3517-3521 (2008).

14 A. Kasai, and S. Fujihara, *Inorg. Chem.* **45**, 415-418 (2006).

15 K. Nakamoto, *Infrared and Raman Spectra of Inorganic and Coordination Compounds*. 4th edition ed.; John Wiley & Sons: 1986.

16 M. Gardener, in, Nottingham Trent University: 2000.

17 S. Aisawa, S. Takahashi, W. Ogasawara, Y. Umetsu, and E. Narita, *J. Solid State Chem.* **162**, 52-62 (2001).

18 V. Koleva, and D. Stoilova, *J. Mol. Struct.* **611**, 1-8 (2002).

19 M. Nara, H. Torii, and M. Tasumi, *J. Phys. Chem.* **100**, 19812-19817 (1996).

20 S. Ogata, I. Miyazaki, Y. Tasaka, H. Tagaya, J.-i. Kadokawa, and K. Chiba, *J. Mater. Chem.* **8**, 2813-2817 (1998).

21 R.-Q. Song, A.-W. Xu, B. Deng, Q. Li, and G.-Y. Chen, *Adv. Funct. Mater.* **17**, 296-306 (2007).

22 E. Hosono, S. Fujihara, T. Kimura, and H. Imai, *J. Sol-Gel Sci. Technol.* **29**, 71-79 (2004).

23 M. S. Tokumoto, S. H. Pulcinelli, C. V. Santilli, and V. Briois, *J. Phys. Chem. B* **107**, 568-574 (2003).

24 S.-H. Hwang, Y.-S. Han, and J.-H. Choy, *Bull. Korean. Chem. Soc.* **22**, (9), 1019-1022 (2001).

25 P. Gerstel, R. C. Hoffmann, P. Lipowsky, L. P. H. Jeurgens, J. Bill, and F. Aldinger, *Chem. Mater.* **18**, (1), 179-186 (2006).

26 P. J. Montoya-Peleaz, and R. S. Brown, *Inorg. Chem.* **41**, 309-316 (2002).

27 S. Ogata, H. Tagaya, M. Karasu, and J.-i. Kadokawa, *J. Mater. Chem.* **10**, 321-327 (2000).

28 M. Meyn, K. Beneke, and G. Lagaly, *Inorg. Chem.* **32**, 1209-1215 (1993).

29 E. A. Meulenkamp, *J. Phys. Chem. B* **102**, 5566-5572 (1998).

30 G. M. Thomas Schmidt, and Lubomir Spanhel, *Chem. Mater.* **10**, 65-71 (1998).

31 M. Rombach, M. Gelinsky, and H. Vahrenkamp, *Inorg. Chim. Acta* **334**, 25-33 (2002).

32 P. Gockel, M. Gelinsky, A. Meiβner, H. Albrich, and H. Vahrenkamp, *Inorg. Chim. Acta* **323**, 16-22 (2001).

33 R. Vogler, M. Gelinsky, L. F. Guo, and H. Vahrenkamp, *Inorg. Chim. Acta* **339**, 1-8 (2002).

34 P. Gockel, M. Gelinsky, R. Vogler, and H. Vahrenkamp, *Inorg. Chim. Acta* **272**, 115-124 (1998).

35 B. A. Krizek, D. L. Merkle, and J. M. Berg, *Inorg. Chem.* **32**, 937-940 (1993).

36 B. A. Krizek, B. T. Amann, J. Kilfoil, D. L. Merkle, and J. M. Berg, *J. Am. Chem. Soc.* **113**, 4518-4523 (1991).

37 J. Zhang, H. Liu, Z. Wang, and N. Ming, *J Cryst. Growth* **310**, 2848-2853 (2008).

38 Marvin 5.0.0 was used for drawing and characterizing chemical structures and substructures, 40 ChemAxon (http://www.chemaxon.com).

39 M. A. Vergés, A. Mifsud, and C. J. Serna, *J. Chem. Soc. Faraday Trans.* **86**, (6), 959-963 (1990).

40 J. Zhang, H. Liu, Z. Wang, and N. Ming, *Appl. Phys. Lett.* **90**, 113117-113119 (2007).

41 B. G. Wang, E. W. Shi, and W. Z. Zhong, *Cryst. Res. Technol.* **33**, (6), 937-941 (1998).

Chapter 6
General Discussion, Conclusions and Future Work

6.1 Discussion and Conclusions

The studies of peptide-mineral interactions presented within thesis aimed to identify and understand the effect(s) induced by peptides/selected motif on mineral formation. Peptide-mineral interactions were studied for amorphous silica and ZnO having a single crystalline phase. Investigations on three aspects were performed namely, the consumption of reactants with time, the level of peptide incorporation (into final products), and the morphology and composition of final products. In this study, the catalytic role of the histidine-imidazole on silicic acid condensation was verified using PVI and P-His (**Chapter 3**). ZnO-BPs or their derivatives (G-12[1] and GT-16,[1] EM-12[2] and EC-12) highly similar in sequence were identified from literature for ZnO studies. Despite their level of similarity, these peptides interact with different forms of zinc. Therefore, distinct effects were observed on Zn^{2+} concentration at equilibrium; the level of peptide incorporation (into final products); and the final products precipitated. G-12 and GT-16 modified ZnO morphology via an adsorption-growth inhibition mechanism (**Chapter 4**). EM-12 and EC-12 suppressed ZnO formation through complexation with Zn^{2+} in solution (**Chapter 5**). A detailed comparison of the level of modification between PVI and P-His; G-12 and GT-16; and EM-12 and EC-12 was carried out. Three common characteristics of how these additives work were revealed and are tabulated in **Table 6.1**. Firstly, a specific functionality was responsible for the effect induced while a supporting functionality enhanced the effect. Secondly, additives can interact with different species formed at different reaction stages. Finally, the type of interaction and interacting species determine the level of additive incorporation and its effect on equilibrium solution conditions.

Table 6.1 Summary of the findings from the study of peptide-mineral interactions.

Reaction System	Additive	Role(s)	Description of Effects and Interactions			Participating Functionality/Factor		Coprecipitation	
			[a]Effect	Species	Forces	Main	Enchancement	Yes/No	Rate
K_2SiCat_3-HCl pH 6.8 ± 0.05	PVI	Catalyst	(i) Increase trimerisation rate constant k_3 by 34%	Monosilicic acid	Hydrogen bond	Imidazole	-	Yes[16-18]	Reduced with time
			(ii) [b]Increase silica precipitation rate to 0.75-1.0mg/hr	NK	NK	NK	-		
	P-His	Catalyst	(i) Increase trimerisation rate constant k_3 by 43%	Monosilicic acid	Hydrogen bond	Imidazole	Flexibility of imidazole ring[4] and peptide backbone	Yes[17-19]	Constant
			(ii) [b]Increase silica precipitation rate to 2.55mg/hr	Polysilicic acid	Electrostatic	Protonated imidazole			
$Zn(NO_3)_2$-HMTA pH 6.9 ± 0.1	G-12	ZnO morphology modifier [1, 3-11] (adsorption-driven)	(i) [c]Reduced length growth rate by 5% and 93%	(0002) plane	Electrostatic	[d]COO^- at C-terminus	-	Yes	NK
			(ii) Complete suppression of diameter growth	(10-10) plane	Electrostatic, hydrogen bond	[d]COO^- at C-terminus, cationic H and K	-		
	GT-16	ZnO morphology modifier [1, 3-11] (selective adsorption-driven)	(i) [c]Reduced length growth rate by 89% and 95%	(0002) plane	Electrostatic	[d]COO^- at C-terminus	Weak interaction of GGGC-tag on (10-10) provides GT-16 with (0002) plane selectivity	Yes	NK
			(ii) [c]Increased diameter growth rate by 16% and 241%	(10-10) plane	Electrostatic, hydrophobic interaction	[d] GGGC-tag at C-terminus			
$ZnAc_2$-NH_3 pH 7.0 ± 0.1	EM-12	Zn^{2+} complexant and ZnO morphology modifier	(i) Delayed/suppressed ZnO formation	Zn^{2+} in solution	Electrostatic	[d] E, H, and M	-	No	-
			(ii) Modification: twinned to untwinned hex. rods						
	EC-12	Zn^{2+} complexant and ZnO morphology modifier	(i) Delayed ZnO formation	Zn^{2+} in solution	Electrostatic	[d] E, H, and C	[e]C retained higher $[Zn^{2+}]$ in solution	No	-
			(ii) Morphology: twinned hex. rods to dumbbell/hourglass	NK	NK	NK	-		

Remarks:

[a] *Effect with respect to the Blank (in the absence of additive)*

[b] *Silica precipitation rate was negligible for the Blank within the first 4 hours*

[c] *Growth rate reduction in the presence of 0.03mM and 0.30mM additives*

[d] *Speculated interacting moiety(ies)*

[e] *% $[Zn^{2+}]$ increase in solution at equilibrium: 5~11% and 9~27% for 0.1-0.5mM of EM-12 and EC-12 respectively*

Abbreviations:

K_2SiCat_3 = Dipotassium silicon triscatecholato

NK = not known

G = glycine, C = cysteine, H = histidine, K = lysine, E = glutamic acid, and M = methionine

G-12 = GLLHVMHKVAPPR, GT-16 = G:HVMHKVAPPR-GGGC,

EM-12 = EAHVMHKVAPRP, and EC-12 = EAHVCHKVAPRP

Biomolecules are known to work specifically and are also multifunctionally.[12] The detection of specific and supporting functionalities in these additives is perceived to be unique for biomolecules. Both PVI and P-His catalyse silica formation. Imidazole catalytic activity at the initial stage of reaction (4 minutes) originates from hydrogen bond formation with monosilicic acid.[13] A much higher increase in k_3 (apparent trimerisation rate constant) was demonstrated by P-His (43%) compared to PVI (34%). It is believed that this synergistic catalytic activity of P-His can be attributed to its peptide backbone and the flexibility of its imidazole groups.[13] In the case of morphology alteration by G-12 and GT-16, the relative growth rates of crystal planes dictate the morphology of the ZnO crystals formed.[14, 15] G-12 adsorbs on both the (0002) and (10-10) planes of ZnO and reduced the growth of both planes. On the other hand, GT-16 with a GGGC-tag discriminates crystal planes and adsorbs preferentially on the (0002) plane of ZnO. Support for this was obtained by growth rate analysis, adsorption test results, and calculated adsorption energies using a computational approach. The anionic COO^- at the C-terminus, the imidazole of histidine and the sulphur of methionine are proposed to provide adsorption capability to G-12 and GT-16. The selectivity or enhanced binding of GT-16 on the (0002) plane is given by its GGGC-tag, most probably via the thiol of cysteine. EM-12 was added into a reaction which forms ZnO via LBZA as the intermediate compound. It forms a complex with Zn^{2+} in solution and 100% of EM-12 was held in solution throughout the reaction. The side chain of glutamate acid (E), methionine (M), and histidine (H) are potential complexing sites. Thus these residues provide EM-12 with complexing capability which enhanced the stability of LBZA and delayed/suppressed ZnO formation. Enhanced complexing capability was observed by EC-12 when methionine of EM-12 was replaced with cysteine. In the presence of EC-12, a 9~27% increase of Zn^{2+} in solution at equilibrium was observed, as opposed to 5~11% in the presence of EM-12. The identification and understanding of how peptides affect mineral formation is very important. Identifying biomolecule-induced effects on mineral formation diversifies the properties of the minerals synthesized; understanding how the effect is induced and how it can be enhanced better the control of experimentalists and allow the tailoring of mineral properties.

Some findings from this study implied the possibility of P-His and EC-12 to interact with species formed at different reaction stages. This is the beauty of using

biomolecules but in many instances complicates the studies performed. PVI and P-His catalysed both the trimerisation of monosilicic acid and silica precipitation. In the presence of additives, a 34-43% increase in k_3 was observed. However, a tremendous increase in silica precipitation rate was also observed. For PVI and P-His, 3-4mg and 10mg of silica respectively was obtained after 4 hours reaction while a negligible amount was collected from the blank precipitation reaction. These values correspond to 22-29% and 73% of the silica weight collected for the Blank at equilibrium (168 hours). This difference between PVI and P-His can be explained by only P-His being partially protonated under the chosen reaction conditions. The partially protonated imidazole of P-His is able to interact with both monosilicic acid and negatively-charged polysilicic acid formed as the reaction progresses. The ability to interact with different species was also shown by EC-12. EC-12 interacts with Zn^{2+} via complexation thus, at equilibrium, 100% of added EC-12 and higher Zn^{2+} concentration were detected in solution. However, it was intriguing that only 40-75% of added EC-12 was detected in solution at the initial stage of reaction. Based on the presence of the amide-I band in the FTIR spectrum of earlier stage precipitates, and modifications in ZnO morphology, the reversible adsorption/incorporation of EC-12 on/into LBZA/ZnO may have been the cause. Although the second species has not been identified, these findings clearly showed the possibility for EC-12 to interact with more than one species. In the case of EM-12, complete retention of EM-12 in solution was observed from the beginning of reaction except for the use of 0.5mM EM-12. The actual cause of this difference from EC-12 is not known but it is highly possible that it is related to the presence of cysteine in EC-12. Due to part of the added G-12 and GT-16 being present in solution (calculated based on TGA data), the possibility of G-12 and GT-16 being able to interact with Zn^{2+} species which are not part of the ZnO surfaces still exists.

The type of interaction and interacting species determine the level of additive incorporation and its effect on equilibrium conditions. The imidazole group interacts with monosilicic acid/polysilicic acid via hydrogen bond/electrostatic interactions.[16] These interactions bring reactants into proximity and thus catalyse their condensation.[16] The incorporation of PVI/P-His was expected for such a catalyst and also other silica precipitating catalysts with amine functionality.[17-19] The adsorption of G-12 and GT-16 on ZnO surfaces occurs via electrostatic interaction or hydrophobic

interaction. The former may develop into permanent bond formation thus their incorporation into ZnO precipitates was anticipated. EM-12 and EC-12 interact with Zn^{2+} in solution via complexation[20-23] and thus all additives were retained in solution at equilibrium. Although more Zn^{2+} was retained in solution, the bound EM-12 and EC-12 were not labile under the reaction conditions employed. As a result, the stability of LBZA (intermediate phase) was increased leading to delayed/suppressed ZnO formation.

Using two materials as platforms for the study of peptide-mineral interactions, diverse roles of peptides have been identified: catalyst, crystal morphology modifier, and complexing agent. Some significant progress was made on understanding the role(s) of biomolecular additives in mineral formation. The segregation of different interactions by the same/different additive functionality(ies), with different species of reactants/products in the same reaction has been attempted. Although a complete picture has not been fully obtained, the specificity and multi-functionality of these additives has been identified, assigned, and reported in this thesis. In this study, all investigations were performed in a systematic fashion and the selected reaction was studied thoroughly before the introduction of additives. In the study of G-12 and GT-16, for the first time, ALD-grown single orientation ZnO films were used to study the adsorption behaviours of these peptides. This adsorption study has provided direct and quantitative evidence for adsorption-driven ZnO modification, a generally accepted explanation for crystal modification by additives.

In the course of this study a few problems have been encountered particularly from the investigation of ZnO-BP adsorption on ZnO surfaces. The use of ALD-grown ZnO films allows the study of G-12 and GT-16 adsorption on one crystalline plane at a time. However such ZnO films have a low surface area to volume ratio and the film area depends on the size of the deposition chamber used. Thus peptide solutions of very low concentration and a protein assay with high sensitivity (for peptide detection) have to be used. Moreover, trace amounts of adsorbed peptide on ZnO films (from the very low concentration of peptide solution exposed) were below the detection limit of FTIR-ATR and thus cannot be quantified. Therefore the quantification of adsorbed peptide was performed using XPS (University of Nottingham). Due to some unforeseen circumstances, limited information has been extracted from this analysis and the results

were not in complete agreement quantitatively with the protein assay results. Samples have been resent and more insights of the adsorption process are anticipated.

The ultimate goal of this peptide-mineral study was two-fold; to explore the phenomenal complexity of the behaviour of peptides in (bio)mineralising systems, and to exploit the ground rules in their interactions (with species in (bio)mineralising systems) for the synthesis of novel nanomaterials with properties tailored for specific applications. Armed with knowledge on the interactions underpinning the effects induced by the presence of biomolecules, one may investigate further to design molecules/polymers to manipulate mineral formation accordingly. The attractiveness of biomimetic synthesis arises from the functional specificity, multifunctionality, and energetic spontaneity of biomolecule-mediated synthesis. However the key issue lies in the complexity and synergistic nature of the interactions which may not allow the design of a simple molecule which could serve the same purpose.

6.2 Further Work

6.2.1 Effects of imidazole functionality on silica formation

The catalytic effect of imidazole functionality on silica precipitation was confirmed. Experimental findings from this study suggest that the extent of catalytic effect depends on imidazole charge, degree of polymerisation, and most probably the presence of the peptide backbone. The essentiality of the imidazole functionality to be in proximity can be studied using imidazole molecules as the additive. The period where reacting species were predominantly monosilicic acid was short implying the importance of electrostatic interactions[16] in catalysing silica precipitation. Silica precipitation via electrostatic interaction may also be more controllable due to steady silica-P-His ratio with time as shown by TGA. To confirm the role of electrostatic interactions on silica precipitation, a pH-dependent study using imidazole/P-His would be informative.

The catalysis mechanism of PVI and P-His and how it affects the properties of silica-PVI/P-His composite requires further investigation. More solid evidence is needed to explain the difference in the co-precipitation rate of silica-PVI and silica-P-His. Evidence of different catalysis mechanisms by highly similar PVI and P-His would allow further insights into the role of the peptide backbone and electrostatic interactions separately on silica precipitation activity. The tremendously rapid silica precipitation rate induced in the presence of P-His compared to the Blank can be very useful when simpler molecule/polymer which serves the same purpose can be designed.

6.2.2 Effects of ZnO-BPs on ZnO formation

ZnO morphology modification by G-12 and GT-16 was studied using a $Zn(NO_3)_2$-HMTA reaction while the delayed/suppression of ZnO formation by EM-12 and EC-12 was identified from the $ZnAc_2$-NH_3 reaction. The differences observed despite the high sequence similarity between the two ZnO-BPs, EM-12 and G-12, are very exciting. The nature of the reaction systems, one forming ZnO directly while in the other occurred via LBZA formation, may have determined the effect induced to a great extent. However the acidic residue in EM-12 may also play a vital role in selecting a solution-solution interaction or a solution-surface interaction. This may have been shown by the formation of mushroom-like ZnO in the presence of EC-12 instead of hexagonal rods. All these observations may suggest the presence of a transition point where the types of interaction can be switched between the two. Projected further work focuses on the way G-12 would behave in the $ZnAc_2$-NH_3 reaction and vice versa for EM-12, to provide a better view of the dominating factor, reaction system or ZnO-BP?

Although EC-12 retained more Zn^{2+} in solution compared to EM-12, the LBZA stabilization effect was more prominent with the presence of EM-12. A comparative study of Zn^{2+}-EM-12 and Zn^{2+}-EC-12 complexation may elucidate the complexity of the interactions by providing insights on the relationship between the level of complexation and the extent of the LBZA stabilization effect.

Further to the morphology control by G-12 and GT-16, the possibility is raised for the formation of ultra-thin single crystalline (0002) planes on a substrate via solution route for applications such as gas and chemical sensors.[24]

Reference:

1 M. M. Tomczak, M. K. Gupta, L. F. Drummy, S. M. Rozenzhak, and R. R. Naik, *Acta Biomater.* **5**, (3), 876-882 (2009).

2 M. Umetsu, M. Mizuta, K. Tsumoto, S. Ohara, S. Takami, H. Watanabe, I. Kumagai, and T. Adschiri, *Adv. Mater.* **17**, 2571-2575 (2005).

3 L. P. Bauermann, A. d. Campo, J. Bill, and F. Aldinger, *Chem. Mater.* **18**, (8), 2016-2020 (2006).

4 M. Jitianu, and D. V. Goia, *J. Colloid and Int. Sci.* **309**, 78-85 (2007).

5 Z. R. Tian, J. A. Voigt, J. Liu, B. Mckenzie, M. J. Mcdermott, M. A. Rodriguez, H. Konishi, and H. Xu, *Nature Materials* **2**, 821-826 (2003).

6 J. Liang, J. Liu, Q. Xie, S. Bai, W. Yu, and Y. Qian, *J. Phys. Chem. B* **109**, (19), 9463-9467 (2005).

7 C.-L. Kuo, T.-J. Kuo, and M. H. Huang, *J. Phys. Chem. B* **109**, (43), 20115-20121 (2005).

8 M. Öner, J. Norwig, W. H. Meyer, and G. Wegner, *Chem. Mater.* **10**, (2), 460-463 (1998).

9 A. Taubert, D. Palms, O. Weiss, T. Piccini, and D. N. Batchelder, *Chem. Mater.* **14**, (6), 2594-2601 (2002).

10 A. Taubert, G. Glasser, and D. Palms, *Langmuir* **18**, 4488-4494 (2002).

11 G. Wegner, P. Baum, M. Müller, J. Norwig, and K. Landfester, *Macromolecules Symp.* **175**, 349-355 (2001).

12 M. B. Dickerson, K. H. Sandhage, and R. R. Naik, *Chem. Rev.* **108**, 4935-4978 (2008).

13 G. Croce, A. Franche, M. Milanesio, L. Marchese, M. Causà, D. Viterbo, A. Barbaglia, V. Bolis, G. Bavestrello, C. Cerrano, U. Benatti, M. Pozzolini, M. Giovine, and H. Amenitsh, *Biophys. J.* **86**, (1), 526-534 (2004).

14 R. A. Laudise, and A. A. Ballman, *J. Phys. Chem.* **64**, 688-691 (1960).

15 W.-J. Li, E.-W. Shi, W.-Z. Zhong, and Z. W. Yin, *J. Cryst. Growth* **203**, 186-196 (1999).

16 T. Coradin, and J. Livage, *Colloids Surf., B: Biointerfaces* **21**, 329-336 (2001).

17 D. Belton, S. V. Patwardhan, and C. C. Perry, *Chem. Commun.*, 3475-3477 (2005).

18 D. Belton, S. V. Patwardhan, and C. C. Perry, *J. Mater. Chem.* **15**, 4629-4638 (2005).

19 D. Belton, G. Paine, S. V. Patwardhan, and C. C. Perry, *J. Mater. Chem.* **14**, 2231-2241 (2004).

20 R. Vogler, M. Gelinsky, L. F. Guo, and H. Vahrenkamp, *Inorg. Chim. Acta* **339**, 1-8 (2002).

21 P. Gockel, M. Gelinsky, R. Vogler, and H. Vahrenkamp, *Inorg. Chim. Acta* **272**, 115-124 (1998).

22 P. Gockel, M. Gelinsky, A. Meiβner, H. Albrich, and H. Vahrenkamp, *Inorg. Chim. Acta* **323**, 16-22 (2001).

23 M. Ruf, R. Burth, K. Weis, and H. Vahrenkamp, *Chem. Ber.* **129**, (10), 1251-1257 (1996).

24 C. Wöll, *Prog. Surf. Sci.* **82**, 55-120 (2007).

Appendix 3.1

The absorbance of molybdenum blue assay at 810nm as a function of hydrolysis time for the hydrolysis of 30mM dipotassium silicon triscatecholate by HCl, at 25±1°C and pH 6.8±0.05 (n=10).

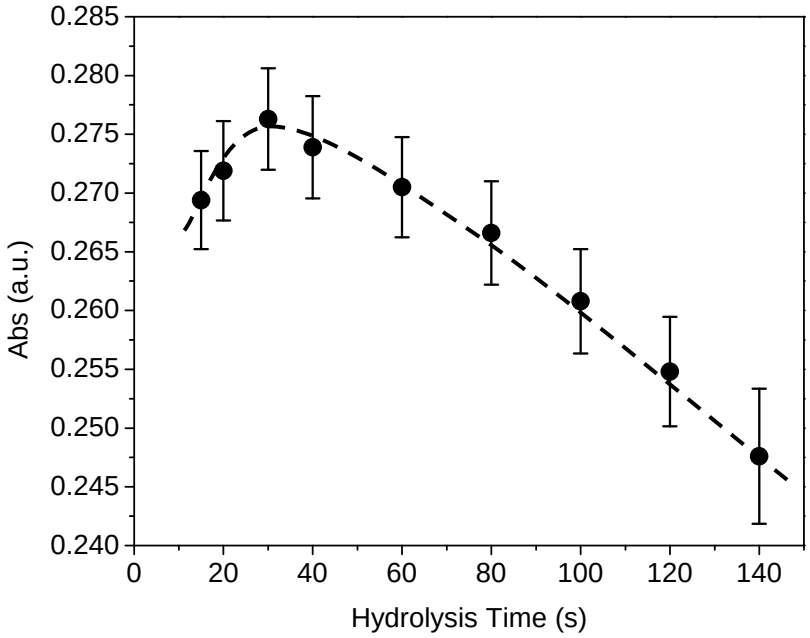

Appendix 3.2

The immediate precipitation of (a) PVI-48 and (b) PVI-530 was observed when silicon-to-imidazole ratio of 3:1 was used, i.e. 20mM of imidazole functionality and 30mM of dipotassium silicon triscatecholate.

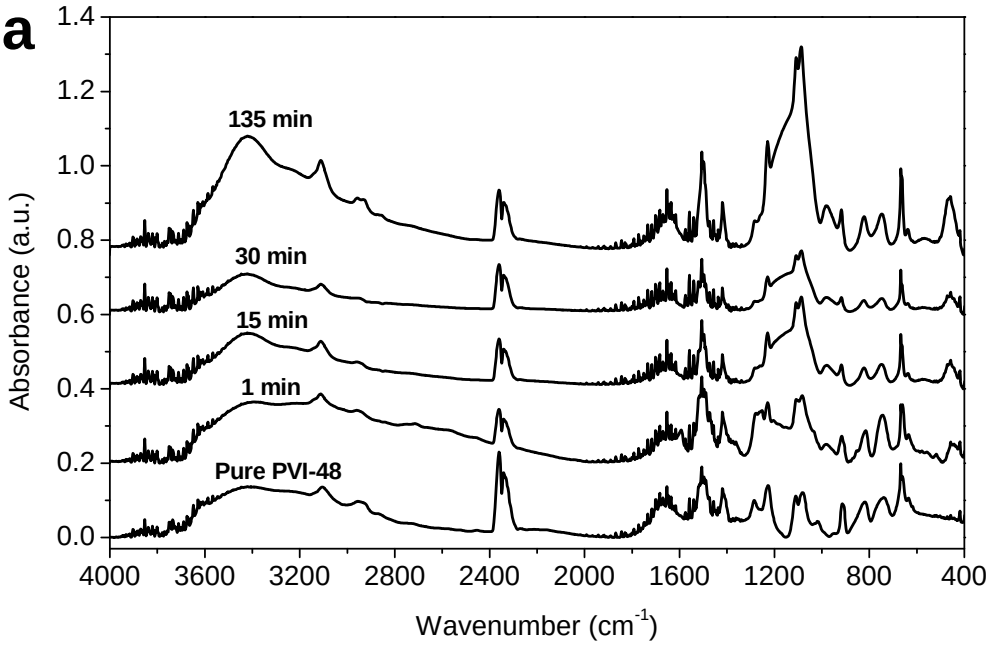

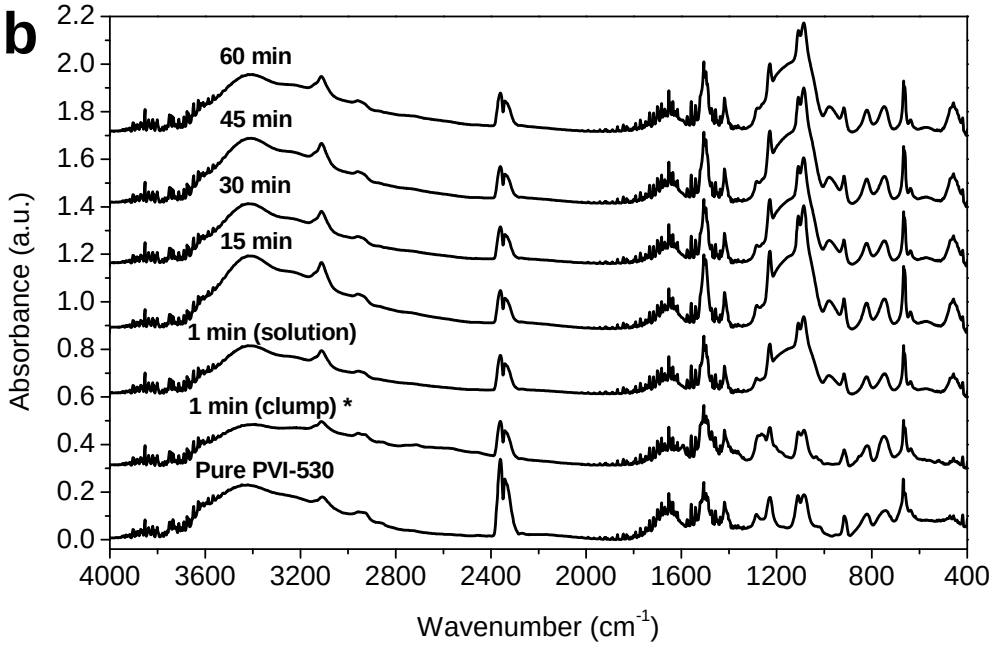

** Big piece of clump was collected from the bottom of the reaction vial.*

Appendix 3.3

FTIR spectra of precipitates obtained in the presence and absence of additives (a) after 4 hours and (b) after 7 days. The labels above the spectra show the additives used.

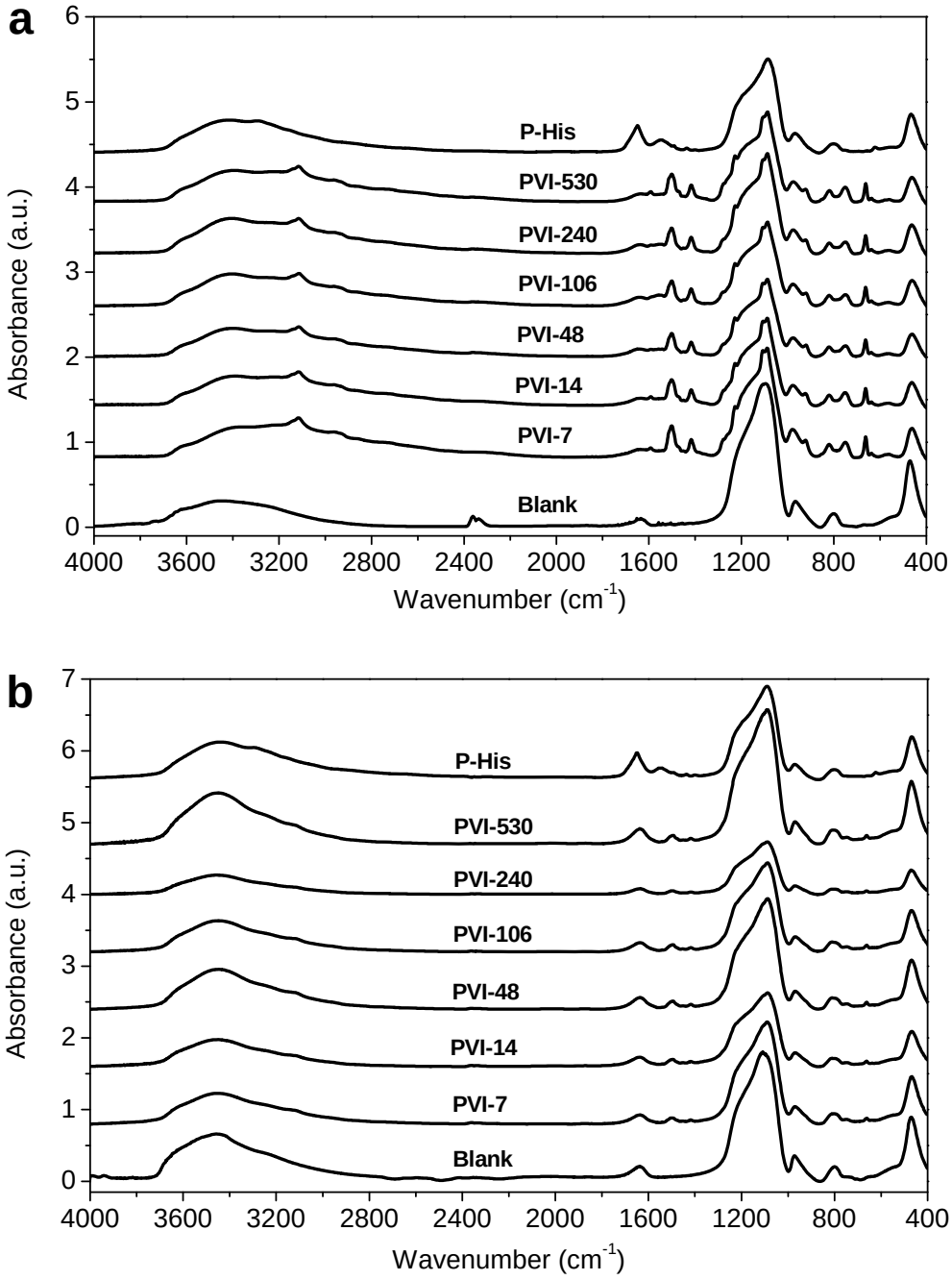

Appendix 3.4

FTIR spectra of the post-TGA materials from precipitates produced in the presence of PVI additives (7 days reaction). The remaining material after TGA was confirmed to be silica.

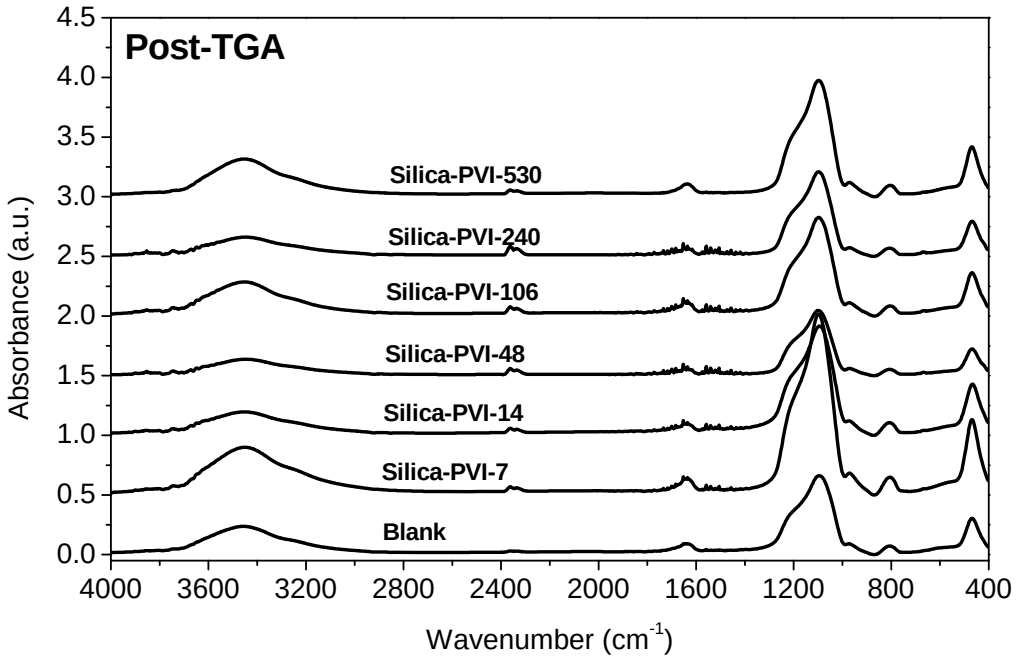

Appendix 3.5

SEM images of precipitates obtained after 7 days reaction. (a) silica-PVI-7, (b) silica-PVI-14, (c) silica-PVI-48, (d) silica-PVI-240, (e) silica-PVI-530 composites, and (f) silica (the blank). Scale bars=5μm.

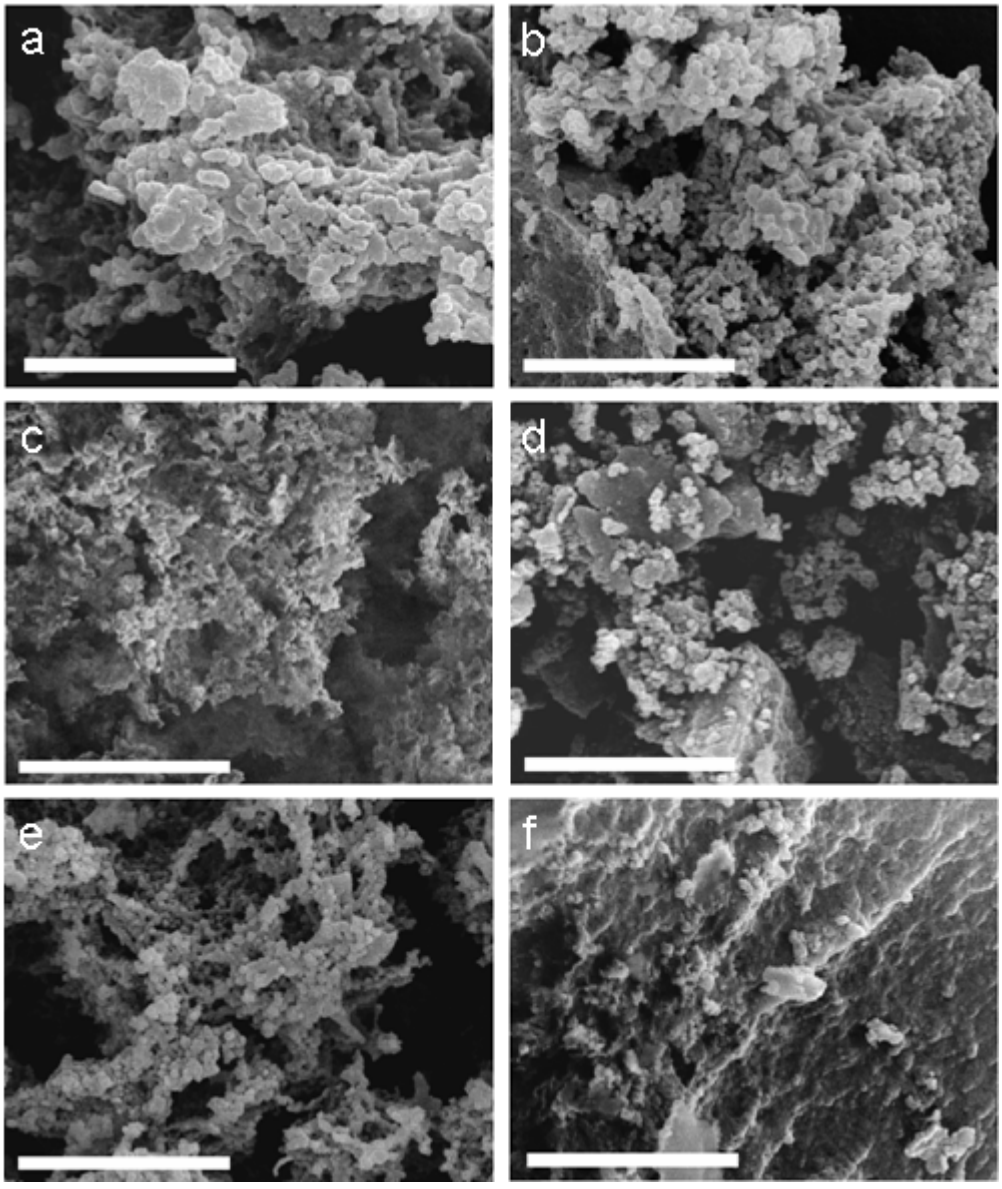

Appendix 3.6

TGA/DSC results for (a) silica-P-His composite and (b) silica-PVI-106 composite. The DSC curves were obtained by subtrating the silica blank (control).

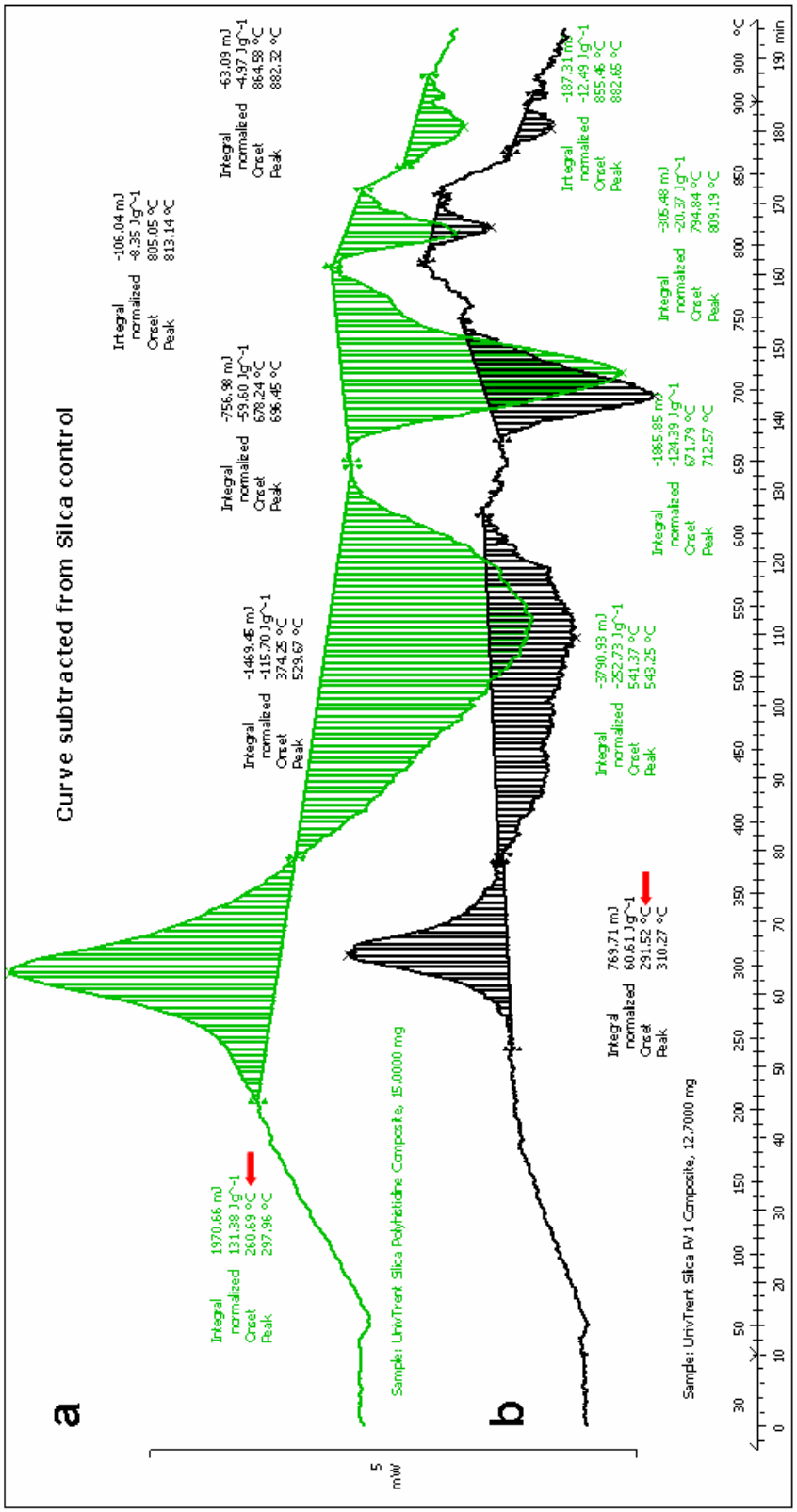

TGA curves for silica-PVI and silica-P-His composites obtained after (a) 4 hours and (b) 7 days reaction. A difference of 20~25°C in the onset temperature (arrow) was observed between the silica-PVI composites and silica-P-His composite.

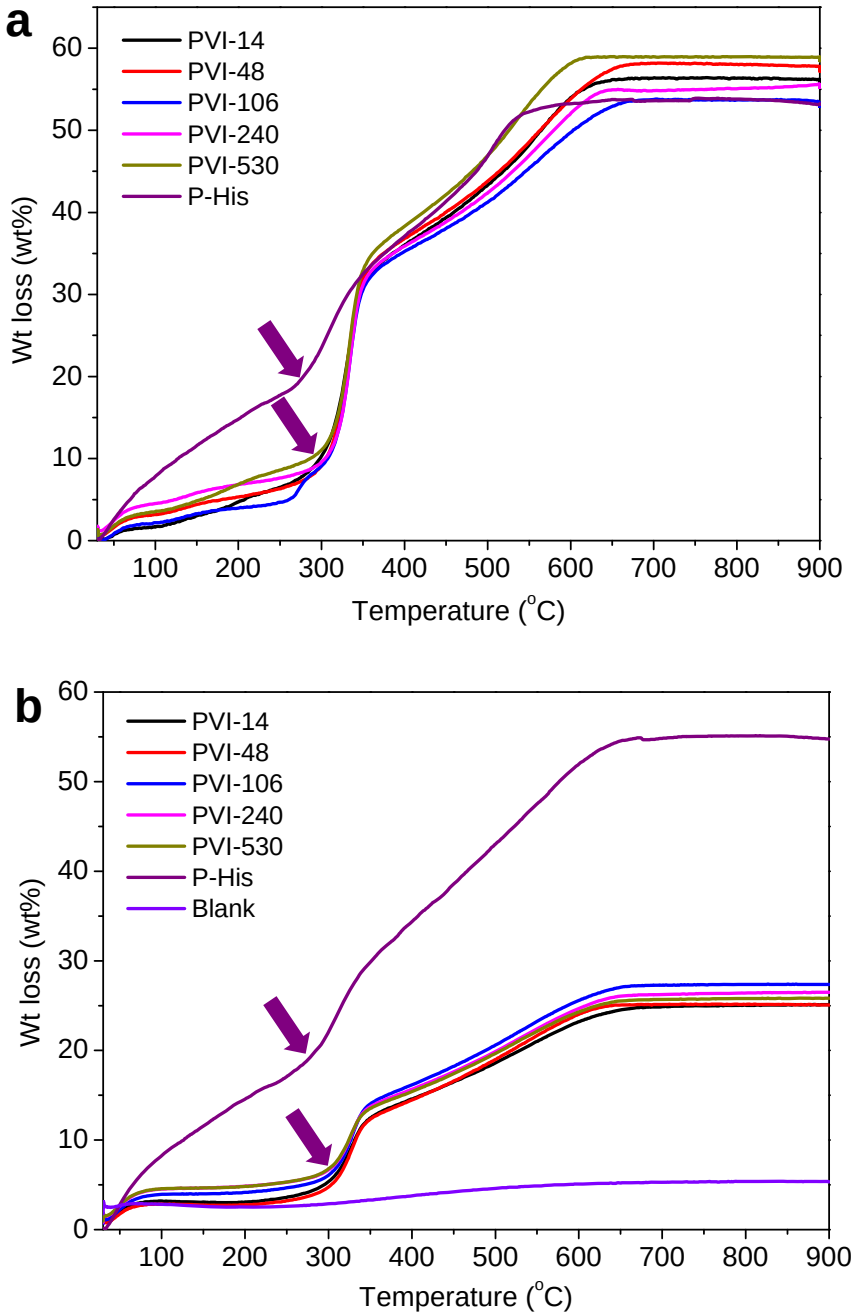

Appendix 3.7

TGA results for P-His, PVI-48 and PVI-240. The onset temperature for P-His (6.7kDa) and PVIs decomposition were 261°C and 271~280°C respectively. The onset temperature of P-His was comparable to the onset temperature of silica-P-His composite but the onset temperature of PVIs were lower than that of silica-PVI composites.

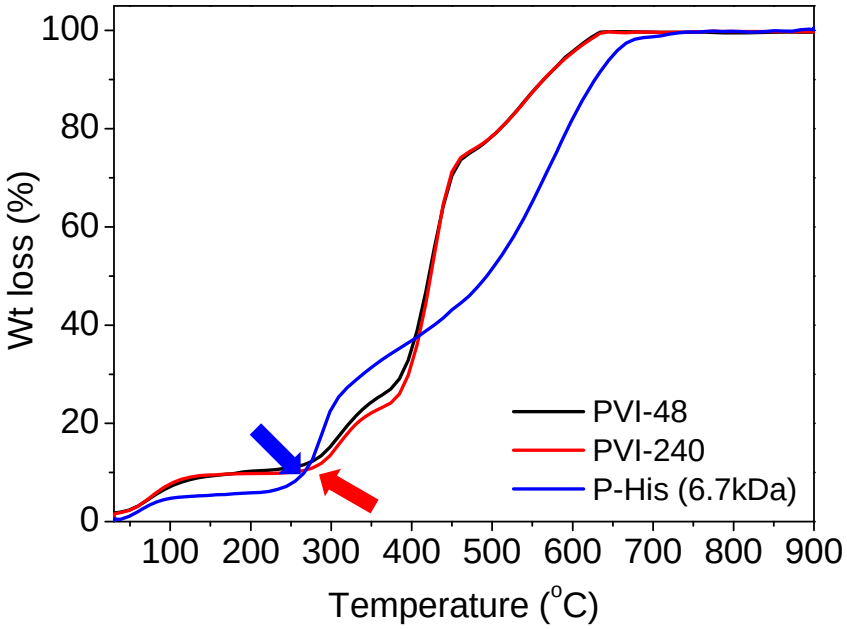

Appendix 4.1

Absorbance of $Zn(NO_3)_2$, HMTA, and G-12 at 214nm using a Unicam UV-VIS Spectrometer. Absorbance was at a saturated state even after 100 times dilution of reaction solution due to HMTA being absorbing strongly at 214nm and at this level of dilution, the absorbance from G-12 has became negligible.

	$[Zn(NO_3)_2]$ (mM)	[HMTA] (mM)	[G-12] (mM)	
			Minimum	Maximum
Reaction condition	50	50	0.03	0.30

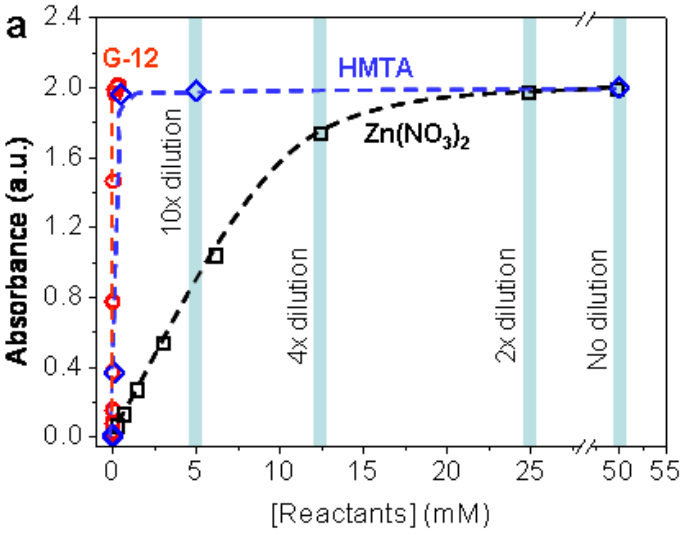

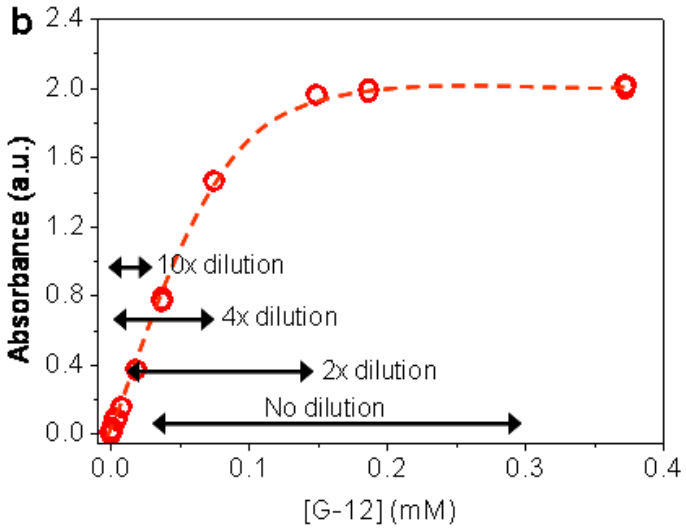

Appendix 4.2

Calculation of (a) planar Zn atomic density for the (0001) plane, (b) planar Zn atomic density for (10-10) planes, and (c) Zn atomic density per unit volume of the ZnO crystal.

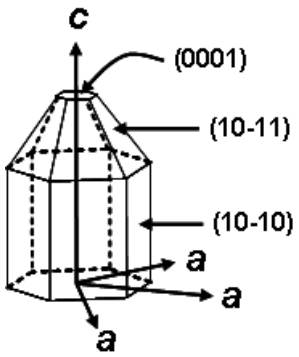

Low index plane of ZnO

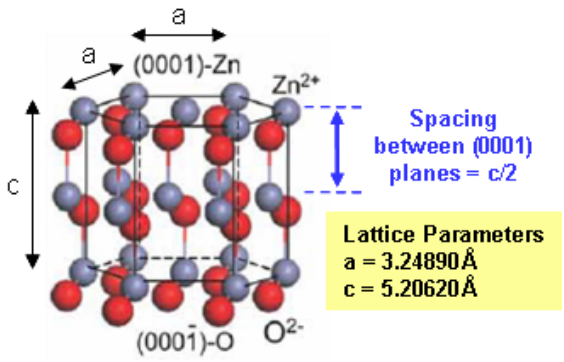

ZnO crystal and lattice parameters
Pearton et. al. *Prog. Mater. Sci.*, **50**, 293-340 (2005)

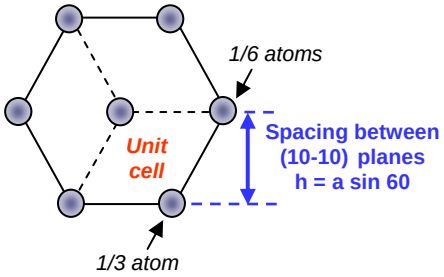

Top view of (0001) plane of ZnO crystal

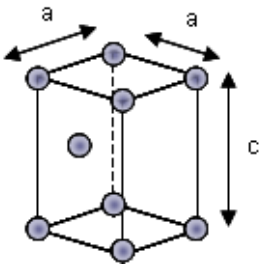

Zn in the unit cell of ZnO

a

No. of Zn atoms on a (0001) plane in a unit cell = 1
1/6 * 2 = 1/3
1/3 * 2 = 2/3
Total = 1

Area of a (0001) plane of a unit cell = 0.091412nm^2
= a * h
= 0.091412 nm^2

No of Zn atoms per unit area of (0001) plane = 10.94
= 1 / 0.091412 nm^2
= 10.94 atoms/nm^2

b

No. of Zn atoms on a (10-10) plane in a unit cell = 1
1/6 * 2 = 1/3
1/3 * 2 = 2/3
Total = 1

Area of a (10-10) plane of a unit cell = 0.169144nm^2
= a * c
= 0.169144 nm^2

No of Zn atoms per unit area of (10-10) plane = 5.91
= 1 / 0.169144nm^2
= 5.91 atoms/nm^2

c

a = 3.24890Å
c = 5.20620Å

No of Zn atoms/unit cell = 2
1/12 * 4 = 1/3
1/6 * 4 = 2/3
1 * 1 = 1
Total = 2

Vol. of unit cell = 0.04759nm^3
= $\sqrt{3}/2$ * a^2 * c
= 0.04759 nm^3

No of Zn per unit vol. = 42
= 2 / 0.04759 nm^3
= 42 atoms/nm^3

Appendix 4.3

Micro-BCA calibration curve for GT-16 and G-12.

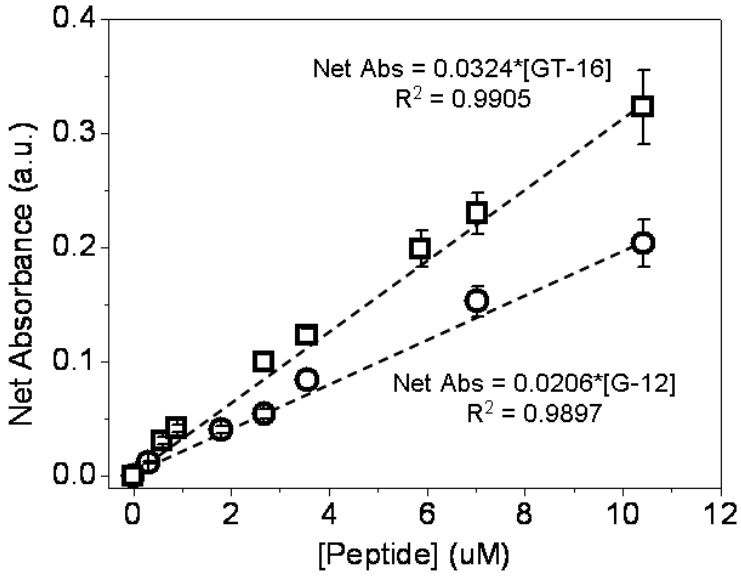

Appendix 4.4

Comparison of the diffractogram of 24 hour precipitates (20°C) in the absence of additive with the diffractogram of $Zn(NO_3)_2 \cdot 6H_2O$ (Sigma Aldrich).

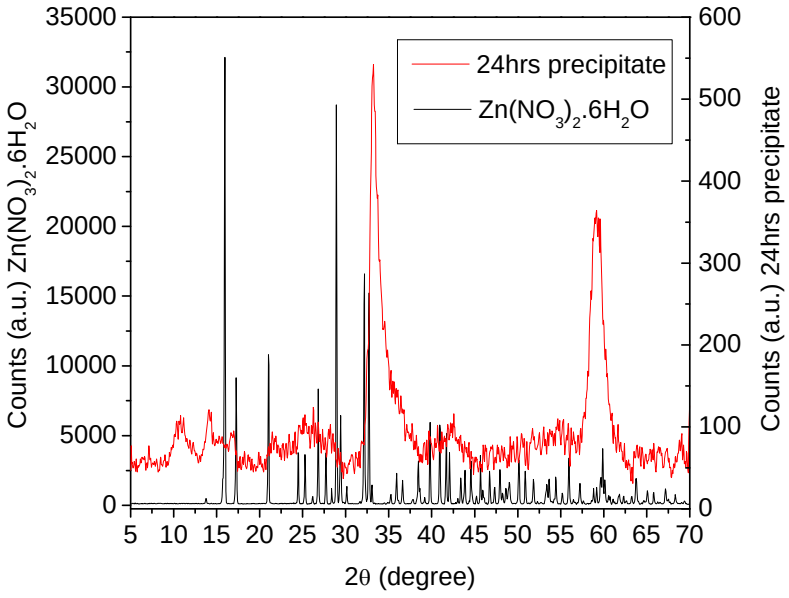

Appendix 4.5

Comparison of XRD diffraction peaks from the control reaction (blank) with reference to H. Sawada, R. Wang, and A. W. Sleight, *J. Solid State Chem.*, **122**, 148-150, (1996).

No	(*h k l*)	2θ (degree)					
		Ref	t = 25hrs	t = 26hrs	t = 48hrs	t = 72hrs	t = 168hrs
1	1 0 0	31.779	31.8704	31.9583	31.9685	31.9198	31.9661
2	0 0 2	34.430	34.5317	34.6225	34.6359	34.5947	34.6341
3	1 0 1	36.265	36.3557	36.4422	36.4468	36.4116	36.4495
4	1 0 2	47.554	47.6148	47.7029	47.7139	47.6859	47.7173
5	1 1 0	56.615	56.6416	56.7292	56.7443	56.7208	56.7576
6	1 0 3	62.876	62.9073	62.9926	63.0056	62.9854	63.0190
7	2 0 0	66.400	66.4028	66.4842	66.497	66.4888	66.5214
8	1 1 2	67.971	67.9736	68.0586	68.0761	68.0633	68.0944
9	2 0 1	69.112	69.0998	69.1896	69.2079	69.1923	69.2314
	a	3.2489	3.2437	3.2309	3.2299	3.2347	3.2302
	c	5.2053	5.1949	5.1772	5.1753	5.1813	5.1755
	c/*a*	1.6022	1.6015	1.6024	1.6023	1.6017	1.6022

Appendix 4.6

SEM images of (a) precipitates obtained from the $Zn(NO_3)_2$-HMTA reaction after 24 hours (20°C), and (b) layered basic zinc acetate (LBZA) structure obtained from the reaction of 100mM $Zn(CH_3COO)_2$ with NaOH (25°C, 45min, hydrolysis ratio=1.7). Scale bars are 5μm.

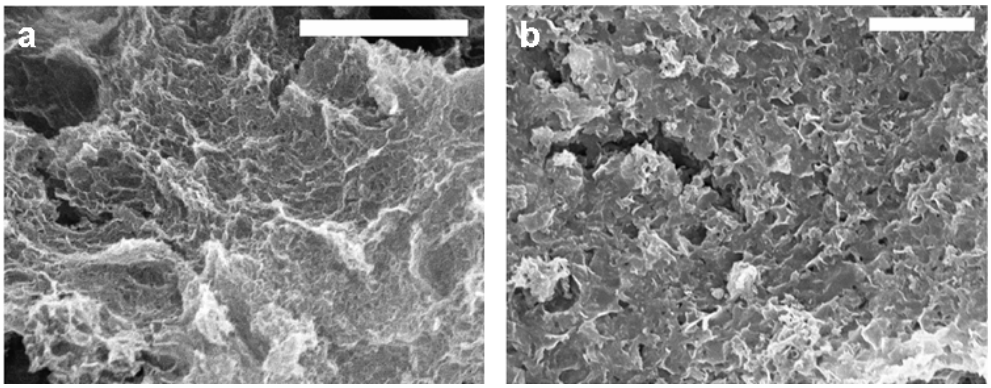

Appendix 4.7

XRD patterns of ZnO formed after 48 hours for GT-16-added and G-12-added reactions. Asterisks mark the diffraction peaks from the aluminium sample holder.

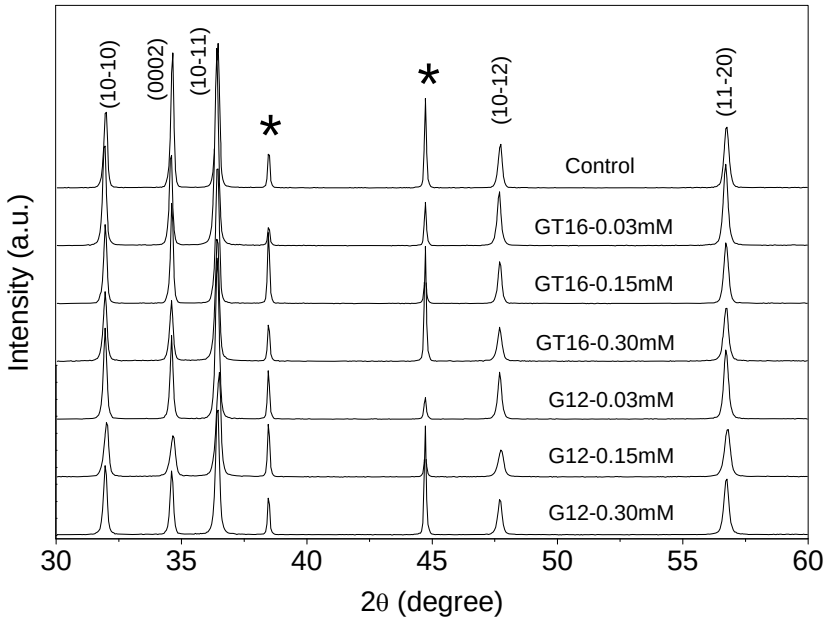

Appendix 4.8

pK_a and structure of (a) G-12 and (b) GT-16 obtained using Marvin at 298K. The side chain of residues with ≥50% protonated or ≥50% deprotonated at pH 6.9±0.1 are circled by solid line and dotted line respectively.

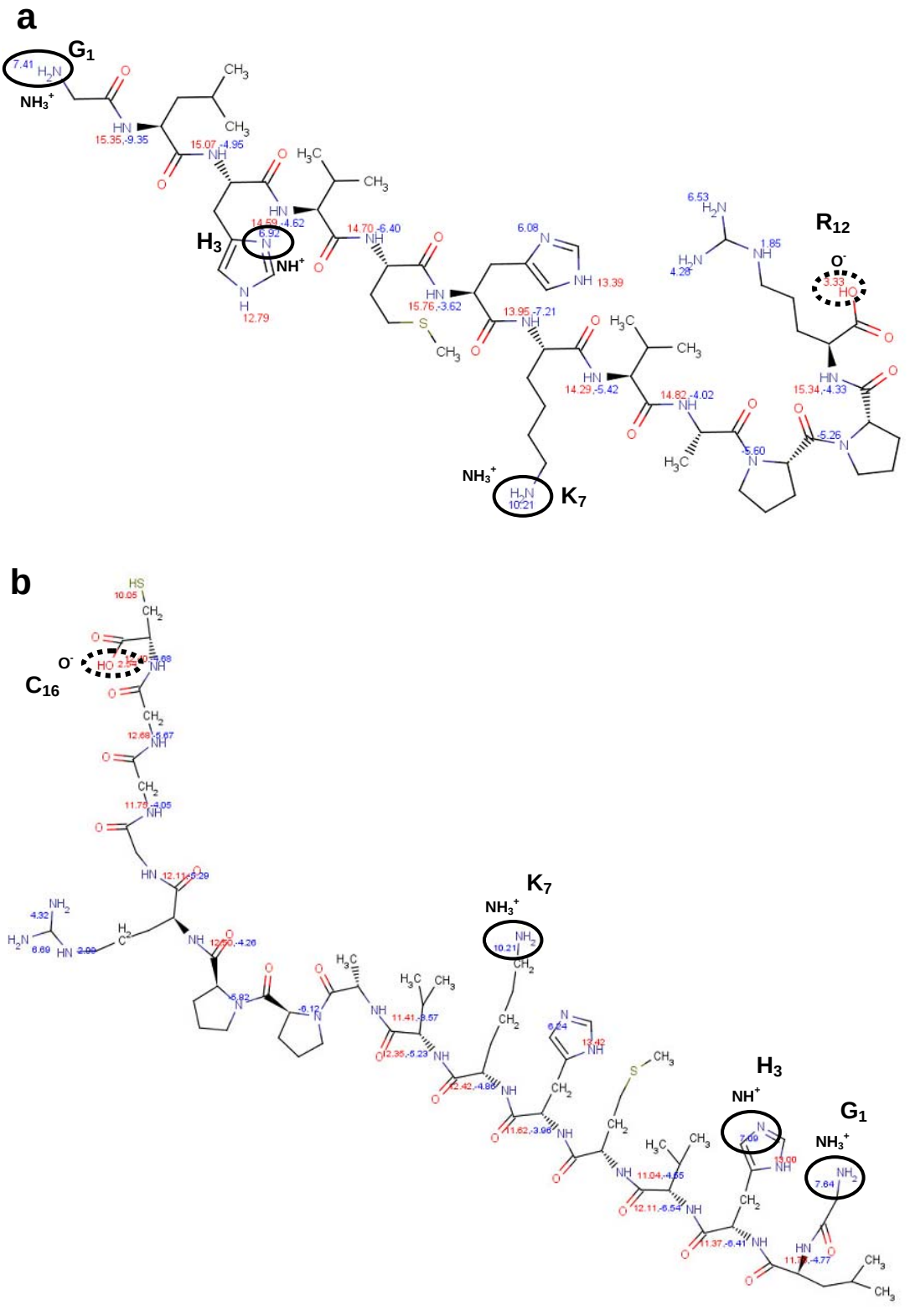

Appendix 4.9

TGA curves of precipitates collected after 48 hours reaction. Zone A, B, and C were assigned to physisorbed water, chemisorbed water, and the organic phase respectively.

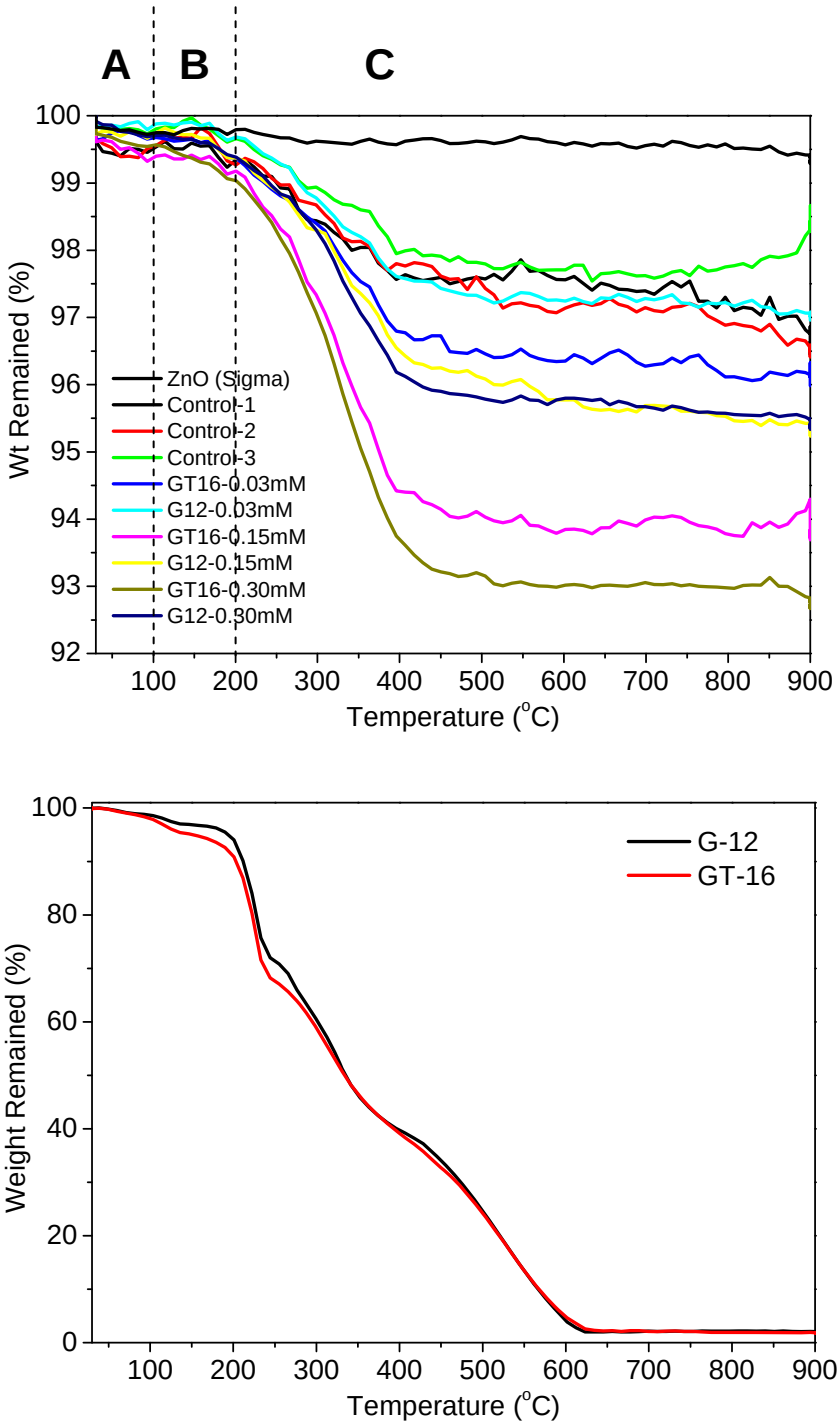

Appendix 4.10

Weight loss attributed to the loss of physisorbed and chemisorbed water from precipitates obtained after 48hr of reaction where the standard deviation bar for the control (0mM peptide) was obtained from three sets of blanks.

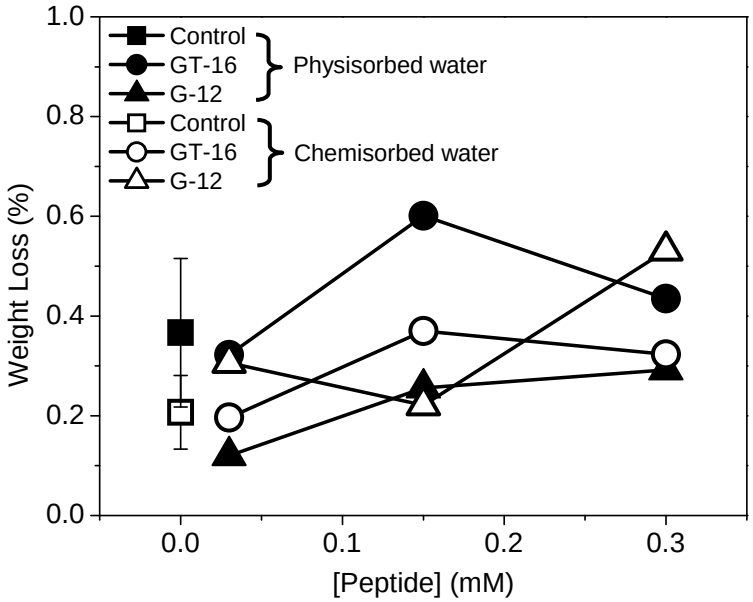

Appendix 4.11

Neither amide-I nor amide-II bands were present in the FTIR-ATR spectra obtained from (cleaned) ZnO films exposed to peptide solution. The analysis was repeated with 30μl of 0.3mM G-12 solution (15pmol of peptide) which was just enough to cover the area of diamond/KRS-5 crystal (~0.018cm^2). Since no peptide characteristic bands were present in the spectrum of 0.3mM G-12 solution, we confirmed that the FTIR-ATR was not sensitive enough to detect peptide of ≤15pmol. Based on the highest adsorbed amount (~4.24nmol on substrate area of 9cm^2) and assuming the adsorbed peptide was evenly distributed, the amount of peptide exposed to the diamond-KRS-5 crystal would be 8.48pmol. Since the amount of peptide exposed to diamond-KRS-5 crystal was at the same order of magnitude with the "detection limit" identified, we can conclude that the non-detection of peptide on substrate surface was not an indication of the peptide's absence.

Appendix 4.12a

XPS wide scan results for (a) G-12, (b) GT-16, (c) G-12 on ZnO(10-10), (d) GT-16 on ZnO(10-10), (e) G-12 on ZnO(0002), (f) GT-16 on ZnO(0002), (g) ZnO(10-10), and (h) ZnO(0002).

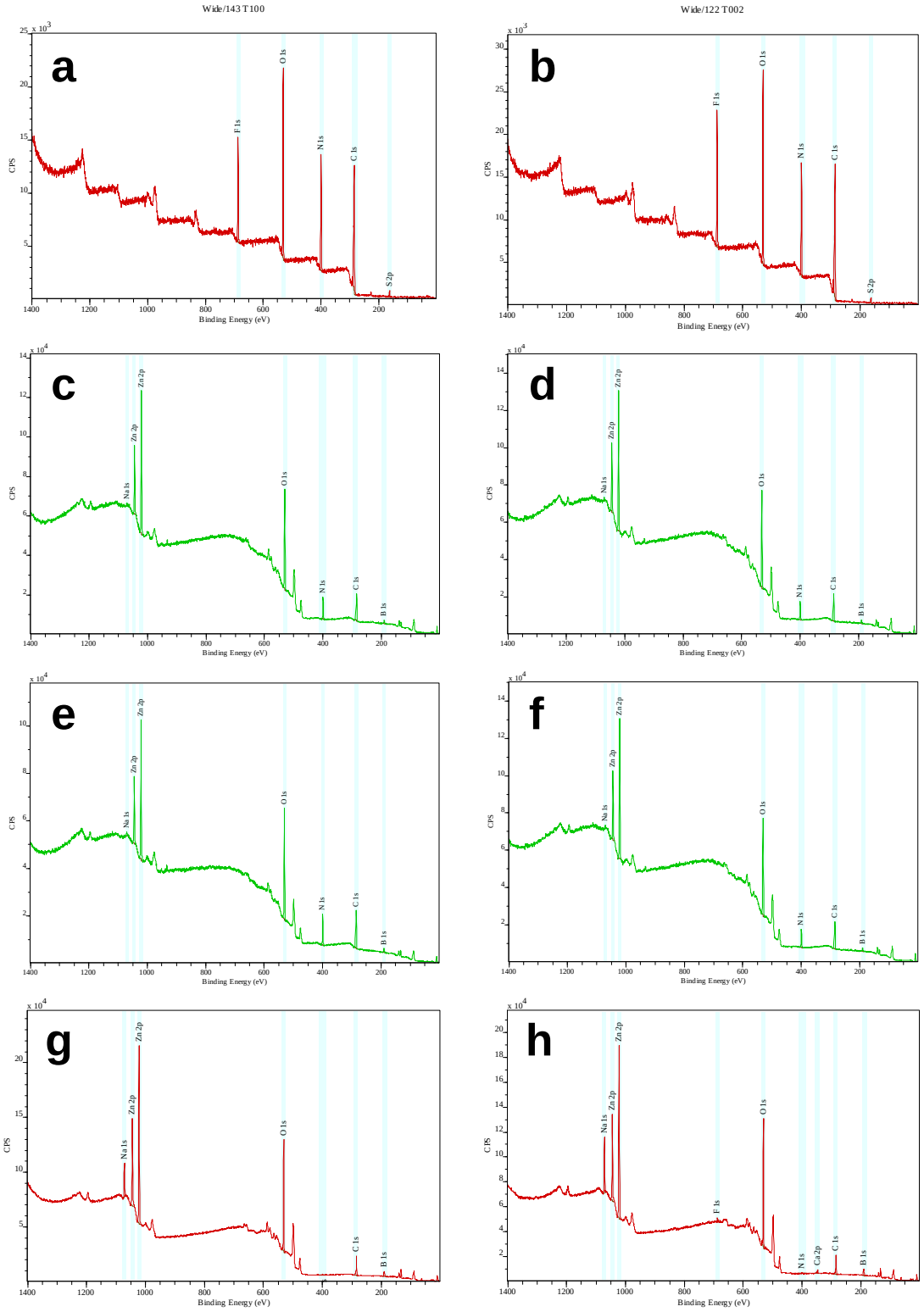

Appendix 4.12b

XPS high resolution scan results for (a) G-12, (b) GT-16, (c) G-12 on ZnO(10-10), (d) GT-16 on ZnO(10-10), (e) G-12 on ZnO(0002), (f) GT-16 on ZnO(0002), (g) ZnO(10-10), and (h) ZnO(0002).

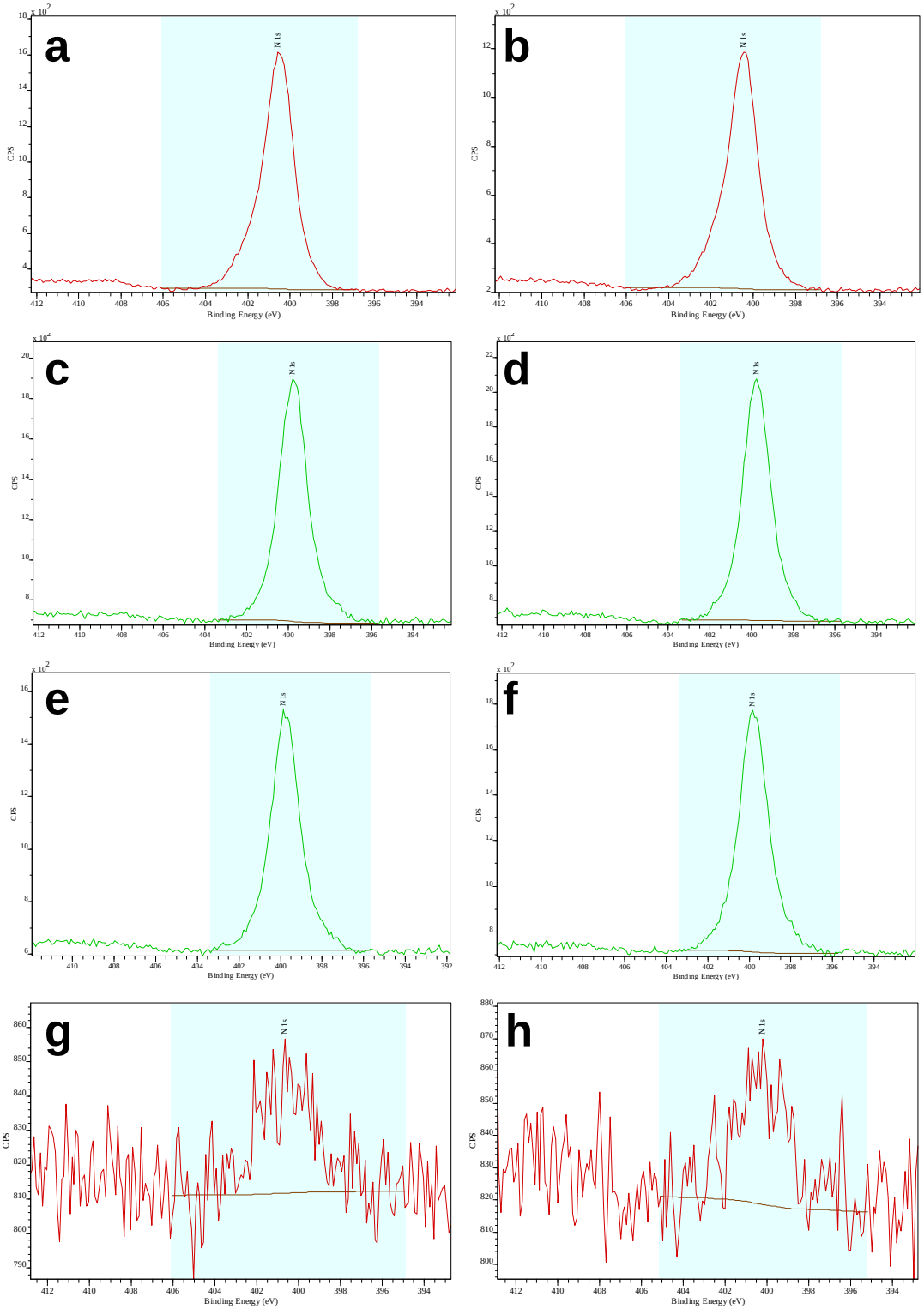

Appendix 5.1

Absorbance calibration curves of (a) $ZnAc_2$ and NH_3, and (b) EM-12 and EC-12, at 214nm using quartz cuvette with Unicam UV2 UV-VIS spectrometer.

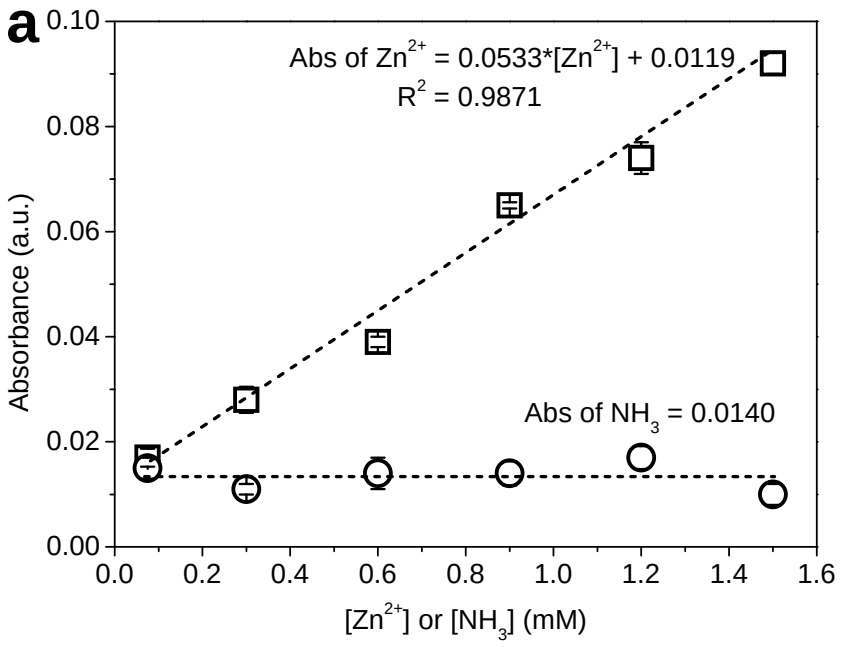

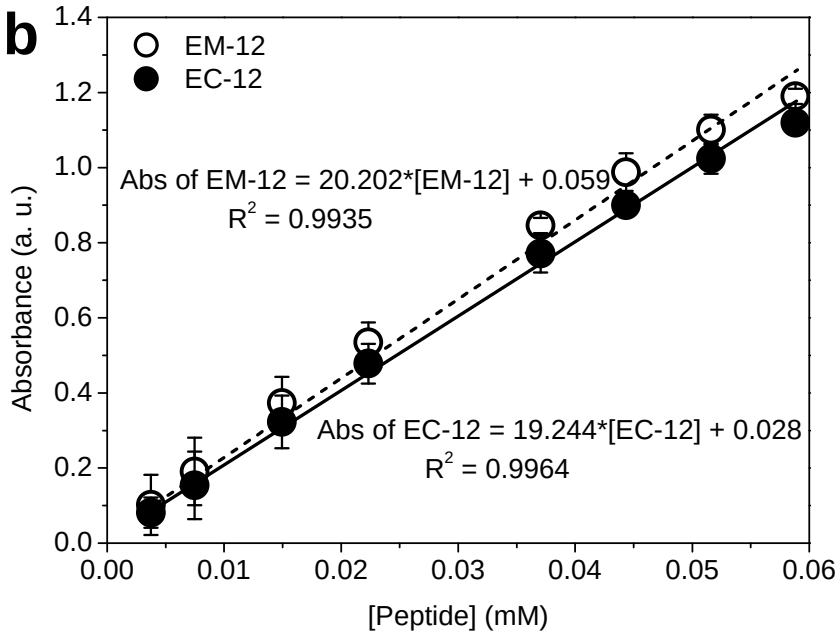

Appendix 5.2

TGA curves of precipitates collected from the reaction of $ZnAc_2$-NH_3 in the absence of additives at different reaction time.

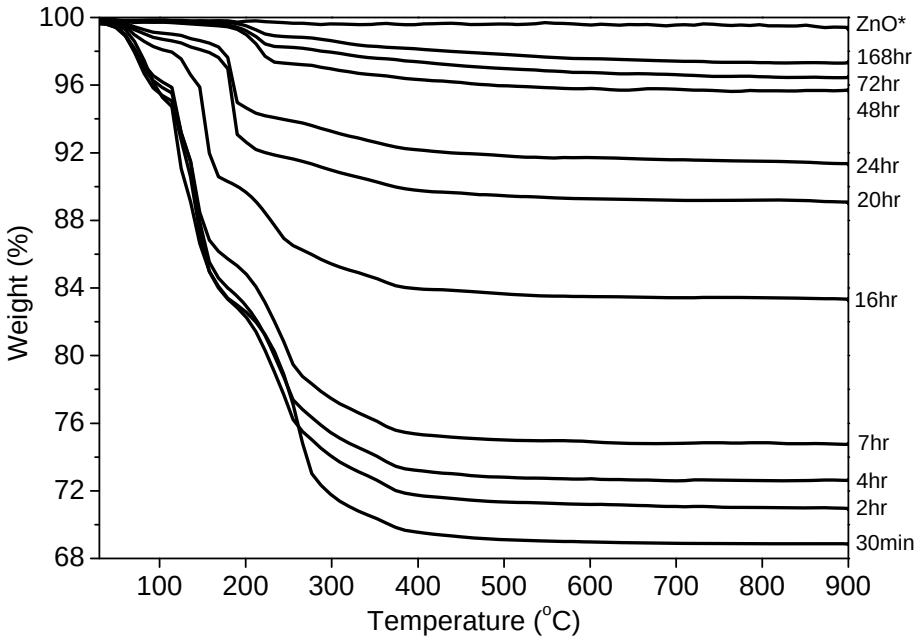

Appendix 5.3

Calculated pK_a for (a) EM-12 and (b) EC-12 by Marvin Calculator (298K). Cationic and anionic moieties are marked with solid-circles and dotted-circles respectively.

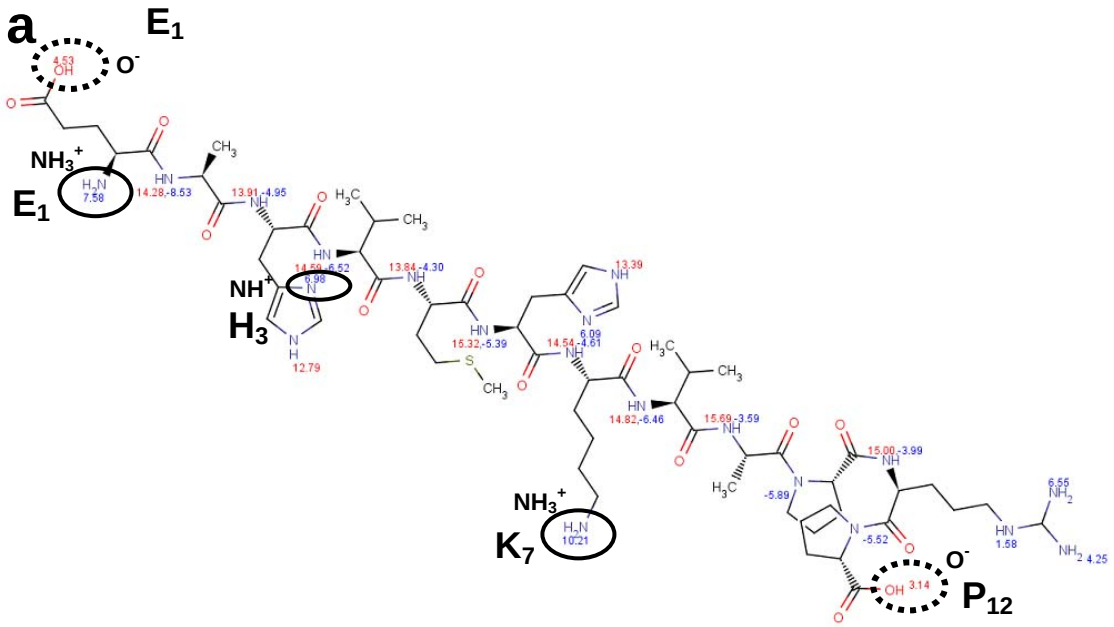

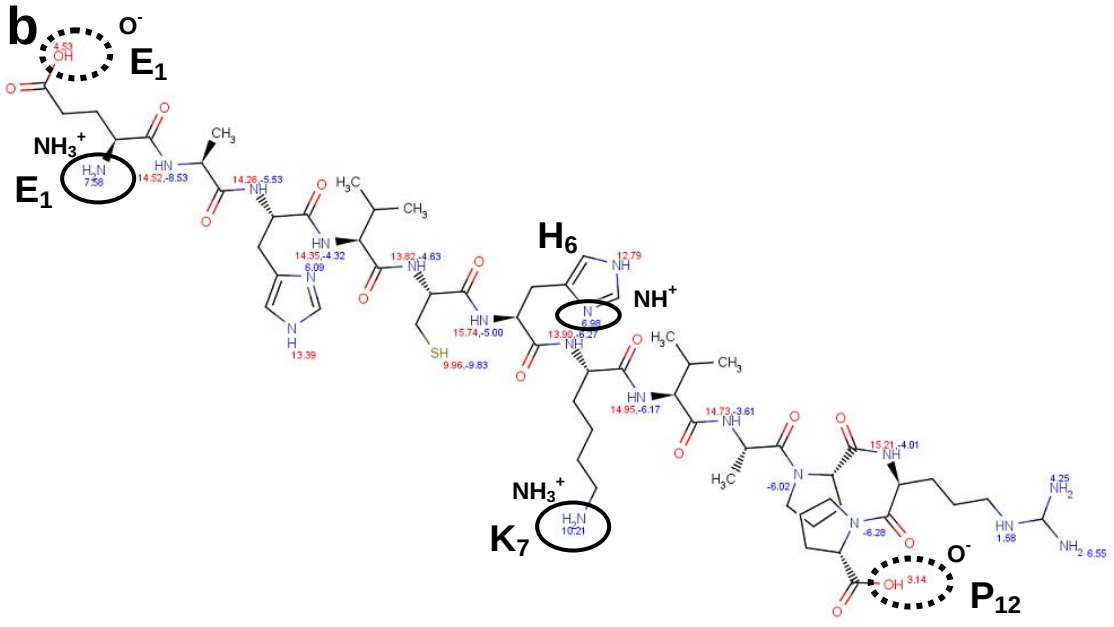

Appendix 5.4

The study of Co^{2+}-EM-12 complexation in pH 7 buffer containing HEPES and NaCl at room temperature was performed. Co^{2+} was selected for its comparable radius with that of Zn^{2+} and easy detection of Co^{2+} coordination using spectrophotometry. The results showed that EM-12 was too weak to displace Cl^- from $CoCl_2 \cdot 6H_2O$ which did not implied that EM-12 was incapable to form complexes with Zn^{2+}.

Materials

$CoCl_2 \cdot 6H_2O$ (Cobalt(II) chloride hexahydrate), HEPES (4-(2-hydroxyethyl)piperazine-1-ethanesulfonic acid, $C_8H_{18}N_2O_4S$), and NaCl (sodium chloride) were purchased from Sigma-Aldrich.

Method

80mM of $CoCl_2 \cdot 6H_2O$ was prepared in a pH 7 buffer solution containing 100mM HEPES and 50mM NaCl [Krizek et al. *Inorg. Chem.* **32**, 937-940 (1993)]. Test samples with 40mM $CoCl_2 \cdot 6H_2O$ and 0-8mM EM-12 were prepared. EC-12 was not tested due to insufficient material. Test samples were scanned using a Unicam UV2 UV-VIS spectrophotometer at 350-800nm after an incubation period of 1 hour. $CoCl_2 \cdot 6H_2O$ prepared in buffer solution appeared red and absorbing at 510nm. A colour change from red (510nm) to blue (640nm) was expected for a change of 6-coordination to 4-coordination.

Results

In the absence of EM-12, buffered $CoCl_2$ solution appeared red. However the addition of EM-12 did not turn the solution to blue but brown which intensified as [EM-12] was increased. The absorbance of solutions shown in (a) and (b) are for 40mM $CoCl_2$ with EM-12 of different concentrations and EM-12 with different concentrations respectively.

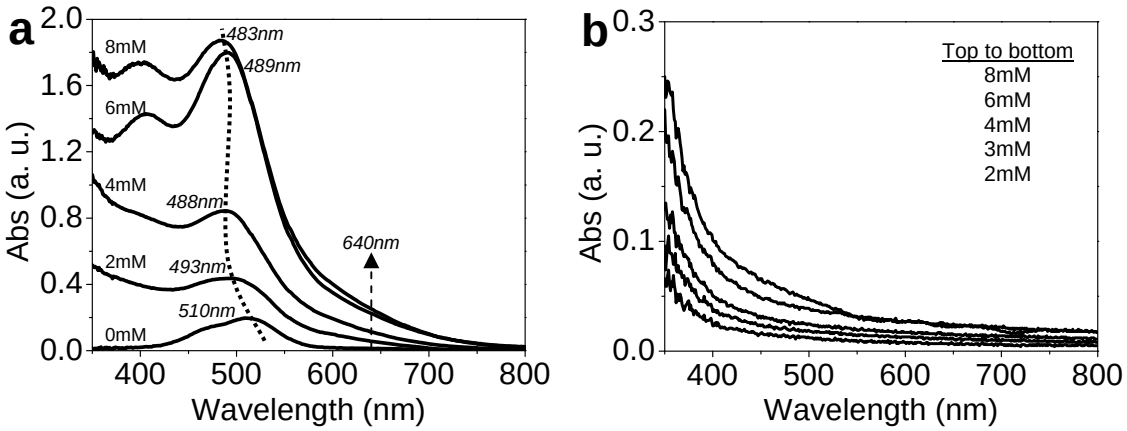

Appendix 5.5

SEM images of typical ZnO crystal morphologies obtained with different [EM-12], 0-0.3mM. Scale bars are 1μm.

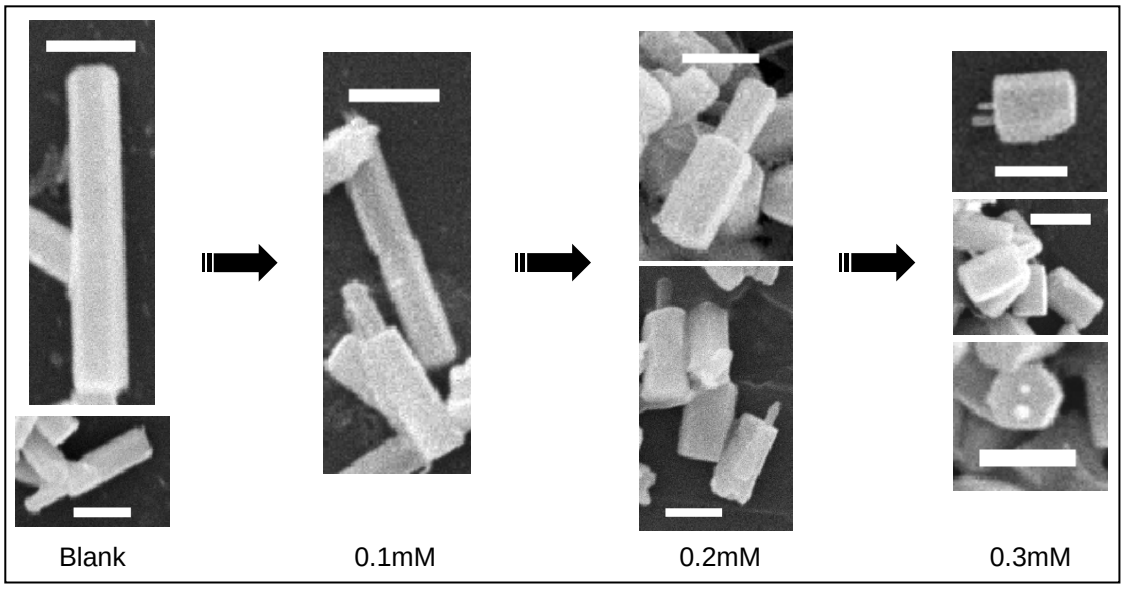

Glossary

A or Ala	Alanine
Ac10L	A leucine-rich peptide with peptide sequence Ac-KTAL10NPC-NH_2
AL	Adsorption Locator
ALD	Atomic layer deposition
ATR	Attenuated Total Reflectance
BCA	Bicinchoninic acid protein assay
BE or E_B	Binding energy
BSA	Bovine serum albumin
C or Cys	Cysteine
CBD	Chemical bath deposition
CI	Confidence interval. Statistics terminology
CSD	Cell surface display (combinatorial technique)
CuO-BPs	Copper oxide-binding peptides
δ	in-plane bending or deformation (FTIR)
D or Asp	Aspartic acid
DBCPs	Diblock copolymers
$\Delta D/\Delta t$	Average diameter growth rate
ddH_2O	Deionised-distilled water with conductivity $<1 \mu Scm^{-1}$
DMAB	Dimethylamineborane
$\Delta L/\Delta t$	Length growth rate
DP	Degree of polymerisation
DSC	Differential Scanning Calorimetry
E or Glu	Glutamate acid
EC-12	Zinc oxide-binding peptide with peptide sequence EAHVCHKVAPRP
EDXA	Energy Dispersive X-ray Analysis
E_g	Direct band gap
EM-12	Zinc oxide-binding peptide with peptide sequence EAHVMHKVAPRP
ESCA	Electron Spectroscopy for Chemical Analysis. Also known as XPS
ESM	Egg shell membrane
F or Phe	Phenylalanine
FE	Formation energy
FTIR	Fourier Transform Infrared
G or Gly	Glycine
G-12	Zinc oxide-binding peptide with peptide sequence GLHVMHKVAPPR
GM-collagen	Genetically modified-collagen-like triple helix peptide

GT-16	Zinc oxide-binding peptide with peptide sequence GLHVMHKVAPPRGGGC
H or His	Histidine
HCl	Hydrochloric acid
HF	Hydrofluoric acid
HMTA	Hexamethylenetetramine
I or Ile	Isoleusine
ICP-OES	Inductively Coupled Plasma-Optical Emission Spectrometry
IEP	Isoelectric point or point of zero charge
IR	Infrared
k_-	Apparent first-order rate constant for the dissociation of oligomeric silicic acid species into smaller oligomeric silicic acid species
K or Lys	Lysine
k_+	Apparent first-order rate constant for the condensation of monomer into larger oligomeric silicic acid species
K_2SiCat_3	Dipotassium silicon triscatecholate complex
k_3	Apparent third-order trimerisation rate constant for monosilicic acid
KBr	Potassium bromide
kDa	Kilo-dalton. 1 dalton=1g/mole
KE	Kinetic energy
KOH	Potassium hydroxide
L or Leu	Leusine
L/D	Aspect ratio or length-to-diameter ratio of crystals
L/D_{Avg}	Aspect ratio or length-to-average diameter ratio of crystals
LBZA	Layered basic zinc acetate
LBZS	Layered basic zinc salt
LCPAs	Long chain polyamines
M or Met	Methionine
Mat-BPs	Material-binding peptides
MD	Molecular dynamics
Micro-BCA assay	Micro-Bicinchoninic acid protein assay, more sensitive than BCA assay
MM	Molecular mass
M_w	Molecular weight
N or Asn	Asparagine
Na_2SO_3	Sodium silicate
ν_{as}	Asymmetric stretching vibration (FTIR)
natSil-$1A_1$	A subunit of natural silaffins extracted using ammonium fluoride
natSil-$1A_2$	A subunit of natural silaffins extracted using ammonium fluoride
natSil-1B	A 10kDa subunit of natural silaffins extracted using ammonium fluoride.
natSil-2	A 40kDa subunit of natural silaffins extracted using ammonium fluoride.
NH_3	Ammonia

NH_4F	Ammonium fluoride
ν_s	Symmetric stretching vibration (FTIR)
π	Out-of plane bending (FTIR)
P or Pro	Proline
P/P_0	Partial pressure
PAA	Poly(allylamine)
PAH	Poly(allylamine hydrochloride)
PAM	Polyacrylamide
PAM-COOH	Carboxyl-functionalised polyacrylamide
PBS	Phosphate buffer saline
PD	Phage display (combinatorial technique)
P-His	Polyhistidine
pI	Isoelectric point
PLA	Poly-$_L$-arginine
PLL	Poly-$_L$-lysine
PVI	Polyvinylimidazole
PVP	Polyvinylpyrrolidone
Q or Gln	Glutamine
R or Arg	Arginine
R5	19-mer precursor of silaffins-$1A_1$
	Peptide sequence SSKKSGSYSGSKGSKRRIL
ρ_r	Rocking (FTIR)
S or Ser	Serine
S. pombe	A single cell rod-shaped yeast
SDAs	Structure directing agents
SEM	Scanning Electron Microscopy
SF	Silk fibroin extracted from Bombyx mori silk
$Si(OH)_4$	Monosilicic acid
Sil-$1A_1$	A subunit of silaffins extracted using hydrofluoric acid
Sil-$1A_2$	A subunit of silaffins extracted using hydrofluoric acid
Sil-1B	A 8kDa subunit of silaffins extracted using hydrofluoric acid.
Sil-2	A 17kDa subunit of silaffins extracted using hydrofluoric acid.
Silicatein-α	A subunit of silicatein extracted from central filament of the spicules of sponges
	T. aurantia and *S. domuncula*
SiO_2-BPs	Silica-binding peptides
SPPS	Solid Phase Peptide Synthesis
T or Thr	Threonine
TEA	Triethanolamine
TEM	Transmission Electron Microscopy
TEOS	Tetraethoxysilane

TFA	Trifluoroacetic acid
TGA	Thermogravimetric Analysis
TMOS	Tetramethoxysilane
TZ1	A derivative of ZnO-BP identified from phage display library. Also labelled as GT-16
TZnO-1	A derivative of ZnO-BP identified from phage display library Also labelled as EC-12
UV-Vis	Ultra-violet and visible
V or Val	Valine
W or Trp	Tryptophan
WGM	Whispering gallery mode of optical emission observed where light was confined in the crystal by total internal reflection
WPI	Whey protein isolates
XPS	X-Ray Photoelectron Spectroscopy
XRD	X-Ray Diffraction
Y or Tyr	Tyrosine
Z1	A ZnO-BP identified from phage display library. Also labelled as G-12
$Zn(NO_3)_2$	Zinc nitrate hexahydrate
Zn^{2+}	Zinc ions
$[Zn^{2+}]$	Zinc ions concentration
$ZnAc_2$	Zinc acetate
ZnO	Zinc oxide
ZnO-1	A ZnO-BP identified from phage display library Also labelled as EM-12
ZnO-BPs	Zinc oxide-binding peptides (identified from combinatorial display libraries)

Publication

Mei-Keat Liang, Siddharth V. Patwardhan, Elena Danilovtseva, Vadim V. Annenkov, Carole C. Perry, Imidazole catalysed silica synthesis: progress toward understanding the role of histidine in (bio) silicification, *J. Mater. Res.*, **24**, 1700-1708 (2009)